Optimizing Image Fidelity with Arrays

Thesis by

Stuartt A. Corder

In Partial Fulfillment of the Requirements

for the Degree of

Doctor of Philosophy

California Institute of Technology

Pasadena, California

2009

(Defended August 29, 2008)

Acknowledgements

My thesis could not have been possible without the guidance and direction of my adviser, Anneila Sargent. Her advice on my writing will, eventually, result in more concise prose. On a daily basis, my interaction with John Carpenter has been invaluable and enjoyable. Whether discussing CARMA upgrades and issues or draining the three, John has been central to many aspects of my life here at Caltech. I wouldn't have continued in physical science without the influence of my undergraduate advisers, Bruce and Barbara Twarog and Bozenna Pasik-Duncan. I have been fortunate to attend lectures by two of the most talented instructors I have known, Sterl Phinney and Peter Goldreich. I have also benefited from the guidance of Geoff Blake and Nick Scoville, who were always willing and ready to discuss projects and approaches. Shri Kulkarni took an interest in my career here and always looked out for my best interests. I also would like to thank Bob Dickman for giving me some realistic advice. Mel Wright helped point me towards high-fidelity imaging studies and provided the seeds for all of the chapters of this thesis. I am grateful not only for his guidance but also for his laugh, which despite his often quiet demeanor was always ready to burst out. I would also like to thank Goran Sandell whose wealth of knowledge pertaining to NGC 7538 is remarkable.

My experience working with CARMA has brought me into contact with a great diversity of characters and I mean that in all possible senses of the word. Thanks also to the OVRO staff for putting up with me for some number of days no less than 225 (the exact number has been lost). Specifically, I would like to thank Tom Costa, Andy Beard, and Rick Hobbs for often following up the question of *Why do you want me to code this?* with *Okay, I'll do it.* Also, Cecil Patrick provided excellent

food in addition to enjoyable baseball conversation. Dave Woody, Steve Scott, James Lamb, Mark Hodges, Paul Rasmussen, and Dave Hawkins were always willing to explain technical details even if I didn't need to understand those details to do my job. Thanks to Curt, Russ, Paul D. and Terry for, among other things, a daily dose of laughter, especially on my more stressful days. In the early days at CARMA, life was often challenging. To Jin Koda and Andrew West, thanks for the sharing Christmas 2006 with Jennifer and me. Jenny Patience and I never transported water from the valley floor to provide ourselves with indoor plumbing, although indoor plumbing would have been nice. Bevin Zauderer shared by far the most painful of CARMA runs with me, and I mean that in a literal sense. She also relieved some of the pain associated with the editing this thesis. Many others have proved excellent company including Misty LaVigne, Dick Plambeck, Holly Maness, Alberto Bolatto, and Lisa Wei to name a few. Thanks to Laura Perez and Scott Schnee for picking up the graduate student-postdoc development torch.

Of my scientific collaborators among the students and postdocs at Caltech, I'd like to thank Kartik Sheth, Josh Eisner, and Hector Arce for making me finish what I started and telling me my ideas are not *that* crazy. The friendship and collaboration with my academic sibling Melissa Enoch will always be remembered. Milan Bogosavljevic and Brian Cameron are like brothers who never let me take myself too seriously. Adam Kraus has provided a link to home and someone who understands what it means to be a Jayhawk. Cathy Slesnick was a fast friend, a good thing in the early days of the small, dark room office. My other officemates, Laura, Margaret, Joanna, George, and Brian (J) have made the existence tolerable and were always willing to listen to (extended) complaints. The lunch crew provided a needed break, thanks to, among others, Dan and Larry. Special thanks to Karin for being there to share fears and frustrations in the late stages of writing this thesis.

Finally, I would like to thank my family, Jennifer and Vivian. Jennifer, without your support this would not have been possible. Thanks for your understanding and willingness to put up with so many nights with only a phone call. You amaze me.

For the adventures past, present, and future. For Jennifer.

Abstract

Through simulations, I have investigated the limitations imposed upon the image fidelity of interferometric observations by primary beam errors. Significant antenna surface and pointing errors lead to the greatest reduction in fidelity for most cases, but, when present, imaginary beam components dominate the degradation. Beam errors were addressed by optimizing the antenna surfaces and aligning the optics and then determining baseline based primary beams. Methods for applying these measured patterns to actual data were discussed. Pointing errors were reduced by improving the fit to the pointing model. Further reduction was achieved by integrating the use of optical pointing observations into standard radio observing. The greatest benefit was seen during daytime observations, but general reduction in pointing error was seen.

The dense uv-coverage of the Combined Array for Research in Millimeter-wave Astronomy (CARMA) coupled with the techniques described above make it an ideal instrument for imaging extended regions with high fidelity. The NGC 7538 star-forming cloud contains dense peaks, many high-mass stars and associated accretion disks, and multiple outflows. I obtained CARMA images at the requisite fidelity, employing the above techniques. These mosaiced, spectral-line, and 3-mm band continuum observations provide a clearer picture of the bulk morphology of the region and the fine-scale structures within it than has hitherto been possible. For the first time in the region, infall signatures were found towards two sources, allowing comparison of the infall and outflow mass and verifying that significant accretion ($>10^{-4}\,M_\odot\ yr^{-1}$) continues well into the stage where a massive protostar has formed. One of the sources, NGC 7538IRS1, shows one of the few definitive signatures of an inverse P-

Cygni profile towards a massive protostar. Three outflows were found centered on sources that are separated by 10,000-20,000 AU in projection. The calculated energy injection rate provides constraints for models of outflow feedback. The NGC 7538 results demonstrate clearly the capability of CARMA to provide high quality images over wide-fields and the benefits of the techniques I developed. While work to improve CARMA image fidelity continues, the program described here lays the groundwork and should help guide further enhancements of image fidelity at CARMA and at other radio facilities.

Contents

List of Figures

List of Tables

Chapter 1

Introduction

1.1 Into the Mainstream

As both single-dish radio telescopes and radio interferometers have gained in resolution and sensitivity, the traditional realms of observation–wide field of view, lower resolution and high resolution, smaller field of view, respectively–have become blended. Instead of using single-dish observations to map large areas and obtaining interferometric images to provide detail over single pointings, the advantages of imaging extended regions with high resolution are becoming evident. New arrays have recently entered into routine function (CARMA[1]) or are under construction (ALMA[2]) that begin to blur this distinction in the submillimeter regime as well. Both of these arrays have significantly enhanced sensitivity, resolution, and/or imaging capabilities when compared to existing arrays while being designed to sample the spatial scales of sources from the entire region mapped down to arcseconds or less.

Studies of sources with large spatial extent and/or large spatial scales are thus poised for significant gains. High resolution images (a few arcseconds or less) of such objects, which include the sun, planets, nearby protoplanetary disks, molecular clouds within the Galaxy, and nearby galaxies, are rarely achieved in the submillimeter regime. The mapping of nearby debris disks has revealed substructures on several spatial scales (e.g. Corder et al., 2008b; Koerner et al., 2001; Wilner et al.,

[1]Combined Array for Research in Millimeter-wave Astronomy
[2]Atacama Large Millimeter Array

2002). Nearby examples of debris disks may also have large spatial extent (e.g. ϵEri, Greaves et al., 2005). The dust in these disks is referred to as debris because the timescale for removal of such dust is much shorter than the age of the systems, i.e. it must be recreated by collisions (e.g. Backman & Paresce, 1993). Figure 1.1 shows an example of such a disk, which surrounds the nearby solar analog, HD 107146. Theoretical models (e.g. Wyatt, 2006) predict that structures in such disks are caused by resonances with orbiting planets. Planets often inferred from these studies are typically analogs to the solar system ice giants, a planet population that is not easily studied, especially at young ages, with any other method. If the planet formation process is to be understood, a full census of planets at such young ages is necessary. Such objects cannot yet be imaged at high resolution, a situation higher frequency observations with ALMA will remedy.

At greater distances, protoplanetary disks have revealed significant substructure. Figure 1.2 shows the complex morphology of the emission surrounding the young star AB Aur. The nature of this structure is poorly understood and may be the result of spiral arms or of infalling envelope material (Grady et al., 1999; Fukagawa et al., 2004; Corder et al., 2005; Piétu et al., 2005). The origin of these features awaits higher resolution observations with improved sensitivity to disentangle, but their nature provides vital constraints on the models of young disks and may indicate that gravitational instability is a valid method of forming massive planets (Boss, 2008). ALMA will observe such objects at very high frequency where the disks will fill a substantial fraction of the primary beam.

The mass distribution of these protostellar disks is also significant in that it allows estimates of the lifetimes and typical properties. In particular, the typical mass of the disks sets limits on which disks are likely to support the formation of planetary systems. Observations of populations of disks are typically carried out by mosaicing large areas in dense star forming regions (e.g. Carpenter, 2002; Eisner et al., 2008).

Nearby star-forming regions have been the subject of intense study, but little work has been done at high resolution over large areas. One of the most important questions regarding star formation is the origin and shape of the initial mass function

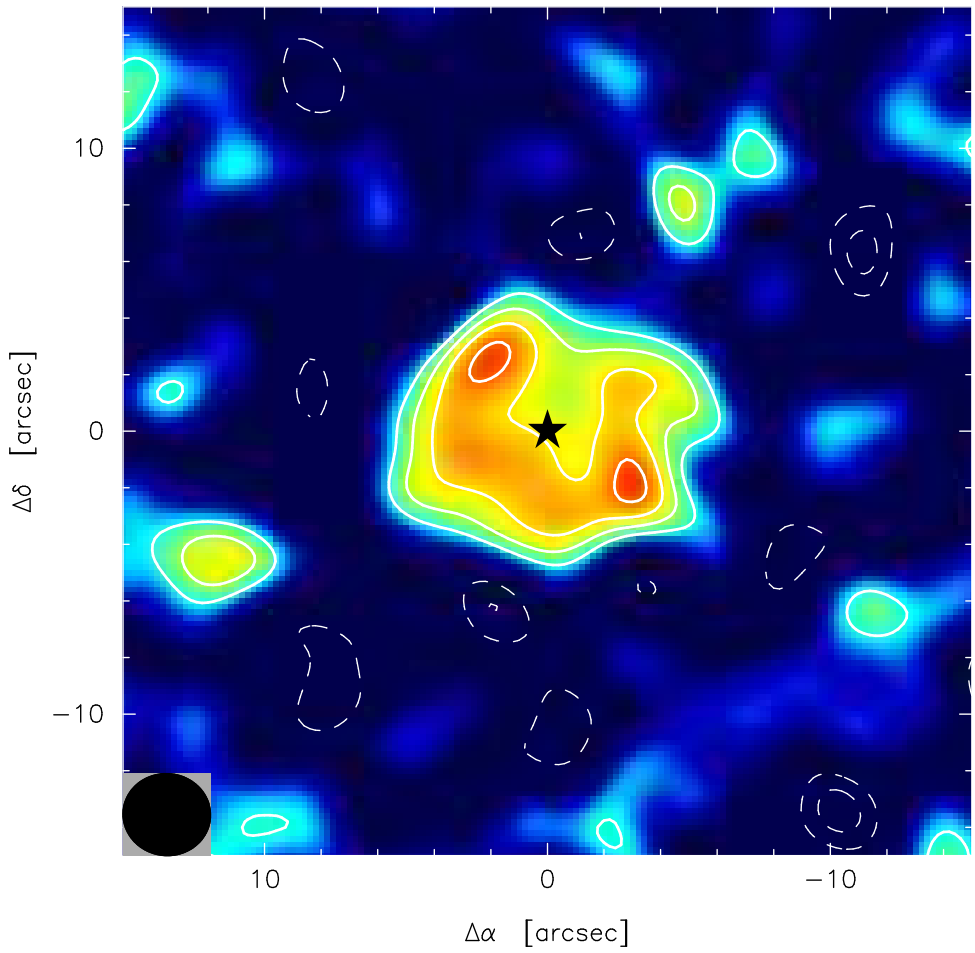

Figure 1.1 1.3 mm continuum emission from the disk surrounding the nearby, solar analog HD 107146 is shown. Contours begin at 2σ and increase by 1σ, where σ is 0.32 mJy beam^{-1}. The central region is depressed relative to an asymmetric ring. The star indicates the stellar position. The beam is shown in the lower left corner. This image is taken from Corder et al. (2008b).

(IMF). While measurement of this quantity has been studied extensively for stars, it is unclear whether the stellar IMF is a signature of the distribution of the clumps and cores from which the stars form or if some evolution has occurred. In the end, it is the IMF of the clumps and cores that constrain the models of star formation (Enoch, 2007). The size of these cores can be 3-5″ at the distance to the nearest star-forming

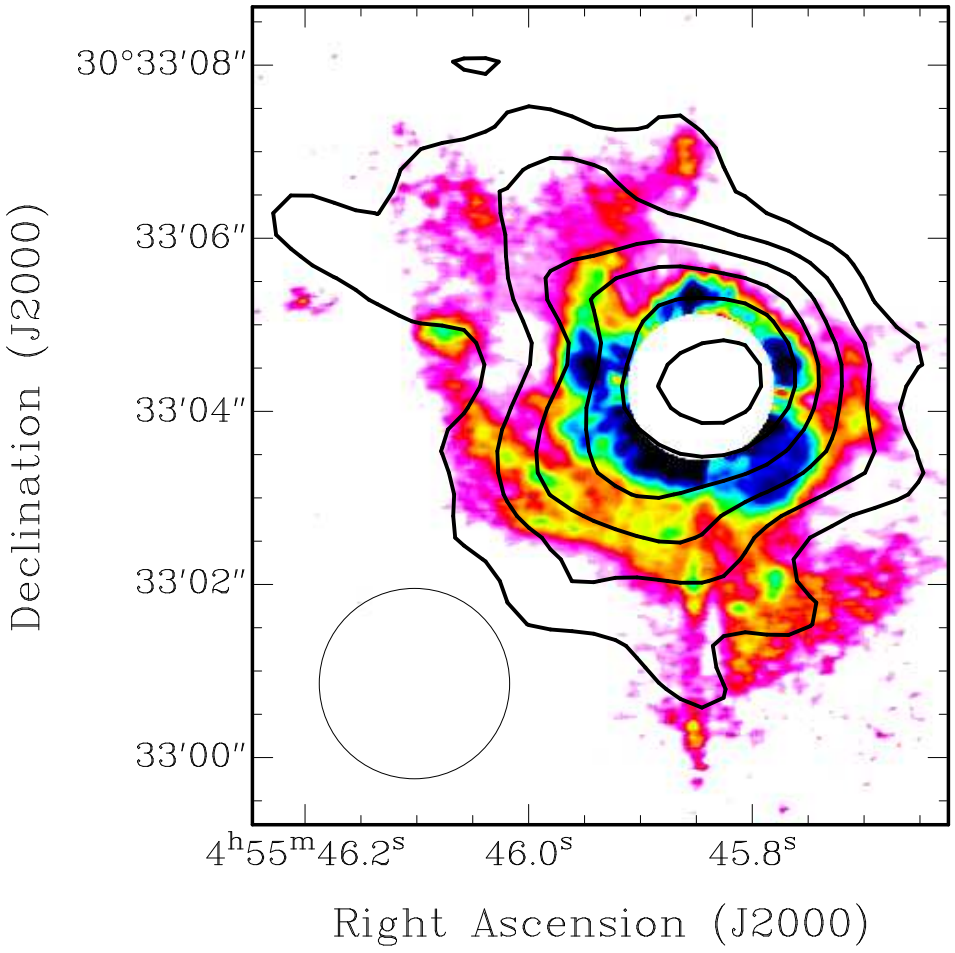

Figure 1.2 The near-infrared scattered light image of Fukagawa et al. (2004) is overlaid with 3 mm, continuum contours from Corder et al. (2005). The contours begin at 3σ, increasing in steps of 2σ=0.72 mJy beam^{-1}. The 3 mm continuum beam is shown in the lower left corner of the image. This figure was adapted from Corder et al. (2005).

regions. High resolution maps have been obtained (e.g. Testi & Sargent, 1998), but the field of view is somewhat limited. Wider field images of several such regions at high resolution are required to determine both the shape of the clump/core IMF and any environmental variations.

It is often difficult to see the big picture while embedded in the details. For this reason, observations of nearby galaxies can reveal properties of galactic structure that

cannot be easily discerned for the Milky Way. One long-standing question regarding nearby galaxies is the origin and properties of inter-arm H II regions and molecular clouds. Spurs, substructures associated with the spiral arms themselves and seen in Figure 1.3, seem to give rise to the inter-arm H II regions (Corder et al., 2008a; La Vigne et al., 2006). The mere presence of inter-arm molecular clouds has long been debated. Recent work by Koda et al. (2008) has revealed copious numbers of such clouds and has determined the apparent mass distribution of these objects, aiding the understanding of the origin of these clouds, the larger molecular associations seen in spiral arms, and global star formation. Nearby galaxies like M51 often cover many square arcminutes on the sky and require large ($\sim$150 pointing) mosaics. They also contain a variety of spatial scales with a nearly uniform component covering a substantial fraction of the disk, linear spiral arm features filling a fraction of the total area, and point-like molecular clouds populating the inter-arm region.

Arrays like the SMA (Submillimeter Array), CARMA, and ALMA allow efficient measurement of submillimeter continuum and line emission at several wavelengths at high resolution. Such multi-wavelength observations are critical. Through the measurement of line ratios, they allow the determination of opacity, temperature, and spectral indices. The spectral line emission also provides kinematic information. Together, these reveal the physical and dynamical structure of nearly every astrophysical object. In addition to the objects discussed above, supernova remnants, asymptotic giant branch stars, and other nebulae contain vital information uncovered through such ratios.

1.2 Lingering Doubt

From the above discussion, it is clear that submillimeter images of large objects and/or of large fields of view are critical to several fields of study. However, high dynamic range is often needed for these observations. The spiral arms of galaxies are bright while the inter-arm molecular clouds and spiral arm spurs are faint. Weakly emitting clumps of cold dust and gas in star-forming regions often occur clustered about bright

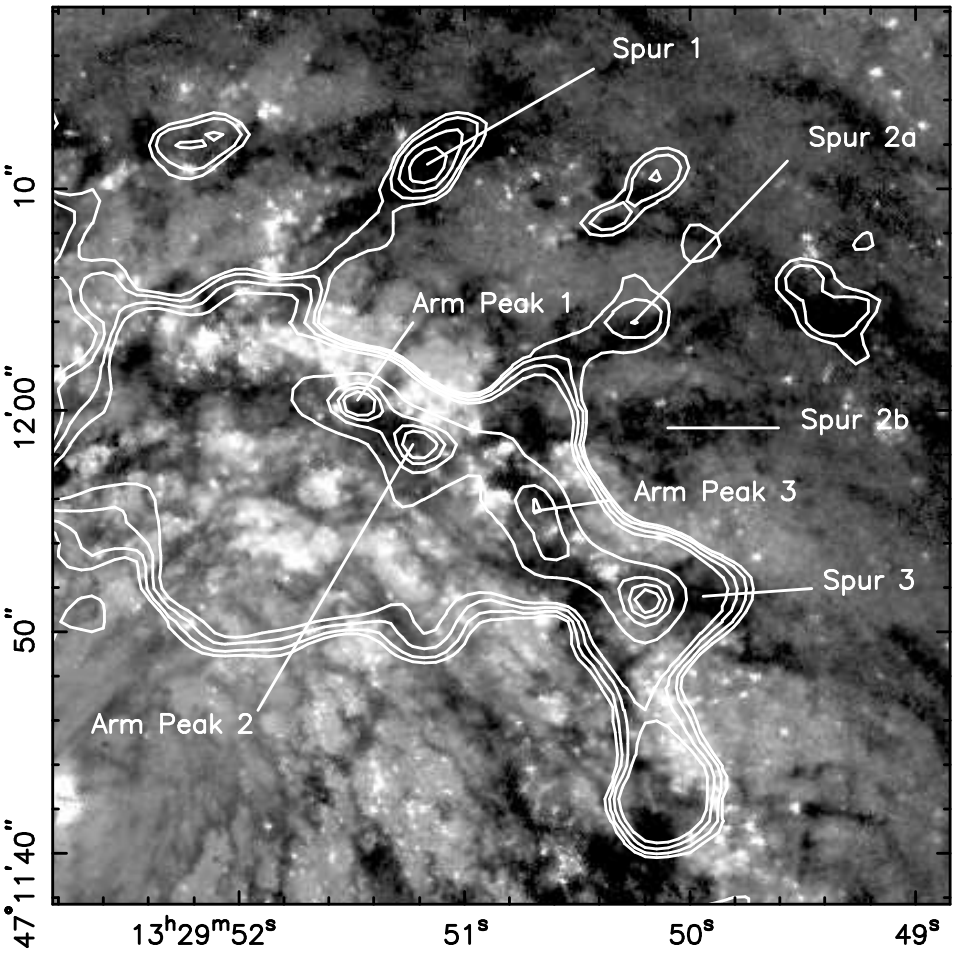

Figure 1.3 Integrated, ^{12}CO(1-0) emission from M51 is shown as contours on a Hubble Space Telescope V-band image. This figure was adapted from Corder et al. (2008a).

protostars. The bright spiral arm-like features or peaks seen in some protoplanetary disks may dominate the emission from the rest of the disk area. The question becomes *How accurate are the resulting images?* If the images are not accurate, the faint end slope of any mass function or the temperature or the mass density determined by any image ratio may be more poorly measured than the precision of the measurements would indicate. The answer to this question is best framed in the study of image fidelity.

The fidelity of an image is defined as the ratio of a well-determined model image, convolved to the resolution of the observations, to the difference between that model and an observed map. The image fidelity, in the most general case, is then an image itself. In practice, various methods are used to determine a single number for the fidelity that is representative of the average fidelity. In this work, image fidelity is determined by the peak of the model image, convolved to the resolution of the observations, normalized by the RMS of the difference between the model and observed map.

Consider the case of a measurement of the clump/core initial mass function. Due to the nature of star formation, protostars are often clustered. This is expected to be the case with natal clumps and cores of protostars as well. A map of a dense, cold cloud might contain sources with fluxes as bright as 200 to 300 mJy beam^{-1} while also harboring faint clumps with fluxes on the order of 3 mJy beam^{-1}, i.e. a ratio of 100. Now also assume that the thermal noise in emission-free parts of the map is $<$1 mJy beam^{-1}. An image of such a region might reveal several faint sources in the vicinity of the brightest peak. This may be evidence of clustered star formation. On the other hand, it may also be the result of poor image fidelity. If the fidelity of the image in the neighborhood of the brightest peak is on the order of 30, then the noise limit is better represented by 10 mJy beam^{-1} and the population of faint objects should not be considered as they would easily bias the determination of the faint end of the initial mass function. Therefore, it is clearly not simply the sensitivity limit which is of importance, but the fidelity as well.

In the above example, fidelity and dynamic range, the ratio of the peak to the RMS in an image, are interpreted similarly. Now consider a map of a nearby galaxy or star forming region in which ^{12}CO(2-1) and ^{13}CO(2-1) observations have been made. The ratio of the two lines gives an indication of the opacity. This opacity is then used to calculate column densities. If the medium is optically thin, then the ratio of the two lines should be between 40 and 89, depending on the physical conditions in the region. However, if one of the lines has poor fidelity, then the ratio is improperly determined. Gross errors in the opacity measurement directly translate into errors in

the mass and any mass moments that are calculated. A similar situation holds for ratios used to construct spectral indices.

Image fidelity is affected by a variety of factors. For single-dish observations, the critical limits come from gain and pointing stability. The most fundamental limit for interferometric observations is the number of samples obtained in the Fourier plane, i.e. the *uv*-coverage (Wright, 1999). Therefore, CARMA provides the best available opportunity for high fidelity, submillimeter imaging to date. CARMA is a heterogeneous array composed of six 10.4-m (hereafter 10-m) antennas and nine 6.1-m (hereafter 6-m) antennas.[3] The 105 simultaneous baselines exceeds other facilities by factors of 3.5 or more.[4] CARMA achieved first light in August of 2005 and has entered into routine function over the last three years.[5] Two significant components of that commissioning effort are discussed in Chapters 3 and 4. The CARMA bands are specifically well suited for observing emission from cold dust and molecular lines. Shorter wavelength bands prove significantly more problematic because of increased attenuation by the atmosphere and increased difficulties with tropospheric phase noise.

The heterogeneous nature of CARMA will eventually grant additional benefits via a unique method of increasing the *uv*-coverage. The 3.5-m and 6-m antennas can be placed at separations significantly less than 10 m. This allows observations using the 10-m antennas as single-dish telescopes, which measures the flux distribution on angular scales from the entire region to $\lambda/10400$, where λ is in millimeters. However, the limits to image fidelity are restricted by far more than incomplete Fourier coverage. Due to more stringent constraints on array performance, high fidelity in mosaiced, interferometric observations is significantly more difficult to achieve (Cornwell et al., 1993; Wright, 2004, 2007). In the near future with ALMA, a significantly larger fraction of projects will be limited by image fidelity because the sensitivity will be greatly increased over any existing facility.

[3]At the time of writing, eight 3.5-m antennas of the Sunyaev-Zeldovich Array (SZA) were moved to the location of CARMA and are currently being integrated into the array.

[4]The addition of the 3.5-m antennas increases this ratio to nearly a factor of 10.

[5]Further details regarding the specifications of the array can be found at www.mmarray.org.

1.3 Interferometry and Mosaicing

1.3.1 Basic Assumptions & Equations

Some of the earliest mosaiced, interferometric observations to include single-dish data to measure the largest scales included M31 and NGC 4258 (Bajaja & van Albada, 1979). Since then, algorithms for improved mosaic deconvolution and mosaic+single-dish combination have steadily improved. Initially, Ekers & Rots (1979) proposed that individual pointing centers be used to recover information on spacings in a neighborhood around the measured baseline, but Cornwell (1988) showed that joint deconvolution of all the mosaic pointings provides similar recovery. The development of the maximum entropy methods for joint deconvolution of mosaic and single-dish observations was also extremely important to the recovery of flux on sources which have a large range of spatial scales (Narayan & Nityananda, 1986; Cornwell & Evans, 1985). However, the desire for the combined benefits of single-dish telescopes and interferometric arrays brings with it a host of difficulties. Very few studies have attempted to address the concerns of fidelity with actual data (Wright et al., 1999) or simulation (Cornwell et al., 1993; Wright, 2004, 2007; Bhatnagar et al., 2008). The problems inherent in mosaicing along with methods for alleviating these challenges is the subject of this thesis.

Before embarking on a discussion of the difficulties inherent to mosaicing, it is important to review the basic equations of interferometry and the typical assumptions used. The signal, S_x, for an antenna is given by $S_x = S\sin(2\pi\nu t)$, where ν is the observing frequency, S is the input voltage amplitude, and t is time. Now, consider signals from two such antennas but with the antennas separated by a distance, D, observing the same source at a position with respect to zenith given by the angle θ. The product of the voltages is then calculated by the correlator.

The separation of the antennas gives rise to a (geometric) delay in the arrival of a signal between the antennas, given by $\tau_g = D\sin(\theta)/c = Dl/c$, where c is the speed of light and $l = \sin(\theta)$. The product of the signals now becomes $S_xS_y = S^2\sin(2\pi\nu t)\sin\left(2\pi\nu(t-\tau_g)\right) = S^2F$. This relation can be simplified to provide an

output of $F = \cos(2\pi\nu\tau_g) - \cos(4\pi\nu t) - \sin(4\pi\nu t)\sin(2\pi\nu\tau_g)$. The latter terms vary more rapidly than the first term, $\cos(2\pi\nu\tau_g) = \cos(2\pi\nu Dl/c)$, by several orders of magnitude in all terrestrial observing conditions and are therefore easily filtered out (Thompson et al., 2001). The voltage input is thus modulated by $F = \cos(2\pi\nu Dl/c)$, the fringe function.

Integration of the fringe function over a finite bandwidth, with central frequency ν_0, results in the fringe function evaluated at the bandwidth center modified by a function with amplitude that falls off with increasing τ_g or bandwidth. For this reason, an instrumental delay, τ_i, is introduced so that $S_x S_y = S^2 \sin\left(2\pi\nu(t-\tau_i)\right) \sin\left(2\pi\nu(t-\tau_g)\right) = S^2 F$ and $F \simeq \cos\Big(2\pi\nu(\tau_g - \tau_i)\Big)$. The value of τ_i is then updated to keep $\tau_g - \tau_i$ small. With this approach, angular offsets, $\Delta\theta$, are defined with respect to the direction θ_0, defined where $\tau_g = \tau_i$, so the fringe function, neglecting the bandwidth function, is $\cos\Big(2\pi\nu_0(D/c)\sin(\Delta\theta)\cos(\theta_0)\Big)$. Now, $l = \sin(\Delta\theta)$ and $u = \nu_0 D\cos(\theta_0)/c$ so that the fringe function, F, is now $\cos(2\pi ul)$.

For a source brightness distribution I, the illumination of the source by an interferometer baseline results in an output power, P, given by (e.g. Thompson et al., 2001):

$$P(l) \propto \int F(l-l')PB(l')H(l')I(l')dl'. \tag{1.1}$$

where PB is the baseline primary beam, and H is the bandwidth function. From the convolution theorem of Fourier transforms, the convolution of two functions is the same as the product of the Fourier transforms. The Fourier transform of F is simply the spatial frequency of a given baseline, while the transform of the brightness distribution, I, is the source visibility function $\mathcal{V}$. The form of H is typically well-known.

Now, generalizing to two dimensions, PB is the product of the two, complex antenna voltage patterns, V_1 and V_2, that constitute a baseline:

$$PB(l,m) = V_1(l,m)V_2^*(l,m) = V_1(l,m)V_1^*(l,m) = |V(l,m)|^2, \tag{1.2}$$

where the second and third equalities follow from the typical assumption that the

voltage patterns are uniform.[6] A given voltage pattern, V, is described by (e.g. Thompson et al., 2001):

$$V(l,m) = \int\int_{-\infty}^{\infty} E(X,Y) \exp\Big(2\pi i\Big[\frac{X}{\lambda}l + \frac{Y}{\lambda}m\Big]\Big) dX dY, \tag{1.3}$$

where E is the field pattern in the aperture, X and Y are positions in the aperture, and m and l are direction cosines on the sky. The field distribution in the aperture depends on the source distribution and the sensitivity to the structure in the aperture plane, i.e. it includes any alteration of the source signal from the illumination pattern and phase response. Typically, a number of assumptions are placed on these voltage patterns. It is customary to assume that a voltage pattern is real, circularly symmetric, and constant in time. It is also assumed that any gross, time variable, symmetric introduction of phase or gain error will be removed via astronomical calibration.

A PB for a specific baseline, given in Equation 1.2, modifies the source brightness distribution described in Equation 1.1, so that the effective brightness distribution convolved by the interferometer response is actually

$$I'(l,m) = PB(l,m)I(l,m) = V_1(l,m)V_2^*(l,m)I(l,m). \tag{1.4}$$

Provided the primary beam or constituent voltage patterns are well known, the true source brightness distribution can be easily recovered by dividing the altered brightness distribution pattern by the primary beam.

1.3.2 Assumptions Violated

In reality, all of the assumptions about the primary beams are not strictly true. The voltage patterns are very rarely perfectly symmetric, inducing a directional dependence on the sampled brightness distribution. Due to the altitude-azimuth mounts employed by most telescopes, this symmetry breaking directly implies a time variable pattern on the sky. The origin of the asymmetries may also change in magnitude and

[6]For CARMA there are different beam patterns but patterns from a given size of antenna are typically assumed uniform.

direction with changing physical conditions, specifically temperature and elevation. Misalignment of the antenna optics can induce phase gradients (to first order) across the voltage pattern that are also time variable and may depend on observing conditions. The most fundamental of errors in the primary beam, pointing, also induces this direction, time, and observing condition dependence on the primary beam pattern. Given that the antennas comprising the array are rarely going to have identical errors, the commonality assumption is also broken. The types of errors in the primary beam patterns will be elaborated upon in Chapter 2.

Even in the presence of these errors, if precise measurements of the voltage patterns can be obtained, the deviations caused to the attenuated sky brightness distribution can be corrected, although additional procedures are needed (see Chapter 2 or Bhatnagar et al. 2008). That is to say, the deviations of the voltage patterns from their symmetrized, real, common models are not a problem, but it is the lack of knowledge of the true voltage pattern which introduces the imaging errors and results in poor fidelity. However, such complete knowledge is difficult to obtain. Pointing errors of δl and δm in one antenna cause the source to be illuminated by

$$I'(l,m) = PB(l,m)I(l,m) = V_1(l-\delta l, m-\delta m)V_2^*(l,m)I(l,m) \tag{1.5}$$

instead of by Equation 1.4. When the final image is made, the synthesized image is divided by the voltage patterns as though the pointing error were not present.

Pointing is a particularly problematic source of primary beam error with respect to image fidelity. It causes the largest deviations from the assumed pattern at typical error levels. It is also varies most rapidly. Other types of error, e.g. ellipticity or beam size errors, introduce additional reductions to the image fidelity, but typically these are less significant. The decrease in fidelity caused by imaginary components in the voltage pattern has not been well characterized.

1.4 Thesis Outline

It is clear that improvement can be made to image fidelity by exploring the effects of the relaxation of standard assumptions about the primary beam and comparing the quantities which result in significant fidelity degradation to the measured deviations in a functioning system. To this end, we have conducted the following studies:

- **Chapter 2: Simulations:** Simulated observations are carried out to determine the magnitude of the reduction in image fidelity as a function of the deviation from standard primary beam model assumptions. A limited range of source models are considered which represent many of the typical observing situations described above. The simulations reveal that highly deviant surfaces, offset illumination patterns, and pointing errors are the leading causes of fidelity reduction. A method for utilizing the individual voltage patterns to correct observations is presented.

- **Chapter 3: Holography:** The surface accuracy of the CARMA dishes was measured. The surfaces were adjusted and the optics were aligned, resulting in significant improvement on the most deviant antennas. Once completed, repeated measurements of the voltage pattern on the sky revealed consistent, repeatable, and significant telescope-to-telescope variation in the voltage patterns implying that the imaging approach discussed in Chapter 2, which accounts for the independent voltage patterns, will likely improve the image quality.

- **Chapter 4: Pointing:** At the time of observation, the leading, correctable cause of fidelity degradation is pointing error. To improve the quality of pointing at CARMA, we created a new optical catalog which contains uniform sky coverage down to the magnitude limit of the current CARMA optical cameras. The data collection routines were modified to utilize the new catalog and decrease the measurement time per source. The new approaches resulted in nearly a factor of four improvement in the data collection rate. The resulting fits to the pointing model were improved with the RMS noise decreasing by a factor

of two. The method was extended to utilize the optical cameras for use during science observations first at night and then, through new software development, by day. The resulting decrease in pointing error during a science track was substantial. This method, called optical offset pointing, is currently used in most science observations at CARMA.

- **Chapter 5: Application to NGC 7538:** The new pointing routines, when possible, were applied to observations of the nearby massive star-forming region NGC 7538. The complex morphology of the region demands reasonably high image fidelity. It is compact, making it possible to mosaic a substantial fraction of the region in relatively few pointings. Spectral line and continuum observations were conducted. The methods of utilizing the measured primary beams were employed for a few pointing positions to determine if the dominant source of error in the images was primary beam errors or some other effect like delay or calibration errors. The high resolution, high fidelity images allow the identification of many outflow sources and association of these outflows with their driving source, the measurement of accretion rates directly from absorption profiles and outflow masses, and the resolution of the dense core NGC 7538S. In turn, these constrain models of massive star formation and massive star feedback.

Bibliography

Backman, D. E., & Paresce, F. 1993, Protostars and Planets III, 1253

Bajaja, E. & van Albada, G. D. 1979, A&A, 75, 251

Bhatnagar, S., Cornwell, T. J., Golap, K., & Uson, J. M. 2008, A&A, 487, 419

Boss, A. P., ApJ, 677, 607

Carpenter, J. M. 2002, AJ, 124, 1593

Corder, S. A., Eisner, J. E., & Sargent, A. I. 2005, ApJ, 622, L133

Corder, S. A., Sheth, K., Scoville, N. Z., Koda, J., Vogel, S. N., & Ostriker, E. 2008, ApJ, accepted

Corder, S. A. et al. 2008, ApJ, submitted

Cornwell, T. J. 1988, A&A, 202, 316

Cornwell, T. J. & Evans, K. F. 1985, A&A, 143, 77

Cornwell, T. J., Holdaway, M. A., & Uson, J. M. 1993, A&A, 271, 697

Eisner, J. A., Plambeck, R. L., Carpenter, J. M., Corder, S. A., Qi, C., & Wilner, D. 2008, ApJ, 683, 304

Ekers, R. D. & Rots, A. H. 1979, Image formation from Coherence Functions in Astronomy, Schoonveld, ed. Reidel, Dordreccht, p 61

Enoch, M. L. 2007, Ph. D. Thesis, Molecular clouds and star formation: a multiwavelength study of Perseus, Serpens and Ophiuchus

Fukagawa, M. et al. 2004, ApJ, 605, L53

Grady, C. A., Woodgate, B., Bruhweiler, F. C., Boggess, A., Plait, P, Lindler, D. J., Clampin, M, & Kalas, P. 1999, ApJ, 523, L151

Greaves, J. S. et al. 2005, ApJ, 619, L187

Koerner, D. W., Sargent, A. I., & Ostroff, N. A. 2001, ApJ, 560, L181

Koda et al. 2008, Nature, submitted

La Vigne, M. A., Vogel, S. N., & Ostriker, E. C. 2006, ApJ, 650, 818

Piétu, V., Guilloteau, S., & Dutrey, A. 2005, A&A, 443, 945

Narayan, R. & Nityananda, R. ARA&A, 24, 127

Thompson, A. R., Moran, J. M., & Swenson, G. W. 2001, Interferometry and Synthesis in Radio Astronomy, New York, Wiley-Interscience

Testi, L. & Sargent, A. I. 1998, ApJ, 508, L91

Wilner, D. J., Holman, M. J., Kuchner, M. J., & Ho, P. T. P. 2002, ApJ, 507, L115

Wright, M., Dickel, J., Koralesky, B., & Rudnick, L. ApJ, 518, 284

Wright, M. C. H. 1999, BIMA Memo Series 73

Wright, M. C. H. 2004, CARMA Memo Series 27

Wright, M. C. H. 2007, CARMA Memo Series 38

Wyatt, M. C.. 2006, ApJ, 639, 1153

Chapter 2

Simulations: Limitations on Dynamic Range and Image Fidelity For Wide Field Imaging

Abstract

Here we present simulations that include the effects of relaxing many typical assumptions about the interferometer primary beam on image fidelity. The degradation of image fidelity as a function of errors in pointing as well as errors in the assumed properties of the primary beam are simulated, allowing for heterogeneity among the constituent beams. Critical characteristics that must be corrected to some degree before high-fidelity imaging can be achieved include surface accuracy, optical alignment, and pointing. Once these deviations are addressed, a more accurate model of the primary beam shape is required to further improve fidelity. Using these simulations, we propose a method of correcting for deviant primary beams in real observations.

2.1 Introduction

The concepts of high image fidelity and dynamic range were provided in Chapter 1 along with their implications for scientific observations. A variety of factors can, however, restrict image fidelity. Some of these, including poor sensitivity, *uv*-coverage,

Portions of this were published as Carma Memo 43 (Wright & Corder)

and atmospheric phase noise, can be attributed to the inherent properties of the array being used. Others arise from more systematic errors such as baseline solutions, improper primary beam models, or instrumental gain variation.

Foremost among the inherent limitations is the fact that interferometers sample finitely many spatial scales. Consider, for example, the measurement of the visibility

$$\mathcal{V}^S(\vec{u}) = \sum_{k=1}^{K} \delta(\vec{u} - \vec{u}_k)\mathcal{V}(\vec{u}) \tag{2.1}$$

where $\mathcal{V}^S$ is the measured visibility function, $\mathcal{V}$ is the Fourier transform of the source flux distribution, i.e. the visibility function, δ is the delta function, and the points $\vec{u}_k$ (the uv-coverage) are the finite positions of measurement for the observation. In reality, the visibility function is averaged over a patch of uv-space of width $\vec{u} \pm d$, where d is the antenna diameter.

In the neighborhood of uv-points actually measured, i.e. over the range $\vec{u} \pm \delta\vec{u}$, some information can be recovered by the deconvolution process by making assumptions about the source extent (Cornwell, 1988), by inverting with respect to individual pointing centers (Ekers & Rots, 1979), or by use of Cauchy relations to constrain derivatives in the complex plane. Also, mosaicing observations allow recovery of information initially lost in averaging over the finite size of the antennas in use (Thompson et al., 2001).

However, the interferometer cannot sample the visibility function everywhere. The effect of this limitation is greatest in cases where there are few antennas in the array or where large regions requiring multiple pointings are observed. In the former case, the number of baselines sampling the uv-plane is inherently sparse. In the latter, the size of the region impacts the density of sampling of the uv-plane associated with individual patches of sky. In principle, repeated observations can fill in the uv-gaps generated by multiple pointings, but in practice this is extremely complicated and source size inevitably limits image fidelity (Wright, 2007).

Arrays like CARMA, with a significant number of antennas and thus dense uv-coverage, provide a marked improvement over previously existing arrays in the ability

to map sources that are large compared to the primary beam. Image fidelity is nevertheless limited by the inability to sample the central region of the uv-plane due to the finite physical size of the antennas. This central region of the uv-plane is associated with the largest angular scales in the map, scales which may contain the vast majority of the flux. On the other hand, heterogeneous arrays, like CARMA, offer a unique opportunity to overcome this limitation using the larger antennas to recover flux on the largest angular scales. In principle, there is no need to utilize smaller telescopes to bridge the uv-gap (Cornwell et al., 1993), but, in practice, overlap aids the relative calibration. A value of two (e.g. Thompson et al., 2001) is often quoted for the necessary ratio of large diameter antenna to smaller diameter antenna to obtain sufficient overlap, although a slightly smaller ratio is likely tolerable.[1]

Further limits to image fidelity exist. Array sensitivity limits fidelity since weak, but real, structure in a map cannot be accurately recovered. Atmospheric phase noise, causing preferential smearing of the smallest structures in the map, will also have an adverse effect on fidelity. These limitations are, at present, unavoidable, although efforts are being made to reduce such phase errors via comparison with phase fluctuations in the water line (water vapor radiometry) and the use of additional antennas to follow the phase on nearby quasars at lower frequencies. Other detriments to image fidelity arise from random and systematic effects that are, in principle, avoidable or at least can be minimized. Among these, imperfect knowledge of the primary beam presents the largest, correctable barrier to obtaining high-fidelity observations of extended objects (Cornwell et al., 1993).

Theoretical arguments and basic simulations that have been used to date to produce estimates of fidelity degradation in the presence of primary beam model error suffer from two fundamental limitations: they assume circular symmetry of the primary beams and they treat the antennas as identical entities. In reality, errors such as a misaligned illumination pattern on the antenna surface, sidelobes, off-axis focus error, or ellipticity in the primary beam result in significant deviations from sym-

[1]The limiting factor is imposed by the taper of the illumination pattern on the constituent antennas of the interferometer and on the single dish antenna. This causes reduced sensitivity in the overlapping region of uv-space.

metry. Since these systematic deviations are rarely uniform across all the antennas, the antennas cannot be regarded as uniform entities. Indeed, pointing errors alone result in the non-uniformity of antenna primary beams. The deviations among antennas result in decidedly different performance and may reduce fidelity in final image reconstruction.

More careful simulations can provide both quantitative measures of the decay of fidelity as a function of various parameters for different models and qualitative representations of the resulting changes in image appearance. However, to date, many difficult parameters have been simulated using simplifying approximations for errors. Specifically, pointing error has been simulated using gain error. Gain errors affect the fidelity by scaling the overall flux response. True pointing and primary beam error affect the image differentially, resulting in gradients across the illuminated sky relative to the assumed illumination.

Here, we present a suite of simulations encompassing various departures from the standard primary beam assumptions. While these simulations are specific to CARMA, the methods are easily generalizable to any array. In practice, the degree of fidelity decay is highly dependent on the exact source structure. We focus on situations where fidelity and dynamic range are likely to be of concern. These simulations, in turn, motivate corrective methods for use in real-time (described in Chapters 3 and 4) and in data processing (described in Chapter 5). Source models and the variables are discussed in §2.2, while the simulations are outlined in §2.3. The simulation results are presented in §2.4 and discussed in §2.5. Conclusions and suggestions for future work are in §2.6.

2.2 Models & Variables

Three general models are considered here. Point source and resolved Gaussian source models represent a large fraction of typical observations with interferometers and have rather simple structure. The third model, shown in Figure 2.1 at the scale used in these simulations, is based on an image of the supernova remnant Cas A taken

with the Very Large Array at C-band (11 GHz). This provides a model that is a reasonable approximation for extended[2] sources such as nearby galaxies, supernova remnants, some debris disks, and asymptotic giant branch stars. In the case of Cas A, the integrated flux of the map is over 700 Jy and the peak flux is ∼10 Jy. This rather large flux ensures that the simulations are truly in the fidelity limited regime, since typical thermal noise in a single, mosaiced, continuum track at CARMA is a few mJy. The Cas A model shown in Figure 2.1 has significant flux out to 100-m baselines, showing that the source indeed has flux on a variety of spatial scales.

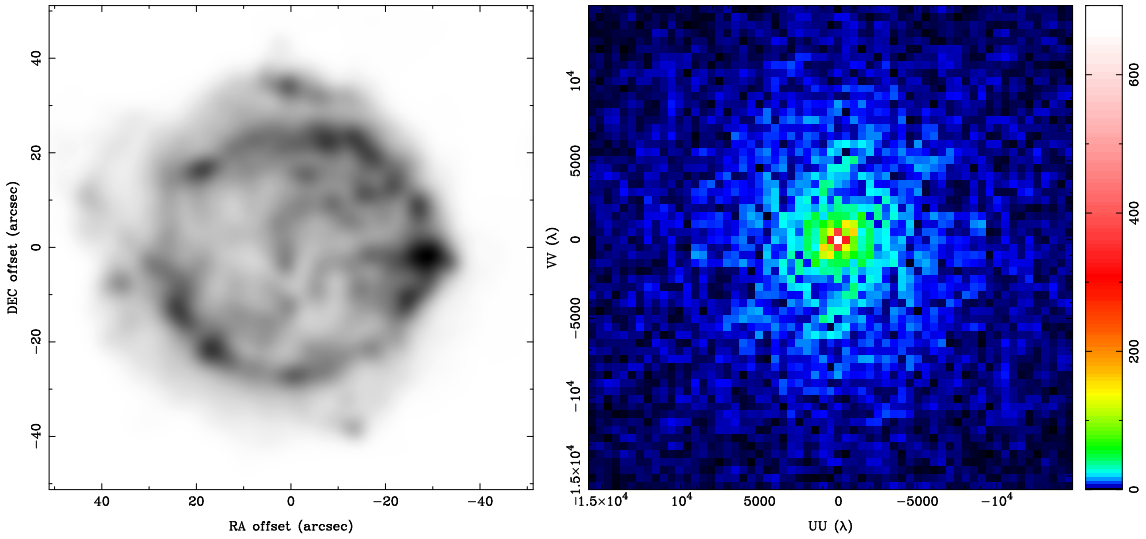

Figure 2.1 The model is a C-band image of the supernova remnant, Cas A. The left panel shows the source scaled to cover a region comparable with the FWHM of the 10-m primary beam. The right panel shows the flux amplitude of the model in the Fourier plane with the pixel scale in Janskys. The axes in the right panel are in units of λ =2.6 cm.

In reality, it is not errors in the primary beam which are a problem but, more specifically, deviations of the assumed primary beam from the actual one which degrade fidelity. In these simulations, the assumption is that a *realistic* primary beam is

[2]In this context, an extended source is one whose spatial extent is comparable to or larger than the primary beam rather than a source which is simply resolved.

used to illuminate the source on the sky and then the *assumed*, model primary beam is used in the imaging process. Image fidelity is affected by other systematic errors as well, but most of these errors are introduced by more fundamental limitations in the array performance.

The primary beam is the product of two, antenna-based, complex voltage patterns given by Equation 1.2. The measured visibility function, $\mathcal{V}^M(\vec{u})$[3] is related to the voltage patterns, V, through

$$\mathcal{V}^M(\vec{u}) \propto \int_{-\infty}^{\infty} V_i(\vec{k}) V_j(\vec{k}) I(\vec{k}) \mathrm{e}^{-2i\pi(\vec{k}\cdot\vec{u})} d\vec{k}, \tag{2.2}$$

where I is the source brightness distribution and the bandwidth function has been ignored since it is assumed to be well known. If one or both of the voltage patterns differ from the assumed model, then $V_i(\vec{k})$ must be replaced by some altered voltage pattern, $V_i'(\vec{k})$. However, since $V_i(\vec{k})$ is still used in the final image construction process via the primary beam, errors in the voltage patterns can adversely affect the measured visibilities and the primary beam correction during the image restoration process.

At the most basic level, deviations from the ideal primary beam are caused by errors in the antenna surfaces that in turn reduce forward gain. While the antenna gain can be measured relatively precisely, flux scattered by small scale imperfections in the antenna surface pollutes the image with a scattered beam outside the main beam. The scale of such deviations is typically a fraction of a wavelength ($\leq$100 μm at millimeter wavelengths), and not systematic for well functioning millimeter telescopes (see Chapter 3). Since it is extremely difficult to model such small scale variations, these errors can be approximated by gain errors, $\delta G = 1 - \exp(-[4\pi\sigma/\lambda]^2)$ where σ is the surface accuracy and λ is the observing wavelength (Ruze, 1966). This representation for the error assumes that the surface/phase errors are Gaussian random numbers which are distributed evenly over the aperture and that the correlation size

[3]This is to distinguish between the visibility function altered by the illumination patterns, the true visibility function $\mathcal{V}$, and the visibility function that arises from the finite sampling of the array, $\mathcal{V}^S$.

scales are much smaller than the diameter of the surface. For a 30-μm RMS surface error, the resulting gain errors are 1.6% and 8.0% at 3 mm and 1.3 mm, respectively.

The next order of primary beam error is simply due to uncertainty in the assumed center of the primary beam, i.e. a pointing error. Consider the case of two, 1-D Gaussian patterns, of widths and σ_1 and σ_2, and one of the patterns is perfectly pointed while the other is offset by μ, the resulting primary beam has width $\sigma^2_{new} = \sigma^2_1\sigma^2_2/(\sigma^2_1 + \sigma^2_2)$, center $\mu_{new} = \mu\sigma^2_1/(\sigma^2_1 + \sigma^2_2)$, and peak

$$A = \exp\Big(\frac{-\mu^2}{2\sigma^2_2}\Big[1 - \frac{\sigma^2_1}{\sigma^2_1 + \sigma^2_2}\Big]\Big), \tag{2.3}$$

where in the limit of $\sigma_1 = \sigma_2 = \sigma$ these reduce to $\sigma^2_{new} = \sigma^2/2$, $\mu_{new} = \mu/2$, and $A = \exp\,(-(\mu/2\sigma)^2)$. For a pair of 10-m antennas, the forward gain is reduced by 1% for antennas offset by 5″ but reaches 5% by a 11.5″ offset. For 6-m antennas, the same 11.5″ error results in a 2% gain error.

It is worth noting that for sources of any finite extent,[4] pointing error does more than reduce the forward gain. The extension of the source and the offset location of the beam center results in a differential effect, as demonstrated in Figure 2.2. A comparison of the upper left and right panels shows the impact of an illuminating beam offset from the true center for a disk model. The errors in the flux reach $\pm$25% at the edge of the disk and are distributed as a linear gradient. The pointing error assumed for this model is within 2 standard deviations of the nominal pointing position based on the repeatability of CARMA pointing offsets (see Chapter 4).

As will be described in detail in Chapter 3, the correct width and shape of the primary beam can be established from detailed measurements of the beam on the sky. In practice, current software imaging packages utilize circularly symmetric profiles for the primary beams. MIRIAD, the default imaging package for CARMA, currently uses a circularly symmetric Gaussian profile for the CARMA primary beams. Errors can be introduced if the size of the profile differs from that assumed in the model. The bottom-left panel of Figure 2.2 shows that this effect results in a quadratic variation

[4]The use of extended is avoided here as the effects to be discussed apply to sources of any measurable extent not just to sources that are large compared to the primary beam.

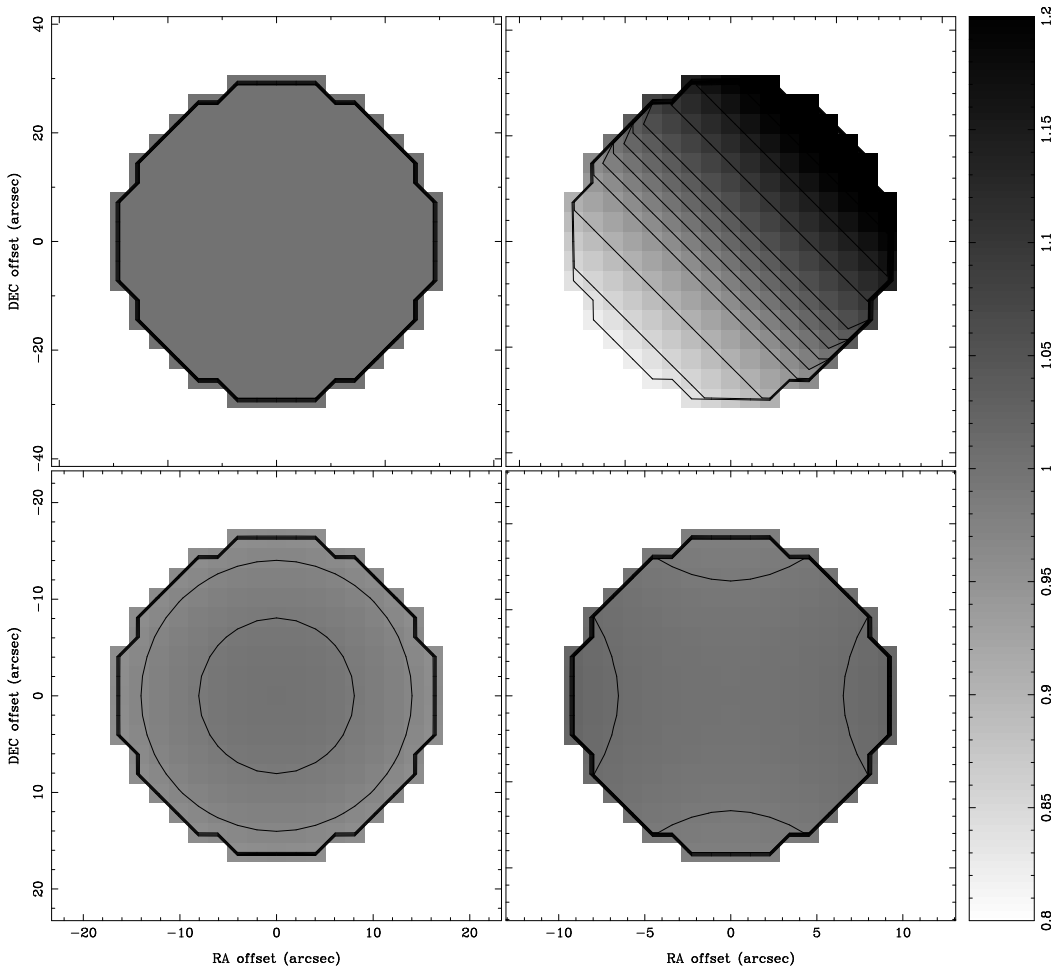

Figure 2.2 The top-left panel shows a uniform disk where the beam used to illuminate the source was also used to correct the final image. The top-right panel shows a primary beam offset by 8% of the FWHM from the nominal pointing location. The bottom-left panel shows the disk restored with a primary beam 3% different in size from the beam model. The bottom-right panel shows the disk illuminated by a beam which has an ellipticity of 3% but of the same size as the beam model. The model disk has unit flux per pixel and is equal to the size of the FWHM of the beam in question. The pixel scale ranges from 0.8 to 1.2. The contours also span 0.8 to 1.2, initially in steps of 0.05. Inside 0.95 and 1.05, the contours are in intervals of 0.02.

across the disk with perfect agreement at the beam center and growing deviation towards the edges. The errors induced, however, are relatively small when compared to the pointing gradient. Further, but still circularly symmetric, deviation from the

MIRIAD models for the CARMA primary beam profiles can come from the deviation of the profile from a Gaussian. The true shape of the beam compared to a Gaussian profile is discussed in detail in Chapter 3. In general, the beam profile appears to be flatter (i.e. wider) in the beam core compared to a Gaussian but steeper (i.e. narrower) than the Gaussian profile in the wings.

To a lesser extent, errors can result from slight deviations from circular symmetry even when the adopted primary beam size is correct. This ellipticity is defined as $e = a_{major}/a_{minor}$, where a_{major} and a_{minor} are Gaussian fits to the FWHM of the beam profile. The bottom right panel of Figure 2.2 shows the influence of 3% ellipticity ($e = 1.03$). Here the error pattern is quadrupolar in shape. Several methods of introducing ellipticity can be envisioned. A common ellipticity for a given antenna style, i.e. all 6-m antennas and all 10-m antennas, with a position angle of 0° could be used. Or, the ellipticity could remain fixed on antennas of a common diameter but the position angle of the ellipticity could vary. Finally, an independent ellipticity and position angle on an antenna basis may arise.

Sidelobes can also be asymmetric. The primary beam of the heterogeneous baselines at CARMA is formed by the geometric mean of the primary beams from the constituent antennas. The low-level sidelobes of the 10-m primary beam are multiplied by higher power points in the 6-m primary beam, resulting in increased sidelobes.

Measurement of the ellipticity, departures from Gaussian profiles, and sidelobe patterns are, in practice, quite difficult. In particular, the ellipticity and sidelobe patterns of the profile can change appreciably with elevation and temperature. A long-term campaign to monitor the primary beam profiles would be necessary to say with certainty that a systematic ellipticity is present or that sidelobe patterns are consistent. Even then, determination of the true primary beam profile would require further observations to average over temporal changes and noise in the inherently less sensitive portions of the beam which typically harbor the deviations.

In addition to any departures from Gaussian profiles, it should be noted that the elements of an array can differ from each other. In reality, CARMA, or any other array, is not an array of $N + \binom{N}{2}$ different primary beam types where N is the number

of distinct antenna types; it is an array of $\binom{M}{2}$ different primary beams where M is the number of antennas, i.e. M independent voltage patterns form independent primary beams on a baseline basis. These antenna voltage patterns might have different sizes, ellipticities, pointing offsets, and even imaginary components. In the limit of common antenna voltage patterns for all antennas, the imaginary components of the beam cancel perfectly in the imaginary beam but these components can give rise to ellipticity in the real component.

If patterns differ, as they in fact do for every antenna in every array, the imaginary components may seriously influence the image fidelity. The panels of Figure 2.3 show examples of baseline-based, homogeneous and heterogeneous primary beams from CARMA. The top panels show the primary beams for a pair baselines composed entirely of 10-m antennas, hereafter a 10-m baseline. On the left, the constituent voltage patterns have imaginary gradients in opposite directions resulting in an amplified gradient of +20% to -15% across the image. On the top-right, the contributing voltage patterns have small imaginary components and thus have peak imaginary components of 6%. The bottom left panel shows a heterogeneous baseline where the 6-m antenna voltage pattern is imaginary component-free, but it illuminates a 10-m antenna voltage pattern which has a significant imaginary component so the gradient persists. The bottom right panel shows a primary beam from a baseline composed of two 6-m antennas, hereafter a 6-m baseline, which are largely free of imaginary contribution. In all, these four examples demonstrate that the assumption of uniformity is far from valid.

2.3 Simulations

All simulations are conducted using MIRIAD (Sault, Teuben, & Wright, 1995), wrapped within Python and supplemented with IDL to perform free rotations of the beams to arbitrary parallactic angle.[5] Simulations are carried out at 100.2 GHz

[5]The names of MIRIAD routines are given in bold while Python based functions of importance are in italics.

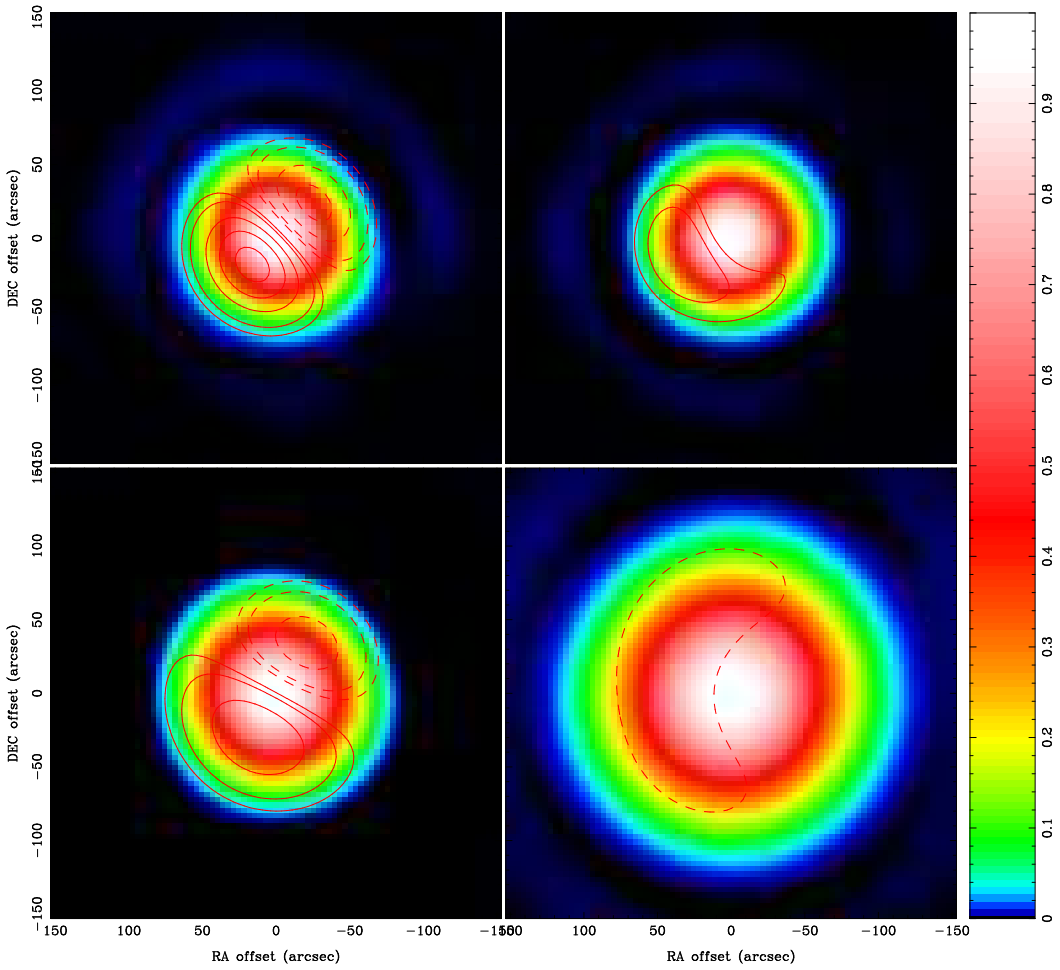

Figure 2.3 A variety of measured real (color) and imaginary (contour) primary beams are shown for a heterogeneous array. The first two contours are at 3% and 5% and then contours increase by 5% thereafter. Negative contours are shown as dashed lines. The top panels display primary beams from 10-m baselines. The bottom left panel shows the primary beam from a heterogeneous baseline while the bottom right shows a 6-m baseline primary beam.

since the true voltage patterns are measured at this frequency (see Chapter 3). It is easy to scale the frequency of the templates used by changing the cell size in the voltage pattern by a factor of the ratio of the frequencies. Only the influence of gain and primary beam error are addressed here, although the simulation package includes a variety of additional parameters, providing a generalized suite.

For the purposes of these simulations, only the CARMA "D" configuration, which gives a resolution of 4-5″ in the 3-mm band, is used. Nyquist sampled pointing offsets for mosaics are used for all simulations. Observations of Cas A consisted of a seven pointing mosaic. Simulated observations span 4 hours centered about transit. A variety of metrics are required to assess the resulting image quality. The basic metric for the simulations will be fidelity, defined as the ratio of the peak flux of the model at the simulation resolution and RMS of the residual image. For Gaussian and point source models, fits to the image profile are also used to determine the quality of the simulated observations.

Simulations begin by separating the specified observing time into subsets since asymmetric beam patterns or real pointing errors require a time evolving pattern. Over the specified time range, *uv*-data for an empty field is generated using **uvgen**, which requires information on antenna performance, configuration, and mosaic pattern, as well as the location of the source to be used in the simulation. The average parallactic angle of the model source is then retrieved from the generated dataset. For each pointing location in the mosaic pattern and antenna pair, the model image is multiplied by the product of two offset voltage patterns resulting in, for the most general case, a real and imaginary brightness distribution. Figure 2.4 shows various primary-beam-illuminated pointings of the Cas A model.

Once the baseline-specific, single-pointing, primary-beam-illuminated model is available, the image is fed to **uvmodel**, using the output of **uvgen** as the baseline visibility file. This produces a file which adds the noise of the original visibility file to the visibilities of the model sampled at the values given by **uvgen**. First the real component is sampled, then the result is fed to **uvmodel** again, now using the imaginary component of the brightness distribution and the option **imaginary**, which permutes the components and changes sign for proper complex algebra.

Gain error is introduced as a percentage of the antenna gain, nominally 1.0. The amplitudes of the simulated visibilities are multiplied by an antenna based quantity, independent for each antenna, that has a value distributed as a Gaussian random variable with mean one and RMS equal to the requested percentage gain error. For

the pointing error, the RMS is reduced by a factor of $10.4/D$, where D is the antenna diameter in meters.[6] A new random number is generated and applied every 30 minutes. This is on the order of the thermal time constant for the antennas. Alteration of this timescale has negligible effect on the final results. Gain errors are introduced where relevant by an additional call to **uvgen** now using a point source at the phase center as the model. A **selfcal** solution is then generated and the resulting gain solution is copied and applied to the simulated visibility datasets for the model. In the limit of no gain error this has the effect of multiplying the model visibilities by a constant function with value 1.

The resulting, baseline-, pointing-, and parallactic angle-based *uv*-files are then merged. The visibilities from the merged file are then imaged using MIRIAD's **invert** task. Deconvolution is done with the task **mosmem**, except for point source models where **mossdi** is employed. The model image is resampled onto the field and cell size of the simulated image and then convolved to the resolution of the simulation. The images are then differenced. This residual image is used to calculate an RMS. The peak of the regrided, convolved model divided by this residual defines the image fidelity. In the case of the Gaussian model, fits to the image are made to compare shearing and size. Figure 2.5 shows an example of the Cas A simulated image, the model convolved to the proper resolution and the residual image stretched by a factor of 50 to emphasize the errors.

The voltage patterns used to illuminate the model are generated in a variety of ways. As a baseline measurement, voltage pattern models identical to those used in MIRIAD for the primary beam correction process were generated using **imgen**. Variations from this size and variations in ellipticity were generated in a similar way. For the elliptical patterns, the size was held fixed to the MIRIAD model allowing only variation in the ellipticity and position angle. In the case of ellipticity, and all non-circularly symmetric patterns, a library of patterns was created in intervals of 20°

[6] One could imagine that the pointing-like gain errors should not be independent antenna to antenna, especially for day-time use where common pointing offsets occur. The simulator is not currently set-up for this approach but can easily be modified to do so.

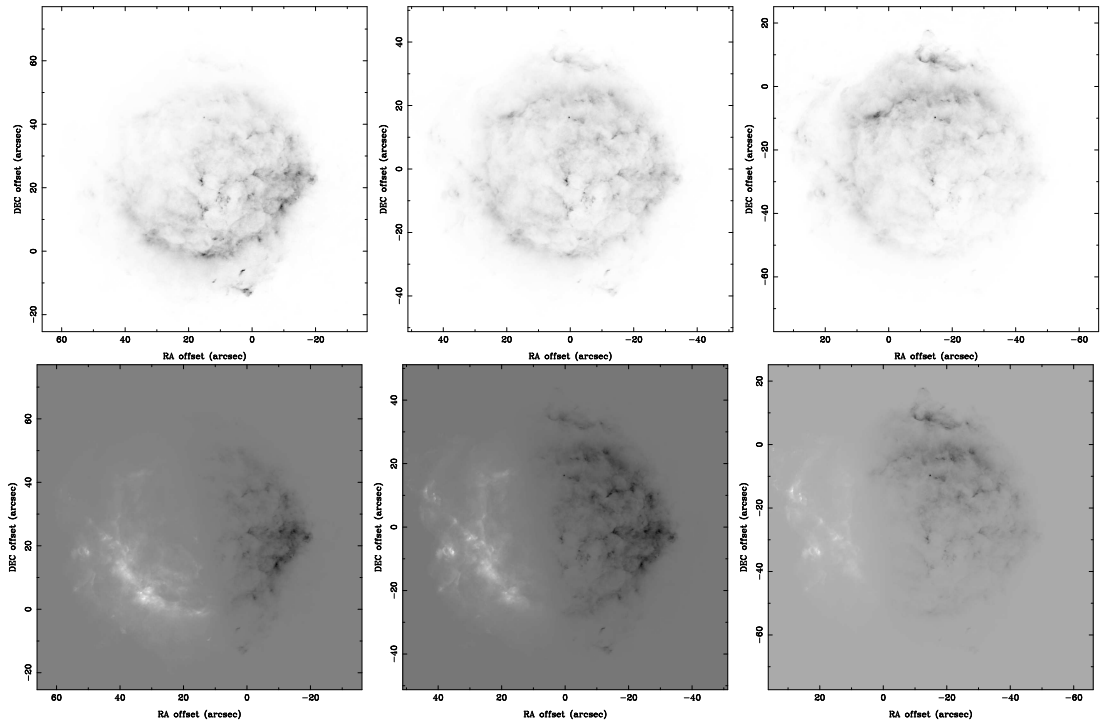

Figure 2.4 The Cas A model is shown illuminated by the real (top) and imaginary (bottom) voltage patterns for pointing offsets to the southwest (left), center (middle) and northeast (right). The pixel scale for the real components is such that white pixels are zero. The imaginary images span positive and negative values and thus have gray zero points. The imaginary component has been stretched by a factor of 30 relative to the real component to emphasize the structure.

of rotation to allow for appropriate application based on parallactic angle. A library of voltage patterns based on actual measurement is also available.

2.4 Results

The types of errors modeled are discussed in §2.2. To summarize, the variables tested are: gain error to approximate surface and pointing error, real pointing error, beam size error and beam ellipticity. The resulting range of fidelity is compared to the fidelity obtained using the measured voltage patterns.

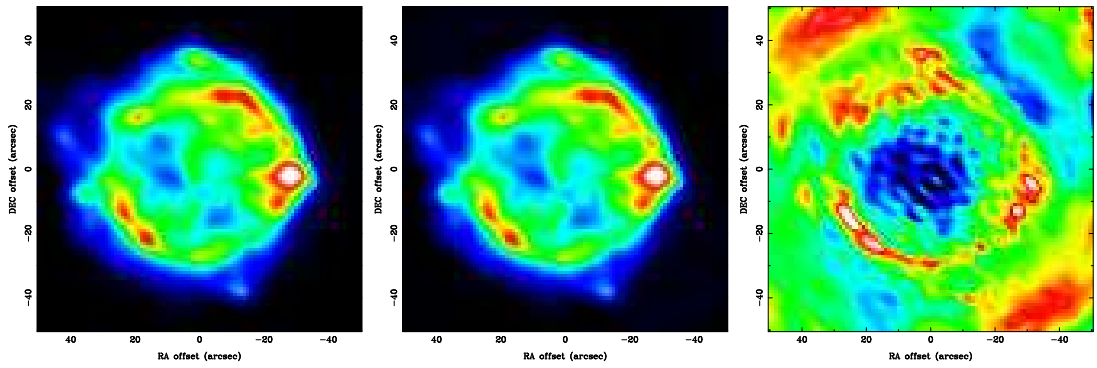

Figure 2.5 The left panel describes the model image convolved to the resolution of the simulated image while the center panel is the simulation of the model. In the right panel, the residual image has been stretched by a factor of 50 to highlight differences between the model and simulation. The peak in the residual image is 2.3% of the peak in the model image.

2.4.1 Gain & Pointing Errors

Gain error can act either like surface inaccuracies or pointing error, depending on whether its behavior is linked to the antenna size. Figure 2.6 shows the trend in image fidelity for the Cas A simulated image as a function of percentage gain error. The left panel is strictly gain error, while in the right panel gain errors are scaled by the antenna diameter to approximate pointing errors. Since the goal is to address whether gain error is a useful proxy for pointing error, only extended sources are relevant. Evidently, gain errors of 7-8% reduce fidelity by a factor of 2 in the "pointing-like" gain error case; a smaller gain error, 4%, is needed in the surface error case to similarly reduce the fidelity.

Figure 2.7 shows the influence of actual pointing error on the image fidelity of the Cas A model. Here, random offsets were generated and the RMS values of the random offsets were scaled to the effective gain error for a point source to allow easy comparison to Figure 2.6. The illumination pattern based on the voltage patterns is offset to the nominal pointing pattern position and then perturbed by one of these

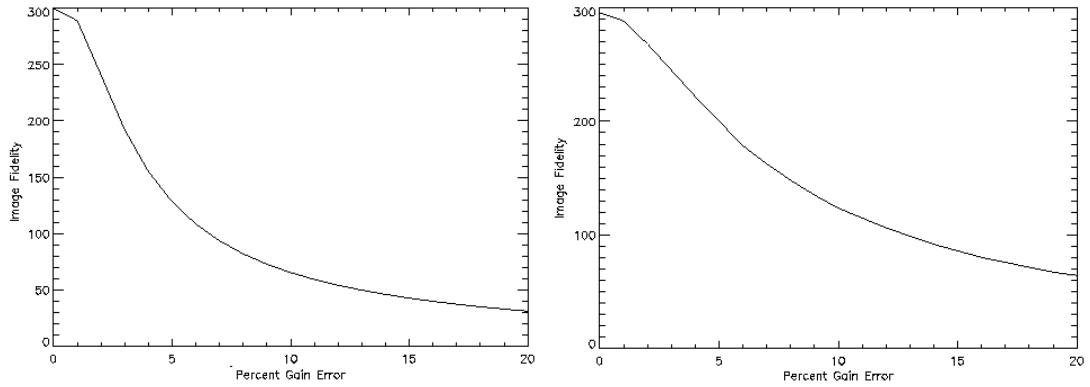

Figure 2.6 The image fidelity of the simulated Cas A model is plotted versus percentage gain error. In the left panel the gain error is applied directly, while the right panel displays the gain error scaled by the antenna diameter to approximate pointing error.

random amounts on an antenna by antenna basis. The offsets are updated every 2 hours. The choppy appearance of the curve in Figure 2.7 is a result of this poor time sampling for a given simulation, i.e. a given pointing error RMS. A finer time sampling of the simulation would enable better sampling of the random distribution of pointing offsets and result in a smoother curve.

For the point source and Gaussian models, there is a similar trend with reduced fidelity as the pointing error increases. The flux of the centrally located Gaussian and point source models strictly decreases with increasing pointing error. For sources located at increasingly greater distances from the center of the beam the decay in fidelity is somewhat more rapid when compared to the sources located at the center of the beam. The trend in flux is less systematic. For the Gaussian models, there is no discernible trend in the difference between the known and best-fit widths with offset position or pointing error. The general effect is to scatter flux and create specific artifacts but not to alter the flux distribution in the immediate vicinity of the source.

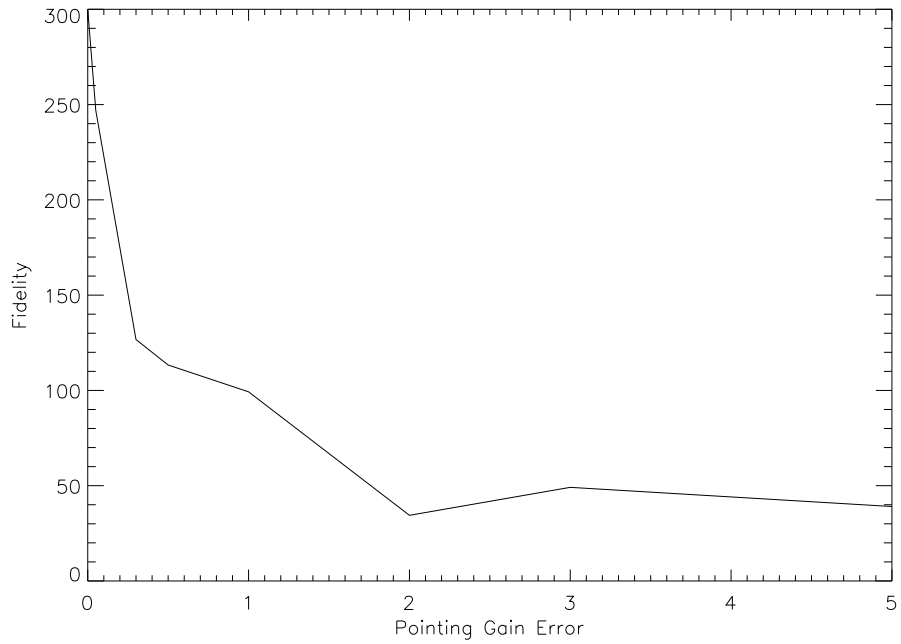

Figure 2.7 As in Figure 2.6, the image fidelity of the simulated Cas A model is plotted as a function of gain error with gain error calculated from the true pointing error assuming a point source, i.e. the simulations were conducted using actual offset illumination patterns but that offset was converted to a common gain error for plotting. For example, 5% gain error is 11.5″and 19.5″ for the 10 and 6-m antennas, respectively. At 2%, the RMS pointing error was 7.5″ and 12″. 0.5% represents a pointing error of 3.5″ and 6.5″.

2.4.2 Beam Size Error & Ellipticity

Figure 2.8 shows the change in fidelity of the Cas A model for changes in the beam size. The beam size was altered by ±1, ±3, ±5, and ±7% over the nominal MIRIAD beam model. The influence of the changes in beam size is most marked on the Cas A model. It is clear from the plot that even marginal error in the beam size, 1%, can cause appreciable degradation in the image quality. By 3% error, the fidelity has been reduced by a factor of two. The use of best-fit Gaussian models to the actual voltage

patterns of the CARMA antennas (square point) has only marginally poorer fidelity than the MIRIAD models.

For the centrally located point source and Gaussian source models there is no change to the fidelity, flux or width as a function of beam size. This is not surprising given that the sources occupy a very small fraction of the central portion of the beam. However, if the Gaussian source is moved around the beam, fidelity is reduced. There is some evidence that the decay in fidelity is somewhat faster for the altered beams when compared to the nominal beam model but the dominant decay in fidelity is common to all realizations of the beam width. Regardless of beam, the decay appears to be roughly linear, with slope, in terms of percent reduction in fidelity, -3.6% per arcsecond of offset from center. The recovered flux varies more or less linearly with error in beam size, with narrower than expected widths providing lower than expected fluxes and wider than expected widths providing more flux. The trend grows more steep as the source is further offset from the beam center. There is no obvious trend in source size with position or beam size.

Figure 2.9 shows the fidelity degradation for the Cas A model as a function of increasing ellipticity, where ellipticity is common to all antennas of a given size and fixed at a position angle of 0. This model of the ellipticity was selected for display because it is the most physically motivated of the three possible models described above. An ellipticity of 1% results in little to no image degradation. The ellipticity required to reduce the fidelity by a factor of two is about 10%.

As was the case for beam size, the influence of ellipticity on the width, position, and flux of the Gaussian and point source models is small unless the source is moved away from the beam center. There is little difference in the fidelity of images taken with beams of 5% and 9% ellipticity, except in extreme cases where the source is more than 15″ from the beam center. In such cases, there is measurable difference between the two levels of ellipticity but the overall reduction when compared to the perfect beam model at the same location is on the order of a few percent.

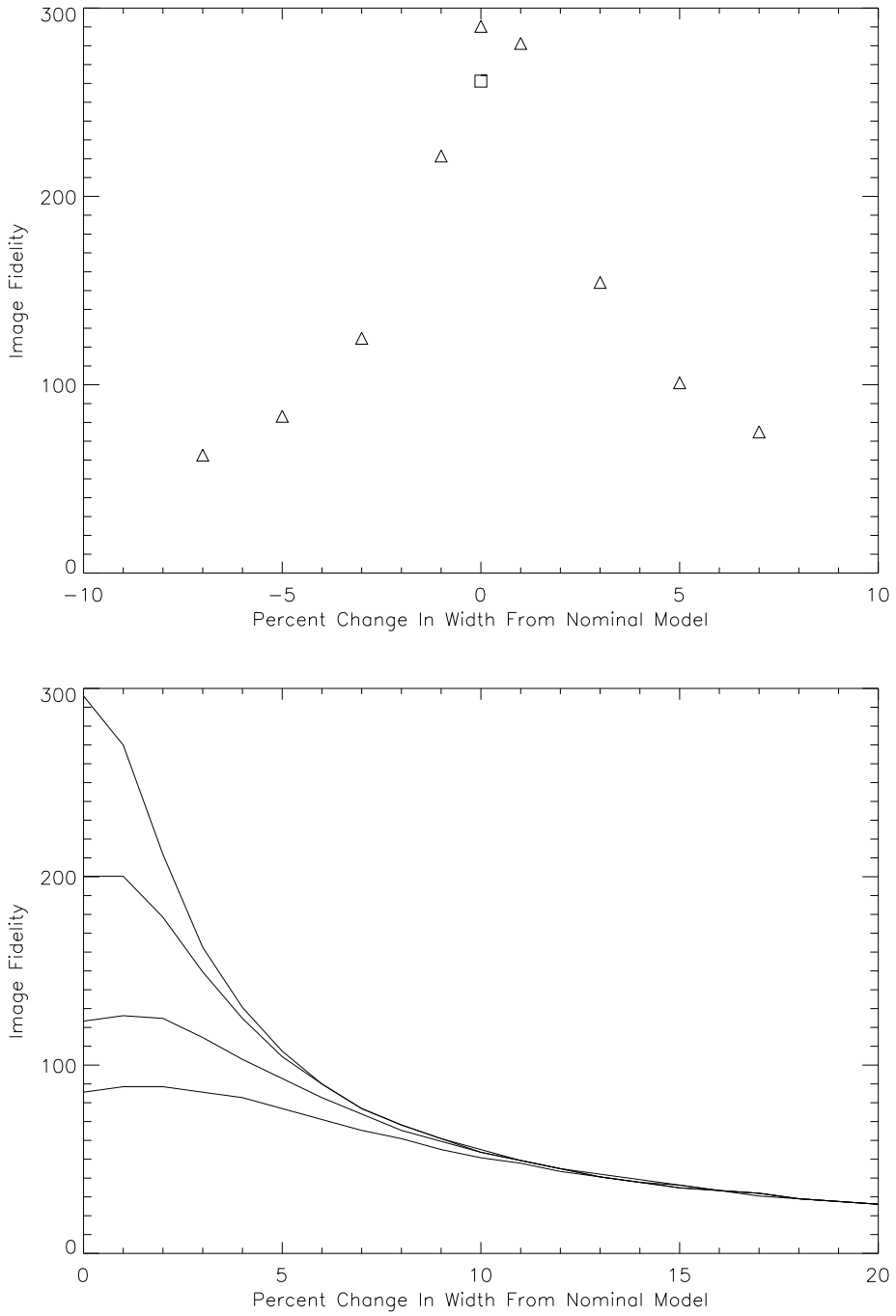

Figure 2.8 The image fidelity of the simulated Cas A model is plotted against percentage difference in the beam size from the nominal beam model used in MIRIAD (top). The square point represents the use of the best-fit, circularly-symmetric Gaussian models to the actual voltage patterns. The bottom image shows a family of curves where the fidelity is plotted as a function of error in the beam width. Each curve is 0, 5, 10, and 15% gain error with the highest curve representing 0% gain error.

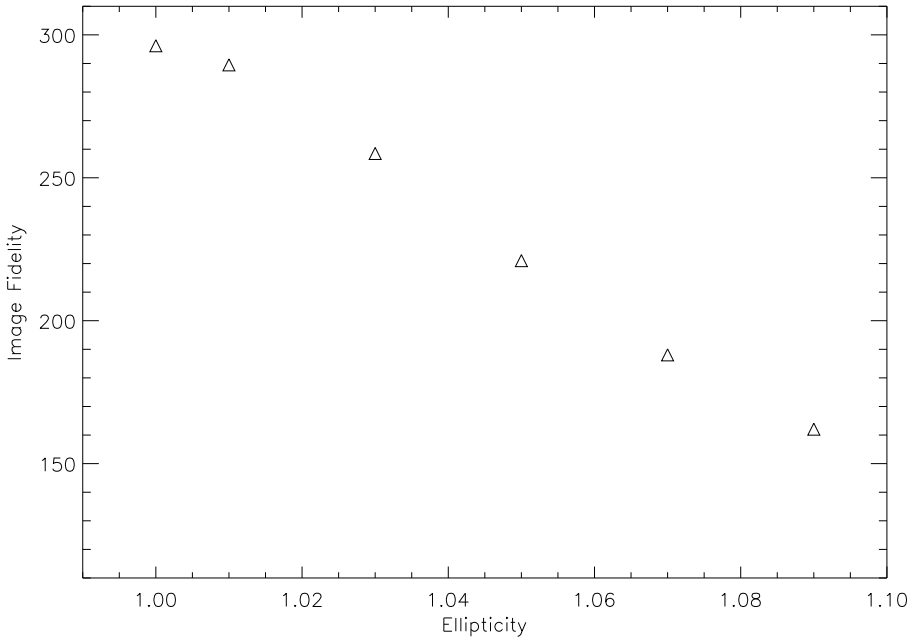

Figure 2.9 The image fidelity of the simulated Cas A model is plotted against the voltage pattern ellipticity. The geometric mean of the voltage pattern axes is equal to the assumed pattern width, i.e. if the MIRIAD model beam has radius r, then the altered beam has semi-major axes a and b such that $ab = r^2$, but a does not equal b.

2.4.3 Measured Voltage Patterns

Simulations using the measured voltage patterns as a function of antenna style were also conducted (see Chapter 3 for a discussion of the measurement). In this, a common pattern was used for all 6-m, 10-m, and heterogeneous baselines. This "style" based pattern includes the influence of the different width compared to the MIRIAD model, an ellipticity in the 6-m antennas and deviations from Gaussian profiles, i.e. all standard primary beam assumptions are relaxed aside from uniformity and realness. Taking the best achievable fidelity as 300, the use of these "style" based patterns results in a factor of two degradation of the image fidelity, to 152. This is the case with perfect pointing and no gain error. The fidelity can only fall in the presence

of other such errors. For the single pointing, Gaussian and point source models, the influence of the "style" beam is less pronounced, providing a fidelity which is ∼75-80% of the perfect beam model. The trend in fidelity decay with increasing distance from the beam center is comparable to the perfect beam model case.

In Chapter 3, the voltage patterns are determined to be decidedly non-uniform and to have measurable imaginary components. The fidelity of the Cas A model, using the measured, antenna-based voltage patterns, falls further still, to 63. If the antenna with the largest imaginary component is replaced by a perfect voltage pattern, the fidelity grows but only to ∼90. Unlike the beam width and ellipticity, the fidelity of the Gaussian and point source model simulations is strongly affected. In these cases the degradation in fidelity grows from a factor of 1.5-2 at the center to a factor of 3-4 at a 15″ offset. This decay is far more rapid than the decay in fidelity seen in other parameters. There is a possible trend in increasing width with increasing offset, although the dominant trend is in the Gaussian-fit ellipticity. At the center, the best-fit Gaussian gives an ellipticity of <0.5%, echoing the 0% ellipticity of the input model. As the source is moved farther out in the beam, the ellipticity grows to as much as 20%. The imaginary components are shearing the flux distribution on the sky, resulting in deconvolved sizes which are far more elliptical than the input model. For a point source at the phase center, this effect is minimal but for distributed point sources, the measured size strongly depends on the presence and form of any imaginary components.

2.5 Discussion

2.5.1 Gain & Pointing Error

The left panel of Figure 2.6 is intended as a proxy for surface accuracy. The fidelity drops by approximately a factor of 2 at a gain error of 4%, or 50 μm surface accuracy at λ =3 mm. This accuracy is not particularly difficult to obtain but half of the maximum fidelity is hardly a reasonable benchmark. The fidelity drops by 10% with

a gain error of approximately 1.5%, which is a surface RMS of about 30 μm, again at λ =3 mm. At λ =1.3 mm, such a surface RMS equates to a much larger gain error, about 8%, and subsequent loss of fidelity, about a factor of 3. Allowing even slightly larger surface RMS, 35 μm or more, reduces the 3 mm fidelity by a third. Clearly, an RMS of 35 μm is a reasonable criterion for 3 mm observations but for high fidelity at 1.3 mm, the accuracy needs to be far greater, $<$20 μm.

When gain is used as a proxy for pointing error, fidelity drops by a factor of two at 10% gain error. At 5% gain error the reduction is over 30%. Converting these gains to pointing error, the 5% point corresponds to 19″ and 11.5″ for the voltage patterns of the 6- and 10-m antennas, respectively. The fact that this is a factor of 3 more than the pointing RMS at CARMA (see Chapter 4) suggests that, if gain is a good proxy for pointing error, then pointing error is not a particularly strong detriment to image fidelity. Indeed, a gain error of 0.5% is equivalent to the standard pointing RMS values at CARMA. The situation induces slightly more concern in the 1.3 mm case where typical pointing RMS is equivalent to a gain error of 2%.

However, a quick comparison of the left panel of Figure 2.6 and Figure 2.7 reveals that antenna diameter scaled gain errors do not represent a particularly good proxy for pointing error. Indeed, this is not entirely surprising since gain error only includes one of the impacts of pointing errors, i.e. the loss of forward gain. It should be noted that finer time sampling of Figure 2.7 would likely result in a slower decay in fidelity with pointing error due to the limitations in the current implementation. However, even with that caveat, fidelity drops by a factor of two somewhere between 0.3% to 0.5% gain error, or 2-3″ and 4-6.5″ in the 3-mm band for the 10-m and 6-m antennas, respectively. This is more on the order of typical good pointing performance at CARMA and is certainly better than typical daytime pointing accuracy. This supports the argument that pointing error may indeed be a significant source of fidelity degradation even in the 3-mm band. In the 1-mm band, a pointing RMS of less than 1″ is needed for minimal reduction in image fidelity. Unlike the prediction from antenna diameter-scaled gain error, true pointing error severely limits the image fidelity even under conditions of modest pointing error.

As the Gaussian and point sources are placed farther from the phase center, the fidelity decreases more and more rapidly as a function of pointing errors. This is due to the steeper response of the beam at greater distances, i.e. if one calculates the factional change in a Gaussian for a fixed "pointing error," this change grows more rapidly with increasing distance from the center of the beam. When such models are placed at the center of the beam, the flux always decreases in the presence of pointing error since offsets in any direction result in a lower than expected response from the beam.

2.5.2 Beam Size Error & Ellipticity

The bottom panel of Figure 2.8 shows that in the presence of large gain errors, the impact of errors in the size of the primary beam is quite minimal. However, in the limit of small gain error, the reduction in fidelity degradation from such errors becomes significant. Errors of $\sim$3% in the assumed FWHM of the primary beams can cause a factor of two reduction in fidelity. The square point in the top panel of Figure 2.8 indicates, however, that the current Gaussian models in MIRIAD are in good agreement with the best-fit Gaussians to the measured voltage patterns. This, however, does not include significant image degradation that can be induced by departures from Gaussian shape or ellipticity.

Ellipticity of the voltage patterns represents a lower order of error than errors in the beam size. This was predicted given the influence on the illumination of the disk model (see Figure 2.2), and is indeed the case in the simulations. The ellipticity only begins to strongly effect the image fidelity when it reaches the 3% level and the half fidelity point appears to occur outside the bounds of the simulation at $\sim$10%. The measured ellipticity of the 6-m antennas is about 3%. The antenna "style" based ellipticity of the 10-m antennas is largely unknown due to the presence of imaginary gradients which induce antenna based ellipticity.

2.5.3 Measured Voltage Patterns

The use of the measured style-based profile shows that, in addition to the expected <50 count drop in fidelity that comes from the ellipticity of the 6-m antennas, a large (>100) drop comes from the deviations from the Gaussian model. The inclusion of antenna-based voltage patterns with imaginary components does the most damage, resulting in a factor of nearly 5 drop in image fidelity. These imaginary components will be particularly damaging to polarization studies as the magnitude of the imaginary component (see Figure 2.4) is comparable to the typical polarization signal and the polarization leakage term becomes a function of parallactic angle (Wright & Corder, 2007).

The image fidelity of a compact Gaussian source degrades at approximately 3.6% per arcsecond offset from the beam center. This degradation in fidelity with location within the primary beam is another incarnation of the result of decreased fidelity with increasing source size (Wright, 2007). For the imaginary components, the dominant effect other than the drop in fidelity with increasing distance from the beam center is the shearing of the flux distribution, resulting in substantially more elongated sources when compared to the model.

2.6 Conclusions and Further Work

The new simulations presented here are the first to utilize non-uniform, non-axis-symmetric voltage patterns. It is clear that largest contributors to the degradation of image fidelity are:

- surface error
- pointing error
- offsets in the illumination pattern (i.e. imaginary components)

Within typical error allowances, these effects can quickly result in a factor of 2 or more reduction in the image fidelity. Surface error and illumination pattern misalignment

can be corrected with standard holography and subsequent adjustment. Pointing error can be corrected using a variety of approaches, chief among them simply using a better pointing model or a better determination of the pointing model. However, these approaches cannot provide sufficient pointing corrections for periods of thermal or physical stresses. During these times, new pointing methods are needed (see Chapter 4).

If surface error, optical alignment and pointing can be conquered, deviations from the assumed Gaussian model and departures from circular symmetry are the next largest degrading forces. However, temporal variation makes it is unlikely that offset illumination patterns can be completely removed and thus independent voltage patterns may be required for each antenna. As the antenna structure changes under thermal, gravitational, or weather stresses the position of the secondary is likely to change. If this deflection is identical for all antennas in the array, the resulting imaginary components appear to result in an increased ellipticity which varies as a function of time. If the deflection is not uniform across the antennas, then the imaginary gradient can change in time. Focus adjustment of the secondary in the plane parallel to the antenna surface can correct a number of these problems but the calibration of such an adjustment may be difficult. In general, the time domain is the next large region of parameter space to explore and will likely be of concern for ALMA where the increased sensitivity results in more sources being in the fidelity limited regime.

Beyond these sources of degradation, the sidelobes and other very low level components of the voltage pattern will begin to contribute, especially on heterogeneous baselines where the sidelobes of the larger antennas are multiplied by significant wings of the wider voltage patterns associated with the smaller diameter antennas. The current simulation package is capable of including the influence of sidelobes but for the sidelobes to become important, larger sources must be imaged. While the current simulator is capable of handling larger sources, such sources require multiple observations to fill in the uv-coverage for the large number of pointings, otherwise fidelity becomes limited by aliasing from poor per-pointing uv-coverage. Future implemen-

tations of the simulation package will focus on speed, allowing sidelobe structure and additional types of observations to be simulated.

It is not difficult to imagine an inversion of the simulation approach. If a source is actually observed and imaged through traditional, circularly symmetric means, a model of the source can be developed. This model can then be used like Cas A was above, where known voltage patterns can illuminate the source and create a visibility file. Instead of utilizing **uvgen**, the actual measured visibility file can be used. The visibilities corresponding to the illuminated model can then be subtracted from the measured visibilities, resulting in a residual image with fewer artifacts. The model can then be updated and the process repeated. One could envision actually solving for pointing offsets with this method, although significant improvements in the run time are required before such a fitting routine would be viable. Such a method allows for recovery of low level features with data that can, in principle, be obtained post-observation using all available information about pointing drifts, primary beams and focus errors.

Errors in the primary beam pattern strongly effect the resulting image fidelity. Several of these factors, particularly offset illumination pattern, surface accuracy and pointing, are best addressed in hardware prior to observation or during observation. However, this is not always possible. The simulations presented here provide a means to estimate the degrading effects of these errors and a means of correcting these errors post observation. This could result in factors of several improvement in the image fidelity.

Bibliography

Ruze, J. 1966, Proceedings of IEEE, 54, 633

Sault, R. J., Teuben, P. J., & Wright, M. C. H. 1995, ASPC, 77, 433

Wright, M. C. H. & Corder, S. A. 2007, CARMA Memo 43

Chapter 3

Holography

Abstract

In order to determine offsets in the antenna illumination patterns and large scale surface errors, holographic measurements of the 15 antennas of the Combined Array for Research in Millimeter Astronomy (CARMA) were made. These measurements showed that the dominant source of error for the 10-m antennas was misalignment of the optical system while the errors in the telescope surfaces dominated the 6-m antenna data. Optical alignment of the 10-m antennas was performed in the 3-mm band, reducing the alignment errors on the primary surface from as much as 1 m to <0.5 m. Surface RMS values of the antennas, which were initially distributed between 110 μm and 25 μm, are now between 37 and 23 μm. After the corrections were performed, holographic measurements were done to determine the actual shape and stability of the voltage patterns on the sky. The width of the default Gaussians used by MIRIAD needs to be altered as the model 6-m and heterogeneous baseline primary beams are too wide compared with measurement. The measured voltage patterns are consistent with Gaussian profiles down to the 10% level but are considerably narrower below this point. At the 5% cutoff points, the voltage patterns can differ by as much as 7″ at the frequency of observation. The 6-m antennas have ∼3% ellipticity on

Portions of this chapter were previously presented in Corder & Wright (2006). Active focus correction and subsequent alignment of the optics will require a re-assessment of the voltage pattern properties described here. Alignment, especially in the 1-mm band, will likely yield substantially different voltage patterns.

the average, although the various antennas have ellipticity varying from $\leq$3% to 6%. There is consistent evidence of phase gradients across several voltage patterns, especially on the 10-m antennas, which dominates the ellipticity in the amplitude voltage pattern. Side-lobes of as much as 15% were found for the 10-m antennas, although maximum values of 10% are more typical. These sidelobe patterns are consistent from run to run at the 20% level. Finally, antenna specific voltage patterns are provided for use when extra image fidelity is needed.

3.1 Introduction

The Combined Array for Research in Millimeter-wave Astronomy (CARMA) is currently composed of the six 10-m (C1–C6) antennas of the Owens Valley Radio Observatory (OVRO) millimeter array and the nine 6-m (C7–C15) antennas of the Berkeley-Illinois-Maryland Array (BIMA). Since transporting the antennas to their current location at Cedar Flat subjected them to a range of unusual stresses, it was critical to verify their optical and receiver alignment and surface shape. Deviations in illumination pattern and large scale surface errors result in poorer than expected signal-to-noise and incorrect primary beam correction for mosaiced images. The goal of holography is to increase the aperture efficiency of the antenna while optimizing and/or determining precisely its voltage pattern.

The voltage pattern is the shape of the response of an individual antenna to emission on the sky. To measure deviations from the ideal illumination and shape of the antenna surface, the shape of this voltage pattern must be measured. The relationship between the voltage pattern in the sky plane and the illumination pattern in the aperture plane is a Fourier transform, given by Equation 1.3. The distribution of E is typically a Gaussian, tapered so that it is small at the edge of the aperture to reduce spill-over. The voltage pattern is related to the more typically used *primary beam* by Equation 1.2. For strictly real, circularly-symmetric, Gaussian voltage patterns, the primary beam is a Gaussian of width a factor of $\sqrt{2}$ smaller than the voltage pattern, given by the standard relationship $FWHM_{PB} = \epsilon\lambda/D$ where $FWHM$ is

the full-width at half maximum, λ is the observing wavelength, D is the telescope diameter, and ϵ is a factor of order unity that depends on the taper.

In its most general form, the voltage patterns are complex leading to a primary beam of the form

$$PB_{12}(\vec{k}) = V_1(\vec{k})V_2^*(\vec{k}) \tag{3.1}$$

$$= (Re(V_1) + iIm(V_1))(Re(V_2) - iIm(V_2)) \tag{3.2}$$

with the resulting amplitude and phase

$$|PB_{12}(\vec{k})| = \Big((Re(V_1)^2 + Im(V_1)^2)(Re(V_2)^2 + Im(V_2)^2)\Big)^{\frac{1}{2}} \tag{3.3}$$

$$\theta(\vec{k}) = \tan^{-1}\Big(\frac{Re(V_2)Im(V_1) - Re(V_1)Im(V_2)}{Re(V_1)Re(V_2) + Im(V_1)Im(V_2))}\Big). \tag{3.4}$$

For modest resolution holography ($\sim$1 m or better), the expected aperture illumination is a broken ring with a depression in the center and a Gaussian taper toward the edges. The central depression is due to subreflector blockage while the breaks in the ring are due to the secondary support legs. There are three and four legs on the 6-m and 10-m antennas, respectively. Ideally the general pattern should be as symmetric as possible and well-centered. The phase across the aperture should be zero. Lower resolution holography, where the secondary is not resolved, generates a Gaussian illumination pattern without breaks or central depressions. High resolution holography, not presented here, generally shows depressions at the panel edges due to small gaps at the panel joints.[1] Ideally, on the sky, the core of the real part of the voltage pattern should have a near Gaussian shape and there should be no contribution from the imaginary part. The locations of the sidelobes are not well known from observations.

Bulk deviations from ideal voltage pattern or aperture illumination and phase have easily calculable implications. Mispointed observations on the sky result in an offset of the voltage pattern from the expected location. A quick application of the

[1]High resolution holography is underway, Lamb & Corder, 2008, CARMA Memo, in prep.

Fourier Transform Shift Theorem:

$$\mathcal{F}^{-1}E(\vec{x}-\vec{x}_0)(\vec{k}) = \mathrm{e}^{2\pi i\vec{k}\cdot\vec{x}_0}V(\vec{k}) \tag{3.5}$$

$$\mathcal{F}V(\vec{k}-\vec{k}_0)(\vec{x}) = \mathrm{e}^{-2\pi i\vec{x}\cdot\vec{k}_0}E(\vec{x}) \tag{3.6}$$

shows that a shift in $\vec{k}$, i.e. a pointing error on sky, causes a phase gradient in the aperture plane. Similarly, misalignment of the antenna optics, an offset of the illumination pattern in the aperture plane, results in a phase gradient across the voltage pattern on the sky, i.e. the imaginary voltage pattern becomes nonzero. Peak-up observations can easily rectify pointing offsets but more complicated optical alignment is necessary to center the illumination pattern. Figure 3.1 shows a concrete example of the impact of offset illumination patterns in the aperture plane. An offset of less than $1/20^{th}$ of an antenna diameter can result in a 15% contribution to the imaginary voltage pattern, where the 15% is measured with respect to the peak of the real beam which is nominally 1.0. This results in phase which ranges between $\pm 20^{\circ}$ from half power point to half point of the real voltage pattern.

Additional bulk deviations are possible. Principle axis (towards/away from the antenna surface) focus errors result in phase errors in the aperture plane. The magnitude of the phase error grows as a function of the square of the distance to the center of the antenna, a consequence of the parabolic shape of the dish. This unfortunately results in a widening of the voltage pattern on the sky. Focus corrections can be made by fitting a quadratic function to the aperture plane phase. Higher order corrections typically result in alternating phase around the surface of the dish. For example, astigmatism, resulting from an antenna surface which is compressed in one direction, has a surface phase pattern where the axis of the compression has one phase sign and the opposite phase sign perpendicular to the axis. Localized panel misalignment will appear as a single deviant region, not a systematic pattern.

A series of moderate-resolution holography measurements were carried out over the course of the spring and summer of 2006 and further, moderate- to low-resolution measurements were conducted in the fall of 2007 to the spring of 2008. Here, *modest*

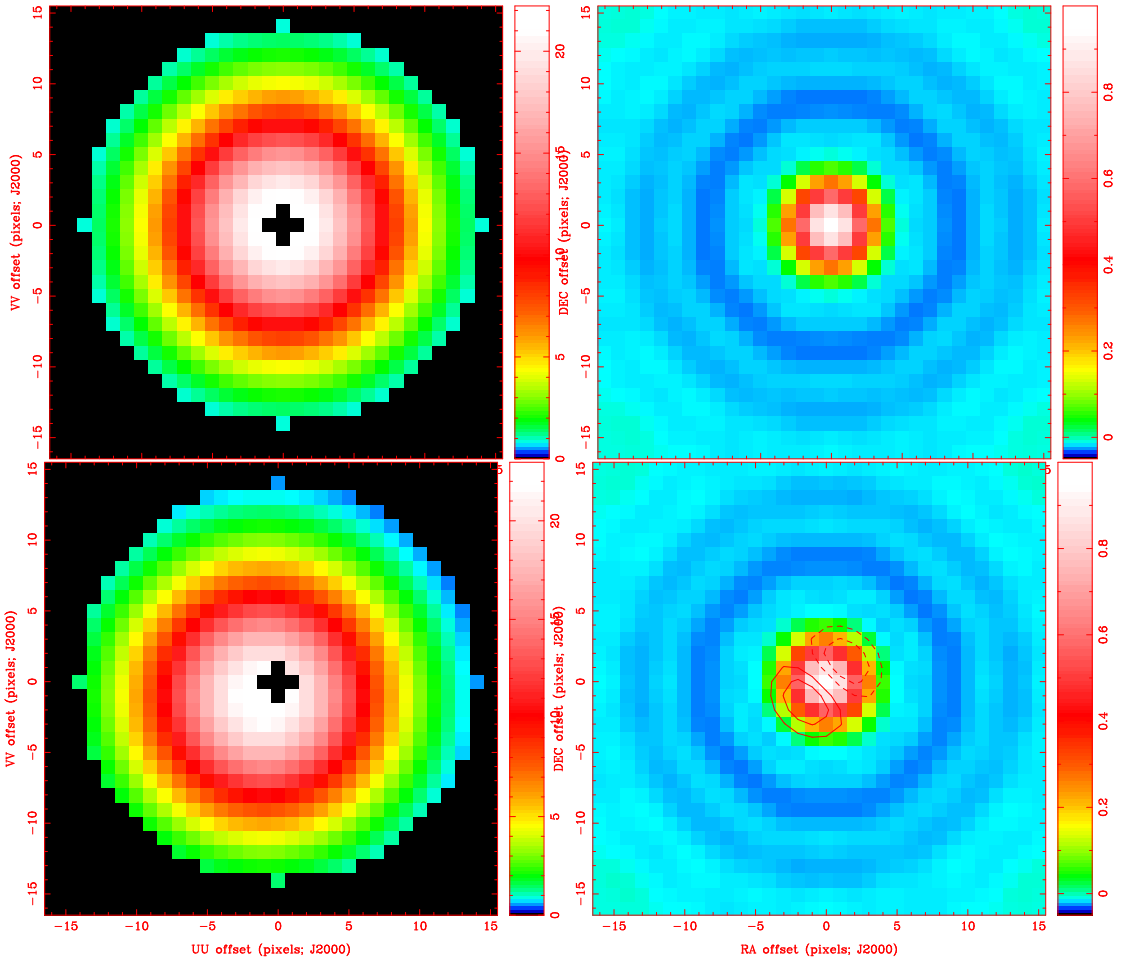

Figure 3.1 The top-left panel shows a model of the aperture plane in the limit of a perfect surface, i.e. no phase contribution and perfect alignment. The depression in the middle of the amplitude pattern is from obstruction by the secondary. The top-right panel shows the corresponding voltage pattern with no imaginary component. In the bottom-left panel, the aperture plane illumination is offset by 1 pixel in each direction, an offset comparable to 0.5 m on a 10-m telescope or 0.3 m for a 6-m telescope. The corresponding voltage pattern, bottom-right panel, shows the sky plane with the real component in color, normalized to 1, and the imaginary part shown as contours. Contours are ±5% and 10% with dashed negative contours and solid positive contours.

resolution implies ∼10 resolution elements across the dish surface while *low* resolution comprises only ∼5 such resolution elements. The goal of the first round of holography was to optimize the dish surface and align the optics. The second run was intended

to measure the stability of the voltage patterns, determine their true shape including departures from a Gaussian profile and circular symmetry, and determine what, if any, antenna specific properties exist for the various antennas.

In §3.2, I discuss the data acquisition and reduction methods in general along with the datasets used to derive the relevant properties. In §3.3, I address the derived optical axis offsets and the values post correction, the preliminary measurements of the 1-mm band optical alignment and the derived panel adjustment and the RMS after the correction. In §3.4, the accuracy of the currently used Gaussian models of the primary beams at CARMA are discussed, the departures from Gaussian profiles and/or circular symmetry are described, and antenna specific voltage patterns are determined for use when extreme image fidelity is required. The principle conclusions and summary of the work are given in §3.5.

3.2 Data Acquisition and Reduction

Voltage patterns of the 15 CARMA antennas were obtained using a bright point source and the CARMA beam-mapping software utility *multiMap*. Initial pointing corrections were obtained on the target itself utilizing the CARMA real-time radio pointing software utility *refPoint* (White & Corder, 2007). When obtaining voltage pattern data for the 10-m antennas, the 6-m antennas were held fixed for gain reference while the 10-m antennas moved to a list of prescribed azimuth and elevation offsets. Conversely, while data were being obtained for the 6-m antennas, the 10-m antennas served as reference.

The offset positions were given as 45% of the Nyquist sampling interval for the moving antennas. The large oversampling was done to verify that there was no significant signal coming from outside the aperture and attempt a measurement of the voltage pattern on the sky without further manipulation.[2] The offsets were required

[2]There was no significant emission outside the aperture. In the end, the attempt to determine the pattern on the sky without further manipulation failed and the voltage pattern was determined by transformation to the aperture plane, masking the aperture plane, and transforming back to the sky plane. The process is described in further detail in what follows.

to lie within a fixed circular radius to provide uniform resolution in the aperture plane and reduce the number of points to be observed. Measurements at the center position were obtained at the beginning and end of the scan for each row and at every seven points within the row for rows larger than 8 points. Taking overheads into account, this provides a calibration measurement at offset position (0,0) every 2 minutes or less.

Given that the constant upgrading and testing of the antennas during the period of these observations at Cedar Flat, the holography datasets never included all 15 antennas at any one time and the number of reference antennas available for verification of repeatability differs from dataset to dataset. A compilation of different datasets was required to cover all antennas. Typically, each 10-m antenna used 5 to 6 reference antennas and each 6-m antenna used 3 to 4 reference antennas. There are inevitable variations in the data quality because some antennas were not available on days with the best observing conditions. Table 3.1 contains specific information on the various datasets.

Calibration and holographic imaging of the antenna surfaces used MIRIAD (Sault, Teuben, & Wright, 1995). Each dataset was split into separate 500 MHz frequency bands for both LO sidebands before self calibration. The number of bands available ranged from one to three per sideband. The central pointings were separated by replacing the u and v coordinates with azimuth and elevation offsets from the center, (Δaz,Δel). The central pointings were then identified for use in calibration by selecting (Δaz, Δel) = (0,0) using MIRIAD's **select=uvnrange**. A call to **selfcal**, using the **amplitude** option, provided antenna-based amplitude and phase correction of these central positions on 5 minute timescales. These corrections were interpolated and applied to the offset pointing positions. For each antenna, the resulting calibrated voltage patterns for each reference antenna and frequency band were converted to real and imaginary parts, Fourier transformed from the sky plane to the aperture plane using the MIRIAD **fft** function, and masked to exclude any information arising from outside the aperture using the **maths** function in MIRIAD. For the modest-resolution

Table 3.1. Holography Data

UT Date	Size arcsec	Step arcsec	Soruce	LO Frequency GHz	Elevation degrees	Antennas
2006-May-10	517/882	27.23/46.42	3c273	88.5	50/35	1,2,4-6/7-15
2006-May-23	517/882	27.23/46.42	3c273	88.5	51/51	1,2,4,5/8-15
2006-May-30	517/882	27.23/46.42	3c273	88.5	44/52	1,2,4-6/7-9,11-15
2006-Jun-12	517/882	27.23/46.42	3c273	88.5	52/52	1,2,4,6/8-10,12,14,15
2006-Jun-22	517/882	27.23/46.42	3c279	88.5	45/43	1,4/7-15
2006-Dec-07	na/908	na/43.25	3c273	95.0	na/47	na/7,9,10,12-15
2007-Aug-12	541/na	25.74/na	Mars	105.8	57/na	1,2,5/na
2007-Sep-07	541/na	26.25/na	Mars	100.2	47/na	1-4/na
2007-Sep-09	na/940	na/44.75	Mars	100.2	59/na	na/7-14
2007-Sep-11	187/312	14.40/24.00	Mars	100.2	55-66/59-71	1-3,5,6/8-14
2007-Sep-11	187/312	14.40/24.00	Mars	100.2	75-68/73-61	1-6/7-14
2007-Sep-16	187/312	14.40/24.00	3c454.3	100.2	65/68	1,3-5/9-14
2007-Sep-16	86/na	6.60/na	3c454.3	227.3	64/na	3,4,6/na
2007-Sep-16	86/na	6.60/na	3c454.3	227.3	64/na	3,4,6/na
2007-Nov-09	187/312	14.40/24.00	3c454.3	100.2	61/57	1-4,6/7-15
2008-Feb-28	187/312	26.25/44.75	3c273	100.2	54/53	2,3,6/7,10,12-15
2008-Mar-21	84/na	6.46/na	3c273	227.2	42/na	1-6/na
2008-Mar-24	535/na	28.18/na	3c273	98.4	54/na	2-6/na
2008-Mar-27	535/na	28.18/na	3c273	98.4	44/na	2-6/na
2008-Mar-27	159/na	12.26/na	3c273	227.2	34/na	2-6/na

Note. — Values which contain a '/' are for 10- and 6-m antennas respectively. All measurements above the double line were conducted prior to adjustment. All tracks taken post-adjustment were done at night with the exception of the Mars tracks which sometimes continued slightly through sunrise. C15 & C8 had significant pointing error in August and September of 2007 and much of that data has been edited. C7 had persistent trouble with phase jumps that rendered most of the imaginary beam information useless upon further inspection. C2 had poor sensitivity until very recently and resulted in poor data quality in the wings of the beam. C6 was out of the array for cryogenic work in much of September and August 2007. The 2007-Sep-16, 1-mm band dataset is suspect for all antennas because there is enhanced phase noise due to the extended nature of the configuration used.

holography, the measurements result in amplitude and phase in the aperture plane with a typical resolution of 1.4 m and 0.8 m for 10-m and 6-m antennas, respectively.

The individual aperture images for phase were then fit using the MIRIAD task **imhol**. **Imhol** fits a function to the aperture phase accounting for the size of the secondary, removes principal-axis focus and pointing errors, and provides a new image dataset with these errors removed. **Imhol** also calculates an RMS surface error from the phase information, in microns, both before and after the phase function fit, as well as an illumination-weighted, post-fit RMS surface error. The illumination weighted, post-fit RMS is typically used as it down-weights phase errors which come from regions of poor sensitivity and therefore are more uncertain. The pointing and focus error subtracted images and fits were examined to verify that the solutions and residuals were consistent across frequency bands, upper and lower sideband of the LO, and reference antennas. A single, average image was then created. This averaging was done in the aperture plane where each separate image was scaled to the wavelength of the 1^{st} LO.

To determine the orientation and phase sign of the resulting images a piece of Mylar was placed on one 6-m and one 10-m antenna. The Mylar, possessing an index of refraction greater than 1, induces a phase lag for incident radiation that appears, in the aperture plane, as a depression in the antenna surface. For the 6-m antennas, the aperture plane images need to be flipped top to bottom to properly reflect the known position of the Mylar sheet. For the 10-m antennas the results are somewhat inconclusive, but it appears as though the sign of the phase shift and position in the aperture plane of the Mylar sheet required that the images be flipped left-to-right and have the sign of the phase terms changed.

3.3 Holography Results: Alignment and Panel Adjustment

In general, optical alignment was necessary for the 10-m antennas and surface panel adjustment was required for the 6-m antennas. Deviations from ideal alignment and surface RMS values were measured for every antenna and are reported here although many were unaltered. Unaltered antennas provide an estimate of the typical repeatability and noise level of the various images.

For high image fidelity, especially for mosaicing, the RMS surface error of the antennas, after the removal of pointing and focus errors, should be $\sim \lambda/40$, where λ is the observing wavelength (Cornwell et al., 1993).[3] Therefore, for 1-mm band observations, the target RMS surface accuracy is 30 μm, although Chapter 2 shows that this accuracy still results in significant fidelity degradation. For optical alignment, the desired accuracy is best expressed as the contribution to the imaginary or phase voltage pattern (c.f. Figure 3.1 and equation 3.6). If this imaginary component represents less than 5% of the peak flux at the half-power point of the voltage pattern, the resulting contribution is negligible in cases where a dynamic range of less than about 250 is required. In what follows, 5% of the peak flux at the half-power point of the voltage pattern is referred to as the alignment benchmark and 30 μm is referred to as the surface accuracy benchmark

3.3.1 Optical Alignment

When determining optical alignment, measurement of the offset direction and magnitude is made more difficult because the most sensitive portion of the feed is obstructed by the secondary. As the offset increases, a simple centroid of the illumination pattern on the antenna surface grows more slowly as the most sensitive portions of the feed are exposed to the antenna surface. To further complicate the measurement,

[3]This provides a fidelity index of 20 in the (Cornwell et al., 1993) definition. For the Cas A model, the conversion to the definition given Chapter 2 requires multiplication by a factor of 10 but the conversion is model dependent.

the truncation of the illumination pattern at the edge of the antenna further causes an underestimate of the offset. In principle the feed legs also cause differences, but the width of these features is much smaller than a resolution element, making the blockage only fractional.

To determine the offset, the centroid of the illumination pattern on the dish was measured and then the derived correction term was applied. The correction was determined by simulating various offsets and measuring the apparent centroid. Figure 3.2 shows two realizations of the model run, one each for a large (top-left) and small (top-right) offset. The correction factor as a function of measured offset is shown on the bottom. These measurements are intended to be approximate and were not used in the actual adjustment of the optics. The correction is 12-13% and is flat for offsets less than 15% of the antenna radius. Beyond 15% of the dish radius, the correction grows rapidly as dish edge effects begin to dominate, reaching more than 50% when the illumination is centered on the dish edge. The correction factor is similar for the 10-m and 6-m antennas because the ratio of the obstruction/hole to the dish size is the same in both cases.

Actual adjustment of the optical alignment for the 10-m antennas was carried out by placing a bright, incoherent illumination source at the center of the secondary and aligning the mirrors and receiver so the optical beam tracks through the center of the four mirrors in the 10-m system, reaching a focus on the center of the feed horn (Woody, 2008). There are no points at which the 6-m antenna receiver system can be easily aligned making misalignment a serious problem if it occurs (Plambeck, 2008). The alignment of the optics can change if the receiver is removed from the dewar and is replaced with a different setting. The process of alignment is described in more detail in Appendix A.

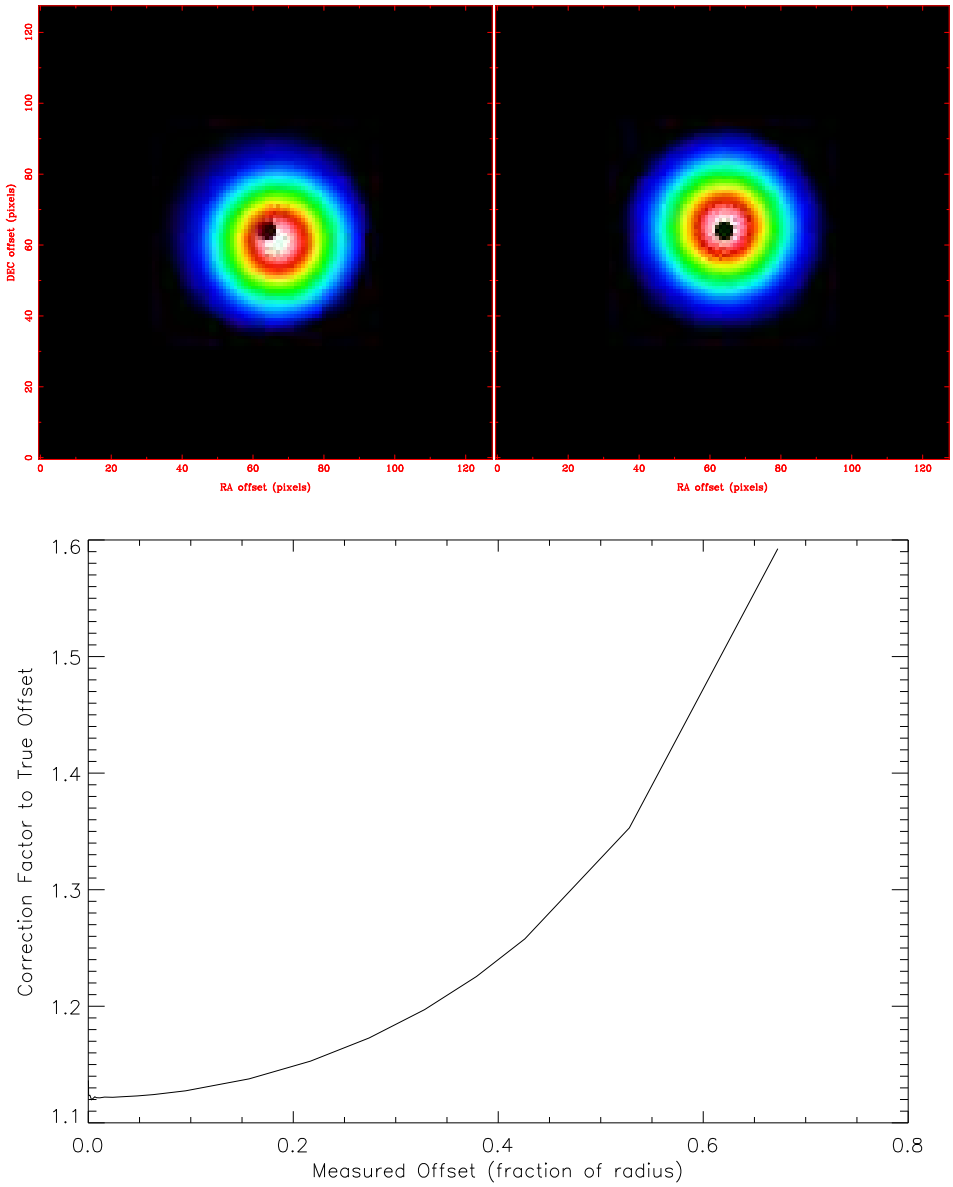

Figure 3.2 Top: The left and right panels show models of the dish surface illuminated by significantly offset (15% of the dish radius) and slightly offset (3.5% of the dish radius) illumination patterns. Bottom: This image shows the correction factor that needs to be applied to a given measured centroid to determine the actual offset in the aperture plane. For measured offsets less than 15% of the dish radius, the correction factor is relatively constant, 12.5±0.5%. At 15-20% offsets the dominant effect changes from obstruction by the secondary to truncation at the dish edge. The correction factor goes quickly to zero for vanishingly small offsets. Discrete pixel sizes, which are present in the actual datasets, yield the apparent, unsmooth behavior at small offsets.

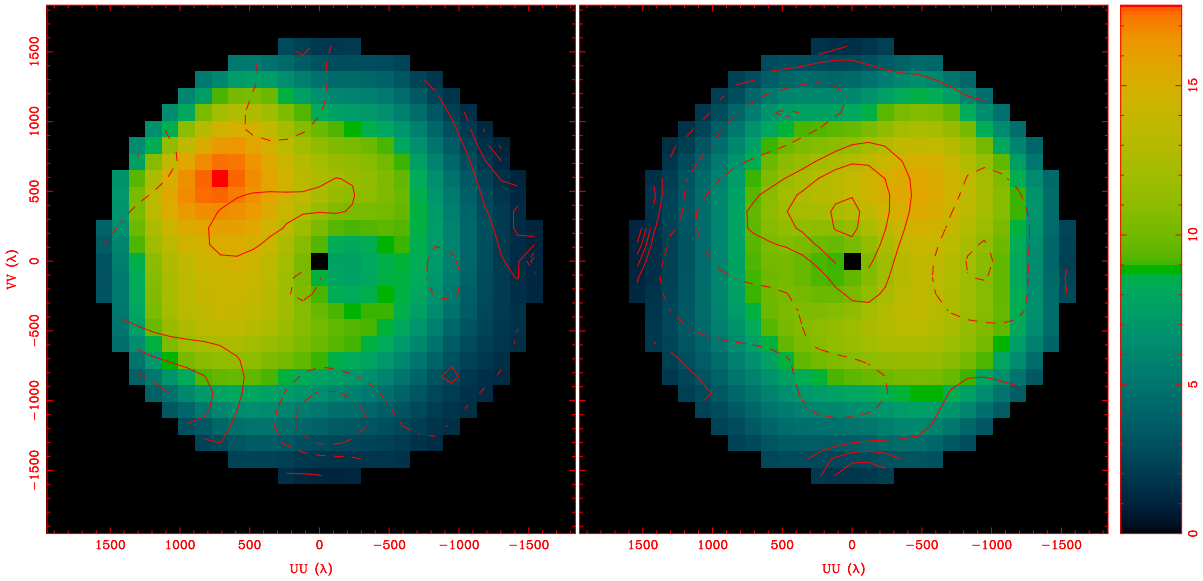

Figure 3.3 The left panel shows C4 pre-adjustment while the right panel describes the post-adjustment state. Contours are in intervals of 25 μm with dashed contours being negative and solid contours being positive. The color scale is the illumination pattern. The axes are in wavelength units where the wavelength is $\sim$3 mm in these observations. There are few significantly deviant panels in the regions where the surface is well illuminated. However, alignment of the optics improved significantly after adjustment.

Figure 3.3, depicting C4, shows an example of 10-m alignment. The left panel is pre-adjustment data taken on 2006 May 10 while the right panel shows post-adjustment results for 2006 June 12. In the left panel the alignment is significantly deviant from the nominal position. The pattern appears to be offset by 1 m at an angle of 24° counter-clockwise from up. Following adjustment the offset was 26° clockwise from up and is offset by 0.46 m. Holography carried out in 2007 September indicates that the magnitude and direction of this offset have remained constant to within 15% in magnitude and 20° in direction, suggesting that the alignment offset may persist over long timescales.

Figure 3.4 displays a representation similar to Figure 3.3 but for C1. Since C1 appeared to be reasonably aligned in the first measurement, no adjustment was made and any deviations represent the repeatability of the measurement. Initially, the offset was between 0.27 and 0.43 m at an angle between 2° clockwise from up and 20° counter-clockwise from up. More recent measurement suggests that this offset may

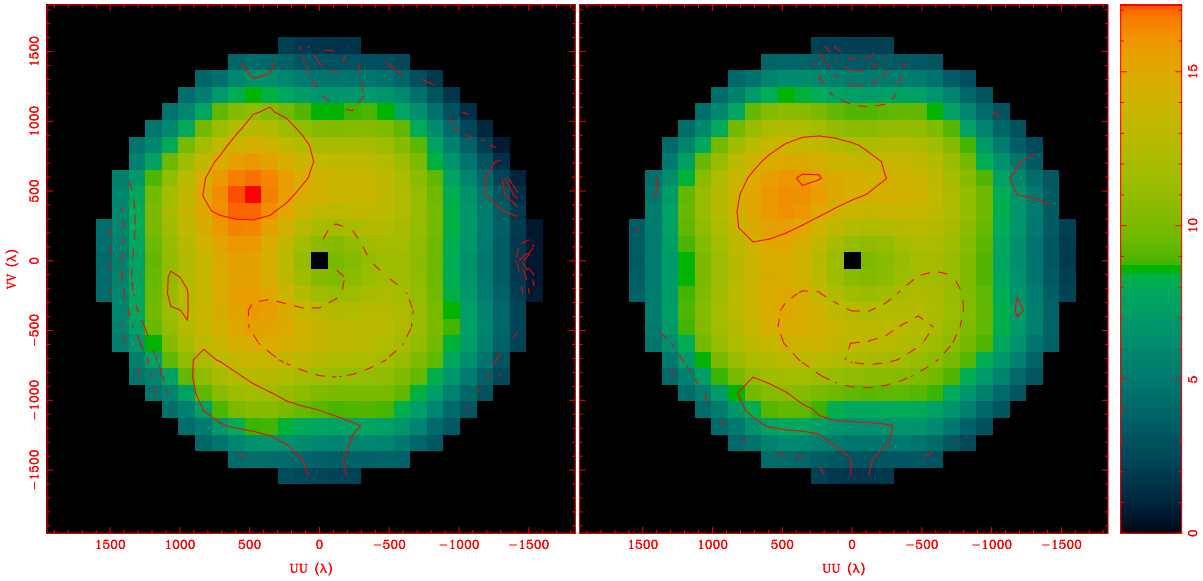

Figure 3.4 Similar to Figure 3.3 except for C1.

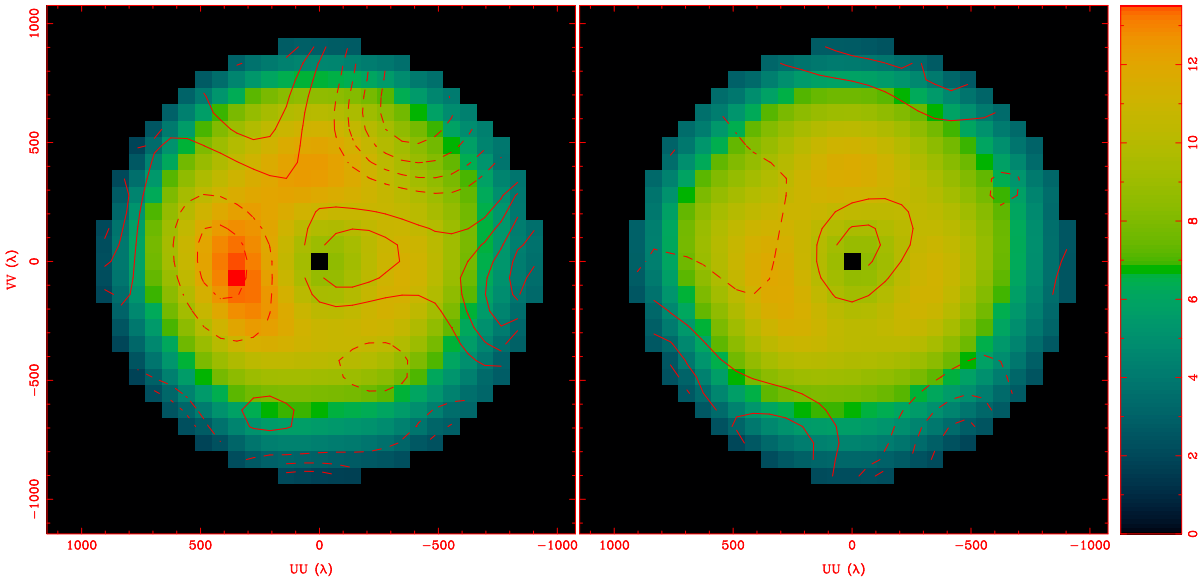

Figure 3.5 Similar to Figure 3.3 except for C10.

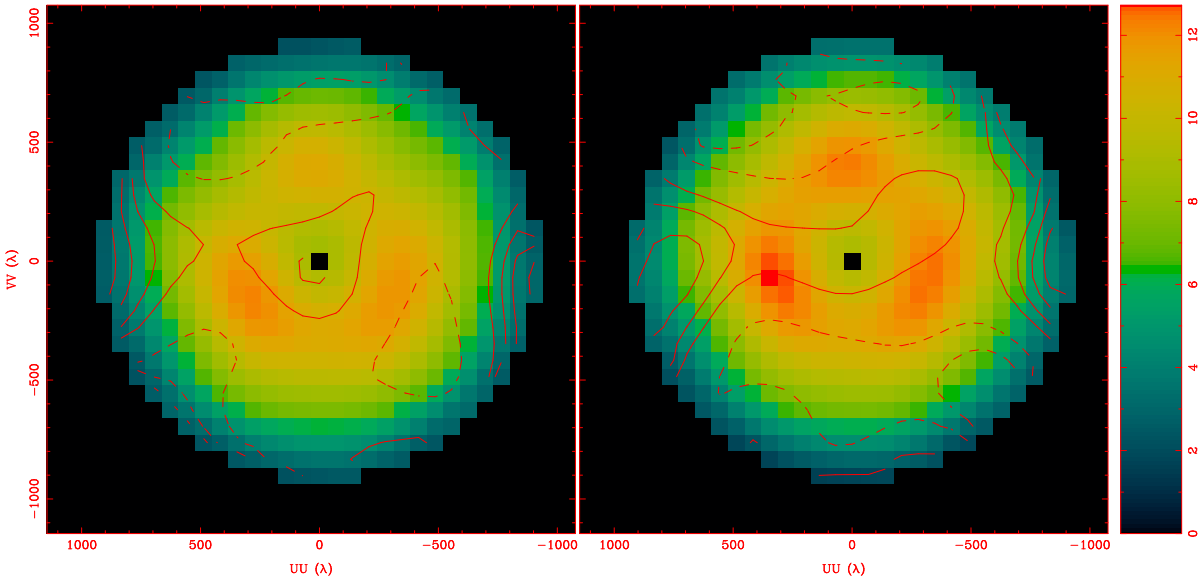

Figure 3.6 Similar to Figure 3.3 except for C9.

have become more significant and that the angle may also deviate significantly. This indicates that there may be some long-term, time-variable component to the offset in alignment.

In general, the 6-m antennas display more well-centered patterns. Figure 3.5 (C10) and 3.6 (C9) show the most deviant and the most well-aligned 6-m illumination patterns, respectively. Here the data are taken 2006 June 12 and 22 for C9 and 2006 May 10 and June 12 for C10. For C9, the offset is $\leq$0.1 m with a poorly determined offset angle. For C10, the offset is between 0.11 and 0.13 m at an angle of 13 to 30° counter-clockwise of up.

Table 3.2 presents the alignment measures for various antennas. Only two antennas (C4 and C6) were intentionally adjusted. Six antennas have imaginary voltage patterns that are consistent and measurable in terms of offsets in alignment in the aperture plane. However, when comparing to the benchmark, only four antennas, C1, C4, C5 and C6, fail the criterion. The other two antennas, C10 and C11, contributed fractionally small imaginary components which will only become significant in cases of extreme dynamic range.

Table 3.2. Adjustment and Alignment Results

Antenna	Offset[a] meters @ °	Offset[b] meters @ °	Surface RMS[c] μm	Surface RMS[d] μm
1	0.43 @ 2	0.27 @ -20	28	27
2	0.28 @ -70	0.28 @ -41	40	40
3	0.29 @ -72	0.13 @ -49	31	31
4*	1.00 @ -24	0.46 @ 26	29	27
5	0.36 @ 20	0.36 @ 54	40	41
6*	0.69 @ -71	0.32 @ -40	33	29
7**	0.09 @ -26	0.13 @ -84	51	31
8**	0.14 @ -37	0.24 @ -37	50	29
9	0.02 @ 2	0.10 @ 82	31	39
10**	0.13 @ -77	0.11 @ -60	44	30
11**	0.09 @ -39	0.13 @ -16	43	29
12**	0.09 @ -53	0.10 @ 13	115	30
13**	0.17 @ -55	0.22 @ -60	54	23
14**	0.09 @ -75	0.12 @ -70	35	30
15**	0.13 @ 14	0.12 @ -83	33	25

[a]Alignment offset prior to any adjustment

[b]Alignment offset post-adjustment

[c]Surface RMS prior to any adjustment

[d]Surface RMS post adjustment

Note. — Offsets are given by the calculated centroid and a correction factor for obstructed 2-dimensional Gaussian patterns (∼13%). Angles are positive clockwise from up. Antennas denoted by * had alignment intentionally adjusted between trials. A change of receiver can also result in small changes to the centering of the illumination pattern. Antennas denoted by ** had panel adjustment performed. Antenna 3 data has a very long time baseline (1.5 years) between measurements due to a variety of issues.

3.3.2 Panel Adjustments

For the 10-m antennas, the panel adjusters are about a meter apart, and the modest-resolution holography is sufficient to determine both the need for panel adjustment and the adjustments themselves. The results in Table 3.2 indicate that there is little need for panel adjustment when compared to the benchmark, with the possible exception of C2 and C5. The possibility of improving surface accuracy for these antennas is shown in Figures 3.7 and 3.8. Note the similarities between the most deviant, high illumination regions on the two datasets. Given that the nature of the 10-m adjustment points, which is such that the intersection of panels has a single adjustment point for all adjacent panels, adjustment of any location requires a global solution and global adjustment. No adjustment of these antennas was performed, although some improvement could be made.

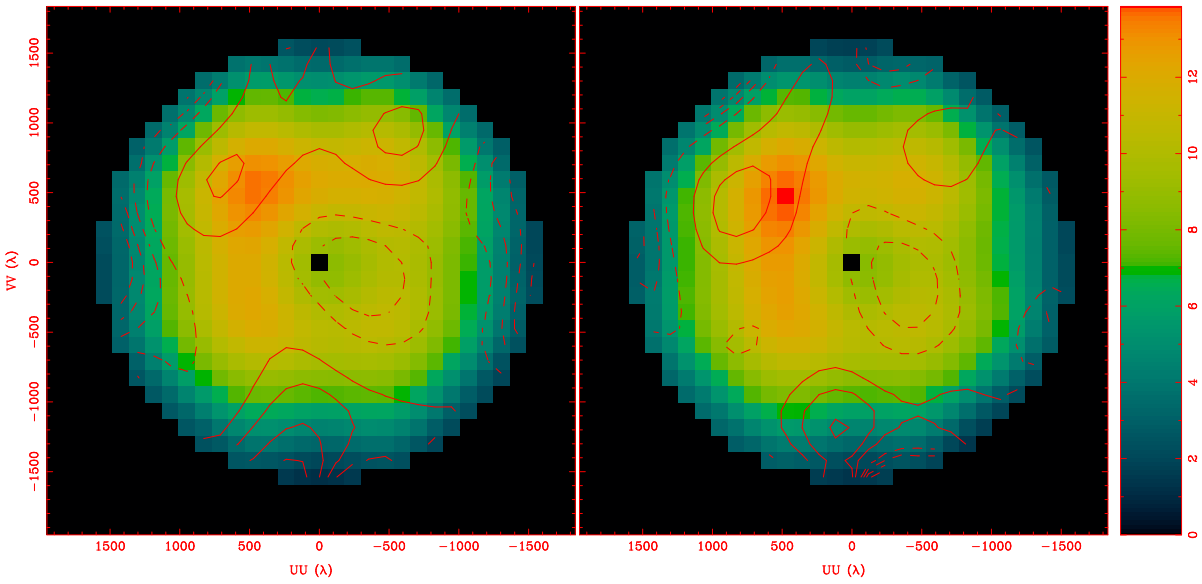

Figure 3.7 Similar to Figure 3.3 except for C2.

Table 3.2 shows a very different picture for the 6-m antennas. While the alignment is generally quite good, the surface RMS values typically did not meet the benchmark. The left sides of Figures 3.9 (C11) and 3.10 (C12) provide an illustration of the two typical modes of deviation for the 6-m antenna surfaces. C11 shows localized deviations without significant large scale structure. C12, on the other hand, shows a

classic astigmatic pattern where the antenna is folded up along the axis left-to-right through the middle of the image which, in turn, depresses two other quadrants.

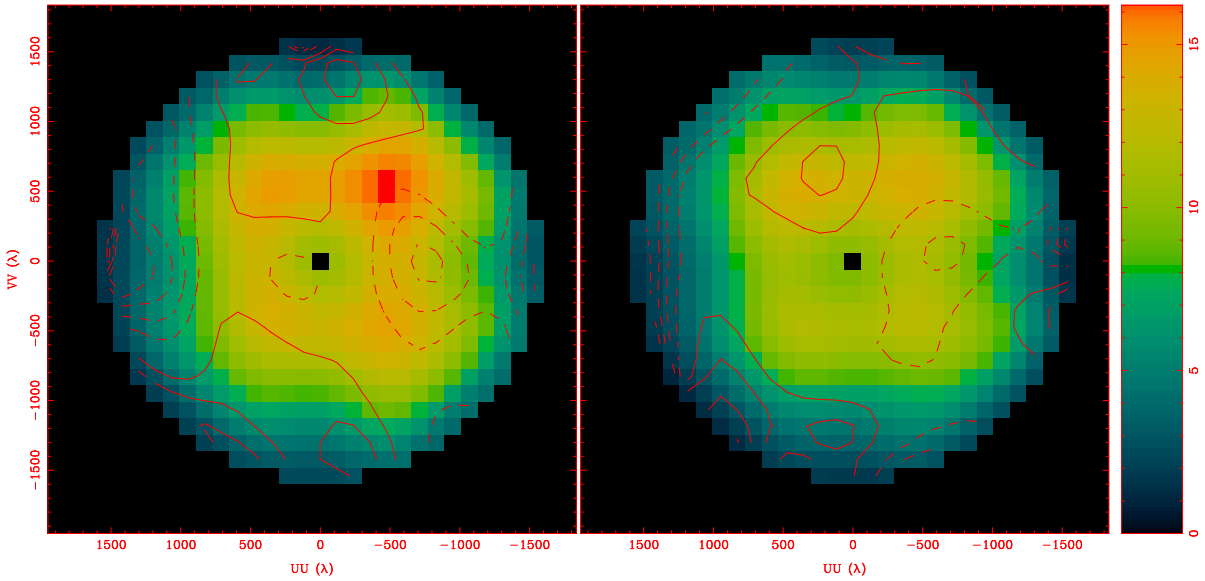

Figure 3.8 Similar to Figure 3.3 except for C5.

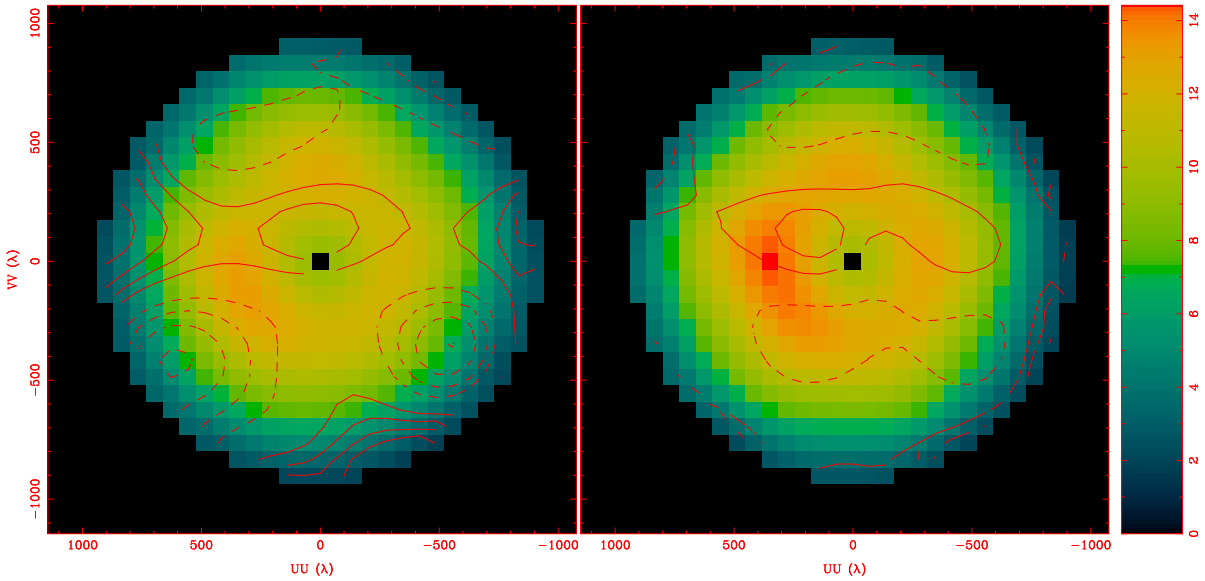

Figure 3.9 Similar to Figure 3.3 except for C11.

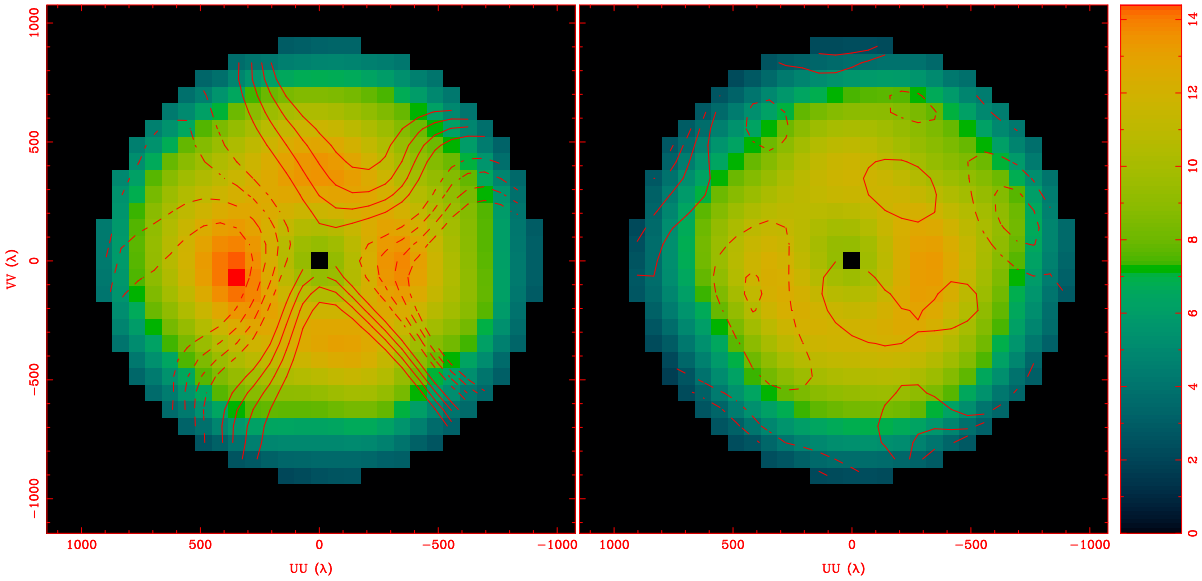

Figure 3.10 Similar to Figure 3.3 except for C12.

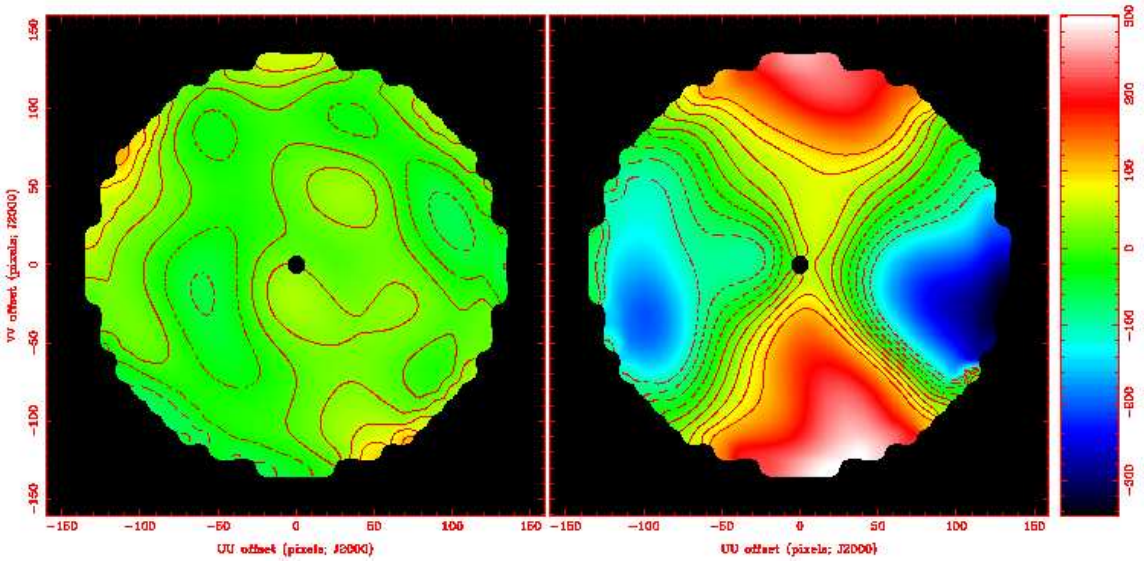

Figure 3.11 C12 holography is displayed post adjustment (left panel) and prior to adjustment (right panel). Here, the contours are in degrees of adjustment needed given the 2.94 μm per degree pitch of the adjuster screws.

The adjuster locations on the 6-m antennas tend to be centimeters away from each other and each panel corner has its own adjuster. Figure 3.11 is an example of the

maps used in carrying out the adjustments. To determine the adjustments needed, the maps were interpolated so as to achieve images well-resolved on the adjustment scale. Adjuster locations whose positions deviated by more than $\sim$60 μm from the ideal surface on the phase plots were corrected. Adjustments were carried out in steps of 5° using a dual-toothed tool that fits directly into the adjusters.

Given that the true resolution is far poorer than the inter-adjuster scale, the immediately adjacent adjusters were altered by identical amounts. It is expected that this technique should remove extremely large local deviation or large scale deformations. Resolution on the size-scale of centimeters must await on-the-fly techniques and the use of a radio transmitter. Post-adjustment, these antennas show far less systematic deviation. The right-hand sides of Figures 3.5, 3.9 and 3.10 show the typical improvement. Figure 3.6 was not adjusted and the data demonstrate the repeatability of the measurements. Table 3.2 presents the surface RMS after any adjustment.

3.3.3 Preliminary 1-mm Band Results

Given that the 1-mm receiver positions in the dewar are not perfectly coincident with the 3-mm receivers, the alignment can differ significantly between the 3-mm and 1-mm systems. The surface accuracy, however, is common to the two systems. Therefore, high- or modest-resolution holography is unnecessary in the 1-mm band but low-resolution holographic data could help determine any independent deviation of the alignment of the 1-mm system from the 3-mm system, aiding the aperture efficiency and image fidelity of 1-mm observations.

However, valid 1-mm holography data are much more difficult to obtain. The required phase stability of the atmosphere for 3-mm holography measurements is similar to that for 1-mm science data, making the phase criterion for 1-mm holography extremely strict. Repeated datasets are thus very difficult and expensive, observationally, to obtain in the 1-mm band. However, a single, high-quality dataset could be useful for constructing model 1-mm beam patterns and determining any offsets in

the illumination patterns. To date, such high-quality data are only available on the 10-m antennas (see Table 3.1).

On average, the 10-m alignment in the 1-mm band is poor and is currently the subject of intense effort at CARMA. Figure 3.12 displays the aperture plane illumination pattern while Figure 3.13 displays the resulting voltage patterns. None of the aperture plane images appear to be well centered, although C2 is close. Antennas like C4 actually show some illumination of the primary by the first side-lobe of the feed horn. Indeed, when examining the voltage patterns on the sky, instances of large gradients are seen on C4, showing a $\pm 40\%$ imaginary contribution over the central parts of the beam. The poor centering of the illumination pattern results in poor aperture efficiency. Considering Equation 3.1 and Figure 3.13, the resulting primary beams will have large imaginary components and, as described in Chapter 2, will have a detrimental impact on image fidelity.

Antennas showing patterns significantly different from a straight gradient (e.g. C1 and C2) are either showing signs of higher order variations across the beam or noise effects as these antennas are comparatively well aligned and are on longer baselines at the time of observation. These variations underscore the difficulty in obtaining quality voltage patterns in the 1-mm band and may be the result of pointing drift in the reference antenna(s) and any, currently unknown, voltage pattern phase gradient. A first attempt to center C3 was made on 2008 March 27 and, while the alignment is not perfect, the improvement is substantial. Adjustments of C4 and C6 have also been made but to date no verification dataset is available. Further optimization of the alignment will require observations in the most compact configuration, likely to occur in the summer of 2008.

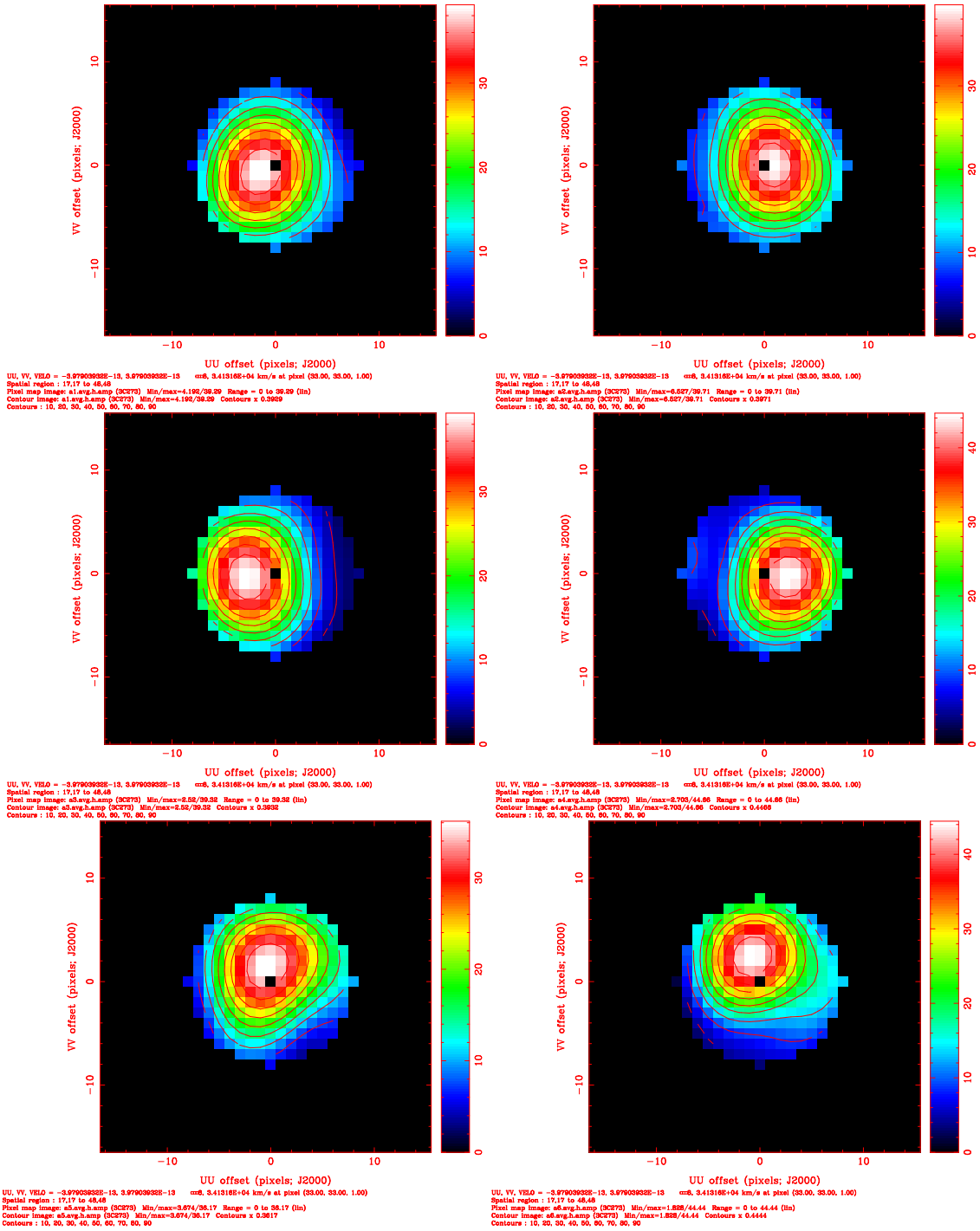

Figure 3.12 Holography at λ =1.3 mm of each of the 10-m antennas is shown. The color and contours both show the amplitude pattern with contours in steps of 10%. The offset from the center is large and obvious in most antenna patterns.

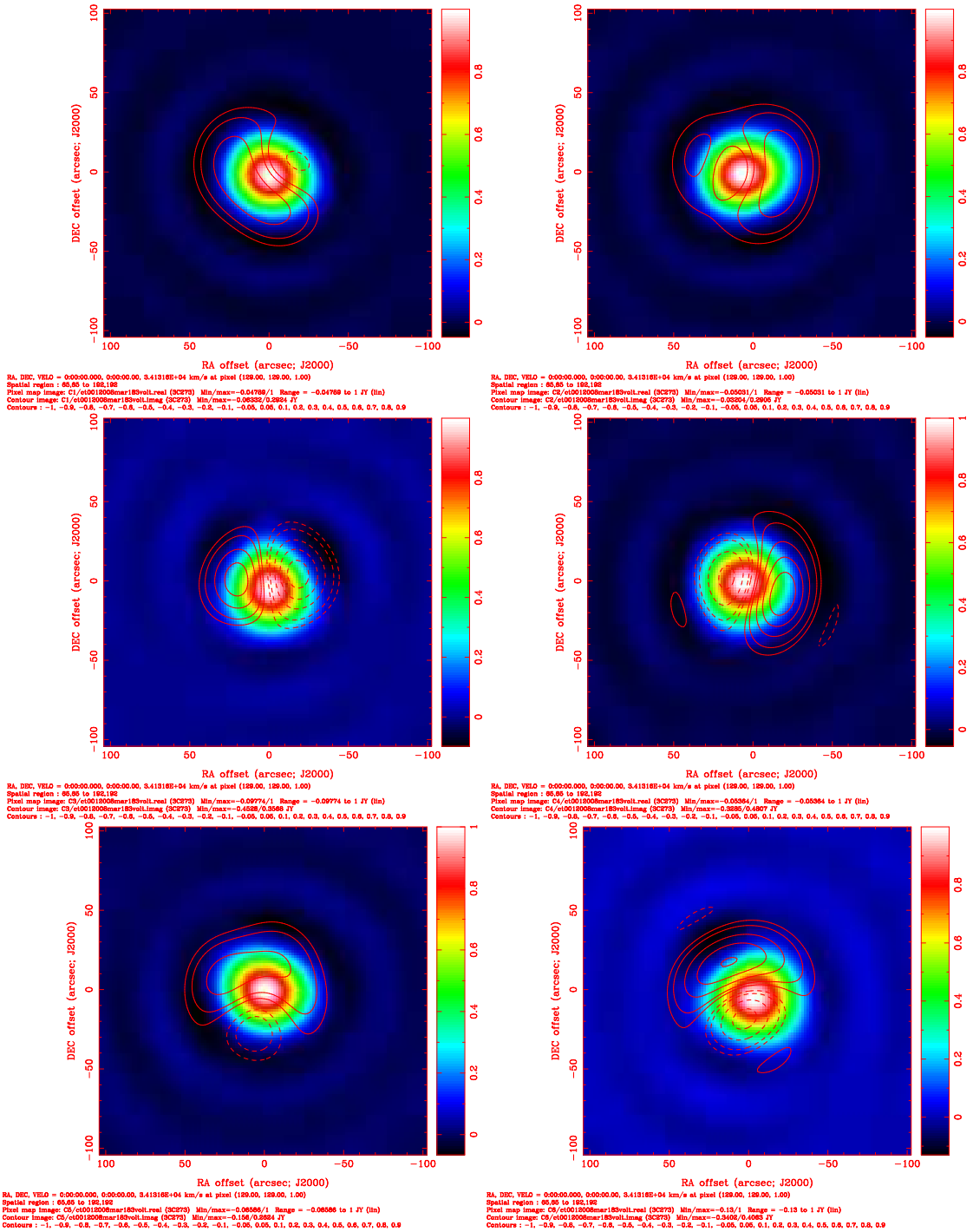

Figure 3.13 The voltage pattern of each of the 10-m antennas at λ =1.3 mm is shown. The real component of the voltage pattern is shown in color and the imaginary component shown in contours. The contours begin at 5% then 10% of the real component peak with intervals of 10% thereafter. The patterns are far more complicated given that that large values of the offsets can result in more complicated patterns as feed sidelobes begin to illuminate the primary.

3.4 Holography Results: Shape and Consistency of the Voltage Patterns

After completion of the initial series of holography measurements to adjust panels and align optics, an additional campaign was undertaken in an attempt to

- **address the accuracy of the assumed Gaussian profiles used in MIRIAD.**
- **address the applicability of the symmetric, Gaussian approximation to the primary beam profiles.**
- **determine any antenna or elevation based variation in the pattern.**

Typical imaging software assumes the primary beam is uniform among antennas of a given style, is free of imaginary parts, and has a circularly-symmetric Gaussian profile. The first two goals address the properties of the antenna styles within the framework of typical assumptions. The results of such studies can immediately be integrated into the MIRIAD routine **pb.for** either by an alteration of the assumed width of the Gaussian model or by a replacement of the current, Gaussian model with a more relevant, but still uniform and circularly-symmetric, model. Pursuit of the third goal relaxes all of the typical software imaging assumptions. Particularly, relaxation of the *uniformity* condition can have dire consequences as imaginary components do not necessarily cancel upon creation of a baseline illuminating pattern, a primary beam in the traditional sense (see Equation 3.1). When the components associated with 1 and 2 are identical, the imaginary components always cancel but if this is not the case the imaginary component can begin to strongly impact the image (see Chapter 2).

3.4.1 Data Acquisition and Reduction

Data collection and reduction were performed exactly as described in §3.2 with the addition of few steps to recover the beam properties on the sky. The mean, masked

real and imaginary aperture plane maps were padded with zeros using MIRIAD **imframe** and Fourier transformed, using **fft** in MIRIAD, back to the sky plane resulting in an interpolated voltage pattern on the sky with some noise filtering. To account for any frequency dependence between datasets, the cell sizes were scaled by the ratio of the frequency of the input dataset to the fiducial frequency. The images were then interpolated to a common resolution on the sky using the MIRIAD task **regrid**.

Data described in Table 3.1 from 2007 and 2008 were utilized in the determination of mean voltage patterns, although individual antennas were sometimes rejected for phase jumps or pointing drift problems. Pointing errors are highly variable from dataset to dataset, in collection of either science or holography data. In addition, such errors can be removed by a variety of means at the time of observation. I will discuss these methods in more detail later (see Chapter 4) but for the determination of voltage patterns, pointing error was removed via recentering the patterns on the sky by using the MIRIAD routines **imgen** to create an approximate beam pattern on the sky but located at the image center and **imdiff** to determine the shift between the model and the true voltage pattern. The derived offset was applied to the true voltage pattern. Focus error, which is not easily determined at the time of observation, was not removed because these errors are present in the science data collection process and therefore the impact on the voltage pattern needs to be included.

3.4.2 Data Analysis

The MIRIAD task **imfit** was used to fit Gaussian profiles to the measured primary beams. It provided major axis, minor axis, position angle and associated uncertainty. The axes were geometrically averaged to estimate the voltage pattern size. The ratio of major to minor axis defines the ellipticity. Fits to both the *real* and *amplitude* components were done because the *real* patterns tend to be more stable but the *amplitude* patterns contain a better representation of the instantaneous voltage response. *Amplitude* patterns include *imaginary* contributions, which tend to be more time variable due to changes in focus, astigmatic or coma induction from gravity in the antenna

surface, or a time variable illumination pattern offset (i.e. time variable optical alignment due to motion of the secondary). The MIRIAD task **pbplot** was used to plot comparisons to the default models for the beams. Azimuthally-averaged profiles were generated with the MIRIAD function **ellint** which integrates over annuli.

The measured voltage patterns were fit with a variety of clippings. The clip value is surprisingly important to the determination of the width of the voltage pattern. Voltage patterns are multiplied by other voltage patterns to create the traditional *primary beam* for a given baseline. The fact that this is a baseline-based parameter is of great consequence. Typically, the primary beams are clipped at the 5% point as the beams are thought to vary dramatically below this level. Inclusion of lower points on the beam can improve image quality if those points are stable. For a homogeneous array, or in the case of CARMA for baselines composed entirely of 10-m antennas, hereafter 10-m baselines, or entirely composed of 6-m antennas, hereafter 6-m baselines, the primary beams are voltage patterns squared. This then requires that the voltage patterns be constant at the 22% level. However, for mixed baselines the 5% location in the primary beam is given by

$$\vec{k}(PB_{mn} = 5\%) = 1.0416 * \frac{F_1 F_2}{(F_1^2 + F_2^2)^{\frac{1}{2}}} \tag{3.7}$$

for antennas having voltage patterns of FWHM F_1 and F_2. For the heterogeneous baselines, the 6-m antenna voltage patterns only need to be consistent to $\sim$50% but the 10-m antenna must be consistent at the $\sim$10% level. Inclusion of even smaller antennas, e.g. the 3.5-m SZA antennas which will soon be relocated to Cedar Flat, requires consistency of $\sim$10% and $\sim$5% for the 6-m and 10-m voltage patterns, respectively. Therefore, the voltage patterns are fit with clippings of 22%, 10% and 5%.

Fits to the imaginary beams were done by identifying maximum and minimum of the imaginary pattern. The maximum and minimum were differenced and divided by two. The position angle of the line connecting the positive peak to the negative peak was also determined. Finally, the location of the imaginary peaks within the

real pattern is calculated as an average of the real beam value at the imaginary maximum and minimum. The first two parameters identify the magnitude of the imaginary component and its location while the last value estimates the importance of the imaginary component to the overall beam profile.

3.4.3 Gaussian Fits to Measured Voltage Patterns

To determine the Gaussian widths for comparison with the default voltage patterns, clippings at the 10% and 22% level are applied. Table 3.3 provides the measured values for the voltage pattern sizes for all relevant clippings and parameters for the 10- and 6-m *style* antennas, i.e. C1-6 and C7-15 considered as ensembles. Properties of individual antennas will be addressed later. For the purposes of CARMA, only the fits for the 6-m antennas at 22% and the 10-m antennas at 22% and 10% are significant. Fits at lower levels are relevant only with inclusion of the 3.5-m SZA antennas and that will be addressed separately.

3.4.3.1 10-m Antennas

Figure 3.14 shows the real (left) and amplitude (right) widths of the 10-m antenna voltage patterns clipped at 22%. These values for the width are most relevant for the primary beams created for the 10-m baselines. The horizontal line shows the value provided by MIRIAD for the voltage pattern width. The amplitude pattern is wider on average for the 10-m antennas. As will be shown below, this is due to large imaginary contribution from several of the antennas.

The real voltage pattern width, clipped at 22%, has standard deviation of the mean within 1σ of the default model from MIRIAD. The width of the amplitude pattern of the ensemble is $\sim$1.5% wider than the default pattern and more significant in the mean, with a 5.5σ difference. However, if I consider only antennas C2 and 3, the antennas without significant imaginary contribution, the deviations with the default model because vanishingly small. These deviations are insignificant when considering

Table 3.3. Mean Parameters of Antenna Styles

Style	Clip %	#	FWHM Real ″	FWHM Amp ″	e Real %	e Amp %	PA Real °	PA Amp °
10.4 m	22	49	91.45 ± 1.20	93.22 ± 1.94	1.45 ± 1.12	2.78 ± 2.48	14.2 ± 50.9	17.9 ± 50.2
10.4 m	10	48	89.88 ± 1.12	92.46 ± 2.51	1.77 ± 1.26	3.19 ± 2.60	14.0 ± 57.1	18.2 ± 48.4
10.4 m	5	49	89.04 ± 1.08	92.22 ± 2.92	1.71 ± 1.51	2.93 ± 2.58	-11.9 ± 57.1	14.0 ± 47.5
10.4 m[a]	22	18	91.32 ± 1.03	92.05 ± 1.40	0.98 ± 0.67	1.76 ± 1.49	18.1 ± 59.1	22.8 ± 56.6
10.4 m[a]	10	18	87.71 ± 0.86	89.65 ± 2.27	2.42 ± 1.37	3.33 ± 2.10	-48.6 ± 53.8	17.3 ± 56.3
10.4 m[a]	5	18	88.88 ± 0.89	90.86 ± 2.34	1.43 ± 1.18	2.28 ± 2.33	-57.8 ± 41.7	31.9 ± 56.5
6.1 m	22	57	152.87 ± 1.94	154.68 ± 2.06	3.16 ± 2.47	3.17 ± 2.33	-5.8 ± 26.7	-8.4 ± 24.2
6.1 m	10	57	150.23 ± 1.84	151.94 ± 2.34	3.47 ± 2.39	3.29 ± 2.50	-10.2 ± 34.9	-12.5 ± 24.2

[a]Indicates the exclusion of antennas known to have large gradients in the imaginary beam.

Note. — All parameters have been scaled to a common frequency, 100 GHz. # is the number of measurements included in the value given. Uncertainties are measured in the sample, not in the mean, i.e. the standard deviation of the mean is the quoted uncertainty divided by the $\sqrt{\#-1}$. Nominal amplitude beam sizes are 91.64″ and 162.92″ for the 10-m and 6-m antennas, respectively. Other imaging assumptions are such that the real component beam size and amplitude beam size are identical, and ellipticity is identically one. The position angle of the beam is expected to be near zero because the dish should deform top to bottom based on gravitational stresses resulting in an elongated beam in the elevation direction.

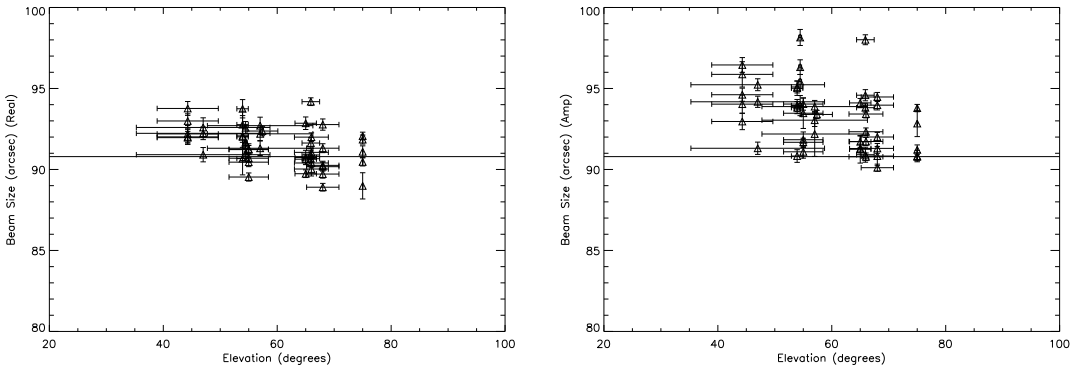

Figure 3.14 The real (left) and amplitude (right) voltage pattern sizes are plotted as a function of elevation. Data from C1-6 are included here. The clip value is 22%. The horizontal axis is the elevation with error bars representing the range of elevation over which the data were collected. The vertical axis is the voltage pattern size with error bars propagated from the **imfit** fits to the axes. The solid line represents the default width from MIRIAD and is 91.64″.

detriments to image fidelity (see Figure 2.8), indicating that the default FWHM for the Gaussian model in MIRIAD is accurate for the 10-m baselines.

Figure 3.15 shows the width of the voltage pattern fits clipped at the 10% level for the real (left) and amplitude (right) components. There is some hint of a narrower voltage width in both the real and amplitude components. This change is also evident in the fits excluding antennas with imaginary components. The deviations of the amplitude component are not statistically significant, but the real component is smaller than the MIRIAD model at the 11σ level in the mean. The difference (2%) is still small compared to the standard deviation of the sample and is small in terms of the possible detriment to image fidelity (again, see Figure 2.8).

In both components, there is some evidence of changes in width as a function of elevation. As the antenna moves to lower elevation, the top and bottom portions of the dish are subject to additional strain and may begin to sag. One could envision a situation where the voltage pattern becomes larger in the vertical direction and the ellipticity becomes larger with a relatively constant position angle. However, the bulk

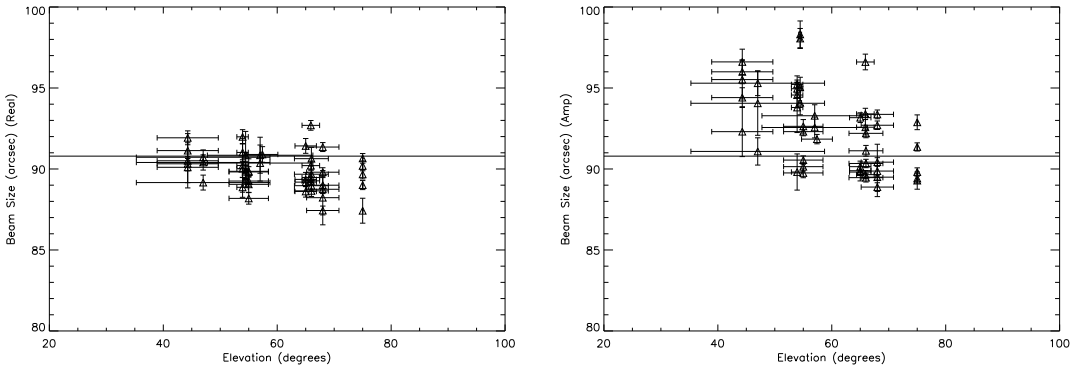

Figure 3.15 Similar to Figure 3.14 except clipped at the 10% level. The default size, shown as the horizontal line, is 91.64″.

of this trend sits within the scatter of the measurements and a linear fit to the data reveals that a constant fits within one sigma.

In terms of the width of Gaussian fits to the voltage pattern, the default values in MIRIAD are acceptable for inclusion in both the 10-m baselines and the heterogeneous baselines. However, the narrowing of the pattern at increasingly lower levels indicates that the voltage pattern may get narrower more rapidly than the Gaussian model.

3.4.3.2 6-m Antennas

Figure 3.16 shows the real (left) and amplitude (right) widths of the 6-m antenna voltage patterns clipped at 22%. The 10% clipping is discussed later in the context of the SZA antennas. These values for the width are most relevant to the baselines created for 6-m baselines and heterogeneous baselines. The solid line shows the value provided by MIRIAD for the voltage pattern width.

The amplitude and real patterns are consistent within the standard deviation of the samples. Here the deviation from the default MIRIAD model (162.9″) is significant. The measured width of the amplitude component is 154.7±0.2″ for the

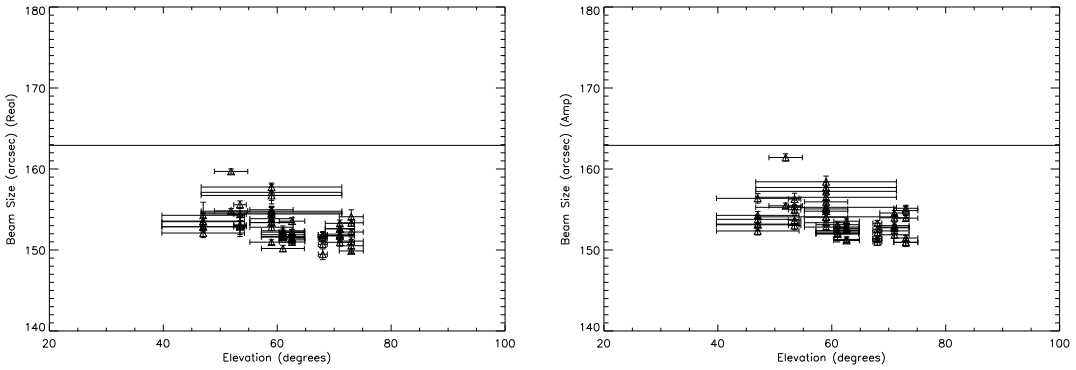

Figure 3.16 Similar to Figure 3.14 except for the 6-m antennas. The default size is 162.92″.

uncertainty in the mean. This 5% difference has significant impact on the image quality (Figure 2.8). The default FWHM in MIRIAD will be altered to account for these differences. Like the 10-m antennas, the 6-m antennas show evidence of a narrowing voltage pattern relative to a Gaussian at low levels. These antennas also show a possible trend with elevation, but the significance of the trend is weak.

3.4.3.3 Heterogeneous Baselines

The heterogeneous baseline creates a voltage pattern that looks like the square root of the product of the 10-m and 6-m voltage pattern on the sky. The product of two Gaussians produces another Gaussian, with $FWHM_{new}^{-2} = FWHM_1^{-2} + FWHM_2^{-2}$ and the resulting voltage pattern width is then $\sqrt{2}FWHM_{new}$. Given Equation 3.7, the fit to the 10-m voltage pattern must be considered down to the 10% level. The value given by MIRIAD for the default model is 117.10″. For the values derived above, the resulting width should be 111.50″. The 5% devivation from the default model will have a significant impact on the image fidelity (see Figure 2.8).

3.4.4 Deviation from Circularly-symmetric, Gaussian Fits

3.4.4.1 Deviation from Gaussians

Figure 3.17 shows the amplitude of the mean primary beams (top) for the 10-m (left), heterogeneous baseline (center) and 6-m (right) antennas, respectively. These were formed by averaging antennas of a given style over time and antenna number. The second row depicts the azimuthally-averaged version of the images shown on the top row. The dashed-line represents a best-fit Gaussian to the average image. The dotted line shows the MIRIAD model. The horizontal lines show the half-power, 5% and 1% points in the primary beam. The next two rows highlight specific regions of the beams and the last row, now with a linear scale, shows the differences between the MIRIAD model and the data (dotted line) and the best-fit Gaussian and the data (dashed line).

At the half power point, the 10-m beam is well fit by the MIRIAD model. The measured profile is actually wider at the half power point than either of the best-fit Gaussian models. This difference is offset at lower levels in the beam. As discussed above, the width of the best fit Gaussian is far narrower than the MIRIAD model for the 6-m primary beam. The apparent difference seems to be mitigated to some extent here but the difference above was discussed in terms of the FWHM of the voltage patterns and the difference here is a radial difference in the primary beam, so the differences are suppressed by a factor of $2\sqrt{2}$. The width difference is similar in the mean profile compared with the fits to the ensemble discussed above. The same is true for the heterogeneous baseline.

The previously identified apparent trend of the voltage patterns getting narrower faster than a Gaussian at low levels is clear in the azimuthally-averaged profiles. In the case of the primary beam, the 5% point (dot-dot-dashed, horizontal line) shows that the Gaussian lies far outside the value for the data. In the best case scenario, the 10-m antenna primary beam is actually slightly wider than the predicted Gaussian at the half-power point and then narrows rapidly. At the 5% level the measured profile is 3-3.5$''$ narrower. This difference grows to 5-9$''$ for the 6-m primary beam depending

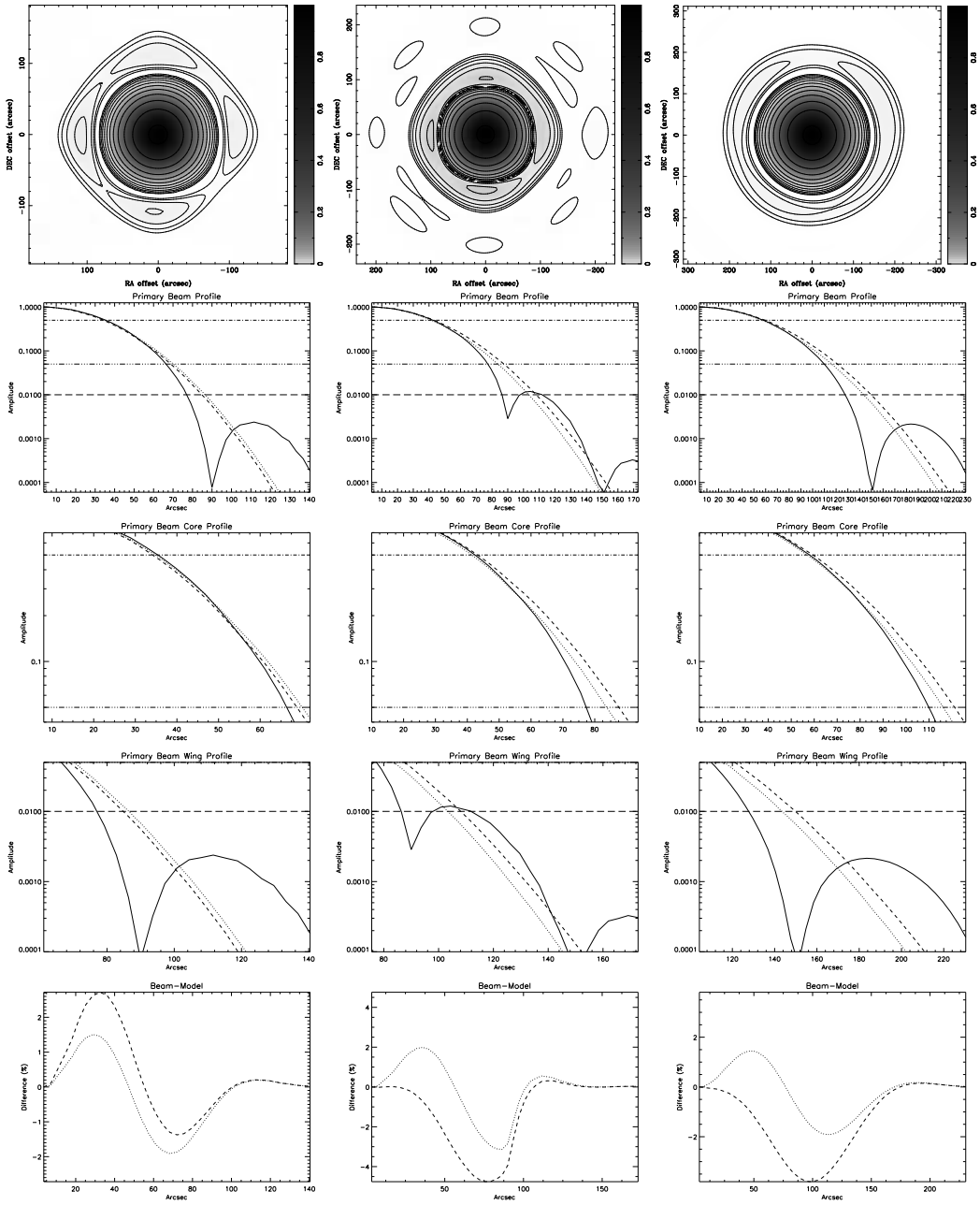

Figure 3.17 The top row shows the primary beam image for the 10-m (left), heterogeneous (center), and 6-m (right) baselines. The gray scale is log-stretch between 0 and 1. The contours peak at 90% and decrease by factors of 2^n. The 5^{th} contour is approximately the 5% point. The lowest contours are ∼0.05% and are shown mostly to outline very faint features. The second row is the azimuthal average of the image directly above it plotted in log scale. The solid line is the data, the dashed line is the best-fit Gaussian and the dotted line is the model from MIRIAD. The horizontal lines are the half-power (dashed-dot), 5% (dashed-dot-dot) and 1% (dashed) points in the primary beam. The third row, again in log scale, zooms in on the half-power and 5% points in the beam. The fourth row shows the low level (1%+sidelobe) parts of the beam. The last row, now plotted in linear scale, is the difference between the best-fit Gaussian (dotted line) and the MIRIAD (dashed line) models.

on whether the MIRIAD model or the best-fit Gaussian is used. The difference at the 5% level for the heterogeneous baseline is between 6 and 10.5″. Deviations at the 1% level will be discussed along with the sidelobes later.

In reality, the Gaussian model represents a compromise averaged over the entire beam. The Gaussian initially gets narrower faster than the measured profile but then the measured profile decreases rapidly causing the Gaussian to under-predict the power at the half power point of the beam, but eventually it over-predicts the power in the wings of the profile. The best-fit averages these contributions with the half-power point providing more power but the wings covering a much larger area. This trend is seen in the residuals as a function of radius shown in Figure 3.17.

The deviation from the model is estimated by integrating the absolute value of the residual profile or weighting by either the amplitude or the amplitude times the area of a given annular region. For the 10-m antenna, the best-fit Gaussian (dotted line) produces less error in the core of the beam but more in the wings. All weightings show that the best-fit Gaussian produces less error than the MIRIAD model but the difference between the models themselves is never more than ∼1%. For the 6-m antenna, the improvement is far greater except in the very central portions of the beam. Here, the use of a wider beam profile by MIRIAD better approximates the very central regions of the beam but near the half-power points, the deviation is more significant. Weighting the profile by the symmetrized beam shows only marginal improvement of the best-fit Gaussian over the MIRIAD model, but weighting by the beam and area shows dramatic improvement. A similar situation is seen for the heterogeneous baseline. Clearly a different model of the primary beam is needed if the discrepancies are to be rectified.

3.4.4.2 Ellipticity

Departures from circular symmetry in the core of the beam are expected. The dish is expected to sag somewhat under the influence of gravity elongating the beam in the vertical direction as the top of the dish sags slightly towards the ground. Differences in the ellipticity of the real and amplitude component are expected when the imaginary

component of the beam dominates as this extends the amplitude beam in the direction of the imaginary component. The ellipticity is also expected to change as a function of elevation with ellipticity growing at lower elevations because of increased sag. Strictly amplitude ellipticity, excited by an imaginary component, will be discussed in the context of the imaginary beam later.

As an ensemble, there is little evidence of ellipticity in the 10-m antennas. Figure 3.18 shows the ellipticity (top) and position angle (bottom) for the 10-m antennas. The left column is the real component while the right side shows the amplitude component. The average ellipticity derived for the amplitude component, 1.12±0.4%, is 3σ consistent with zero. The real component ellipticity, 1.94±0.2, appears to be significant but the spread in the sample of position angles, ±51°, leaves little doubt that the ellipticity is not real as the position angle is symmetric about ±90°. It is possible that there is some significant ellipticity but it is masked by imaginary beams, which are often antenna-based parameters.

Figure 3.19 shows similar data to 3.18 but for the 6-m antenna voltage patterns. Here, the ellipticity is consistent in the real and amplitude components, with values 3.2±2.5 @ -6±27° and 3.2±2.3 @ -8±24°, respectively. The consistency of the real and amplitude ellipticity, and the consistency and relatively small spread of the position angle suggests that this ellipticity may be inherent to the 6-m antennas. If the standard deviation of the mean is calculated for these values the errors are reduced to 3.16±0.33 @ -5.8±3.6° and 3.17±0.31 @ -8.4±3.2° for the real and amplitude patterns. The values are consistent with a 3.2±0.3% ellipticity at a position angle within 3σ of zero. There is no evidence of ellipticity changing with elevation but the precision of the measurements may mask such a trend.

The position angle of the ellipticity will rotate on the sky with parallactic angle and therefore requires a more detailed treatment of the imaging process than software currently allows. In Chapter 2, the tools for addressing the ellipticity via simulation were developed. In Chapter 5, they will be applied.

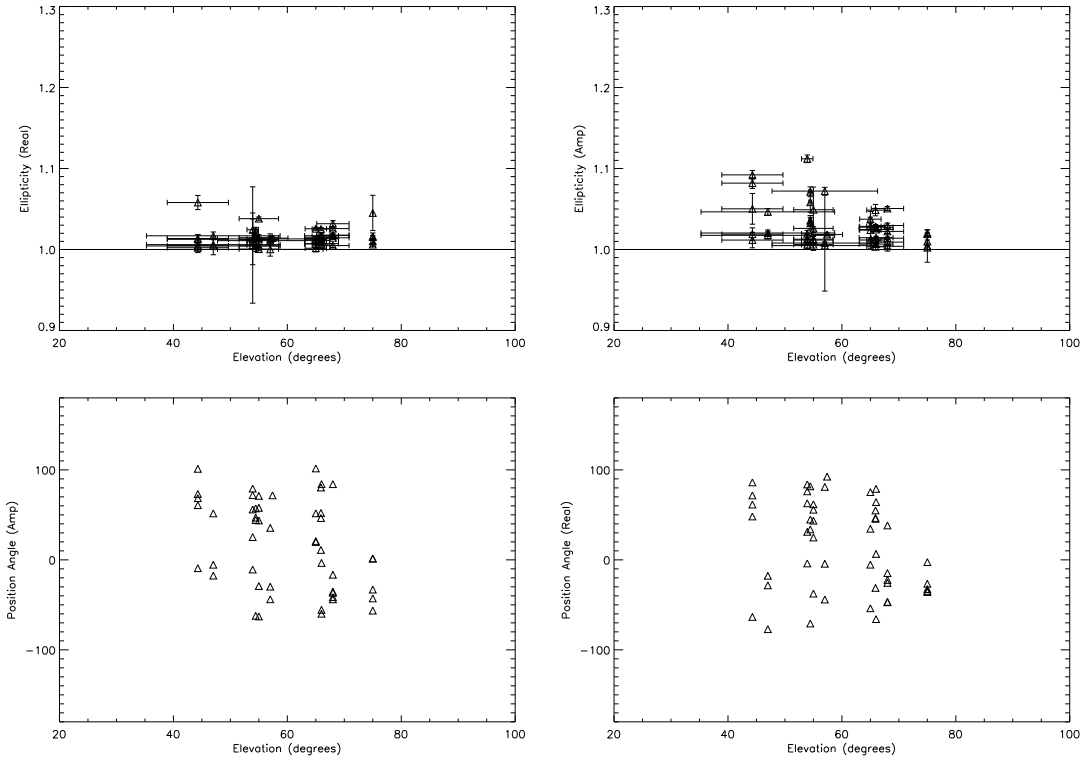

Figure 3.18 The real (left) and amplitude (right) voltage pattern ellipticity (top) and position angle (bottom) are plotted as a function of elevation. Data from C1-6 are included here. The horizontal axis is the elevation with error bars representing the range of elevation over which the data were collected. Position angles are in degrees. The vertical axis error bars are the propagated error from the **imfit** fits to the axes.

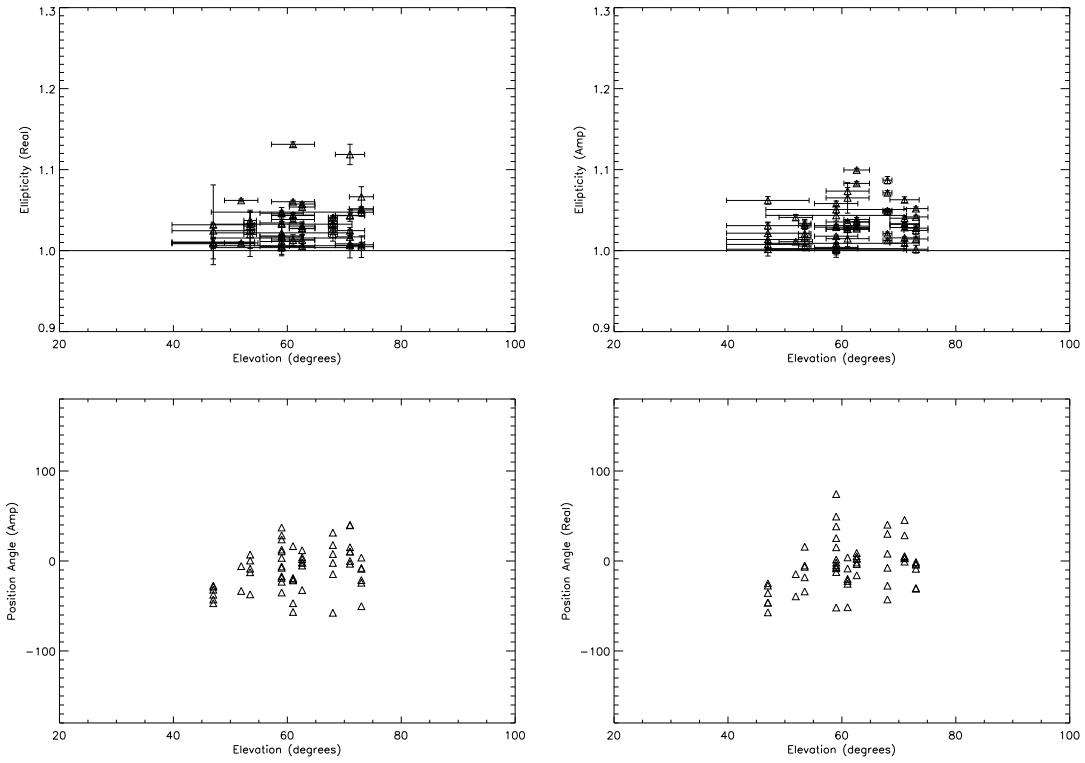

Figure 3.19 Similar to Figure 3.18 except for the 6-m antennas.

3.4.4.3 Low Levels and Sidelobes

The inclusion of the 8-element, Sunyaev-Zeldovich Array (SZA) into CARMA (hereafter CARMA-23) provides an excellent opportunity to enhance wide-field imaging capabilities. A single baseline composed of a 10-m and a 3.5-m antenna is nearly equivalent in collecting area to a 6-m baseline and 48 such baselines would represent a non-negligible enhancement to the overall sensitivity, especially in mosaics. The inclusion of the SZA more than doubles the instantaneous *uv*-coverage, from the 105 baselines of the current array to 253, and the baselines composed of two 3.5-m antennas, hereafter 3.5-m baselines, can probe flux on scales of 2-3′. Enhancing the *uv*-coverage on these very large scales will enable recovery of the remaining, largest spatial scales by the 10-m antennas in total power.

However, there is a concern. The voltage response of the 3.5-m SZA antennas is wide, with a 4′ FWHM at a wavelength of 3 mm. The 10-m antennas, with FWHM of ∼1.4′ at the same wavelength, have sidelobes well within the 3.5-m antenna main beam. Ordinarily, in homogeneous arrays, the primary beam for a baseline has the sidelobes of one antenna illuminated by the sidelobes of the other so the sidelobes are highly suppressed relative to the main beam. In the case of CARMA, even the first sidelobes of the 10-m antenna voltage pattern are illuminated by the main lobe of the 6-m antenna voltage pattern at the 20-25% level. Figure 3.20 demonstrates both the small influence of the 10-m antenna voltage pattern sidelobes when illuminated by a 6-m antenna voltage pattern (left panel) and the larger influence when that illuminating voltage pattern is changed to one generated by a 3.5-m antenna (right panel). The residual contribution from the sidelobes increases by a factor of three from an often negligible ∼3% to a fairly significant ∼10%. However, the detriment to fidelity will still depend strongly on the flux distribution.

If the 10-m antenna voltage pattern sidelobes are neither stable nor predictable, the benefit of the SZA will be restricted and the use of baselines with 10-m and 3.5-m antennas cannot be included in high fidelity imaging. Modeling the behavior of the sidelobes and determining their overall stability at a level necessary for high fidelity

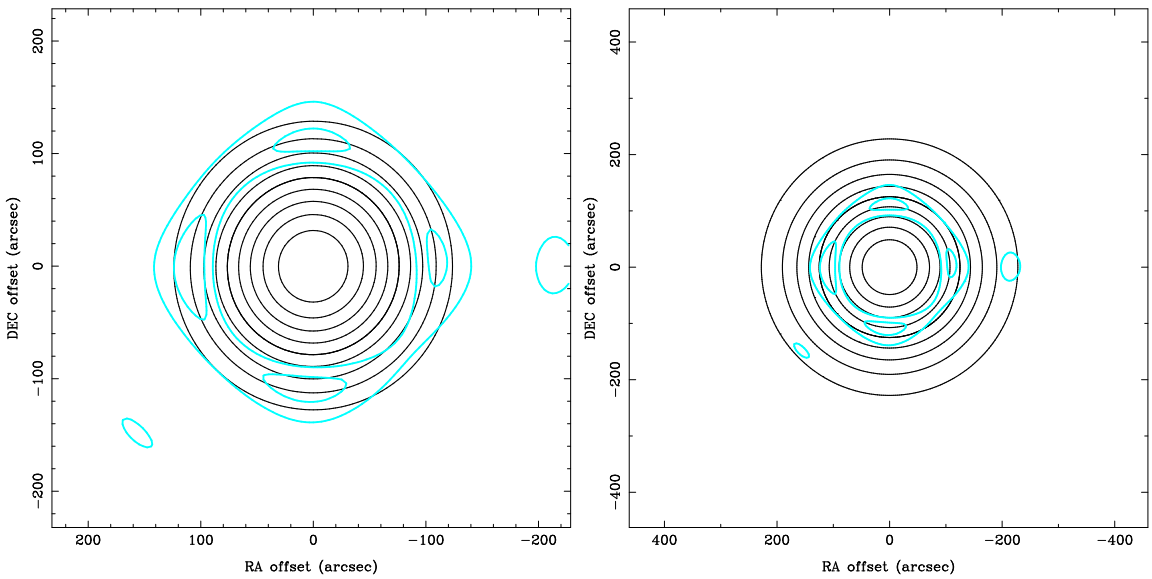

Figure 3.20 The left panel displays the negative, low-level sidelobes of the 10-m voltage pattern overlaid on the main beam of the 6-m antenna voltage pattern. The right panel shows the same but the main beam is that of a 3.5-m voltage pattern. The negative contours, shown in blue, are -5% and -10% of the peak of the 10-m antenna voltage pattern. The black contours of the main beam are 5%, 10%, and then increasing by 10% up to 90% of the peak. When multiplied by the 6-m antenna voltage pattern, the peak 10-m voltage pattern sidelobes, ∼-13%, are multiplied by 25% resulting in 3% residual contribution which is significant in cases where the dynamic range needs to exceed about 100. On the right, the -13% sidelobes are now multiplied by 70% of the peak in the main beam giving 10% residual contribution which will be significant when the needed dynamic range is 30. A 6-m antenna voltage pattern overlaid on a 3.5-m antenna voltage pattern will look much like the left panel above given the proportions of the antenna sizes.

imaging is an expensive enterprise, requiring repeated, modest-resolution holography over a variety of observing conditions spanning day- and night-time conditions. However, an initial estimate of the stability can be made with our current, night-time restricted dataset. While I would hesitate to use the beams described here for imaging, I can verify whether more detailed study of the sidelobes is merited.

Figures 3.21 and 3.22 display the intra-antenna variation of the six 10-m antennas in the real and imaginary component, respectively. The averaged (real-only) sidelobe pattern is visible in Figure 3.17, although the relevant quantity now is the square-root of the displayed primary beam. The dataset from 2008-Mar-24 (see Table 3.1) was used as the base image as this was the dataset which included the greatest number of 10-m antennas. Data from 2007-Aug-12, 2007-Sep-07, and 2008-Mar-27 in the 3-mm band were used for comparison. C1 uses data from 2007-Sep-07 as the template and only 2007-Aug-12 is available for comparison, hence C1 is largely ignored in the following discussion due to the lack of sufficient data for comparison.

In general the agreement between the various real components is remarkable. The bulk of the sidelobe pattern subtracts out extremely well, with voltage pattern sidelobes of 5-10% being typically consistent to within <2-3% of the voltage pattern peak. Given that the nominal beam patterns are assumed to be Gaussian and have no sidelobes, use of an appropriate model of the sidelobes can easily reduce the error induced by using this Gaussian from 5-10% to 2-3%, an improvement of a factor of 2 to 5 even without a detailed treatment of the sidelobe variations with time or observing conditions.

Instances of >5% are rare, with C2, C3 and C4 showing single instances of such deviation. For all but C4, these differences are common to the datasets separated significantly in time indicating that there may be time evolution involved or that the more significant deviations seen in the red and cyan contours may be related to the marginally resolved source used in these beam patterns. The RMS of the residual images is always less than 0.9% with datasets taken more closely in time reducing this deviation to 0.8% or less. The largest deviations are seen near the half-power point of the illuminating, 3.5-m antenna voltage pattern indicating that, while the overall

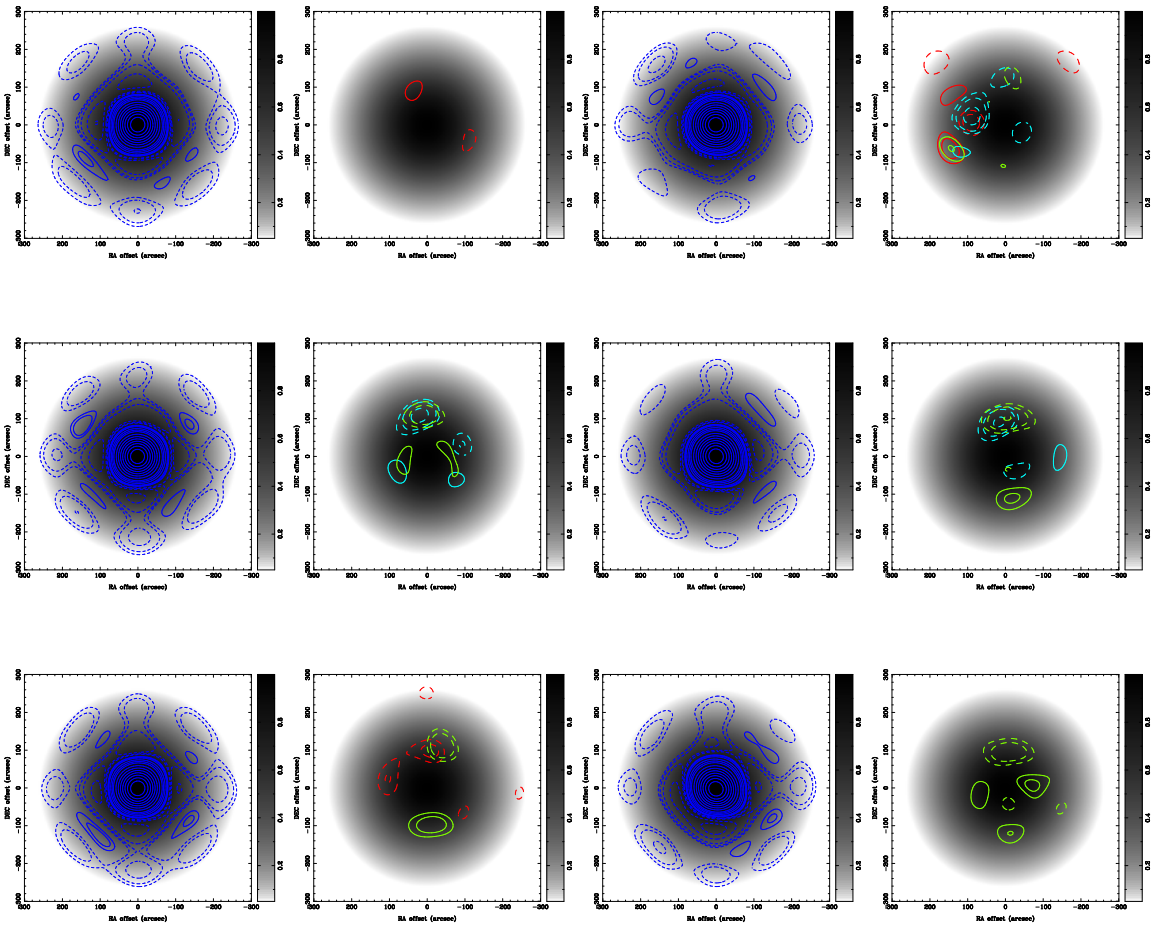

Figure 3.21 Real component voltage patterns for the six 10-m antennas. The image is a model of the real voltage response of a 3.5-m antenna. The dark blue contours represent the six template images, one per antenna. Other datasets were subtracted from these templates and are shown in red, cyan and green contours. In all cases except for C1 (top left of the figure) the green contours were taken close in time and on the same source as the template image, whereas the red and cyan contours were taken close in time to each other and on a common source but at a time and on a source different than the template dataset. For C1, only two epochs were available. For this antenna, the template and red contours were from datasets taken close in time on the same source. The absence of contours indicates the absence of data, not a perfect fit. Contours are at 2%, 3%, 5%, 10%, 15%, 20%, and then increasing in 10% steps thereafter. Solid contours are positive and dashed contours are negative. The pair to the top left is for C1, top right is C2, middle left is C3, etc. The stability of a feature is best seen by noting the strength of the feature in the template image and then noting the variation, i.e. a sidelobe at 10% which has a 2% residual is 10±2%.

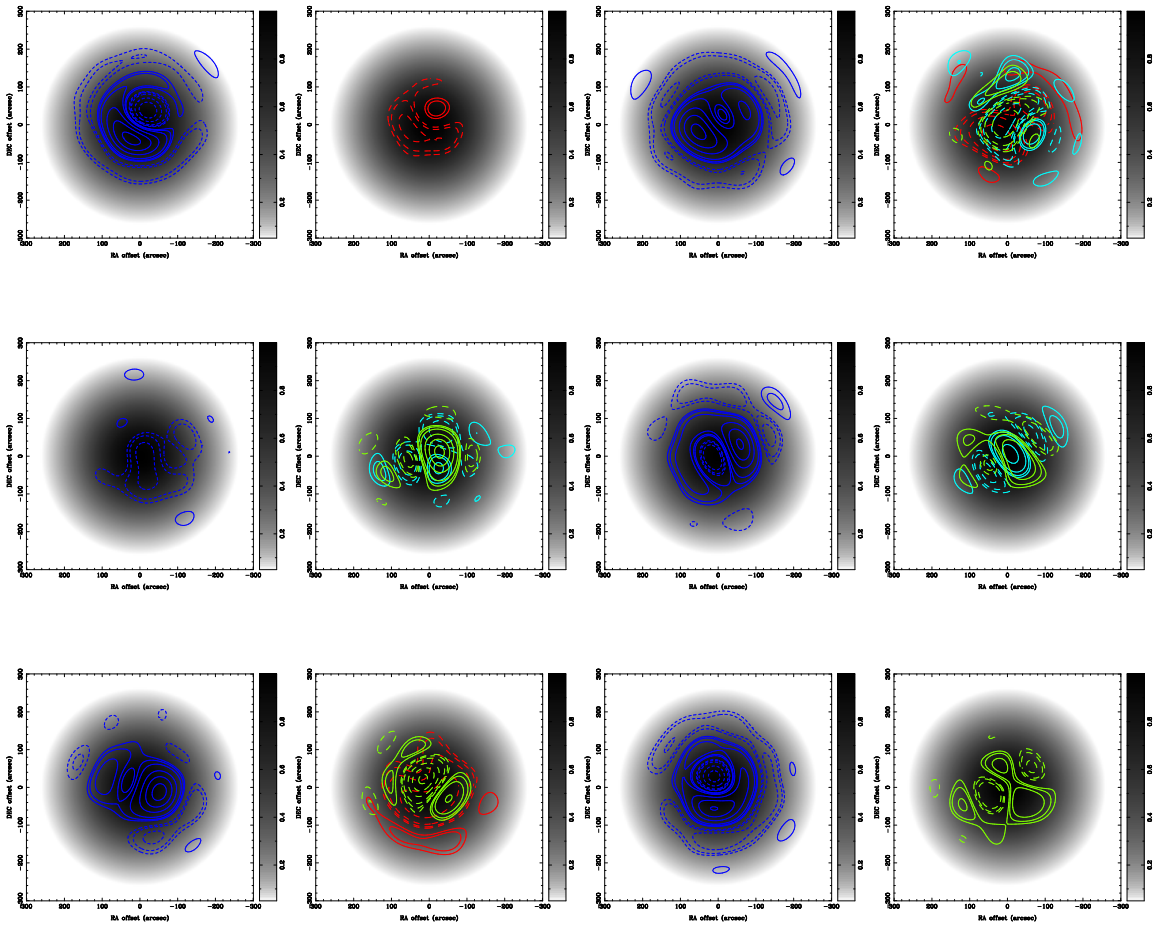

Figure 3.22 Same as 3.21 except for the imaginary component.

consistency of the real component of the voltage pattern is strong, work remains to be done.

The agreement of the various imaginary components is less striking. In general the signal in the imaginary beam is rather small. In Figure 3.22, the peak signal is typically 0.2, i.e. $\pm 20\%$ of the nominal beam peak. Variations in the imaginary beam in C1 are 3-5% out of 20%, i.e. still showing the signal is significant. The receiver in C2 was changed between the taking of the data shown in red and cyan contours and the data shown in the template and green contour data. The old receiver had significantly higher noise than the other antennas and the more recent data are more likely to represent the true repeatability of the voltage pattern. C2 and C5 have structures which appear to be constant phase offsets and are likely the result of poor phase stability during the observation or closure errors.

The structure of the 10-m antenna main lobe voltage pattern also needs to be consistent down to the 5% point in the pattern. Table 3.3 and Figure 3.17 display the properties of the main lobe down to this level and beyond. Clearly, CARMA-23 will require the new model for the primary beam profile to be implemented. The 5% point in the voltage pattern is the 0.25% point in the primary beam. At this point, the main lobe deviates from the Gaussian model by $20''$ or more at a frequency of 100 GHz. The fact that, as ensembles, the Gaussian fits to the width get smaller with lower clip levels implies that all of the antennas will show a faster decrease in the voltage pattern than a Gaussian would predict.

It appears as though further effort to measure and monitor the sidelobes and the low power levels of the voltage pattern is merited based on the consistency seen in these datasets and the measured profile. Such a monitoring campaign serves two purposes. First, it provides an opportunity to monitor the properties of the beams and may catch sudden changes in focus and determine if sudden changes in aperture efficiency may be likely while simultaneously providing the means by which to correct such issues. Second, it allows a build-up of beam profiles which would provide a long time baseline spanning a variety of observing conditions which will be vital to obtaining high image fidelity in the future.

3.4.5 Antenna-Based Results

The voltage patterns are, at the most fundamental level, antenna-based phenomena. The results for individual antenna voltage patterns are provided in Table 3.4. This table provides information on the number of relevant datasets per antenna along with derived properties. As was the case for the ensemble properties, the uncertainties quoted are of the sample, not the mean, unless otherwise stated. Three additional parameters are included here, namely the magnitude of the imaginary beam as calculated by half the difference between the maximum and minimum contribution, the position angle of the line connecting the maximum and minimum, and the mean value of the real beam at the location of the imaginary maximum and minimum.

While the number of datasets available for a given antenna style is typically rather large ($\sim$50), several antennas were offline for large portions of the summer of 2007. Antennas C8 and C15 were subject to massive errors in the pointing model resulting in pointing *drift* during the observations. Such pointing drift does not simply result in the offset of the beam center but shears the beam and can result in alteration of any phase behavior in the pattern. Antenna C2 has, until very recently, had persistently high system temperature and thus poor sensitivity. Antenna C6 was often warm and was not present in many of the datasets. Antenna C7 had persistent phase jumps during this time and almost all of the datasets needed to be flagged.

Figure 3.23 shows an example of the real (left) and imaginary (right) voltage patterns over the range of observing parameters. The sets of three overlaid contours are from three distinct datasets. Some properties, e.g. ellipticity, are sufficiently small that they are not obvious in the datasets while others, such as the size and orientation of the imaginary beam, are clear and consistent over the various runs.

3.4.5.1 Frequency, Source and Sampling Dependence

In what follows, all voltage pattern beam widths have been multiplied by the mean frequency of observation and divided by 100 to normalize all sizes to 100 GHz. The difference in IF frequency has been accounted for in the first transform from sky to

Table 3.4. Voltage Pattern Parameters

Ant#	#	FWHM Real ″	FWHM Amp ″	e Real %	e Amp %	PA Real °	PA Amp °	Peak to Peak Imag	PA Imag °	Real @ Imag Real
1	7	88.91±1.10	91.16±2.24	2.1±1.3	2.8±1.1	14.8±33.7	1.4±16.8	0.163±0.023	151.0±11.0	0.542±0.033
2	7	90.42±0.63	91.98±2.04	1.8±1.1	3.5±2.2	-39.0±50.8	-67.1±23.4	0.091±0.040	123.5±86.2	0.398±0.201
3	11	89.33±0.91	90.56±1.59	1.1±0.6	1.7±0.7	53.4±49.1	-2.3±2.2	0.086±0.045	-96.9±81.8	0.379±0.194
4	8	91.45±0.71	95.03±1.98	2.0±1.2	3.7±3.4	35.1±42.0	-65.6±5.8	0.172±0.042	-58.1±11.0	0.542±0.043
5	9	89.74±0.64	92.55±2.13	1.5±0.7	3.3±2.9	-17.3±34.3	59.5±8.0	0.169±0.052	-125.8±47.7	0.510±0.128
6	6	89.50±0.54	94.48±2.08	2.8±2.3	5.4±3.7	55.2±21.6	40.9±13.5	0.221±0.028	-146.7±19.4	0.561±0.027
7	3	153.18±1.27	153.15±0.88	1.2±0.7	2.8±1.8	-23.6±26.8	-23.5±29.1	0.055±0.013	-17.9±90.0	0.119±0.168
8	5	152.62±2.53	152.74±2.58	3.3±1.5	4.5±3.7	-1.8±12.2	-0.5±12.8	0.057±0.013	83.9±76.3	0.475±0.145
9	8	152.44±1.32	153.23±1.49	3.7±4.3	2.9±2.4	-14.9±26.3	-12.7±9.8	0.062±0.007	81.3±57.4	0.342±0.210
10	9	153.06±1.76	154.24±1.91	3.1±2.0	2.3±1.5	-13.4±26.4	4.0±24.5	0.098±0.017	36.5±15.8	0.461±0.075
11	6	150.79±0.92	152.78±1.27	3.1±1.3	2.5±2.5	3.7±25.9	4.0±30.9	0.088±0.012	110.2±18.9	0.273±0.177
12	8	152.55±1.57	153.57±2.09	4.5±3.2	4.0±2.4	-13.8±26.4	-9.3±29.1	0.080±0.018	88.7±80.4	0.286±0.178
13	8	153.81±1.98	154.16±2.19	2.2±1.7	2.7±2.2	7.9±25.8	11.0±35.2	0.071±0.020	-2.5±49.9	0.394±0.132
14	6	152.65±1.06	153.26±1.17	3.4±1.6	3.4±2.9	-10.7±17.2	-20.8±25.1	0.067±0.010	42.9±79.9	0.356±0.237
15	4	155.60±2.89	156.04±3.89	2.7±2.6	4.1±1.7	-17.6±16.9	-26.8±19.6	0.069±0.027	-82.7±100.3	0.266±0.187

Note. — All values are scaled to represent the parameter at 100 GHz. MIRIAD amplitude beam sizes are 90.78" and 162.917" for the 10-m (1-6) and 6-m (7-15) antennas, respectively. Fits are clipped at the 22% and 10% level for the 6- and 10-m antennas, respectively. Uncertainties listed are determined from the maximum of the peak to peak divided by two and the standard deviation of the sample.

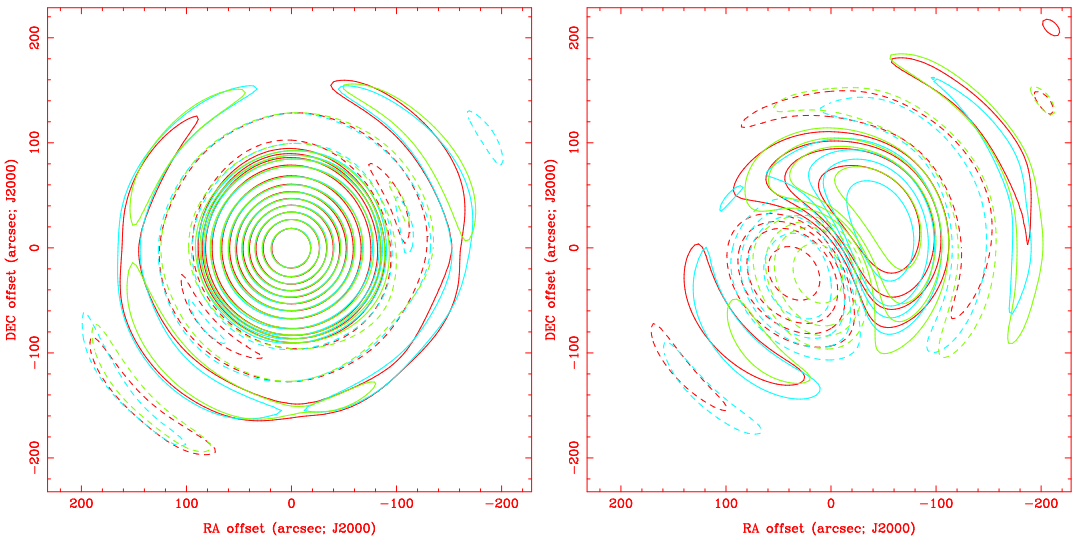

Figure 3.23 The real (left) and imaginary (right) voltage patterns are shown for C4 over three observing runs. Each run is highlighted in a different color with red, blue and green contours representing 2007-Sep-11 (two runs) and 2007-Sep-16. Dashed contours are negative structures while solid contours show positive features. The contours are 1%, 3%, 5%, 10%, then increasing at 10% intervals, normalized so that the amplitude has a peak of 1.

aperture plane, normalizing the patterns to the LO frequency. Most datasets were taken with a mean frequency of 100.2 GHz. However, the 10-m and 6-m each had a single dataset at a frequency 5 GHz different from the regular 100.2 GHz. In each case, the 5 GHz difference has no significant impact on the measured properties of the voltage pattern.

Most of the datasets were taken in CARMA's extremely compact, E-array, which has a resolution of $\sim$10.5″ at 3 mm. Mars ($\sim$7.25″ at the time of observation) was often utilized as a 3-mm holography source. First order amplitude scaling was removed by self-calibrating against a Mars model for all positions. Still, offset positions could in principle be affected by the finite size of the planet. In general, these effects should be minor as the typical baseline length used for the beam patterns is half the array size, or about 40 m. Mars is poorly resolved on such baselines. The expected irrelevance of a resolved Mars is echoed in the data with no discernible difference between values determined using the point sources 3c273 and 3c454.3 and those determined using Mars.

Finally, some of the datasets were taken with a factor of four oversampling of the voltage pattern on the sky while others were taken in at roughly twice the Nyquist sample rate. The more sparsely sampled patterns are taken over larger regions of the voltage pattern in an attempt to measure the sidelobe pattern. On average, consistency was seen on most antennas. Pointing drift on the longer timescales required to obtain the larger patterns resulted in noticeable deviations for some antennas in a few datasets. These antennas and datasets were not included in the final analysis. There is some hope that optical offset guiding (Chapter 4) can be integrated into the process providing longer timescales for pointing stability.

3.4.5.2 Beam Sizes

Beam sizes were fit in the same way as for the ensemble properties. Figures 3.24 (amplitude component) and 3.25 (real component) show the trends of voltage pattern size with elevation for the fifteen CARMA antennas. Each panel shows the voltage pattern size in arcseconds and the elevation in degrees. The error bars in elevation

indicate the range over which the data were collected. Error bars in beam size are the propagated errors in the original axis determinations. The dashed line provides an indication of the FWHM used by MIRIAD. Fits were clipped at the 10% level for the 10-m antennas and 22% for the 6-m antennas as the 10-m antennas contribute down to the 10% level for the heterogeneous baselines. In the future, the fits down to the 10% level for the 6-m antenna and 5% for the 10-m antennas will need to be considered as the SZA is included in CARMA.

In general, disagreement between the real and amplitude sizes (seen either in Figures 3.24 and 3.25 or Table 3.4) of the voltage pattern would indicate that there is a significant imaginary component in the amplitude fit. An imaginary gradient, for example, would widen the beam in the direction of the gradient while having little effect on the orthogonal direction. Larger than expected amplitude patterns and amplitude-only ellipticity would result. Shared deviations in the real and amplitude component or deviation of the real component alone are indicative of an overall error in the beam model. Such deviations could be as simple as a focus error or perhaps something significantly more sinister.

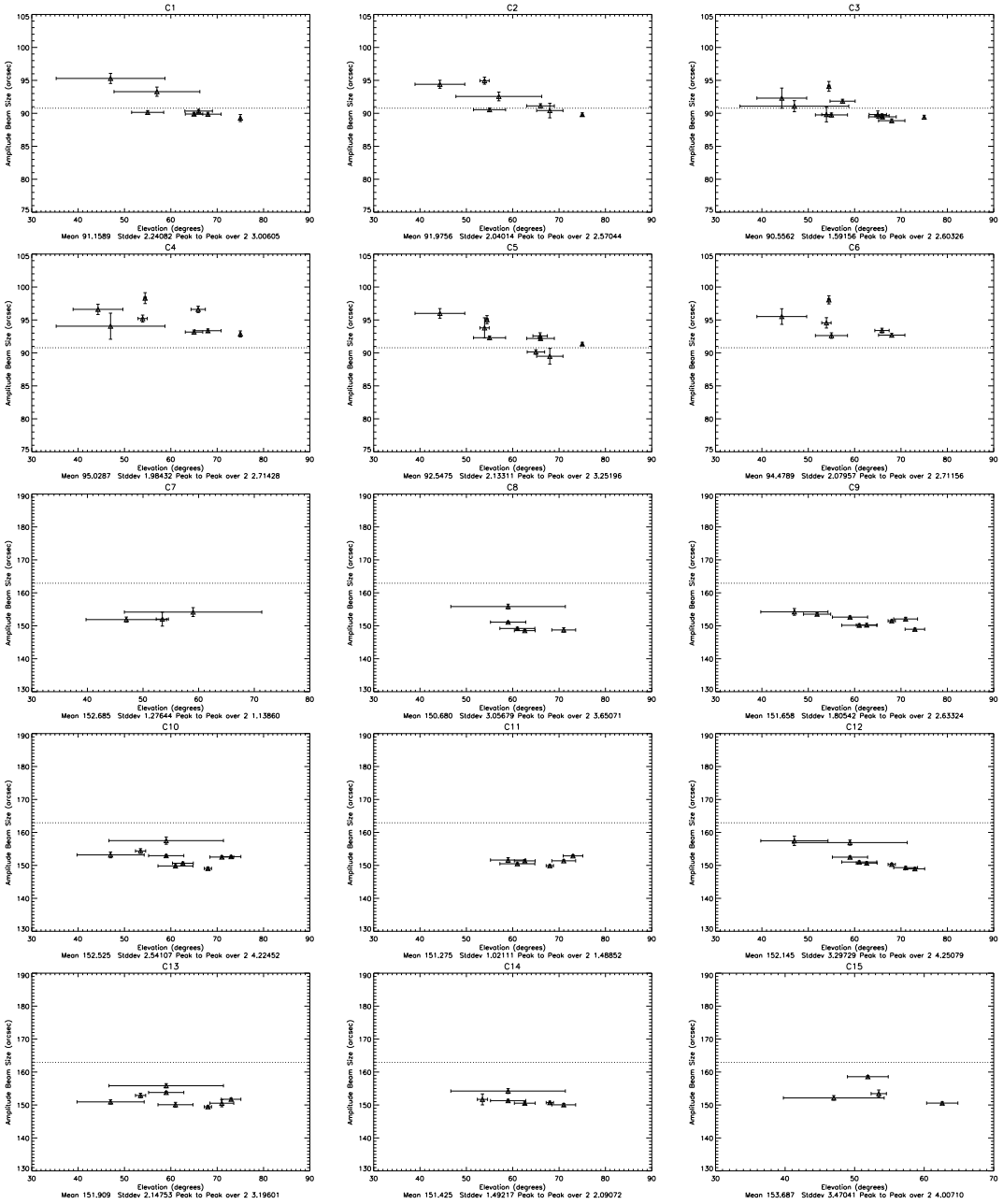

Figure 3.24 Each of the CARMA antenna amplitude voltage pattern widths is plotted against elevation. The horizontal error bars represent the range of elevations over which the data were taken. The vertical error bars are derived from the uncertainty in the original fit parameters.

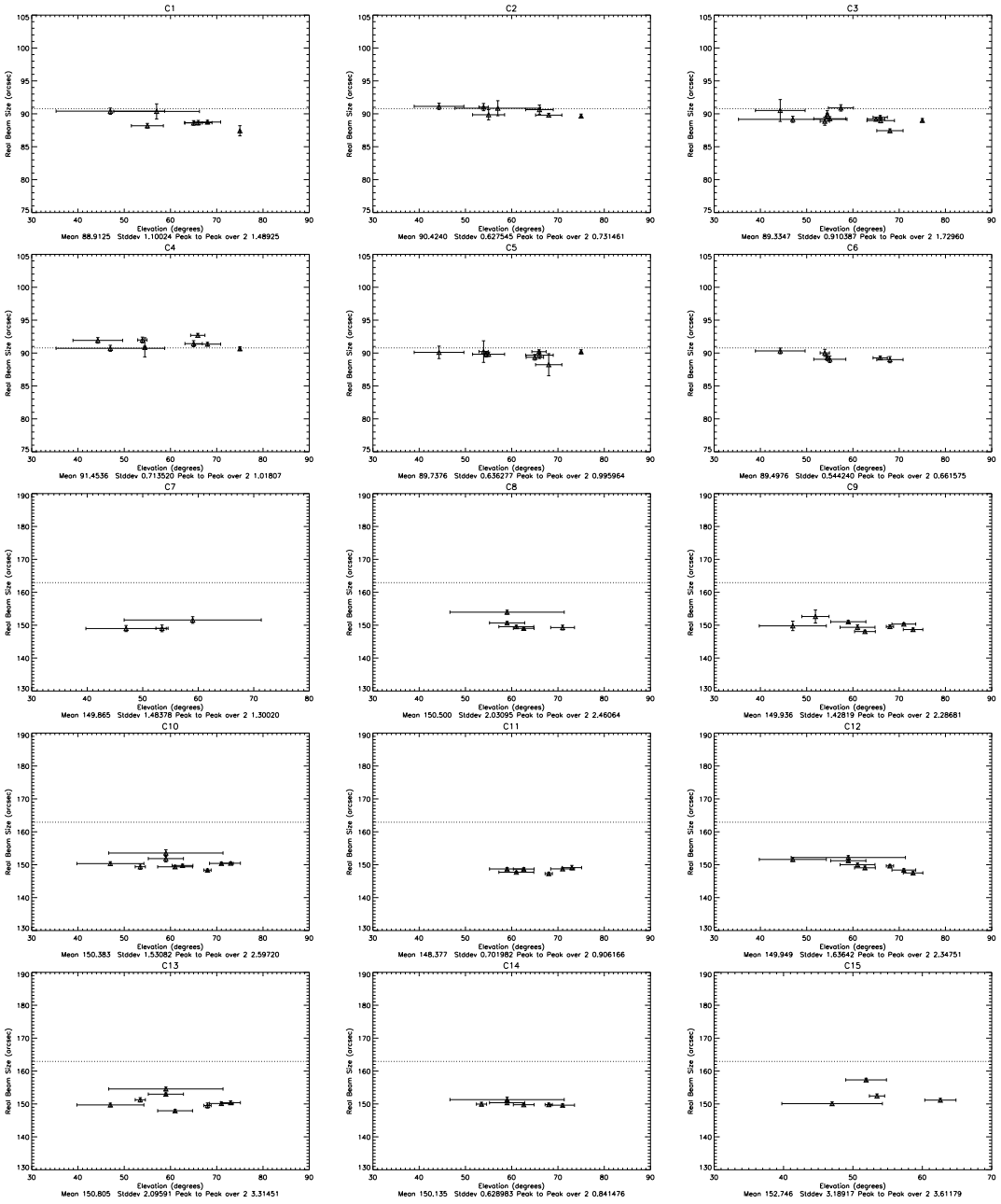

Figure 3.25 Same as Figure 3.24 except the fit to the real component of the voltage pattern is plotted.

Several of the 10-m antennas (C1, C2, C5) show evidence of variation in amplitude voltage pattern size as a function of elevation. However, the same trend is *not* seen in the real components. Once again, this most likely implicates the contribution of the imaginary component. The sag of the secondary as a function of elevation can change the illumination of the primary. This would effect only the size of the amplitude ellipticity and/or beam size but would not effect the real component. In addition to the principle axis focus control available on both the 6-m and 10-m antennas, the 10-m antennas have the capability to change the position of the secondary with respect to the principle axis so this problem can be rectified. The more stiff 6-m antennas show no such evolution and have strong agreement between the real and amplitude component in general, indicating that any imaginary component, if present, is at a low level.

Of the 10-m antennas, only C4 shows any significant deviation in the real pattern size with the balance of the antennas showing remarkable agreement with the FWHM given by MIRIAD. The most likely source of the deviation of C4 is a focus error. Indeed, quadratic fits to the phase pattern in the aperture plane reveal this antenna typically has a factor of two larger contribution than its normal sized counterparts for the runs in question. Proper adjustment of the antenna focus will likely return the real component of C4 to the nominal value for the other antennas. For the 6-m antennas, all of the difference is accounted for by the aforementioned difference between the ensemble properties of the 6-m antennas and the values in MIRIAD.

3.4.5.3 Ellipticity & Position Angle

Ellipticity was calculated as described above. Figures 3.26 and 3.27 show the trends of the amplitude and real component ellipticity as a function of elevation for the fifteen CARMA antennas. A dashed line is provided at an ellipticity of 1, i.e. circularly symmetric, for reference. Figures 3.28 and 3.29 show similar plots for the position angle of the ellipticity.

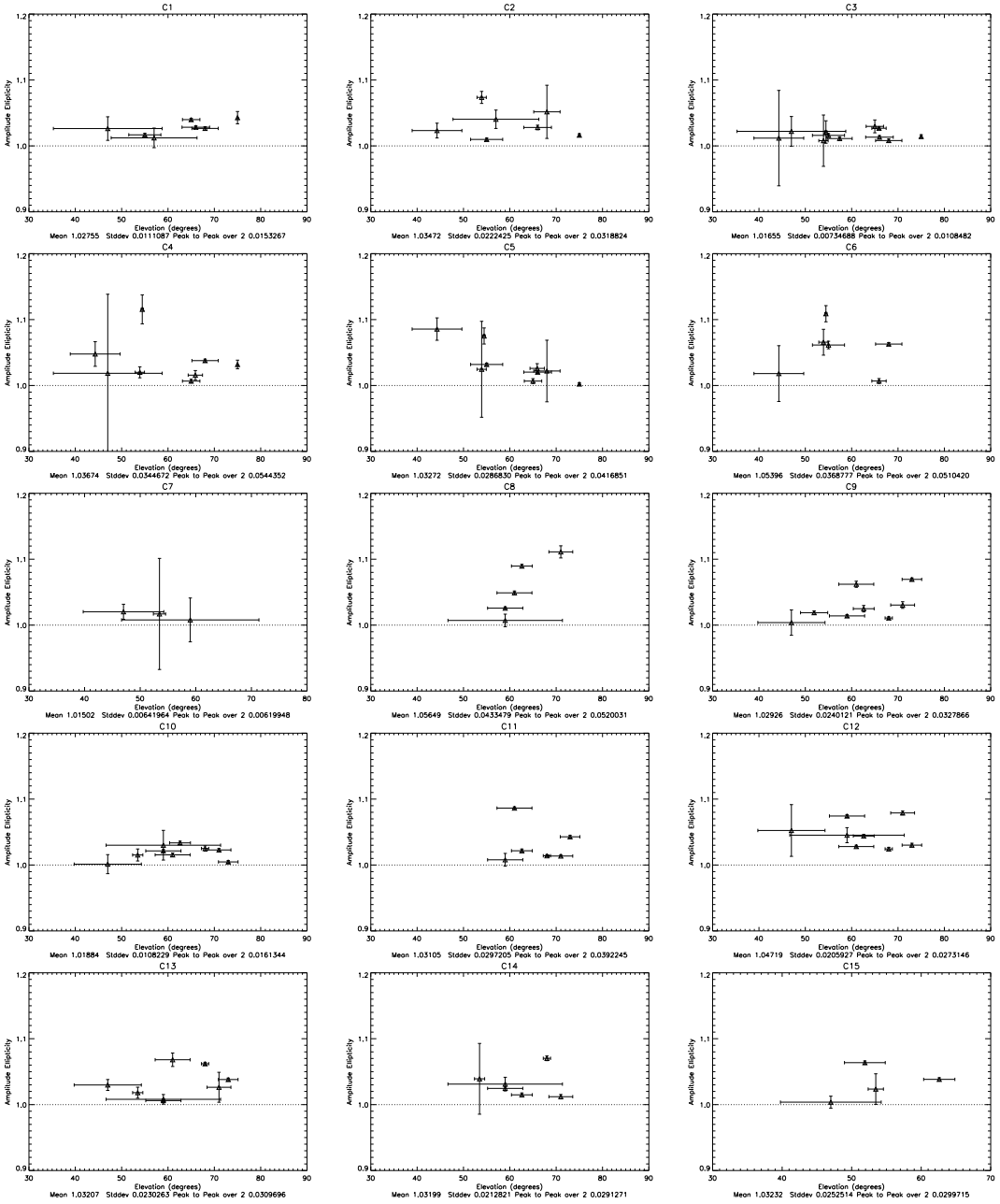

Figure 3.26 The CARMA antenna amplitude ellipticity is plotted against elevation for each. The horizontal error bars represent the range of elevations over which the data were taken. The vertical error bars are derived from the uncertainty in the original fit parameters. The dashed line is an ellipticity of 1, i.e. circularly symmetric. Enhanced scatter is likely due to pointing drift in the antenna in question or other systematics that escaped the flagging process.

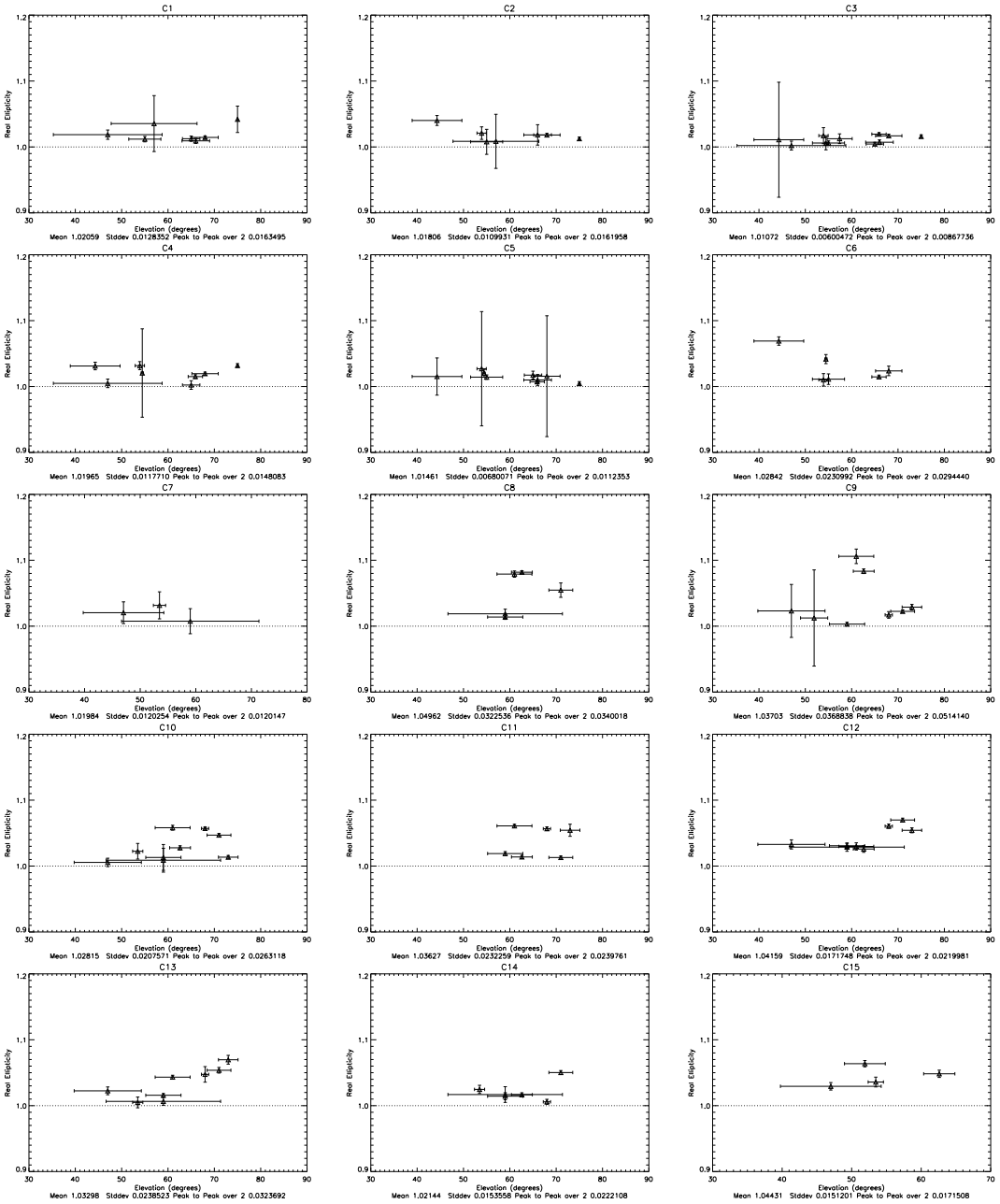

Figure 3.27 Same as Figure 3.26 except the fit to the real component of the voltage pattern is plotted.

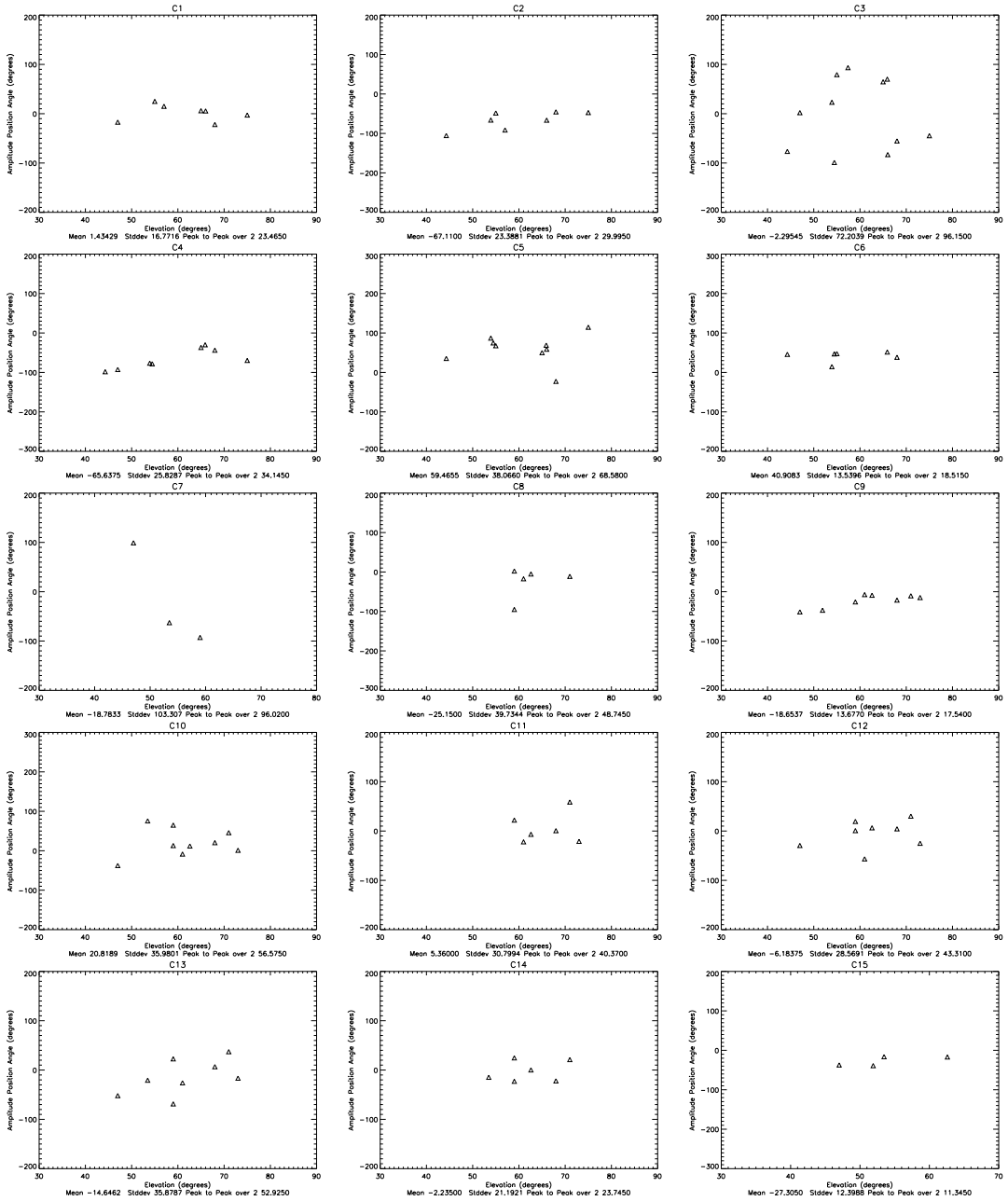

Figure 3.28 Plots of the position angle of the ellipticity in the amplitude voltage pattern are shwon as a function of elevation for the various antennas.

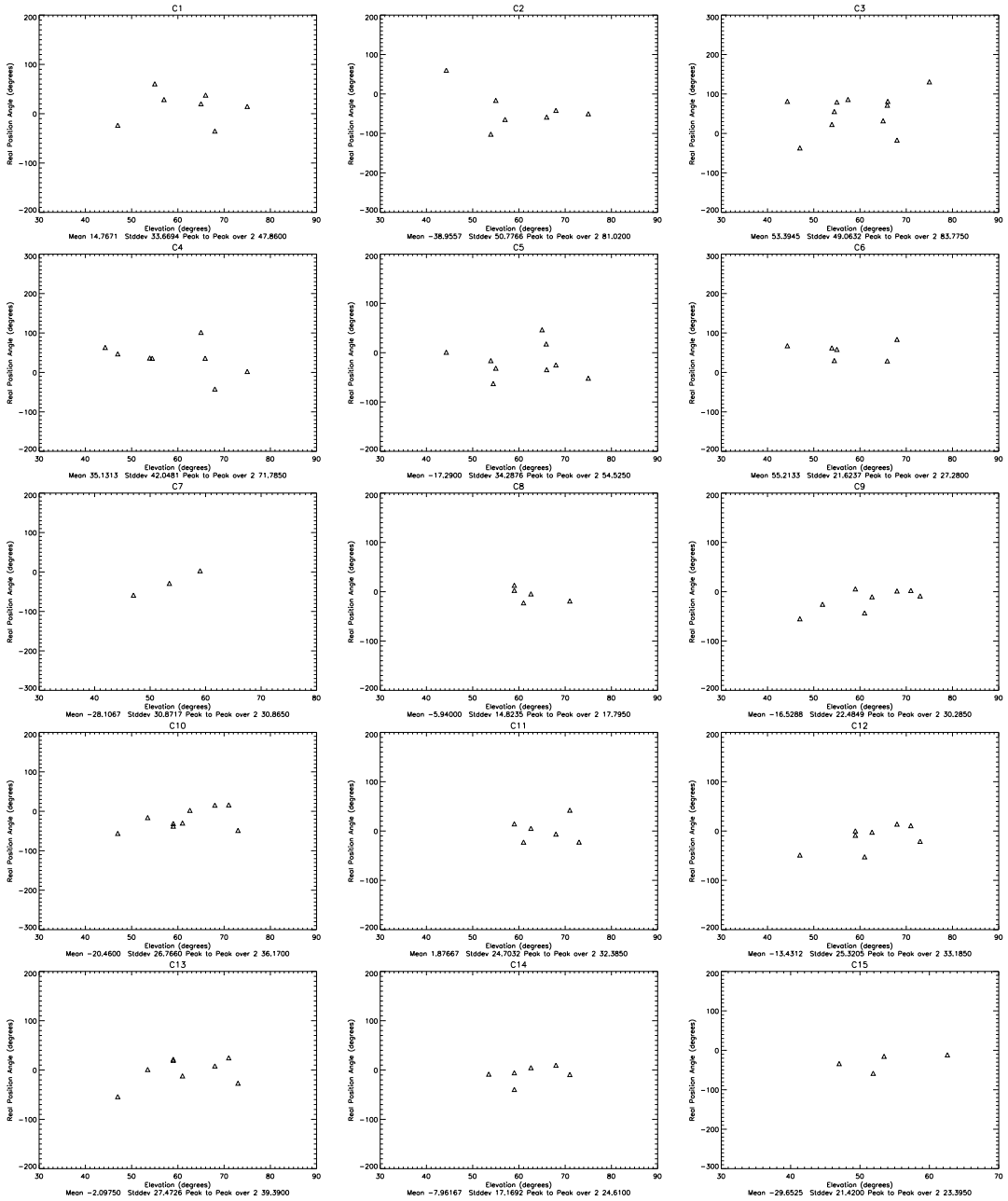

Figure 3.29 Same as Figure 3.28 except the fit to the real component of the voltage pattern is plotted.

In general, one might expect the position angle of the real component ellipticity to be near zero while the amplitude ellipticity could mirror the real component or vary due to imaginary contributions. The amplitude-based ellipticity should either be comparable to the real ellipticity or larger. Contribution to the ellipticity of the amplitude pattern can come from either inherent beam elongation or imaginary components whereas the real component should only be susceptible to elongation due to dish structure. In order for a definitive assignment of ellipticity to be made, the position angle should be roughly consistent trial by trial or have some definitive behavior as a function of elevation.

Few of the 10-m telescopes show signatures of true ellipticity where true ellipticity is contrasted here with ellipticity induced by the presence of an imaginary beam. C1 (top left panel of 3.26 through 3.29) has a persistent measure of ellipticity and a position angle consistent with zero. In the mean the ellipticity is 2.8±0.4% for the amplitude pattern and 2.1±0.3 for the real pattern. These have position angles of 15±13 and 1±7, respectively. The ellipticities and position angles are the same within 2σ and 1σ, respectively. None of the other 10-m antennas show evidence of consistency between the real and amplitude ellipticity or position angle. There is no obvious trend of ellipticity or position angle with elevation, except for C5. This antenna has far larger amplitude ellipticity than real ellipticity, suggesting that the evolution may be in the illumination pattern on the antenna surface rather than inherent to the antenna.

The 6-m antennas showed consistent, 3% ellipticity as an ensemble. Table 3.4 and figures 3.26 through 3.29 indicate that for a given antenna the ellipticity derived for the real and amplitude components agree easily within the spread. The variation of ellipticity from antenna to antenna is not large and any evidence of departure from the ensemble property comes from antennas which have very few datasets.

3.4.5.4 Imaginary Beams

In §3.1, it was shown that offsets in the aperture plane result in imaginary beams across the sky via a simple simulation and application of the Fourier transform shift

theorem. Figures 3.30 and 3.31, as well as Table 3.4, show the half peak-to-peak of the imaginary components and position angle of that imaginary component, respectively. The magnitude of the imaginary beam can be interpreted as a percentage of the contribution to a completely real beam. A value of 0.1 implies that one quadrant of the beam will receive a positive, 10% imaginary contribution relative to the beam peak while the opposite quadrant will receive the same, but negative contribution. For the imaginary beam to be interpreted as believable, consistency of the magnitude of the peak-to-peak value and the position angle are required. Here, unlike the ellipticity, the position angle does not have a preferred direction and has no 180° symmetry. An additional constraint is applied by considering the magnitude of the real beam at the location of the peak imaginary component. If the peak imaginary component occurs at the 10% point of the real beam the phase error contribution to the measured visibility will be small.

In general, contributions to the imaginary beam could arise from phase noise in the measurement of the beam on the sky. Some filtering is done by first transforming to the aperture plane, clipping emission beyond the aperture, padding the image with zeros and transforming back to the sky. This removes much of the spurious imaginary signal that can exist in the sky only data and provides interpolation in the sky plane.

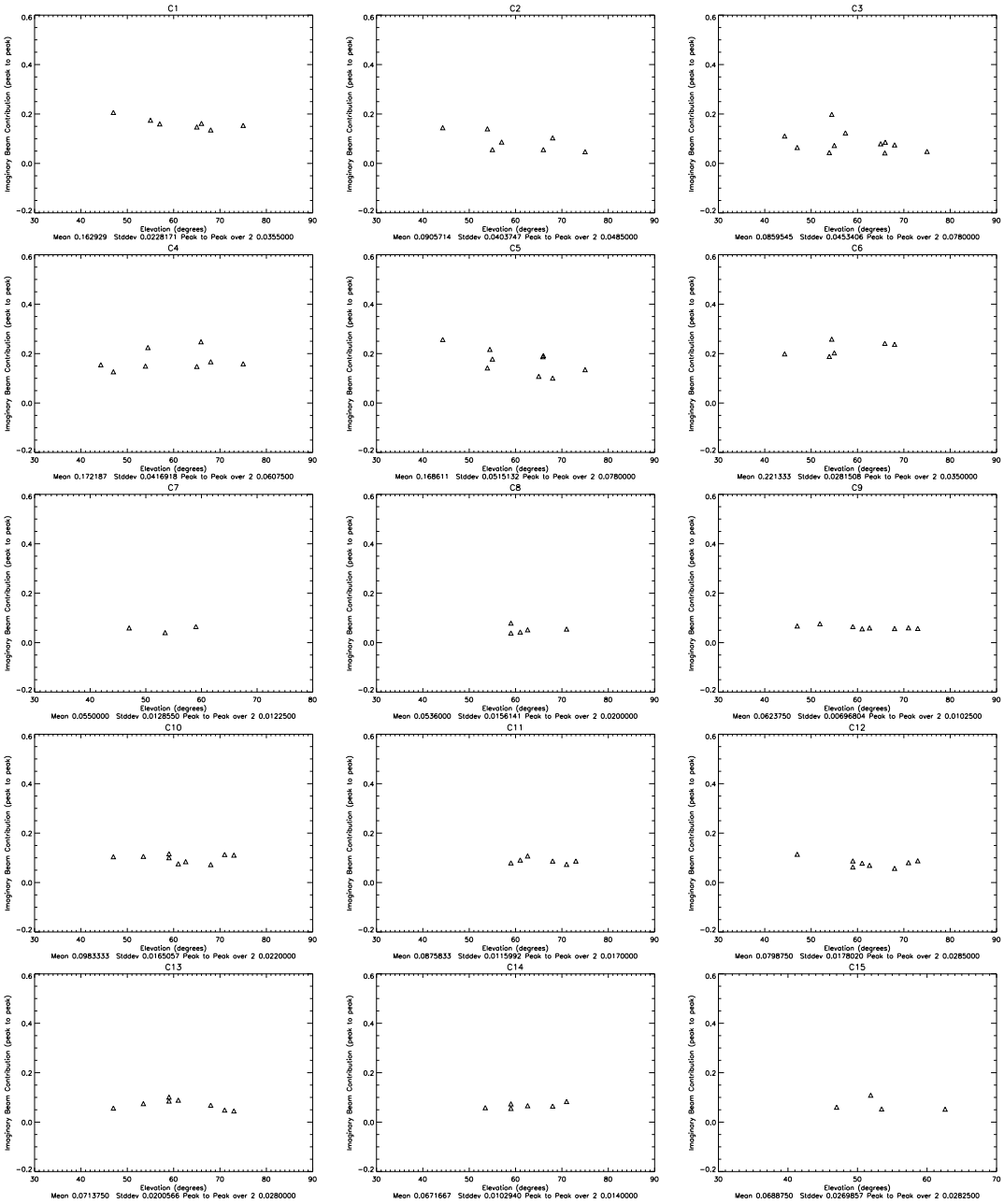

Figure 3.30 The magnitude of the imaginary component of the voltage pattern for each of the 15 CARMA antennas is plotted against elevation.

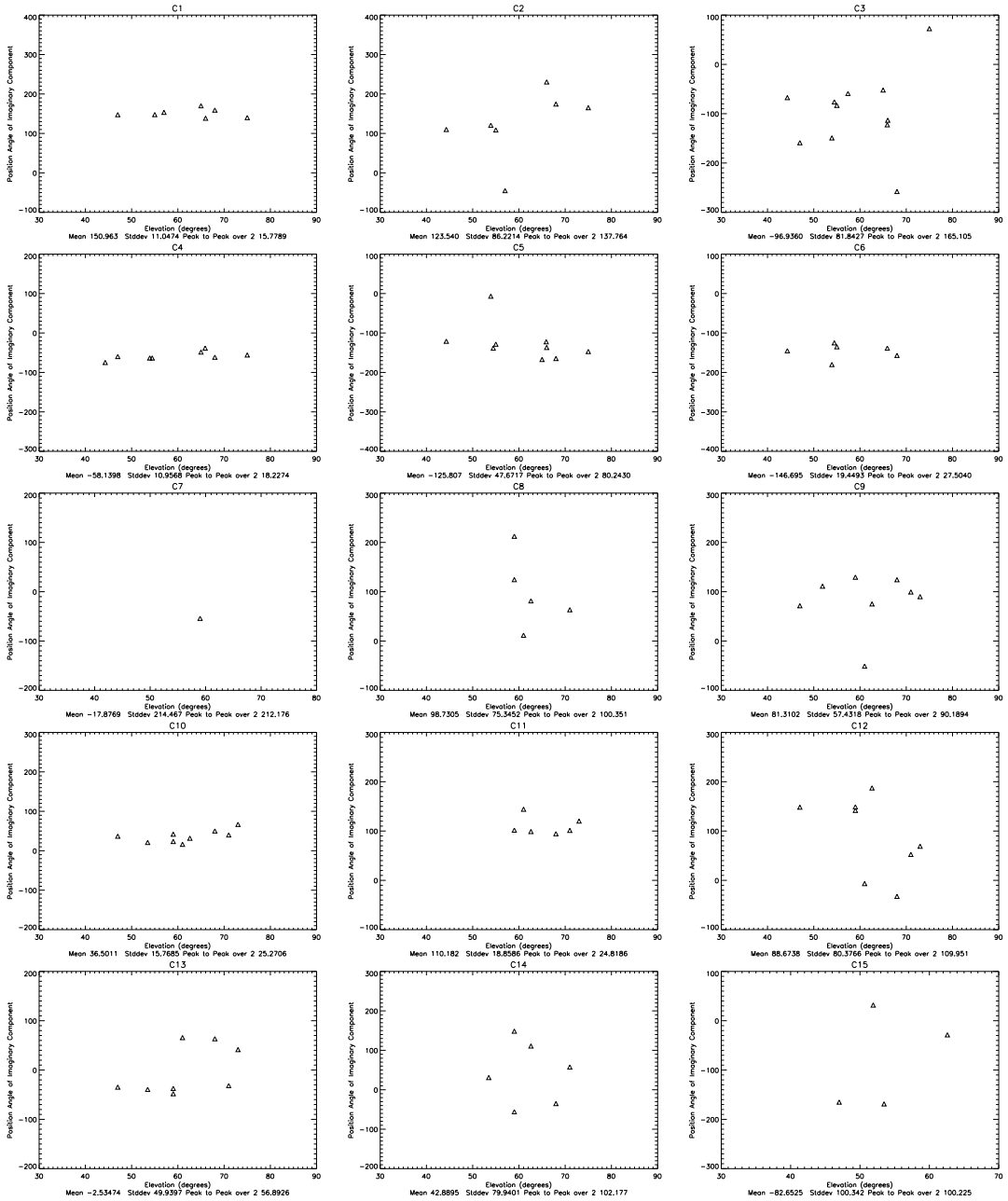

Figure 3.31 The position angle of the imaginary component of the voltage pattern for each of the 15 CARMA antennas is plotted as a function of elevation.

Given that the principle contribution to the imaginary beam is an offset in the illumination pattern, little consistency is expected between the ensemble of antennas for any style of antenna. There are a variety of adjustment points for the 10-m antenna alignment, although ideal alignment is difficult. Indeed this is the case and a uniform model of the imaginary beam could not be constructed for either antenna style. One could envision a situation where the presence of feed legs and other circular symmetry breaking components could result in uniform phase contributions but CARMA does not see such deviations at the level of repeatability of these measurements.

Several 10-m antennas show compelling evidence of imaginary beam contributions. C1, 4, 5 and 6 show small scatter in the peak-to-peak value and the position angle of the imaginary component. Considering deviations of the mean the relevant values are 0.163±0.009 @ 151°±4°, 0.172±0.016 @ -58°±4°, 0.169±0.018 @ -141°±7°, and 0.221±0.013 @ -147°±9° for C1, 4, 5, and 6, respectively. In each instance, the average location of these peaks is above the 50% point in the real beam. C2 and C3 have very low peak-to-peak values and nearly 90° uncertainty in the position angle of the imaginary component. Given this would include all possible angles at 2-3σ and the contribution comes at <40% in the real beam, there is little doubt that these gradients are not real.

Of the 6-m antennas, only C10 and C11 show consistent evidence of an imaginary component as the scatter in the position angles is far too great in the other antennas to be interpreted as an actual gradient. The components are 0.098±0.006 @ 37±6° and 0.088±0.005 @ 110±8° for C10 and C11, respectively. The peak imaginary component for C10 comes at the 46% point in the real beam while the C11 component comes at a much lower level, 27%.

The contributions from the 6-m antennas are far less worrisome in the short term as these imaginary components are multiplied by the 46% and 27% point in the beam of other 6-m antennas and at the ≤10% of the 10-m antennas and are thus suppressed in 6-m baselines and strongly suppressed in heterogeneous baselines. For CARMA-23 this will no longer be the case. For the 10-m antennas, the contribution is far more serious. The 50% point of the 10-m voltage pattern is at the 80% point of the

6-m voltage pattern and these imaginary components are not strongly suppressed. CARMA-23 will only make this problem worse.

3.4.5.5 Antenna-Based Templates: 2006Aug-2008May

In the end, when maximal image fidelity is needed, a given array of N elements needs to be treated as a heterogeneous array with N real voltage patterns and N imaginary voltage patterns. The degree of variation seen in the antenna-based properties reenforces this concept at CARMA. This is a departure from how imaging software treats the situation. In MIRIAD, the heterogeneous aspects of the array are treated by the number of distinct baseline types, three in the case of CARMA (six for CARMA-23). In the approach taken here, the voltage pattern of antenna **A** must be multiplied in a complex sense by the conjugate of the voltage for antenna **B** to create a baseline based primary beam. In general, it is better to rely on the voltage patterns as this is the minimal number of independent patterns needed to produce the full array and it allows for pointing errors to be introduced or corrected post-processing on an antenna basis which is the way pointing error is actually introduced.

Figures 3.32 through 3.46 display the final, $\lambda = 3\,\mathrm{mm}$, voltage patterns for use with observations over the shared-risk period, the first full observing season, and part of the second season. The patterns are available for public use upon request. The patterns shown here are unique to 100.2 GHz observations. These patterns can be scaled to any 3-mm band frequency by utilizing the Python code **alterFreq.py**, similarly available. In general, the patterns must be rotated to various parallactic angles to be applied to simulated or measured data. See Chapter 2 for information regarding routines to apply these beams to simulated data or Chapter 5 for applications to real data.

3.5 Summary & Conclusions

There were two goals of this work. First, the properties of the antennas were to be optimized. To this end, I have optimized the surfaces of the 6-m antennas and aided

in the optical alignment of the 10-m antennas. There are surface improvements which could be made to the 10-m antennas based on the repeatability of the holography but the surface RMS is within tolerable limits. I have determined that the alignment of the 10-m antennas in the 1-mm band is poor and the alignment process is now underway. No credible dataset is available to assess the alignment of the 6-m antennas in the 1-mm band. A single adjustment of the C3 1-mm receiver was made and the results indicate that the alignment is dramatically improved over that shown in Figure 3.12. The alignment and surface RMS post-adjustment are listed in Table 3.2. There are several instances of large alignment offsets, while all of the antennas are at or near the benchmark for surface accuracy.

The second goal was to measure the empirical voltage patterns and provide:

- **A better estimate of the width of the symmetric, Gaussian approximation used for the 6-m, 10-m and heterogeneous primary beams for immediate integration into MIRIAD.**
- **An estimate of the deviation from the symmetric, Gaussian approximation.**
- **A suite of antenna specific voltage patterns to be used in cases were the maximal image fidelity is needed.**

In these goals, I have succeeded. The width of the default model for the 6-m antennas and heterogeneous primary beams were significantly larger than the measured value and these values will soon be integrated into MIRIAD, the default imaging program for CARMA. The symmetric, Gaussian model was found to be a reasonable approximation for the three CARMA primary beams but there are limitations which are affecting the current imaging process in noticeable ways. The 5%, or *cutoff*, point is uniformly narrower for the measured primary beams when compared to a best-fit Gaussian model. The deviations from the best-fit Gaussian range from 3 to 6″ at that point. At the 1% level, which will become important with the inclusion of the 3.5-m, SZA antennas, the measured profiles are even more narrow. Given these 1%

points will actually be multiplied up to 10% or more when combined with the 3.5-m antennas, a model must be provided. The profiles measured here can easily provide that model. Finally, I have provided an empirical suite of voltage patterns for each antenna to be used in cases where the highest dynamic range and image fidelity is required and these models are available for public use.

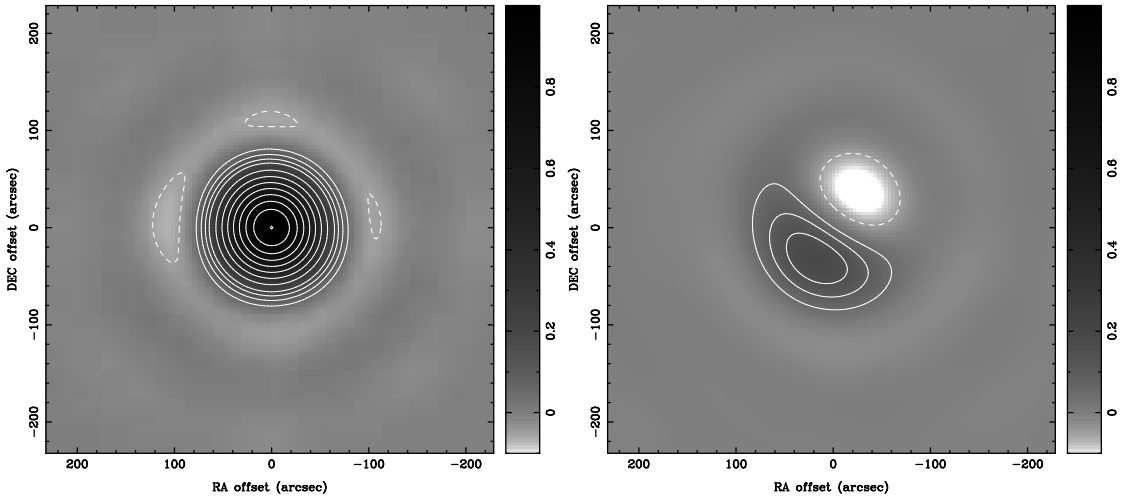

Figure 3.32 The real (left) and imaginary (right) mean voltage pattern at 100.2 GHz are shown for antenna C1. The image stretch is logarithmic ranging from -10% to 100%. The contours are drawn at 5% intervals until 20%, increasing in 10% intervals thereafter with dashed contours showing negative values and solid contours showing positive values.

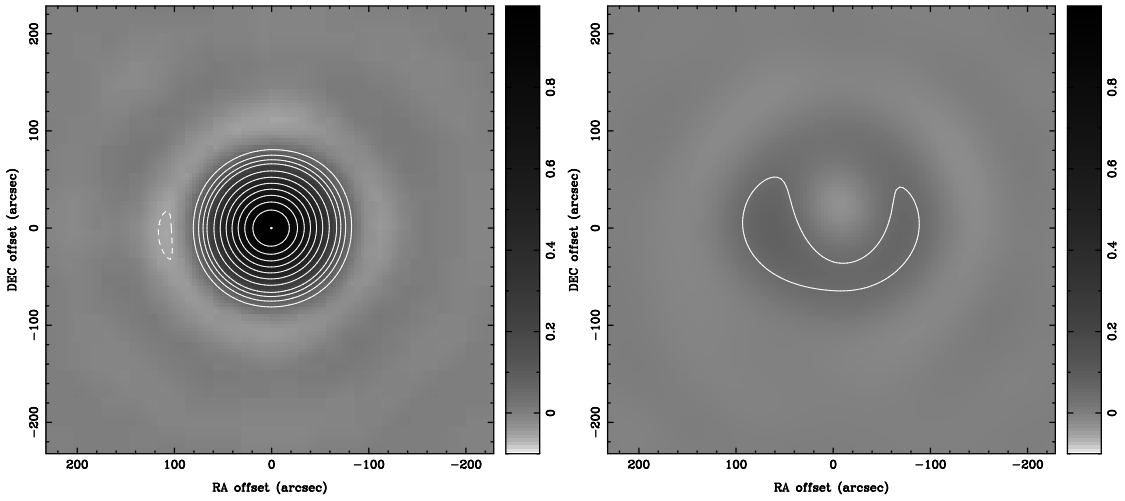

Figure 3.33 Similar to Figure 3.32 but for antenna C2.

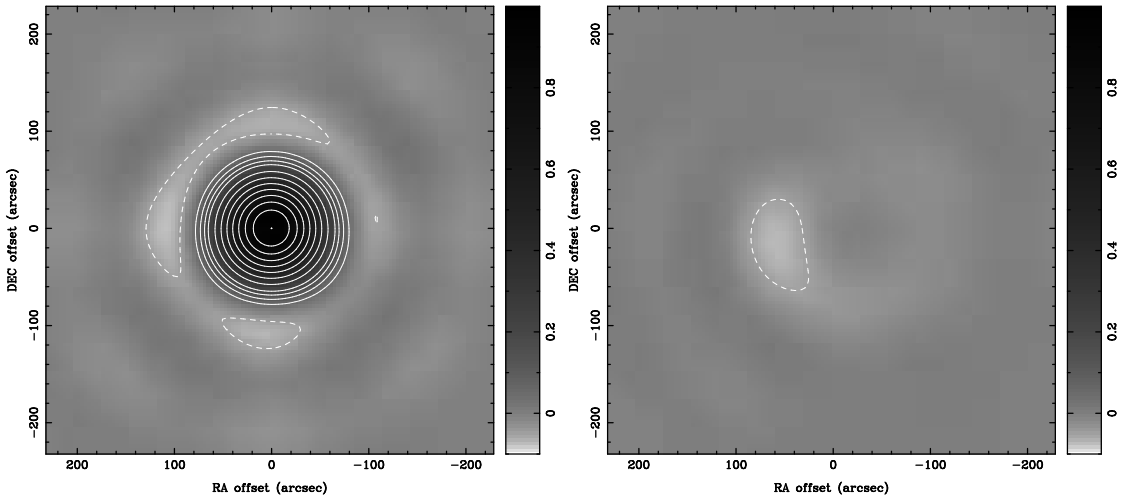

Figure 3.34 Similar to Figure 3.32 but for antenna C3.

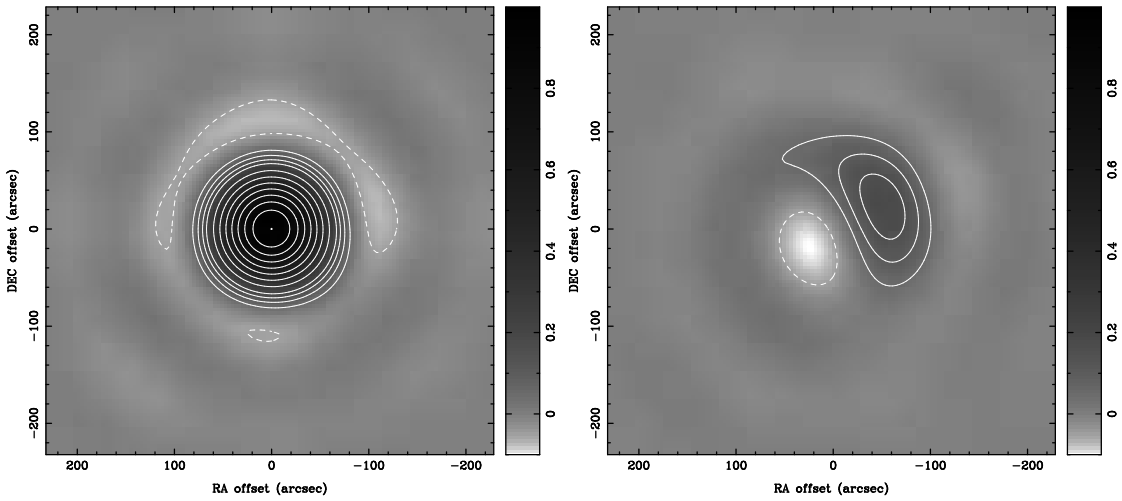

Figure 3.35 Similar to Figure 3.32 but for antenna C4.

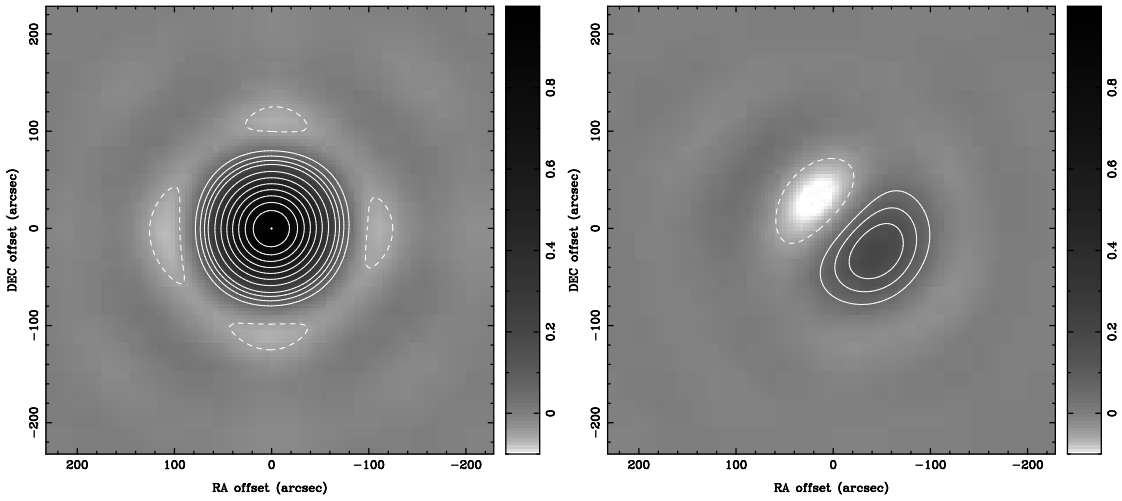

Figure 3.36 Similar to Figure 3.32 but for antenna C5.

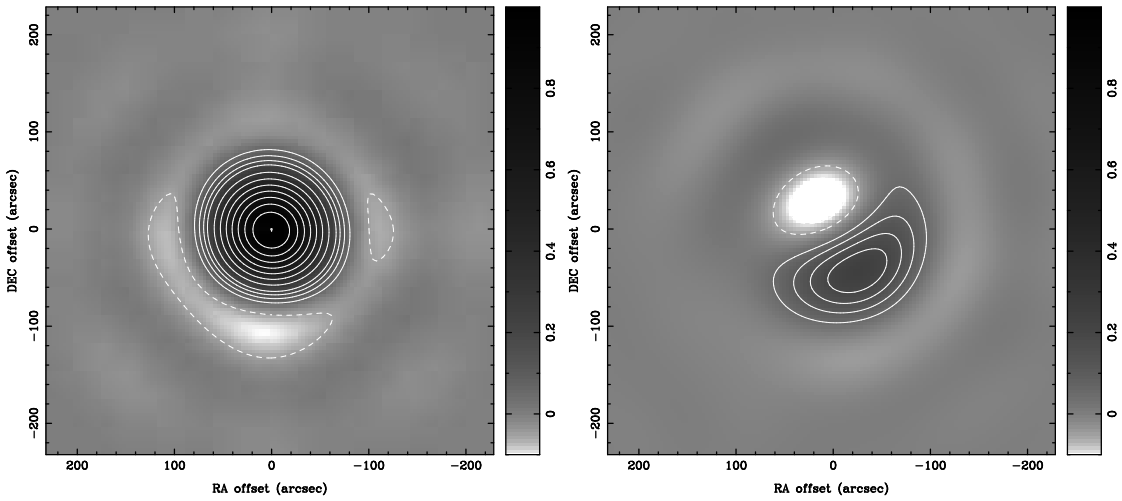

Figure 3.37 Similar to Figure 3.32 but for antenna C6.

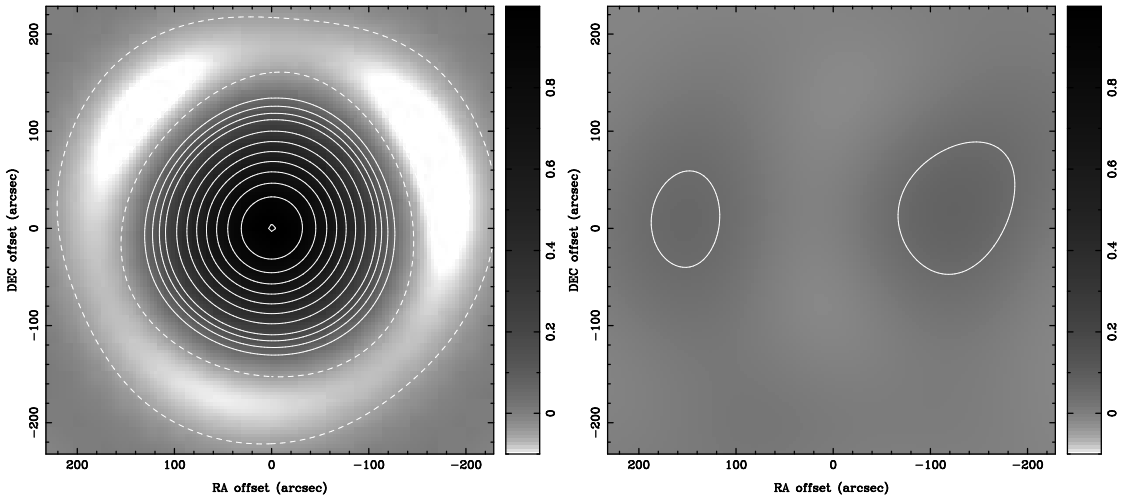

Figure 3.38 Similar to Figure 3.32 but for antenna C7

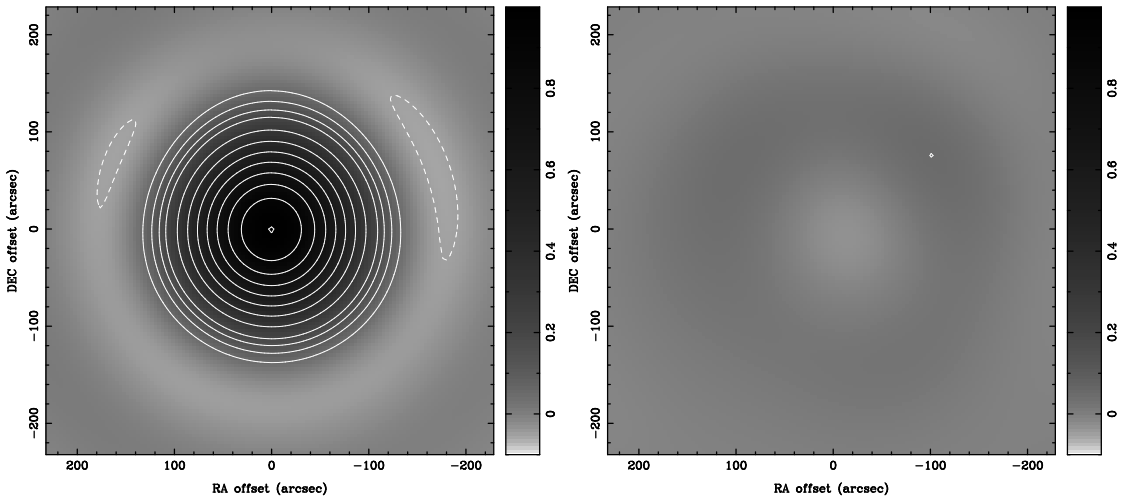

Figure 3.39 Similar to Figure 3.32 but for antenna C8.

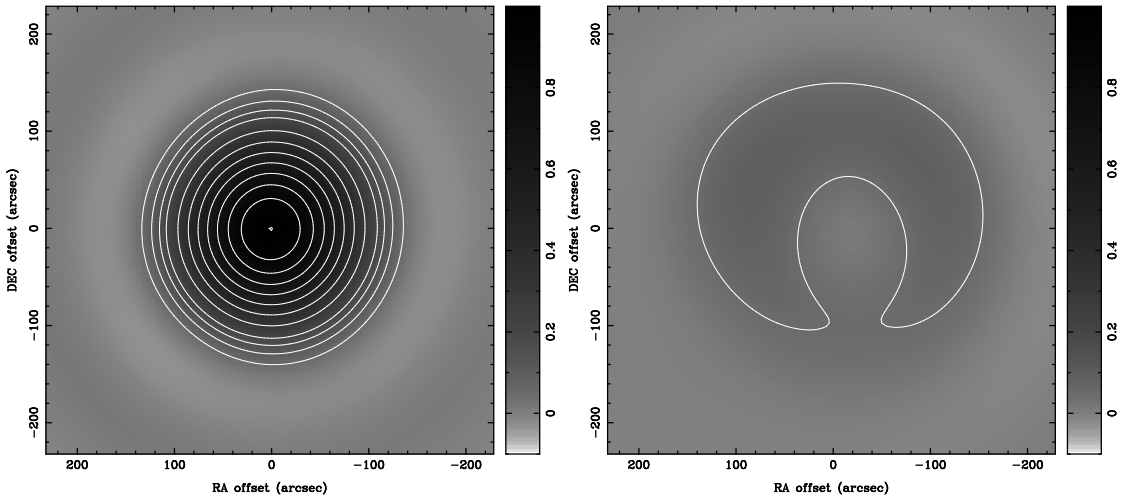

Figure 3.40 Similar to Figure 3.32 but for antenna C9.

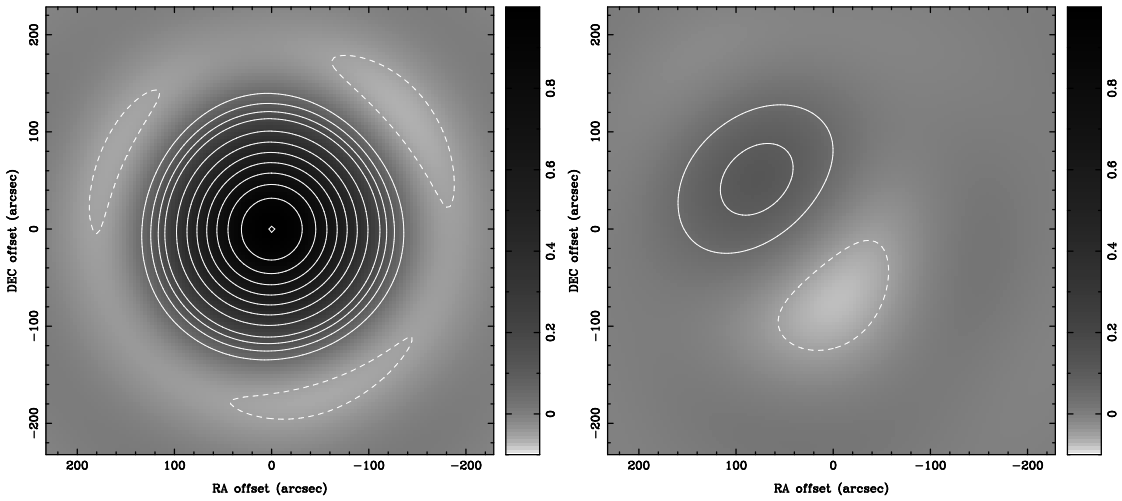

Figure 3.41 Similar to Figure 3.32 but for antenna C10.

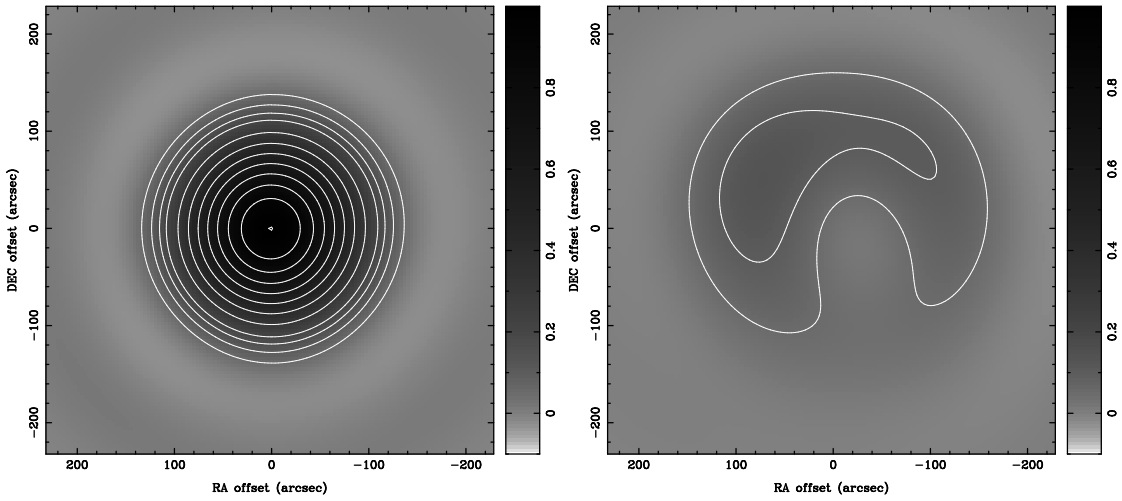

Figure 3.42 Similar to Figure 3.32 but for antenna C11.

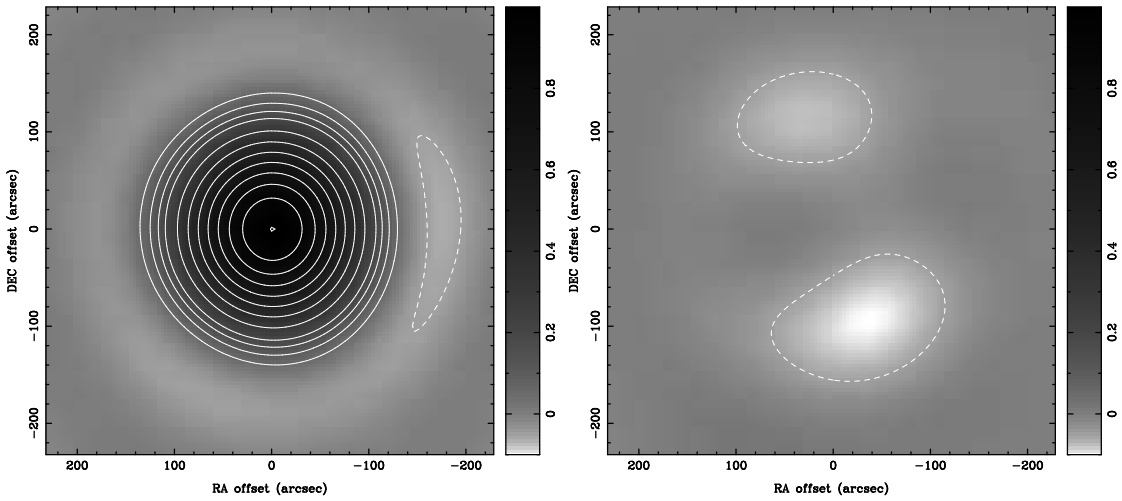

Figure 3.43 Similar to Figure 3.32 but for antenna C12.

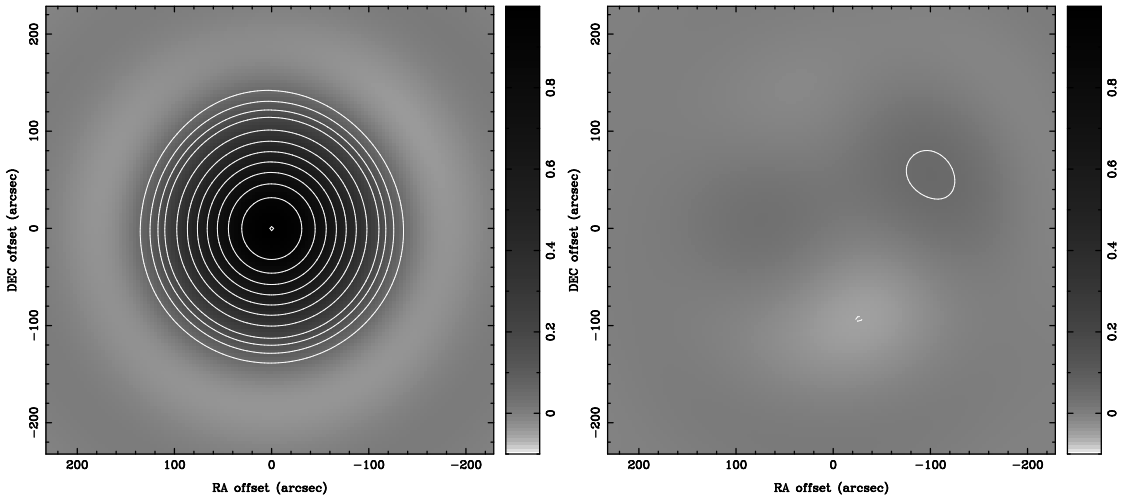

Figure 3.44 Similar to Figure 3.32 but for antenna C13.

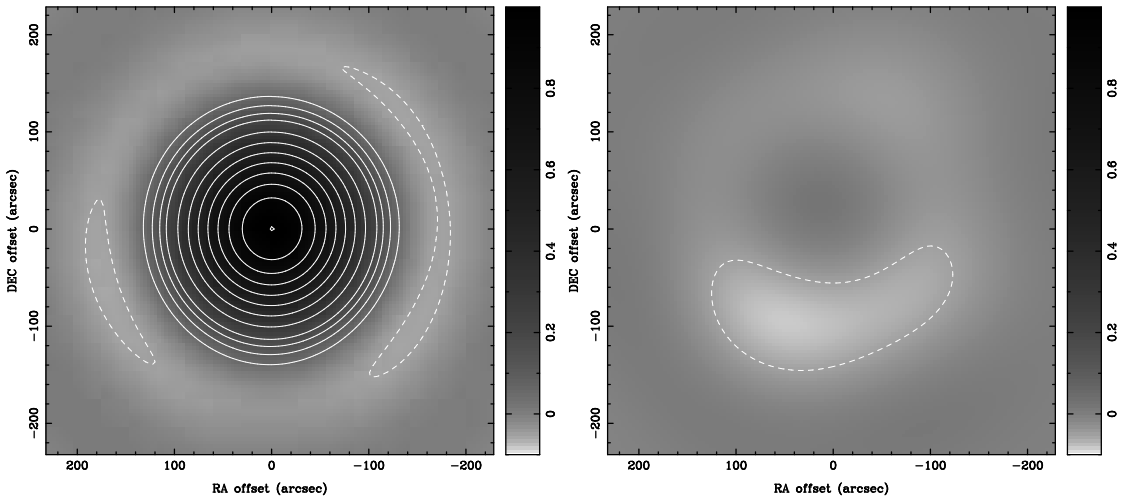

Figure 3.45 Similar to Figure 3.32 but for antenna C14.

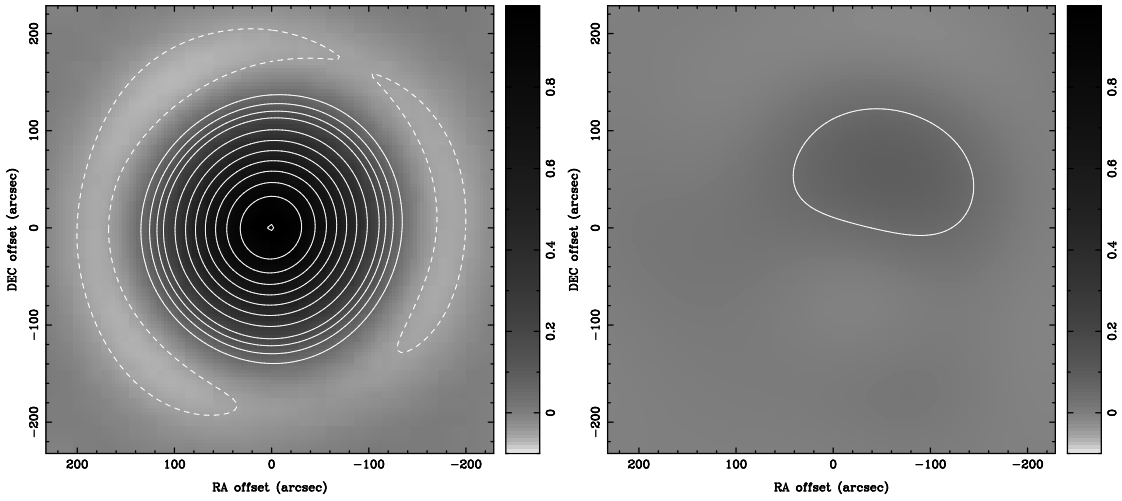

Figure 3.46 Similar to Figure 3.32 but for antenna C15.

Bibliography

Corder, S. A. & Wright, M. C. H. 2006, CARMA Memo 36

Plambeck, R. L. 2008, private communication

White, S. & Corder, S. A. 2007, CARMA Memo #40

Woody, D. P. 2008, private communication

Chapter 4

Optimizing Pointing

Abstract

The pointing error of antennas in an interferometer begins to have significant influence on the resulting synthesized, mosaiced images when it reaches 0.5-1% of the antenna primary beam FWHM (see Chapter 2). I have devised and completed a multi-step process to improve the pointing of all CARMA antennas. First, the size of the CARMA optical catalog was increased by a factor of ∼4. The additional sources were specifically selected to provide uniform sky coverage and enable better characterization of the pointing model. Characteristic errors in the resulting fits were reduced by 40% from the initial 4-5″ for the 10-m antennas and 5-10″ for the 6-m antennas, and were also more stable than before. Second, I designed and implemented a system to integrate local optical peak-up observations into standard observing. This optical offset pointing approach results in a reduction of peak-to-peak gain oscillations by night of a factor of 2 in some cases, typically on the 6-m antennas. Typically, day-time pointing drifts of 30-50″ and 10-12″ on the 6- and 10-m, respectively, are reduced to mostly randomized pointing errors of RMS 4-8″ on the 6- and 10-m antennas, although some systematics remain. Here I report on the improved pointing model measurements and the tests, implementation, and benefits of optical offset pointing.

Portions of this work were included in Corder & Wright (2005) and White & Corder (2007). The optical offset pointing work will be included in Corder et al. (2009).

4.1 Introduction

There are two decisions to be made in pointing approaches for interferometers. First, it must be decided whether radio pointing measurements will be used to characterize the underlying pointing model or if optical observations, with special parameters set to differentiate the optical characteristics, will provide the basis. Second, the pointing model can contain terms that are physically motivated, i.e. a minimum set of parameters that arise from errors in position or structural properties of the antennas, or that maximally reduce the residual pointing error regardless of any physical origin.

While the second decision is largely a matter of preference, the first typically depends on the sensitivity at a given wavelength compared to the on-sky source density and brightness distribution. At traditional radio wavelengths, the sky density of bright pointing sources (where *bright* is a function of the typical sensitivity of the instruments in question) is sufficiently high and uniform that strictly radio observations can provide enough data to characterize antenna pointing. This is the case for the Very Large Array (VLA). At (sub)millimeter wavelengths, the brightness of the distributed population of quasars used by the VLA is falling off and the absolute sensitivity of these submillimeter instruments is typically lower. The pointing source sample begins to be dominated by blackbody sources which are generally confined to the plane of the galaxy or the ecliptic, leading to less uniform coverage. As a result, the optical pointing approach is used for most (sub)millimeter interferometers including CARMA. At CARMA, optical telescopes and cameras are permanently mounted to each radio antenna. Further detail about the cameras and centroiding procedures can be found in Appendix B.

The use of optical pointing, however, has its disadvantages. Refraction corrections differ (Schubert & Walterscheid, 2000) and require adequate weather data and a reasonable weather model as a function of frequency. The optical telescopes are typically mounted in the antenna backing structure. This can lead to pointing changes based on local deformation of the dish in contrast to radio pointing changes which respond only to bulk variations. In addition, the motion of the radio subreflector

under the influence of gravity, also called sag, may differ from the response of the optical system to gravity. The pointing model adopted must deal properly with these differences. At CARMA, optical pointing is used to determine all but three parameters of the pointing model, two axis collimation terms and a gravitational sag term (White & Corder, 2007), while refraction is handled by a frequency dependent model using input from local measurements of pressure and humidity.

Improvement to antenna pointing can be made in five basic ways:

- Characterizing the current pointing model properties more accurately.
- Adding additional terms to the pointing model.
- Improving the thermal and gravitational stability of the antenna mount and support structures.
- Performing local peak-up observations more frequently.
- Using active feedback based on some instantaneously measurable property.

Better characterization of the existing pointing model can provide immediate and substantial benefit but only to model terms that change slowly in time. Simply adding additional terms to the pointing model will not necessarily improve overall pointing if the newly fit terms are time variable and time consuming to measure. In addition, more terms require more data to obtain a better fit. Thermal insulation of the mount may lead to better pointing since degradation often results from the presence of changing thermal loads or mechanical stresses. Local pointing updates assuming strictly collimation terms, i.e. constants on the sky, are helpful as long as the pointing error field is sufficiently flat in the range of coordinate space over which repeated collimation corrections are performed. Finally, real-time feedback can result in the improvement of pointing provided the variability and uncertainty of the feedback is small compared with all other sources of uncertainty. Systematic errors in the feedback could in fact cause additional or amplified pointing errors.

The CARMA pointing model is presented in §4.2. In §4.3, typical pointing errors at CARMA are described. In §4.4, the improvements to pointing made by modifications of the CARMA optical pointing system are discussed, including changes to the optical pointing catalog and data collection (§4.4.1) and the use of optical offset pointing (§4.4.2). In each of those subsections, the motivation for the improvement, the approach and implementation, any tests required, the benefits, and limitations and future direction are discussed.

4.2 The CARMA Pointing Model

The need for a pointing model arises from the conversion of hour angle, H, declination, δ, and latitude, L, to azimuth, Az, and elevation, El. This coordinate system is used almost universally because of the benefits to mount stability and cost. For a perfectly aligned, timed and rigid telescope, the conversion is governed by simple mathematical relationships. In reality, corrections must be applied to these conversions based on the inherent properties of the telescope system. Errors in these corrections give rise to an error which has a magnitude and direction at each location on the sky, i.e. a vector field. Typical properties that require correction are:

- **Tilt:** any difference between the vertical axis of the antenna and the local vertical will produce pointing errors in the form of a rotation. This tilt may be fixed in time, or may vary as a function of thermal heating or other environmental factors. Additional correction is required for the difference between the local gravity vector and true coordinate vertical.

- **Axis misalignment:** any misalignment of the elevation axis with respect to the azimuth axis. This causes an azimuth offset.

- **Encoder errors:** any misalignment of the encoder zero reading with the true zero creates an error in the relevant axis in the encoder frame.

- **Sag and other gravity effects**: any antenna deformation as a function of elevation induces deflections of the antenna pointing. The largest effect is solely

in elevation and is caused by the secondary reflector sag, although asymmetric weight on the elevation axis can produce torques resulting in azimuthal deflections as a function of elevation.

- **Global location**: any error in the assumed placement of the antennas on the surface of the Earth produce errors in H and L and therefore affect both El and Az measurements. While baseline solutions for radio data can refine the relative positions of the antennas well, gross errors in the assumed location of the array center may remain.

- **Thermal deformation**: any uneven temperature distributions across the dish and backing structure cause uneven expansion and irregular deformation of the dish that is not always reproducible. Thermal effects therefore cannot be removed *a priori* and are sometimes ameliorated by using fans to blow air over the dish and maintain an even temperature distribution.

- **Ellipticity of drive structure**: any deviation from circular symmetry in the drive structure will, to first order, induces a twice coordinate error and possibly higher order harmonics.

- **Mechanical restrictions**: any mechanical restriction of the telescope body can result in the excitation of harmonics in the pointing error field. For example, the presence of n-many support legs for the antenna may result in n times coordinate errors to be excited.

- **Collimation**: any deviation of the telescope pointing center from the mechanical center is treated as a constant offset in both Az and El.

At CARMA, pointing models are characterized by functions that typically described the pointing error field, i.e. sines and cosines. The pointing model for the 6-m antennas has terms which are not fixed to represent strictly physical behavior, while terms of the 10-m antenna model are constrained to take on a physically meaningful form. For example, in a tilt correction, four components may be treated

independently or the tilt may be represented strictly as a rotation with two terms. The former approach results in freedom to fit additional behavior while the latter allows such additional terms to be isolated and perhaps corrected by other means. The mount model components are those that are independent of optical and radio observations. Terms that depend on the wavelength are called aperture coefficients. The combined set of parameters is collectively known as the pointing model.

Below is a mathematical description of the pointing models used for the BIMA/6-m antennas and the OVRO/10-m antennas. Notice that there are terms which appear in both the azimuth and elevation errors components of the 10-m model. The OVRO model also contains an *encoder wobble* term per axis. These terms are fine-tuned in hardware and are therefore not included in the pointing model. As of November 2007, the typical contribution from these wobble terms to the pointing RMS is $1.5''$ per axis for 3 antennas and $\sim 0''$ for the other three. New encoders used exclusively in the later three antennas have little to no inherent wobble. These encoders have since been installed on all 10-m antennas.

$$
\begin{aligned}
BIMA\ dAz &= a(1)\cos(El) && \textbf{Azimuth encoder and mount offset}\\
&+ a(2)\sin(El)\sin(Az) && \textbf{Tilt of Az axis}\\
&+ a(3)\sin(El)\cos(Az) && \textbf{Tilt of Az axis}\\
&+ a(4) && \textbf{Collimation error}\\
&+ a(5)\sin(El) && \textbf{Misalignment of El axis wrt Az axis}\\
&+ a(6)\cos(El)\sin(Az) && \textbf{Cabin ``wobble''}\\
&+ a(7)\cos(El)\cos(Az) && \textbf{Cabin ``wobble''}\\
&+ a(8)\cos(El)\sin(2Az) && \textbf{Drive ellipticity}\\
&+ a(9)\cos(El)\cos(2Az) && \textbf{Drive ellipticity}
\end{aligned}
$$

$$
\begin{aligned}
BIMA\ dEl &= b(1) && \textbf{Elevation encoder offset}\\
&+ b(2)\sin(Az) && \textbf{Tilt of Az axis}\\
&+ b(3)\cos(Az) && \textbf{Tilt of Az axis}\\
&+ b(4)\sin(El) && \textbf{Elevation axis sag}\\
&+ b(5)\cos(El) && \textbf{Elevation axis sag}\\
&+ b(6)\sin(2Az) && \textbf{Drive ellipticity}\\
&+ b(7)\cos(2Az) && \textbf{Drive ellipticity}
\end{aligned}
$$

$$
\begin{aligned}
OVRO\ dAz &= o(1) && \textbf{Azimuth collimation offset}\\
&+ m(1)\cos(El) && \textbf{Azimuth encoder offset}\\
&+ m(3)\sin(El) && \textbf{Misalignment of El axis wrt Az axis}\\
&- m(4)\sin(Az)\sin(El) && \textbf{Tilt of Az axis (North} - \textbf{South)}\\
&- m(5)\cos(Az)\sin(El) && \textbf{Tilt of Az axis (East} - \textbf{West)}
\end{aligned}
$$

$$
\begin{aligned}
OVRO\ dEl &= m(2) + o(2) && \textbf{Elevation encoder and collimationoffset}\\
&+ o(3)\cos(El) && \textbf{Elevation axis sag}\\
&- m(4)\cos(Az) && \textbf{Tilt of Az axis (North} - \textbf{South)}\\
&+ m(5)\sin(Az) && \textbf{Tilt of Az axis (East} - \textbf{West)}
\end{aligned}
$$

4.3 Pointing Errors

Chapter 2 provides estimates of the tolerable pointing error for high fidelity imaging. Here, the details of the random and systematic pointing errors at CARMA are discussed. When not limited by the centroid signal-to-noise ratio,[1] the random pointing error mostly arises from atmospheric turbulence. Systematic error, which gives rise to the pointing error field, comes from imperfect determination of the pointing model terms, from errors in the data collection that are also systematic, unaccounted for pointing terms, pointing model terms that are time and/or weather dependent (e.g. tilt), and environmental effects that introduce new terms (i.e. wind). An overview of relevant CARMA pointing parameters is given in Table 4.1.

The random component to the pointing error can be determined by repeated centering of a single object over a timescale which is short compared to the time it takes for coordinate changes to cause the source to move to a location in the pointing error field with a significantly different value. There is no physical reason to assume this random component changes dramatically without changes to drive control or the telescope drives. Given the time required to measure radio offsets at CARMA is large (7 to 10 minutes per measurement), it is more efficient to carry out the repeated measurement optically. This has been done frequently at CARMA, typically after major changes to the underlying drive code or changes in hardware. The most recent measure of this random component, on September 13, 2007, is consistent with the three previous measures and provides $0.5''$ per axis for the 10-m antennas and 0.5 to $0.75''$ per axis for the 6-m antennas, setting a lower limit on the pointing error to be expected for the two different antennas. This is significantly less than the minimum errors, $3.5''$ and $6.5''$ for the 10- and 6-m antennas respectively, needed to produce a factor of two reduction in image fidelity of mosaic observations (see Chapter 2 Figure 2.7) and implies that controlling systematic errors will determine the degree to which high fidelity can be achieved.

[1] Optically, stars brighter than V_{mag}=4.75 are not limited by signal-to-noise. For the current, 3-mm band, radio pointing at CARMA, sources brighter than $\sim$2 Jy are not limited by single to noise.

Table 4.1. CARMA Pointing Parameters

Parameter	10-m	6-m
Short-term Repeatibility[a]	$0.5''$	$0.5\text{-}0.75''$
Short-term Repeatibility (Radio)[a]	$1.5''$	$2.5''$
Post-fit RMS	$2.1''$	$2.0''$
Blind pointing[b]	$2.7''$	$3.5\text{-}5''$
Decay Time[c]	$\sim$30 days	$\sim$14 days
Half-fidelity Limit[d]	$3.5''$	$6.5''$
Daytime RMS (optical)	$5''$	$11''$
Radio Pointing RMS	$5''$	$6''$
Daytime Radio Pointing RMS	$6''$	$11''$
Common Error Gradient	$<0.06\frac{''}{^\circ}$	$0.06\text{-}0.2\frac{''}{^\circ}$
Common Day Error Gradient	$\leq 0.3\frac{''}{^\circ}$	$0.2\text{-}0.9\frac{''}{^\circ}$
Limiting V Magnitude of Cameras	4.75	3.2 (4.75)[e]
Limiting Daytime V Magnitude of Cameras	<3	<3

[a]The short-term repeatibility describes the RMS of the centroid values obtained on datasets taken in rapid succession.

[b]Based on short term measurements typically on the night following the measurement of pointing model.

[c]Time for the pointing model to decay by 20% over the blind value.

[d]Pointing error at which the fidelity of mosaics is reduced by a factor of $\sim$2 (see Chapter 2 Figure 2.7). This value is valid for 3 mm and should be considered to be a factor of two smaller for high-fidelity 1 mm observations.

[e]The style of camera on the 6-m antennas was changed recently resulting in better performance and a fainter limit

Note. — All values are representative of typical, night-time behavior unless otherwise noted. All of the values quoted here already benefit from the improvements discussed in §4.4.1. Radio pointing measurements utilize the CARMA Software Utilities multiMap (S. Corder) for data collection and refPoint (S. White) for calculation of offsets. Daytime camera use involves the coaddition of frames and subtraction of the background. The techniques and proof of concept were by Corder & Carpenter while the final implementation of the coaddition code was by Beard & Scott. The V-band limits are approximate. Daytime optical limits depend strongly on the angular distance between the source in question and the sun.

The errors in the pointing model are often introduced in the frame of the telescope so the coordinate distance between sources is often of greater importance than on-the-sky separations. As discussed above, the systematic effects give rise to a vector field of errors. Large error field *derivatives* in coordinate space, rather than large magnitudes, are more problematic with respect to pointing. Derivatives are more relevant because large but constant errors appear as collimation terms which can be corrected by a single measurement at any location on the sky, although in the limit of very large collimation errors small angle approximations may be violated.

Since the error field is likely a combination of trigonometric functions, the form of the derivative is complicated and can change sign several times over the full coordinate space. Indeed, if the form of the error field were simple, it could be corrected globally. In what follows, the derivatives are treated as being linear. Typical, large-scale errors can be represented as sinusoidal functions of period 360°, as shown in the top panel of Figure 4.1. For such functions, the assumption of a linear gradient introduces, at most, a $\sim$10% error over a range of $\pm$30 degrees. For more highly structured or higher harmonic errors, as shown in the bottom panel of Figure 4.1, restricting the errors to the same $\sim$10% requires restricting the linear range by a factor of three to $\pm$10 degrees. By night, these higher order errors contribute much less to the overall pointing error. During the day, however, serious environmental influences may reduce this linear range as they amplify terms which may not be trigonometric.[2] In these cases, the linear treatment is not appropriate and the accuracy of a pointing correction decays far more rapidly than presented here. This only serves to amplify the need for frequent, nearby pointing correction.

[2]The day-time pointing model is not at all well known given the limited time over which the optical cameras have functioned well by day.

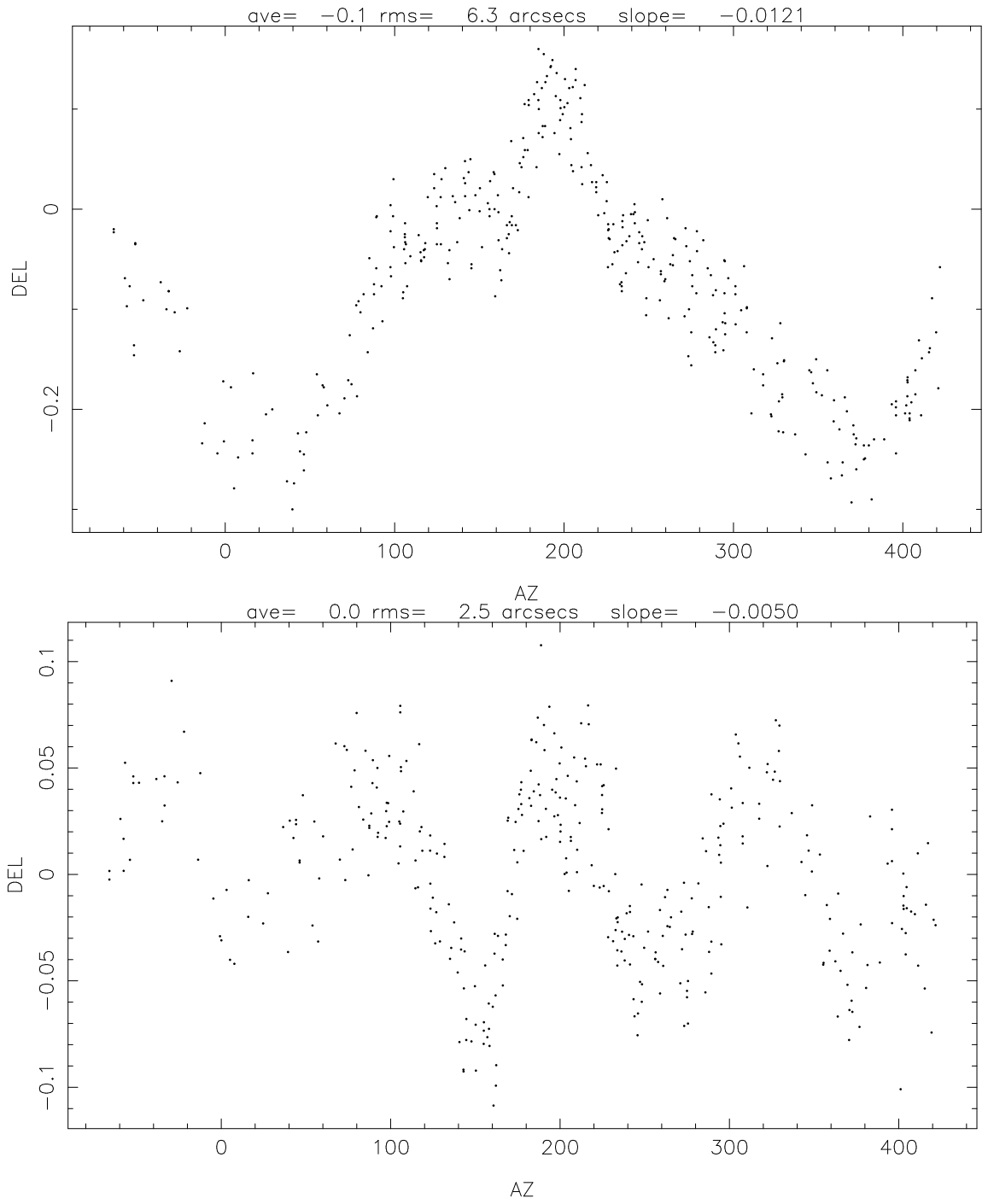

Figure 4.1 The horizontal axis is the azimuth coordinate which is not wrapped, i.e. 400 degrees and -40 degrees represent different positions on the antenna encoder/wrap. The vertical axis is the offset from the nominal pointing model and is in arcminutes. The top panel shows a sinusoidal oscillation probably from a tilt. The bottom panel shows higher order oscillations with form $\cos(3az)$.

Non-zero derivatives of the field produce two critical limiting scales on antenna pointing. These depend on the separation of the pointing source and target,

$$D_{char} \sim \frac{\epsilon}{dF/d\phi}, \tag{4.1}$$

and the time between collimation corrections,

$$T_{char} \sim \frac{\epsilon}{d\phi/dt\ dF/d\phi}, \tag{4.2}$$

where D_{char} is the separation between target and pointing source, T_{char} is the time between pointing updates, ϵ is the allowed error, F is the error field, ϕ is the coordinate and t is clock time. D_{char} is introduced because local pointing corrections are collimation terms, i.e. constants. If there is a non-zero derivative in the pointing error field, the assumption of constant correction induces a systematic pointing error as a function of position on the sky. T_{char} arises because the local correction to the pointing is good only as long as the coordinates have not changed sufficiently such that the value of the error field at the source location is unchanged. Ideally, the error contribution, ϵ, should be much smaller than the random component described above. In practice, this creates unreasonable limiting scales while ϵ (much) less than the RMS in the derived pointing model provides more tenable limits.

Table 4.1 presents the typical residual pointing errors after a new pointing model has been derived for the CARMA antennas. Also included are typical *blind* pointing results from datasets taken on subsequent days. Blind pointing accuracy is given by the RMS of the pointing dataset with respect to the mean, not zero. The residuals after fitting represent the lowest reasonably achievable limit to the pointing error. These are typically less than the "half-fidelity" limits described in Chapter 2. However, these residuals are the best case scenario. Table 4.1 also describes a number of other typical pointing errors that contribute to the total pointing error, including typical error field gradients.

4.4 Results: Pointing Improvement

A number of different approaches were taken to try to improve CARMA pointing, including better measurement of the existing pointing model, identification of new pointing model parameters and/or corrections to the existing model, and implementation of new techniques to improve overall pointing within radio observations. Some innovative efforts failed, most notably the attempt to perform active tilt correction on the 6-m antennas. Shading of different fractions of the antenna mount indicated that the bulk of the thermal drifts in tilt were induced by changes in the yoke structure, which are not measured by the tiltmeters (Wright & Plambeck, private communication). This confirmed the results of similar tests carried out at Hatcreek Radio Observatory (Wright & Forster) as well as initial tests indicating that a pre-determination of the tilt value using tilt meters at night resulted in little to no improvement in the pre-fit residuals of the pointing data (Corder). In addition, a comparison of directly measured antenna tilt with the tilt term measured by optical pointing revealed significant differences, suggesting that significant deformation comes from the yoke structure.

In the end, improvement in the quality of CARMA pointing resulted from three, well-defined procedures. The first, the development of the software utility *multiMap* (Corder) and its subsequent integration into the active system via *refPoint* (White), is described in detail by White & Corder (2007). This routine measures the cross sections through the voltage pattern, calibrates the data, calculates offsets derived from Gaussian fits to the cross sections, and applies the offsets on-line. All radio pointing measurements at CARMA rely on this routine. It is used in the final alignment of the telescope and source and the measurement of the relative radio and optical collimation terms. The remaining important steps involve (1) improving the CARMA optical data collection methods and (2) using optical offset pointing within radio observations.

4.4.1 Optimized Optical Catalog & Collection Methods

4.4.1.1 Motivation

Initially, an optical catalog of 58 individual stars was used to derive the CARMA pointing model. Of these stars, 5 effectively sampled the same location, given the typical source separation. At that time, the mean separation on the sky was $\sim 30^{\circ}$ and the sky coverage was poor and not particularly uniform given the catalog design.

Historically at OVRO, intervals of two to three hours were found to be a limiting timescale for pointing model measurements. Observations taken over longer times resulted in changes in the collimation terms due to weather effects (Woody, private communication). Since approximately half of the stars were above the elevation limits at a given time, two cycles through the catalog provided observations of ~ 50 stars in 100 to 120 minutes. The bottom left of Figure 4.2 displays the typical coverage of a pointing run using the original catalog. Within the uncertainties of the data, statistically significant tilt/timing terms (m(4) & m(5) in the above model) were rarely seen and the pointing model appeared to be adequate (Woody, private communication). The residuals obtained using the original catalog over a two hour span are shown in the top section of Figure 4.2. In general, the RMS pointing error after the fit is 3-4$''$ per axis. Typical blind pointing accuracy was 4-5$''$ per axis, i.e. larger than the half-fidelity limit in the 3-mm band (see Figure 2.7), and would seriously degrade images made in the 1-mm band.

At BIMA, optical pointing was used less often than at OVRO as sessions separated by a day tended to yield vastly different solutions; a solution producing $<2''$ RMS per axis one night could yield $\sim$5-10$''$ RMS the following night (Forster, private communication). Because of the larger number of parameters in the 6-m pointing model (16 compared to the 7 of the 10-m antennas) considerably more data are needed to adequately fit the model. Even with fits to 100 stars, roughly double the density in Figure 4.2, it was difficult to break the degeneracies of the 6-m pointing model.

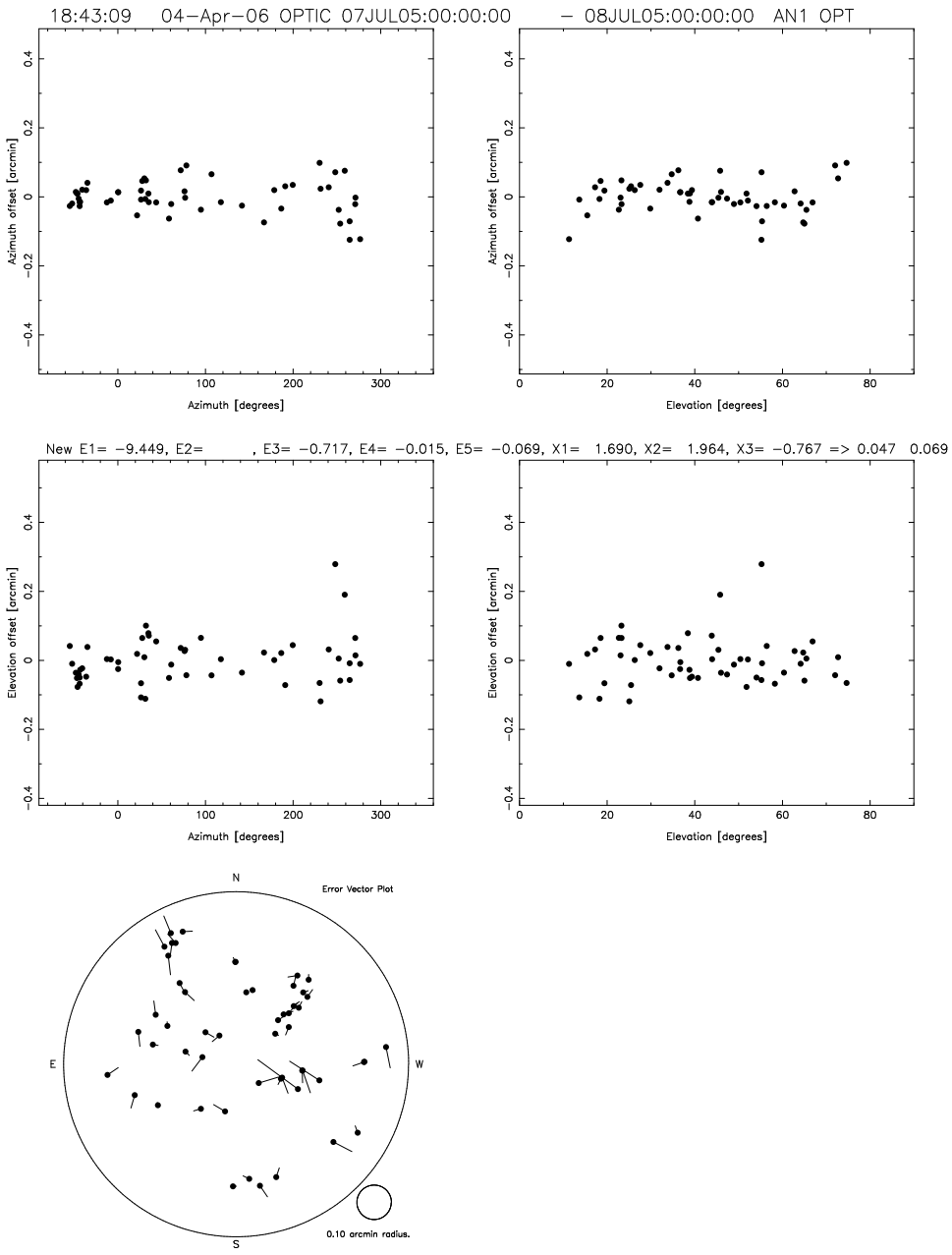

Figure 4.2 The figures shown are automatically generated by the *runpoint* program (Myers & Woody, 1985-1992). The program simultaneously fits the azimuth and elevation model to obtain the best overall minimization of residual pointing errors. The top four images display azimuth and elevation error as a function of azimuth and elevation after the fit has been applied. The horizontal axes are in degrees of azimuth or elevation while the vertical axes are in arcminutes. The circular plot to the bottom of the image is a scatter plot of the observed stars. North is up and elevation is measured as the deviation from the circular boundary, which represents the horizon. The center of the plot is the zenith. The lengths of the lines attached to each point are a measure of the offset required to bring the data into agreement with the model.

4.4.1.2 Approach & Implementation

The simplest way to improve the pointing at CARMA was to increase sky coverage and thus better measure the pointing model on the sky. It was also recognized that the speed at which data were collected had to be enhanced to handle the increased number of stars to be observed. A new optical pointing catalog for CARMA was developed. To construct the catalog, the sky was divided into a $10^\circ \times 10^\circ$ pattern, centered on Sirius. The brightest source in each patch was selected from the Hipparcos catalog. Only sources above $\delta = -30^\circ$ were included due to CARMA elevation limits. While this ensured relatively uniform sky coverage with a source within $\sim 5^\circ$ of any position on the sky, some of these stars are fainter than the CARMA optical detection limit of V_{mag} $\sim$4.75 at the horizon. Limiting the catalog to V_{mag}=4.75 results in a catalog of 228 stars, slightly lower coverage–a source within about 7° of any position on the sky. The original catalog had included 17 very bright stars that were not selected by the above procedures. These were added to produce a catalog of 245 stars.

At any time, 120 stars are above the elevation limits. With the existing data collection methods, it was difficult to measure 50 stars in two to three hours let alone 120 stars. Enhanced speed was achieved by changing the observing procedures. For example, following OVRO practices, CARMA pointing sessions were initially carried out serially. Due to the greater number of CARMA antennas, pointing sessions with the entire array could observe only $\sim$40 stars over an entire night, violating the two to three hour time limit for the 10-m antennas and not acquiring sufficient data for the 6-m antennas. Using the antennas in groups of 3 allowed the time constraints to be met but then require two complete nights to obtain the necessary pointing data. A new command that allowed individual antennas to slew to and track sources independently was therefore created (*trackSingle*). By carrying out the optical pointing session in parallel, 60 data points per hour could be obtained. In this way, the entire new catalog can be sampled in two hours.

Further optimization was based on simulations that calculated the approximate slew time between various targets. Since the slew speeds of the 10- and 6-m antennas

differ by a factor of about two and the axes of given telescope also slew at different rates, a simple least path minimization is not optimal. In addition, the time to calculate this least path exceeds the time gained by using this procedure. If the sources are sorted first in azimuth, with boundaries carefully selected to handle the antenna wrap logic, then binned in the azimuth coordinate and sorted again in each bin, with alternating bins being sorted in elevation or zenith angle, the only free parameter is the bin size. The sorting is done only once at the beginning to reduce time spent in sorting as bin crossing does not provide a substantial reduction in efficiency. The simulation tool generated several star lists and calculated the expected time to complete the observation given a azimuth bin size. The results are shown in Figure 4.3. Although, the different drive speeds and axis speed ratios for the 10- and 6-m antennas resulted in a slightly different optimum bin size for the two antennas, 25° of azimuth space proved to be a good compromise.

4.4.1.3 Tests & Verification

The new catalog and enhanced collection methods described above resulted in vast improvements to the overall sky coverage, the speed of data collection and the quality of fits to the pointing model. Figure 4.4, similar to Figure 4.2, displays the new sky coverage which includes two passes through the catalog for 10-m antennas. Now, approximately 240 stars are observed over two hours with nearly uniform coverage. The antennas are driven through the catalog twice, once forward in azimuth and once backwards, to uncover possible hysteresis. The data rate is a factor of more than 4 greater than before and the coverage in coordinate space is much better. For the 6-m antennas, three passes through the catalog ($\sim$360 stars) typically takes two hours.

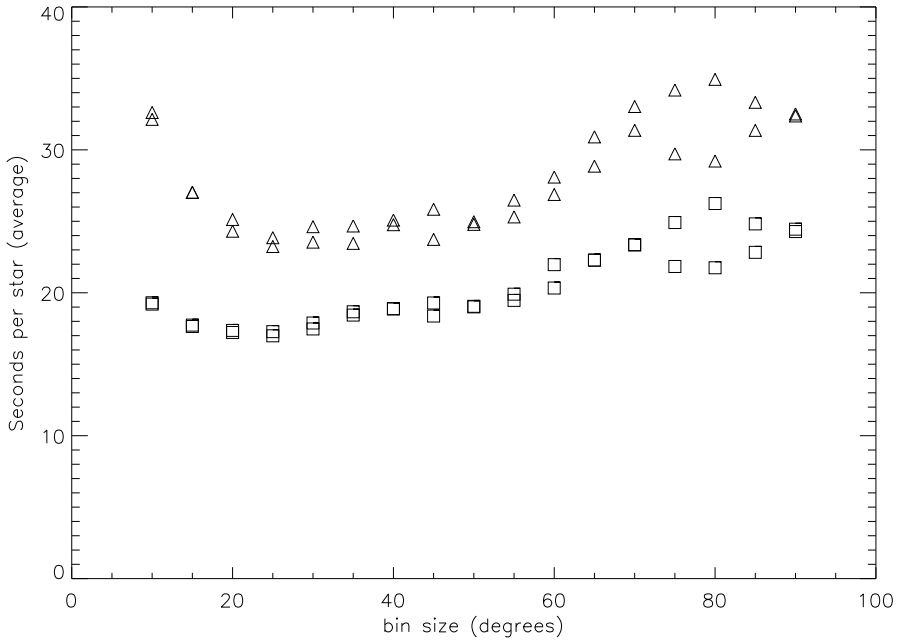

Figure 4.3 The average time to center a star is plotted against the azimuth bin size. The triangles and boxes represent the 10- and 6-m antennas, respectively. The 10-m antennas are inherently slower and require longer slew times between stars. For this reason, time is a stronger function of bin size for the 10-m antennas when compared to the 6-m antennas. At large bin sizes, there is large scatter because the specific locations of the stars and can dominate the timing.

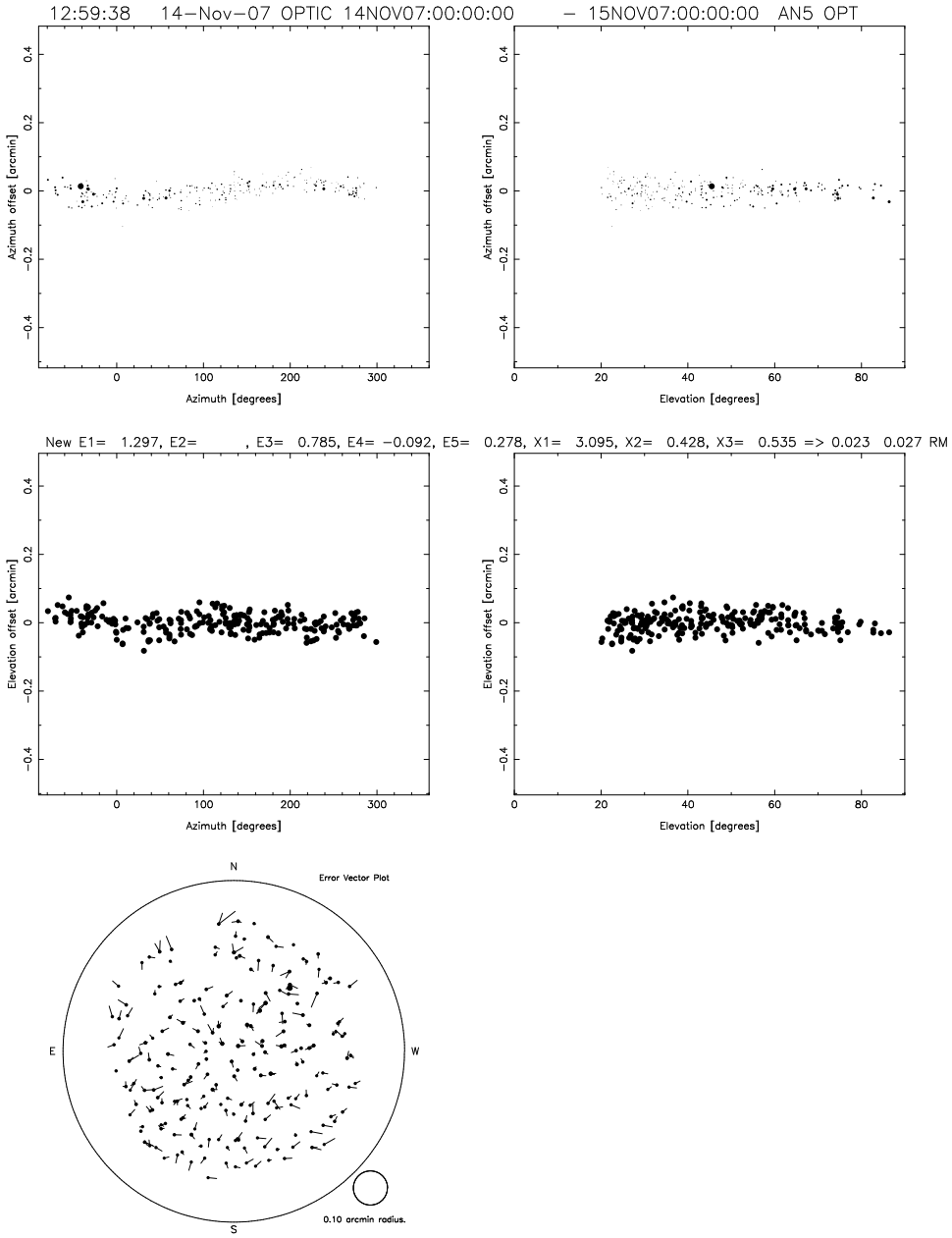

Figure 4.4 Similar to Figure 4.2 except the new data collection methods are employed. The time taken to collect the data is the same. The sky coverage plot in the bottom left contains a factor of four more points and the points are far less clustered given the design of the catalog.

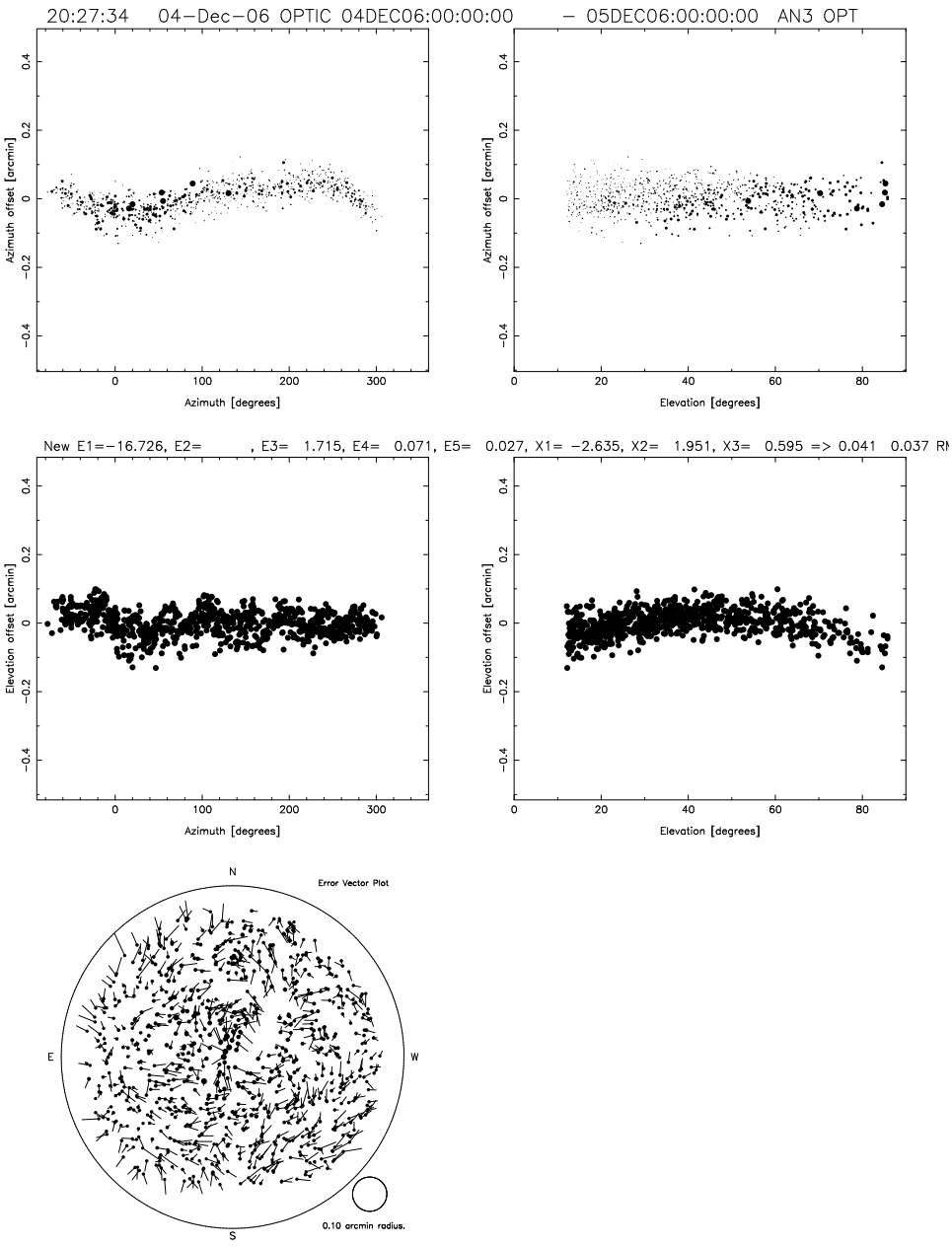

Figure 4.5 Similar to Figure 4.2 except the new data collection methods are employed and the data are taken over 3 full cycles, measuring over 850 stars. A significant azimuth error versus azimuth and elevation error versus elevation term is seen.

4.4.1.4 Benefits & Applications

The benefits of the catalog expansion and optimized observing techniques are seen in the reduced residual scatter of the fits to the pointing model, the resulting stability of those fits and the revelation of errors in the pointing model implementation or new terms. For the 10-m antennas, pointing RMS post fit per axis is reduced from 3-4″ to 2″. There is little reduction in the pointing RMS for the 6-m antennas. However, the truly relevant result pertains to the blind pointing, which describes the applicability of the determined model over several days. By this measure, both antenna styles have residuals reduced by ∼40%. The 4-5″ RMS of the 10-m antennas is reduced to 2.7″ and the 6-m residuals are reduced from 5-10″ to 3.5-5″. The high end of this latter range is usually dominated by two particular 6-m antennas which are historically known to have poor pointing behavior and/or have poorly functioning cameras.

The new catalog and data collection routines also revealed the presence of a systematic, residual oscillations in both the 10- and 6-m antennas. For the 10-m antennas, significant azimuth error versus azimuth and elevation error versus elevation terms are seen in Figure 4.5. The terms are constant in phase and mostly constant in amplitude, at ±1.8″, from antenna to antenna and over time, suggesting some software error. While this error appears to be small, it represents most of the residual error in the pointing fits for the 10-m antennas.

In addition, it became obvious that the implementation of the 6-m antenna pointing model at high elevation was in error. Altering the pointing model to subtract the large collimation error term before the rest of the correction was applied, resulted in a significant reduction in the pointing error for elevations above 75°. The need for a new parameter in the 6-m antennas is illustrated in the bottom panel of Figure 4.1. There is already a $\cos(2az)$ term in the pointing model, which is thought to be associated with the ellipticity of the drive plate. This $\cos(3az)$ term is the next highest Fourier residual and may be associated with the tripod structure in the 6-m mount. The amplitude of this component varies from antenna to antenna, although the phase of the oscillations appears to be fairly constant. The example shown in Figure 4.1

shows that, for this particular antenna, this oscillation is the largest contributor to the post-fit pointing RMS. The consistency of this parameter over time is unknown.

4.4.1.5 Limits & Future Directions

The fundamental limit to increasing the catalog size still further is slew speed and centroiding timescale. Increased camera sensitivity would be of little benefit without improved measurement time per source because the entire pattern on the sky should be completed at least twice in two hours. With improved day-time camera sensitivity, a pointing model solution for day-time operation and more dense coverage for optical offset pointing would be possible. However, the current cameras have some day-time functionality and are relatively new. The cost of cameras with sufficient infrared sensitivity is approximately $1500-2000 per camera and significant software development would be required.

Both the 10- and 6-m antenna pointing models need additional parameters. However, the addition of such parameters has been delayed until the pointing models of the 10- and 6-m antennas are unified. The functional form of the 10-m errors appears to be co-sinusoidal in both axes, though the elevation term appears to require a $\cos(2el)$ term. Possible addition of the $3az$ component to the 6-m pointing model awaits the verification of these properties in light of recent changes to the drive code and a test of the stability of these terms from night-to-night.

4.4.2 Optical Offset Pointing: Active Optical Pointing

4.4.2.1 Motivation

Characterization of the pointing model can only improve the pointing to a degree. In addition, the pointing model cannot be arbitrarily well determined every night and the parameters are known to drift over time. Thermal variations, even possibly differences in ambient temperature from night-to-night, are sometimes hysteretic. It would not be surprising if the higher order term in the 6-m model discussed above

was highly variable. It could depend on the stiffness of the mount and by implication the ambient temperature modified by the thermal properties of the mount.

Such systematic errors in the pointing data lead to in the decay of the applicability of any given model with time. Active tilt correction and thermal insulation of the 6-m antennas have proved ineffective at reducing the overall pointing drift in the presence of thermal gradients. The active tilt correction of the 10-m antennas follows most of the thermal tilt variations but cannot keep up with the rapid variations that cause degradation of pointing over sunrise and sunset (see Figure 4.6). From Table 4.1, it can be seen that any additional systematic error can be extremely detrimental to high fidelity imaging because the blind pointing at night is very close to the half-fidelity point (see Chapter 2).

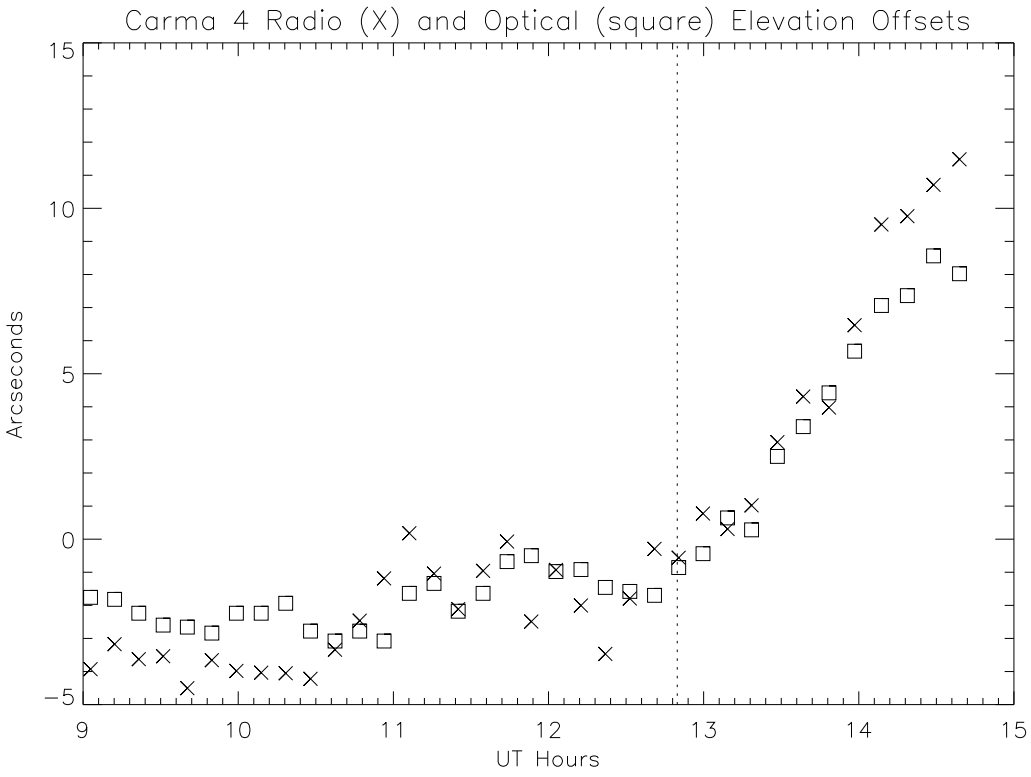

Figure 4.6 The elevation pointing offset for C4 in arcseconds is plotted versus time. Sunrise, indicated by the dashed line at UT 12.83 hours, excites a trend in pointing error of 12″ over two hours. The different style of points show the radio and optical trends.

A possible solution is to make more frequent collimation corrections. If the critical scales D_{char} and T_{char} can be met with regular pointing corrections, systematic deviations in the pointing of the telescope will not result in serious fidelity degradation. It is a fundamental assumption of the CARMA pointing model that the optical to radio offset is a constant, so, in principle, the optical cameras mounted on every CARMA antenna can be used to actively correct pointing. Initial work at BIMA to utilize this functionality is discussed in Swift (2002). These tests were carried out on a single telescope over a single night. Radio pointing fits and the optical to radio offset were calculated offline. It is worth noting that the camera used in that experiment reveals that far fainter stars can be seen at night with off-the-shelf CCD cameras ($V_{mag} \sim 10$) with reasonable integration times (<1 s) rather than the TV-style cameras used in this work, i.e. far fainter stars could be detected at CARMA with changes to the camera.

For the CARMA pointing model, the only difference between the optical and radio pointing of the telescope is an on-the-sky collimation term in azimuth and elevation, gravitational sag and refraction. Refraction can be calculated from the CARMA weather station and the source elevation. Gravitational sag can be derived from significant quantities of radio and optical pointing data; the sag parameters at night tend to evolve very slowly in time and thus do not introduce errors on track time scales. Thus only two parameters, azimuth and elevation collimation, need to be measured to track the difference between optical and radio pointing over small timescales. If the difference between the optical and radio collimation varies slowly in time compared to typical lengths of observation and evolves minimally in the presence of strong thermal gradients over this timescale, or at least to a lesser extent than the radio term alone, then the optical and radio separation can be assumed constant and changes in the optical value can be assumed to apply to the radio pointing as well.

The video-style cameras are inherently two dimensional allowing both azimuth and elevation offsets to be measured at the same time. Typically, a single radio pointing measurement of quasars at CARMA can take upwards of 7-10 minutes; a single repetition of the optical centroiding routine requires about 8 seconds. While

there have been discussions of ways to dramatically improve the radio pointing times, it is likely they cannot be reduced below 3-4 minutes. Moreover, the short measurement time for the optical cameras allows convergence to be tested while 7-10 minutes for radio pointing precludes any attempt to check convergence within regular science observations.

A further advantage is the sheer number of stars visible with the cameras when compared to the number of bright quasars, a property exploited to make the new optical catalog. Radio pointing requires quasars with flux $\geq$2 Jy, although atmospheric conditions and exact observing frequency cause this limit to vary between $\sim$1 and 4 Jy. Inevitably, the density of radio pointing sources in the 3- and 1-mm bands is low compared to the 7° typical separation for stars as described above. The distance to the nearest radio pointing source can often be 25° or more in the 3-mm band and significantly greater in the 1-mm band.

Here, the process of actively applying optical pointing corrections to the CARMA data is called optical offset pointing or guiding. The development of the technique was rather long, with a variety of tests and realizations. Here, only on the tests that were most fruitful, the limitations, and current implementation are reviewed. However, one piece of history is noteworthy. Originally, only the 10-m antennas were equipped with optical cameras that were usable during the day. Time-consuming, hand focusing of the 6-m antennas was required to see day-time objects with subsequent readjustment at night. In September of 2007, entirely due to the demonstrated success of this optical offset pointing method, day-time functional cameras were purchased for every antenna at CARMA. The method can now be applied by day or night.

4.4.2.2 Approach & Implementation

The main software for optical offset guiding can be found in the software utility *opticalGuideMain* (Corder). An interface to the general user scripts (Carpenter) is also available and is robust for day- or night-time function. The original testing and implementation of the coaddition and background subtraction routines was done in *quickGrab* (Corder), and later integrated into the CARMA centroiding code (Scott)

by Carpenter. In the end, centroiding, coadding and background subtraction were ported to low level code to optimize speed (Beard).

The detailed implementation of optical offset guiding and the software packages used to support it are discussed in Appendix C. The basic approach is to assume that the optical to radio offset is constant over the course of an observation. Initially the radio pointing is centered on any available bright quasar or planet. Then the offset of a nearby optical source from this newly localized pointing model is determined. This difference is stored for later use. Then, subsequent pointing updates are performed by first loading in the stored offset and then determining the relative change on an optical source near a flux calibrator, gain calibrator or science target. In practice, the selection of optical sources is done automatically. The approach is robust against malfunctioning cameras and overcast skies.

At the time of writing, greater than 40% of the scripts in the most recently completed configuration utilize the optical offset guiding approach. This speaks to the benefits of the approach and the ease of use, which requires a single parameter to be added for reasonable defaults. The fraction of scripts utilizing the approach has grown considerably over the last 18 months. This is certainly due to the evolution of the interface from specialized scripts outside the realm of the standard CARMA user interface to night-time integration into the standard user methods and finally now 24-hour use and robust function.

4.4.2.3 Tests & Verification

The optical offset measurements are differential in nature while standard radio pointing is not. A comparison of differential radio pointing measurements with optical pointing is irrelevant. If the density of radio pointing sources were high enough to allow regular, differential measurements, there would be no need for optical offset pointing except in cases where changes in the pointing error field occur on timescales short compared to the time required to obtain radio pointing updates, i.e. in situations where pointing is required every hour or more frequently. Differential radio pointing measurements will always be more accurate *when available* since the optical

Table 4.2. Required Limits on the Optical to Radio Offset

Coordinate Speed ″/s	Day/Night	Mount Error ″/degree	Limit ″
15	Night	0.06	2.5
20	Night	0.06	3.0
50	Night	0.06	6.8
15	Day	0.2	7.9
20	Day	0.2	9.8
50	Day	0.2	22.6
15	Night	0.2	8.2
20	Night	0.2	10.1
50	Night	0.2	22.8
15	Day	0.9	35.5
20	Day	0.9	44.3
50	Day	0.9	101.9

Note. — The value of C, the correction factor used to represent the ratio of the on-the-sky distance to the coordinate distance, is assumed to be 1, setting the most strict limits. The distance to the radio pointing source was taken to be 25°. The time taken between radio pointing observations was taken to be a reasonable minimum, 2 hours and fifteen minutes, although night-time observations often stretch this to 4 hours. For these assumptions, the contribution from the time difference typically contributes about twice the error of the distance separation for values of C∼1. A relaxation of any of these assumptions beyond typical "best-case-senarios" results in an increase to the limit. For example, for C∼1.25 and a 40° pointing source separation, the limiting error is increased by 40-45%. Or, if the time to radio point is increased to four hours, this roughly doubles the limiting error. The values provided here are independent of frequency except in that re-tuning to the 3-mm band for pointing observations adds to the radio pointing measurement time and the distance to 1-mm band pointing sources is typically far greater than 25°.

pointing is limited to the accuracy of the radio pointing plus some additional errors associated with the optical measurement and the systematics associated with the assumptions about the optical to radio offset. It is exactly in cases where such pointings sources are *not available* where optical offset pointing gives the greatest benefit.

The appropriate comparison is presented in Appendix D. The maximal error allowed in the quantity δR_{vec}, defined in Equation D.4, is presented in Table 4.2. These limits are based on the parameters described in Table 4.1 where the derivatives in the error field are expressed as arcseconds per degree, coordinate speed is in arcseconds per second, final errors are in arcseconds, times are in minutes and separations are in degrees.

Tables 4.3 and 4.4 provide the details of the RMS estimates for the different conditions as well as the RMS of the radio pointing measurements only over these ranges for night-time and day-time use, respectively. If the δR_{vec} values have greater RMS than the radio pointing measurements, then optical offset guiding certainly does not help the situation. Often there are systematic trends in the pointing offsets but a comparison of the RMS of these trends still results in the quantity with the smaller trend also having the smaller RMS. Typically for the 10-m antennas, the repeated source observations and measurements all over the sky and on repeated sources at night have RMS of about 3.5-5″. The 6-m antennas have slightly larger RMS values of 4.5-5.5″. During the day, these numbers increase. For the 10-m antennas the azimuth scatter grows significantly and is on average larger than the radio pointing alone value. However, this is not the case in elevation, where the elevation scatter is often much smaller than the radio alone value. The combined RMS is between 5.5 and 7.5″. In the case of day-time observations with the 6-m antennas, the optical to radio offset is almost always significantly smaller than the radio values alone, indicating that there are systematic trends in the radio pointing. The RMS of the vector components is comparable in both axes and is about 7″.

If these values are compared to the allowed, night-time values in Table 4.2, it is found that for a well behaved mount model, i.e. mount error derivatives of the order 0.06″ per degree, the use of optical offset guiding is actually detrimental to the pointing for sources at low elevation, if the pointing source is at or within 25° and pointing is done every two hours at night. This is because the additional scatter in the optical to radio offset vector is greater than the systematic error introduced by the evolution of the mount model. This is the typical situation for the 10-m antennas. The 6-m antennas often have error gradients more on the order of 0.1 to 0.2. In these cases, it is beneficial to use optical offset guiding.

Table 4.3. Scatter in the Optical to Radio Vector at Night

Antenna	Repeat Source Night				All Sky Source Night			
	Az (Rad) RMS (″)	Az (Opt-Rad) RMS (″)	El (Rad) RMS (″)	El (Opt-Rad) RMS (″)	Az (Rad) RMS (″)	Az (Opt-Rad) RMS (″)	El (Rad) RMS (″)	El (Opt-Rad) RMS (″)
1	[1.51,3.07]	[1.58,3.24]	[1.53,2.06]	[1.56,2.46]	[4.71]	[4.86]	[3.88]	[2.75]
2	[3.50]	[2.70]	[3.16]	[2.76]	[4.44]	[3.95]	[3.46]	[3.70]
3	[NA]	[NA]	[NA]	[NA]	[3.85]	[2.05]	[2.81]	[2.15]
4	[1.32,2.48]	[1.55,3.46]	[1.46,2.14]	[1.27,1.53]	[8.30]	[3.00]	[3.44]	[2.06]
5	[1.83]	[2.30]	[3.57]	[1.64]	[3.02]	[3.15]	[3.34]	[2.46]
6	[0.88]	[1.03]	[1.57]	[1.61]	[3.59]	[2.63]	[3.21]	[2.75]
7	[2.23,5.16]	[2.65,2.18]	[3.42,4.05]	[3.11,3.93]	[4.43]	[2.87]	[6.38]	[2.86]
8	[3.83,3.32]	[1.79,2.58]	[2.53,4.81]	[2.19,4.21]	[6.23]	[2.33]	[6.58]	[3.16]
9	[1.75,4.25]	[1.68,3.06]	[2.27,3.18]	[2.45,2.30]	[3.97]	[3.29]	[3.43]	[2.59]
10	[2.22,4.00]	[2.00,1.27]	[3.12,4.95]	[2.02,2.11]	[3.32]	[2.31]	[6.02]	[2.40]
11	[4.49]	[2.34]	[5.94]	[1.51]	[3.90]	[3.12]	[5.94]	[4.97]
12	[1.96]	[4.16]	[2.13]	[2.07]	[4.42]	[1.75]	[8.22]	[2.69]
13	[4.20,2.51]	[3.12,1.59]	[4.66,2.32]	[2.50,2.50]	[4.29]	[3.23]	[6.74]	[4.65]
14	[4.07,3.45]	[3.22,1.60]	[2.76,7.78]	[2.76,4.26]	[3.77]	[2.05]	[4.05]	[3.94]
15	[4.52]	[2.19]	[12.4]	[5.83]	[4.21]	[2.56]	[4.28]	[2.54]

Note. — Rad implies radio pointing whereas Opt-Rad is the relevant optical minus radio vector component. NA implies no data was taken on the relevant night. Repeated datasets were taken on 10 July 2006 (∼23 data points) and 02 November 2007 (∼50 data points), although the 2006 trial was missing several antennas. The all sky data was taken 29 March 2007 (∼30 points).

Table 4.4. Scatter in the Optical to Radio Vector by Day

Antenna	Repeat Source		Day		All Sky Source		Day	
	Az (Rad) RMS (″)	Az (Opt-Rad) RMS (″)	El (Rad) RMS (″)	El (Opt-Rad) RMS (″)	Az (Rad) RMS (″)	Az (Opt-Rad) RMS (″)	El (Rad) RMS (″)	El (Opt-Rad) RMS (″)
1	[3.95,3.59]	[6.34,5.57]	[4.99,5.16]	[2.64,4.07]	[2.04]	[3.74]	[3.09]	[3.79]
2	[4.60,2.90]	[4.40,4.13]	[4.13,3.25]	[2.72,4.76]	[3.42]	[4.83]	[4.21]	[3.47]
3	[1.04,4.60]	[1.26,6.24]	[3.76,3.34]	[4.08,3.84]	[4.97]	[5.87]	[1.10]	[1.10]
4	[2.41,4.70]	[7.47,7.60]	[4.11,4.66]	[2.54,2.38]	[4.32]	[4.47]	[3.64]	[2.70]
5	[1.71,5.31]	[2.28,6.92]	[2.65,6.11]	[1.34,2.93]	[2.84]	[4.45]	[3.46]	[2.86]
6	[4.23]	[5.49]	[4.84]	[2.34]	[3.43]	[5.16]	[3.31]	[3.21]
7	[1.58]	[1.57]	[5.17]	[2.89]	[7.00]	[3.57]	[11.69]	[4.33]
8	[4.19]	[3.65]	[11.39]	[6.03]	[7.68]	[6.16]	[14.59]	[5.74]
9	[4.89]	[4.13]	[5.37]	[3.99]	[5.73]	[4.32]	[8.79]	[4.43]
10	[6.65]	[4.98]	[7.05]	[6.55]	[8.05]	[3.87]	[14.07]	[5.02]
11	[10.02,5.98]	[2.92,3.78]	[8.89,5.99]	[2.97,4.52]	[11.14]	[4.87]	[13.42]	[6.15]
12	[2.62]	[2.76]	[5.20]	[3.79]	[7.18]	[5.94]	[3.02]	[2.79]
13	[7.52,2.62]	[3.63,3.89]	[8.59,7.13]	[2.52,5.43]	[10.24]	[5.36]	[11.20]	[5.86]
14	[4.58]	[4.00]	[10.52]	[6.51]	[7.55]	[5.63]	[11.87]	[7.46]
15	[6.00]	[3.94]	[8.21]	[5.70]	[9.22]	[5.59]	[12.17]	[5.46]

Note. — Rad implies radio pointing whereas Opt-Rad is the relevant optical minus radio vector component. Repeated source datasets were taken on 01/02 November 2007 (∼23 points) and 22/23 November 2007 (∼50 points except for C7 which had 16). The all sky data was taken 29 November 2007 (∼10 points).

By day, an odd result emerges. It appears as though the 10-m antennas would benefit from optical offset guiding in elevation but not in azimuth. If both axes are corrected, the degree of improvement or detriment depends on the magnitude of the elevation error gradient. A more detailed exploration of the systematics is required to address this. For the 6-m antennas, it is clearly beneficial to use optical offset guiding in all cases. A benefit not considered here is that the use of optical offset guiding always provides time benefits over radio pointing alone.

Aside from this decrease in pointing RMS over typical observing conditions, systematic trends are also removed. Figure 4.7 shows the change in elevation offset as a function of time over a period of thermal stress, i.e. sunrise. C4, seen in the left panel, has a systematic change associated with sunrise. Here the pointing changes by $\sim 12''$ over the course of two hours. Given the width of the primary beam at λ=1.3 mm is about $30''$, an observation would have the half power point of the beam being pointed towards the source and the sensitivity would be reduced by a factor of two for this antenna. These periods of thermal stress are times when the magnitude of the gradient in the elevation error field is large enough that the introduction of increased RMS in azimuth would be more than counteracted by the correction of this large elevation change. In the right panel, C13 is experiencing both a systematic change due to thermal stress and an error in the mount model. Here the pointing changes by over $30''$ over the course of just 3 hours and 30 minutes. In both cases the pointing is evolving at 6-$9''$ per hour. Radio pointing every hour is both inefficient and insufficient in such situations. Corrections every 20-30 minutes would allow sufficient time resolution for the correction. Optical offset guiding allows this.

In general, systematic trends persist in the optical to radio offset vector. Figures 4.8 through 4.11 display examples of systematic trends in both antenna styles by day and by night. The magnitude of these systematics is typically reduced for the 6-m antennas with the use of optical offset guiding. The variations seen in the first and third columns are almost always larger or are comparable to the variations in the second and fourth columns, i.e. those which show the optical to radio offset. There

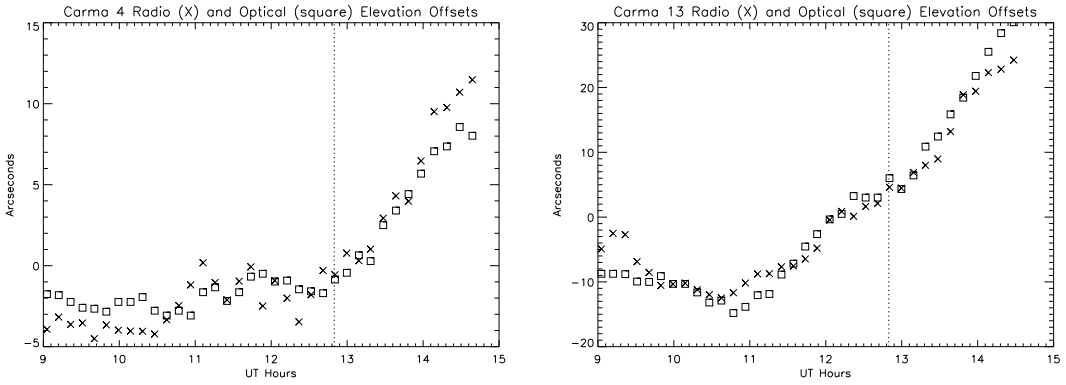

Figure 4.7 Optical and radio elevation offsets are plotted versus time. The X points are radio offsets while the squares are optical offsets. The left panel, which was also shown above, is the pointing offset of C4 under the thermal stress of sunrise, denoted by the dashed line. The right panel displays the elevation offsets of C13 over a similar time period.

are a few instances at night where the trends are somewhat larger in the optical to radio offset but in general the systematics are reduced.

The case for the 10-m antennas is somewhat less clear. At night, the systematic evolution in the radio elevation term is almost always greater than the trend in elevation for the radio to optical offset. However, there is not such clear evidence for the evolution of the azimuth components. The evolution of the radio pointing alone in the azimuth component is typically smaller or comparable in magnitude to the evolution of the optical to radio offset, again arguing that perhaps the optical offset should only be applied to elevation. By day, the result is similar. The elevation component of the optical to radio offset typically has less systematic variation than the radio pointing alone but this is clearly not the case azimuth.

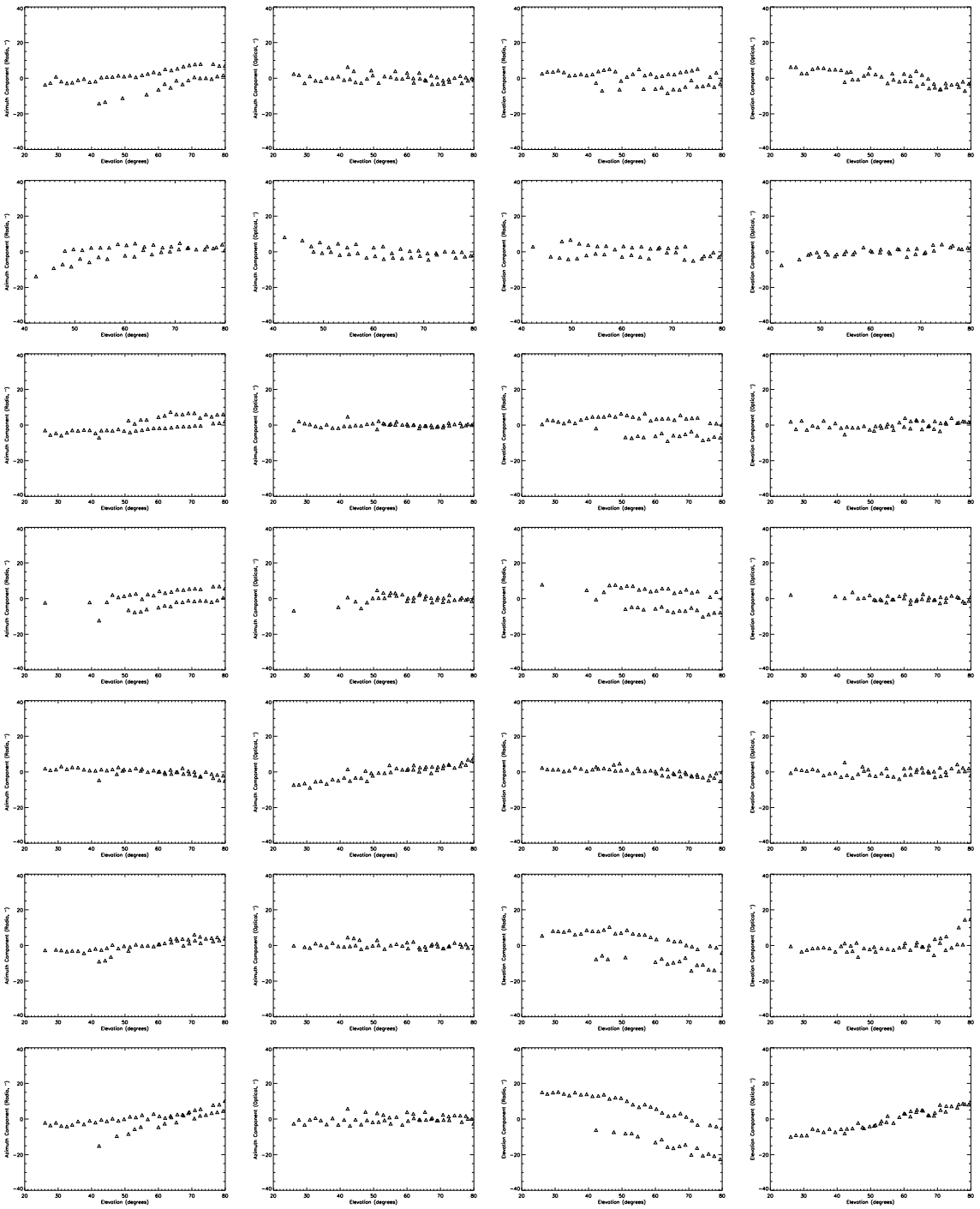

Figure 4.8 Systematic trends in night-time data for the optical to radio offset vector compared to systematic trends in the radio pointing alone for the 6-m antennas are shown. All values are plotted against elevation. The first column of panels shows the azimuth component of the radio pointing. The second column shows the azimuth component of the optical to radio offset. The third and fourth columns are the same but for the elevation component of the radio pointing and the optical to radio offset, respectively.

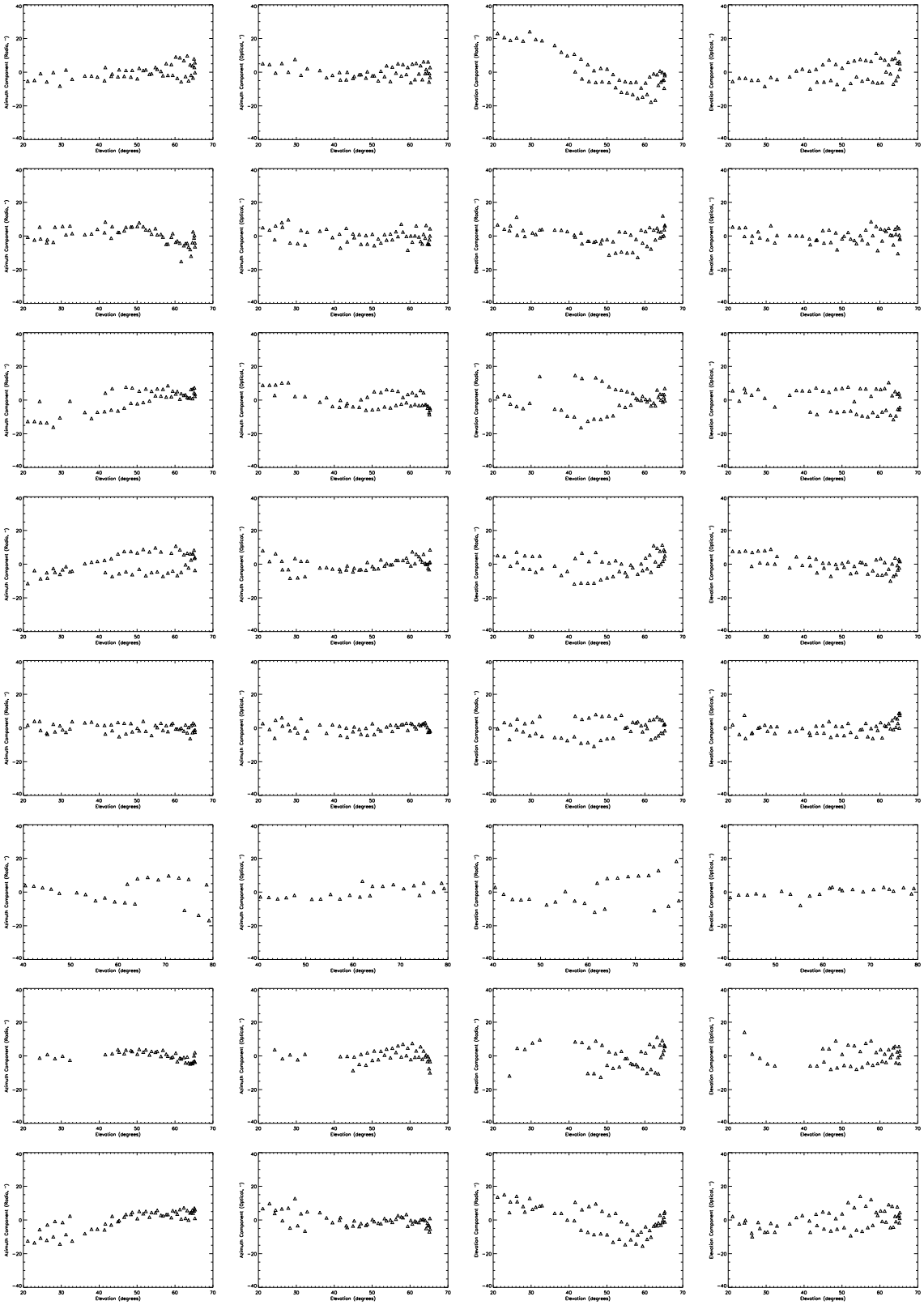

Figure 4.9 Similar to Figure 4.8 except for day-time observations.

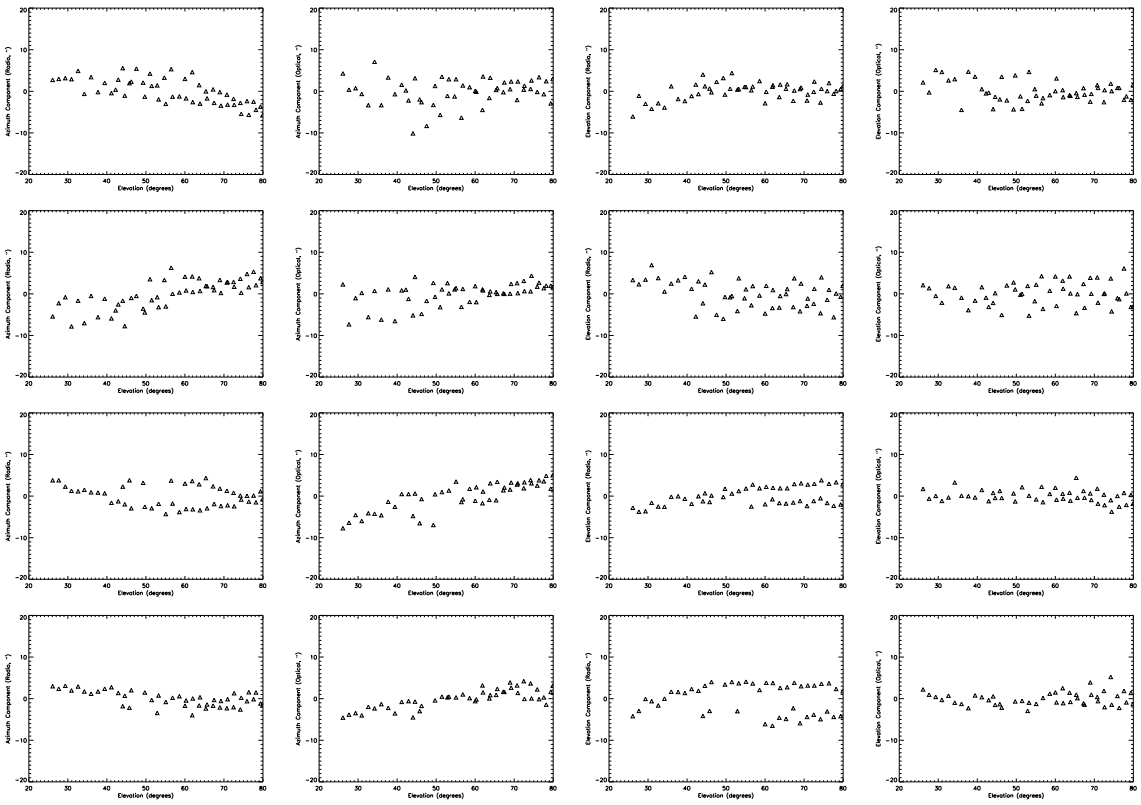

Figure 4.10 Similar to Figure 4.8 except for the 10-m antennas.

The entire discussion of whether the azimuth component of optical offset pointing should not be applied is complicated by the fact that observations sometimes show systematic trends and obvious results but on subsequent attempts the trend is absent. This is likely an example of the hysteretic effect of thermal heating on pointing. Figure 4.11 shows examples of systematic trends where some antennas have data from different days however. It might appear as though the bottom two rows show the same antenna, however, this is not the case, these are two different antennas. On the other hand, rows 5 and 6 show the same antenna. The trends are clearly different from day to day.

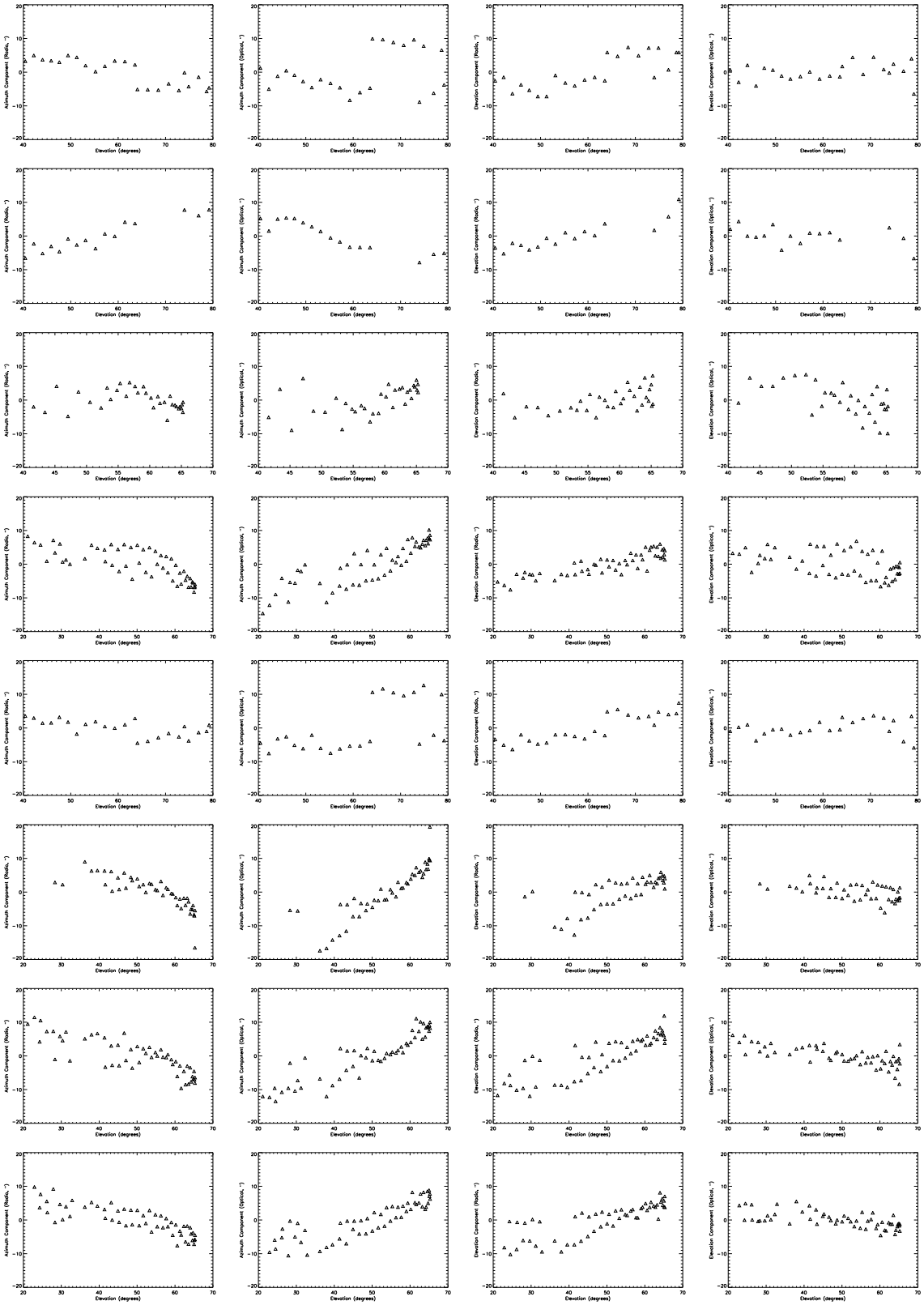

Figure 4.11 Similar to Figure 4.9 except for the 10-m antennas.

4.4.2.4 Benefits & Applications

Improvements to the pointing at levels below those obvious from variations in the gain are difficult to demonstrate. In this, the RMS calculations and comparisons above argue that the image fidelity will be improved by the smaller pointing changes. The most obvious test, however, is whether the gain stability is improved in actual observations.

There are two cases to discuss. The first is primarily applicable at night. If an antenna has a particularly bad mount model, the amplitude on a point source will evolve in time. This case is not as rare as it may seem. Thermal changes to the 6-m antennas can amplify tilt-like terms. So, if the ambient temperature has changed significantly since the pointing model was determined, it can degrade the 6-m pointing. However, if optical guiding is on, the evolution should be much weaker or absent. Figure 4.12 shows the amplitudes on C11 for the southern source 1625-254 taken at night during two sets of observations spaced by two days. The top panel shows a specific baseline where optical offset guiding was not on. These observations, done at 90 GHz, have a very tight amplitude trend but there is obvious decay with time. This decay cannot be from phase decoherence because the trend is seen on all baselines with this antenna and not on most other antennas. The lower panel shows 110 GHz observations. Here the evolution is completely absent with optical offset guiding on. The scatter about the line is somewhat larger than in the 90 GHz case but this is mostly attributable to the higher noise at this frequency. The peak-to-peak gain variations were reduced from 37% to 17%.

Figure 4.13 displays the corrections that were applied to the data in the bottom panel of Figure 4.12. The magnitude of the correction is about $0.4'$ over 70°, a gradient of $0.3''$ per degree. This example is at the high magnitude end of the range quoted in Table 4.1 for night-time observations, however, such large gradients are not uncommon on specific antennas. A change of $0.4'$ in a single 6-m antenna would result in a 10% drop in sensitivity for baselines including this antenna, assuming other baselines are perfectly pointed. The damage to image fidelity would be far greater.

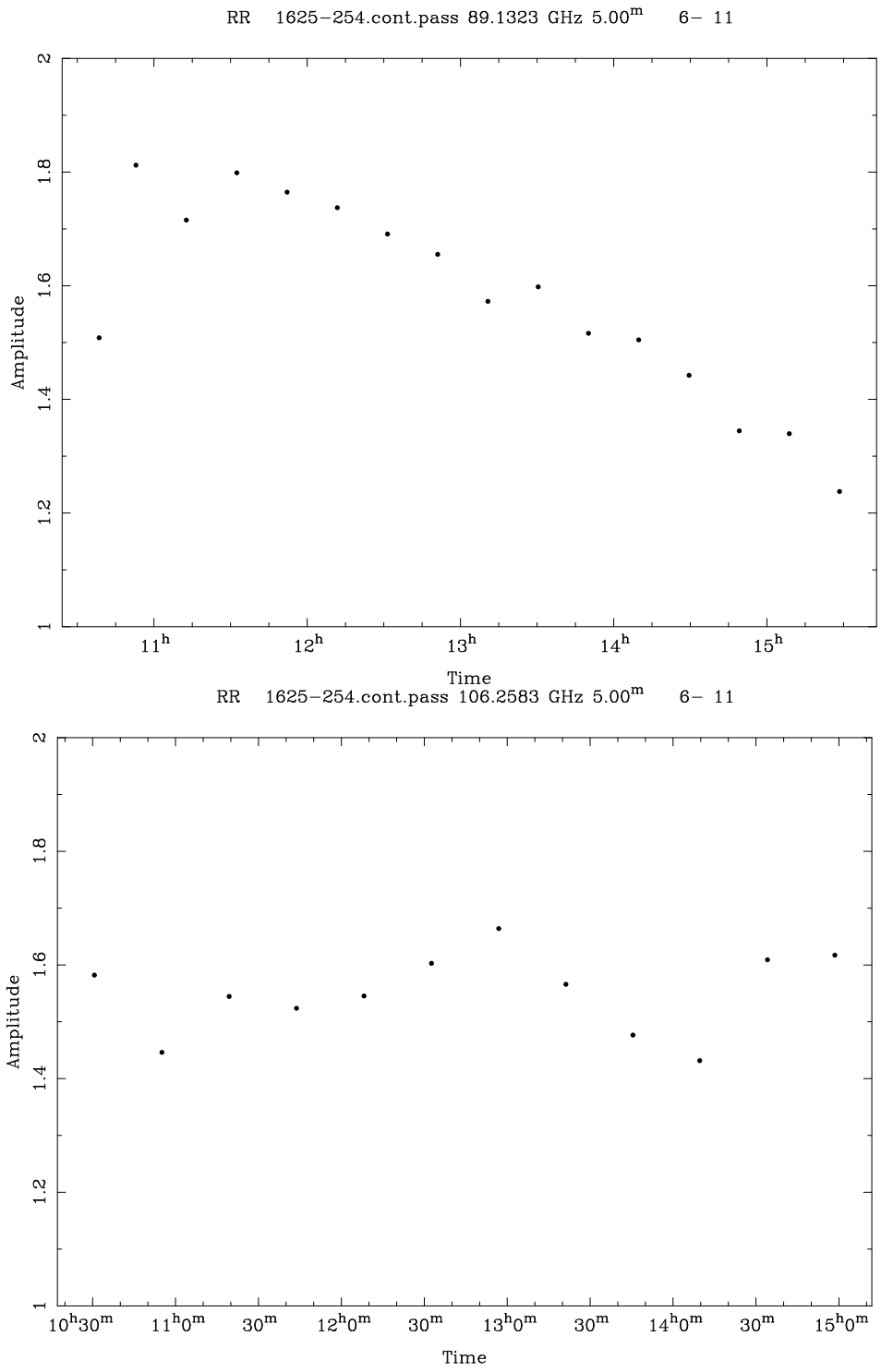

Figure 4.12 The top and bottom panels show amplitude (in Jy) versus time for a specific baseline of C11, an antenna whose mount model was corrupted by environmental effects since the last derivation of a new pointing model. The source is the same and the datasets are separated by two days. The top panel is a 90 GHz observation by Lommen et al. without optical offset guiding. The bottom panel is a 110 GHz observation by Andrews et al. with optical offset guiding.

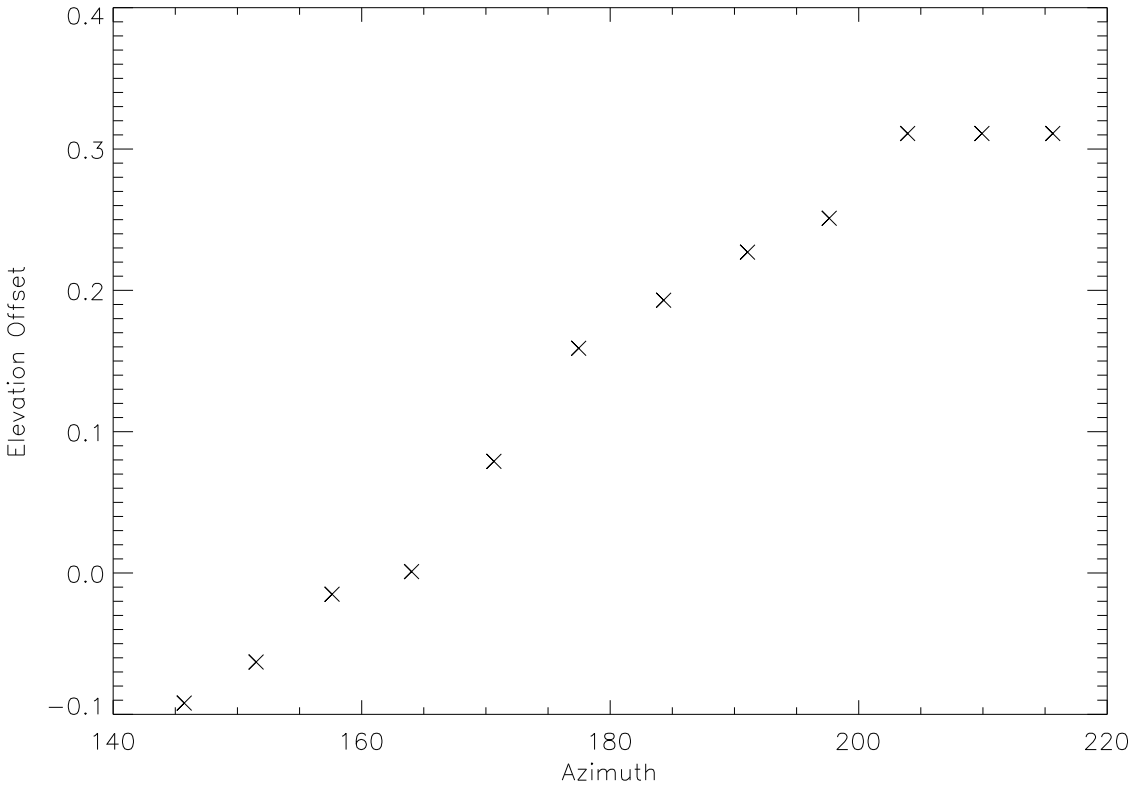

Figure 4.13 The offsets applied by the program *subOptical* are plotted in arcminutes against the azimuth of the calibrator. These offsets apply to the lower panel of Figure 4.12.

The second case involves the use of optical offset guiding by day, where the benefits are great. Instead of correcting pointing drifts on individual, particularly deviant antennas, corrections can be made for large scale thermal drifts on timescales which sample the change in pointing sufficiently fast as to keep pointing error low. The performance in the 1-mm band highlights the utility of this method because the beam is small.

A recent dataset, taken on June 12, 2008 by Maness et al., demonstrates the improvement to day-time pointing and sensitivity. The observation is set to observe a faint debris disk with a southern declination and begins at 4:59:50 PDT. The sun had not reached the horizon at this point. Default parameters are selected in the script, i.e. the PI simply included the parameter *doOptPoint* in their observing script and the remainder of the decision making process is internal. Initially, the very bright (10+ Jy at the time observation) source 3C454.3 was used to center the radio pointing. The nearby (2.75° separation) optical source HIP113963, V_{mag}=2.5, was automatically selected as a counterpart. The optical offset vector was successfully derived for all antennas.

By the time initial pointing, passband and flux calibration were complete, the sun had reached the horizon and the script logic successfully switched to selection of brighter optical counterparts when compared to night-time observations. The optical counterpart HIP003419 (V_{mag}=2) was selected for the gain calibrator 0006-063. The separation was 14.7°. Pointing updates were obtained every 26 minutes and approximately 2 minutes were required to calculate the pointing update and slew to the optical source.[3]

Figure 4.14 depicts the behavior of the changes in azimuth and elevation offset applied by *subOptical* (see Appendix C) over the course of the track. There is common behavior among antenna styles, so a single example of the 6- and 10-m antennas are shown. The trend is significant in both cases, although the changes in the 6-m antennas are more severe. The total change in pointing for the 10-m antennas is

[3]Due to improvements to the centroiding code installed on June 18, 2008, the 1.6 minutes required to centroid the star will be reduced by a factor of 2-3.

typically 10-15″ per axis, while the change per axis to the 6-m antennas is ∼40″. These changes occur over a period of 60-80° is azimuth or 4-5 hours in time. The gradient in pointing is then between 0.45-0.83″ per degree for the 6-m antennas and 0.13 to 0.25″ per degree for the 10-m antennas. This is well within the range of errors for which optical offset guiding will greatly benefit the observations.

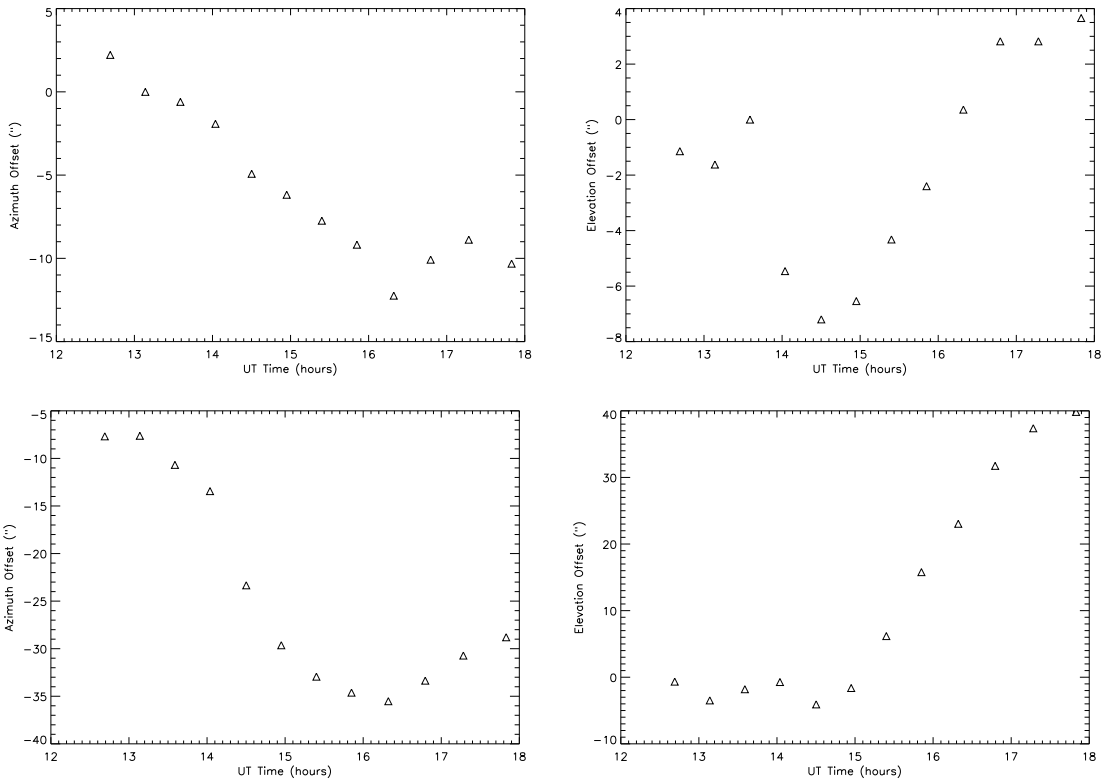

Figure 4.14 The offsets applied by the program *subOptical* are plotted in arcminutes against UT time. The top row shows the offsets for C1, although the magnitude of the change and the functional behavior is similar to other 10-m antennas. The left side shows the evolution of the azimuth offset. The right side shows the evolution of the elevation offset. The bottom row shows similar plots for C13. Again, the magnitude and functional form of the changes are typical among 6-m antennas.

Since the changes in pointing are common among all antennas of a given diameter, the offsets are treated as offsets in the power pattern, differently from above where loss of sensitivity was calculated assuming a single antenna in a baseline pair was offset from the nominal pointing position. The FWHM of the 10-m at λ=1.3 mm is

26″ while the 6-m antennas have FWHM of 44″. If no pointing corrections were done over the course of the track, the response of the 6-m antennas would have dropped to 3 to 17% of peak by the end of the observation. For the 10-m antennas, the behavior is less drastic but still significant. By the end of track, the calibrator amplitude would have dropped to 40-65% of the peak value. If pointing corrections were done every two hours as is advised for day-time, 1-mm band observations, the response could be increased to 40-60% for the 6-m antennas, i.e. the amplitude response would vary by a factor of two periodically over the observations. For the 10-m, these numbers are 10 to 20%. However, the overhead associated with the radio pointing is rather large and the reduced time on source would further reduce the relative sensitivities, i.e. the reduction in sensitivity for the entire track would be at least 50% for 6-m antennas and 15% for 10-m antennas, a significant detriment.

In the absence of optical offset guiding, the expected amplitude stability would be poor. These 1-mm band, day-time observations would have suffered significant loss of sensitivity and degradation to image fidelity (see Chapter 2). However, the amplitude stability in the presence of optical offset guiding is quite good. Figure 4.15 shows the calibrator data from the Maness et al. dataset. Given the absence of in-track radio pointing, the amplitude variations should be 50% for the 10-m antenna (top panel) and more than this factor of two drop for the 6-m antenna (bottom panel). However, the individual baselines shown in Figure 4.15 show remarkably little variation. Overall, the changes are random, not systematic, in contrast to the situation in the top panel of Figure 4.12. The amplitudes would have approached zero on the 6-m antennas by the end of the track in the absence of optical offset guiding. The RMS of these points is about ±7% in each case.

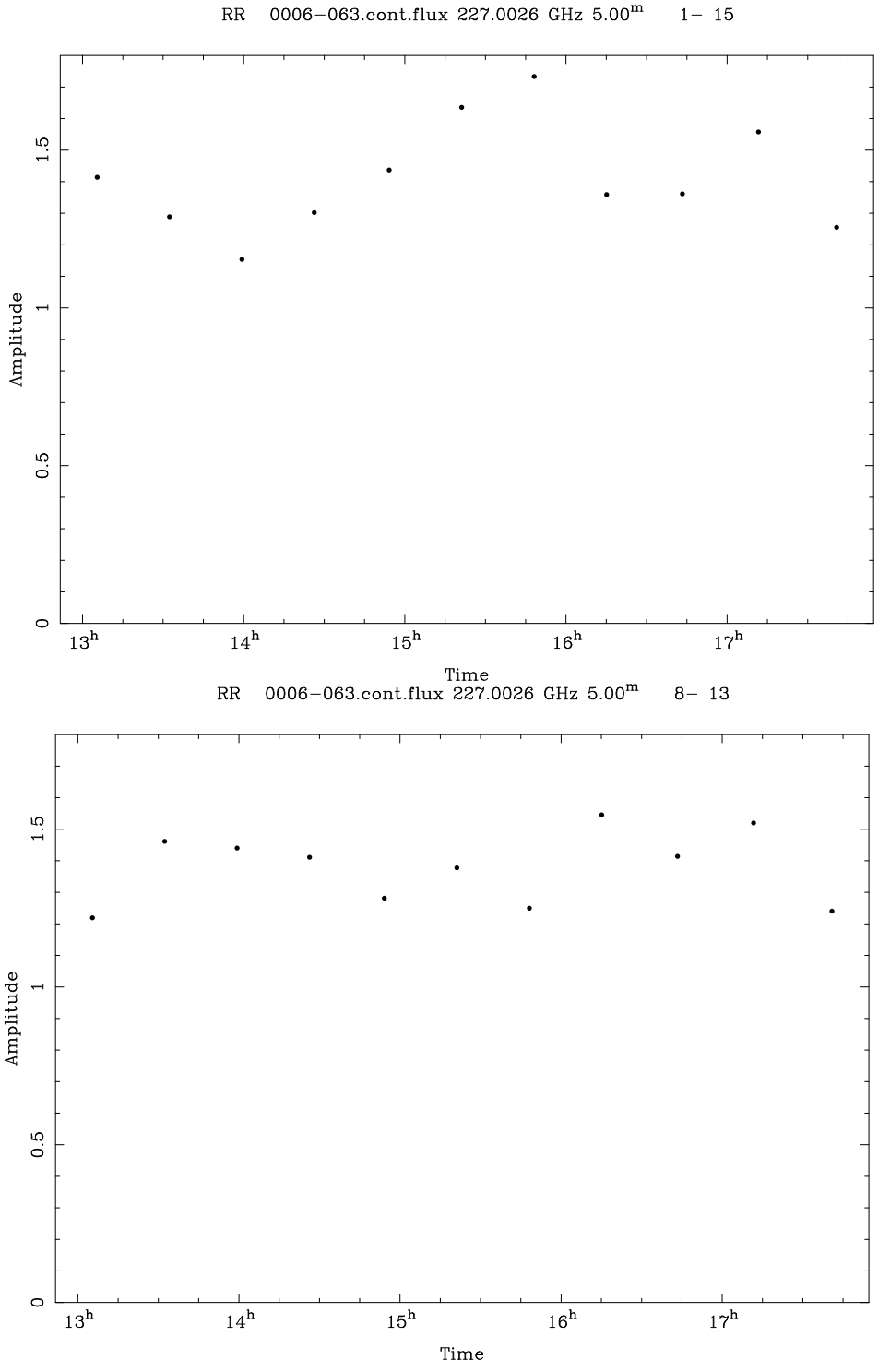

Figure 4.15 Two baselines of the Maness et al. dataset are shown. The top panel shows the amplitudes of 0006-063 plotted versus time for baseline 1-15. The bottom panel shows a similar plot for C8. Other antennas show comparable stability.

4.4.2.5 Limitations & Future Development

The most basic limitation of optical offset guiding is the presence of clouds. However, the failure modes of the software have been configured to make the impact of clouds minimal. An additional limitation comes when the target or calibrator in question is close to the sun. If the optical source is $\lesssim 30^\circ$ from the sun, the optical cameras often fail to find centroids even on very bright stars.

The method also assumes that the other independent terms in the radio and optical pointing model are perfectly determined. If the weather station improperly reports the humidity, pressure or temperature, the refraction is not properly calculated. Given that differential refraction between radio and optical wavelengths is on the order of $\sim 3''$ at 40° elevation, this could be a significant contribution; however, weather station failures are now incredibly rare. It is also not beyond the realm of possibility that the sag terms may, especially by day, evolve by values of $6''$ or more. If the sag terms differ in their degree of change, a differential change of this magnitude can result in a $4.25''$ difference at 45°. If the optical to radio offset is derived at a significantly different elevation than that at which the data will be collected, the offset vector will have an improper elevation component.[4] To combat this problem, the radio sag term must be determined with greater accuracy. This in turn requires increased speed of radio pointing measurements.

Systematics in the radio to optical offset vector remain, especially during the day and in the azimuth coordinate for the 10-m antennas. Most of the systematic effects in the optical to radio offset are likely functions of elevation. The minimization of such systematics, in the absence of detailed determinations of their source, can be done by simply deriving the optical to radio offset at an elevation consistent with the range over which most of the science data will be taken, i.e. 3C84 near transit should not be used to derive the offset when the data are to be obtained in the southern reaches of the Orion Molecular Cloud.

[4] It should be noted here that error in the elevation component at high elevation appears mostly in the azimuth coordinate and could explain many of the problems at high elevation. This is made clear by the realization that the azimuth components are divided by $\cos(el)$ which has a steep derivative at high elevations, i.e. the quantity $1/\cos(el) - 1/\cos(el + \delta el)$ can be quite large.

Given that the optical centroiding routines have been improved to include camera rotation and camera specific pixel scales, the speed of night-time optical centroiding has reached its maximum. Day-time use has been further improved by porting the centroiding routines to the antennas, i.e. the images are no longer sent over the network, only the centroid parameters are sent back. This allows 15 frames per second to be coadded. The current performance of the day-time centroids has not been well characterized in terms of speed. However, existing routines can be used to both characterize the performance and collect day-time pointing data. In the absence of new cameras, there is little chance of further improvement to the optical component of the optical offset guiding technique except that which would come from determination of the pointing model by day.

There is considerable room for improvement in the speed of radio pointing. Due to constraints on the data structures returned from the control system, radio pointing cannot be adaptive, i.e. a fixed integration time is required at each beam location and there is no mechanism for adding more integration time if that which was acquired proves insufficient. Once the control system can return structured visibilities, the speed of radio pointing can be improved greatly. In the presence of improved speed of radio pointing the measurements presented here should be repeated.

The systematics seen in R_{vec} above may be a result of the different pointing models by day. The improved function of the optical cameras by day should allow measurement of the day-time mount model and the day-time aperture corrections. The changes to the mount model terms are assumed constant across aperture, but this assumption is only known to be valid in the absence of significant thermal stress. It is possible that by day some of these terms are no longer common among apertures.

Improved sensitivity of the radio pointing measurement results in decreased distance to typical radio pointing sources. This will come with increased correlator bandwidth. This will simply reduce the benefits of optical offset guiding without comparable increases to the limiting magnitude of the optical cameras.

Finally, deeper optical imaging, especially during the day-time, could allow real-time application of pointing offsets as is done for guiders for optical/near-infrared

telescopes. The needed increase in depth is 5 magnitudes by night and 6-7 magnitudes by day for regular function. Since the greatest need for rapid pointing updates comes by day and the needed contrast is unlikely to be gained without significant improvement to the cameras and possibly the optical telescopes themselves, such real-time corrections are unlikely to be realized in the immediate future. However, the necessary limits at night have been achieved on a single 6-m antenna with an off-the-shelf, electronically cooled CCD camera (Swift, 2002).

4.5 Summary

In addition to reducing the typical pointing errors within the context of standard pointing at CARMA by a factor of two, I have designed and implemented the use of an optical pointing procedure to update the pointing of the antennas at CARMA within radio science observations. In the worst case scenario, the use of the routine may result in small degradation of the 10-m pointing by night. For the 6-m antennas and the 10-m antennas by day, the use of this capability usually results in significant decrease in systematic amplitude trends associated with pointing drift on timescales which are not currently accessible with regular radio pointing. Image fidelity will be enhanced in mosaiced observations and sensitivity will be increased, especially for 1-mm band observations. There remain a handful of basic approaches to further improve the method, most of which include measuring the pointing model by day. There is some hope that these measurements can help to reduce the residual systematics that currently represents the limit to the benefit of the method.

Bibliography

Corder, S. A. & Wright, M. C. H. 2006, CARMA Memo #34

Corder, S. A., Carpenter, J. M., & Wright, M. C. H. 2009, PASP, in preparation

Schubert, G. & Walterscheid, R. L. 2000 in *Allen's Astrophysical Quantities*, Editor A. N. Cox, p. 262

Swift, J. 2002, BIMA Memo #88

White, S. & Corder, S. A. 2007, CARMA Memo #40

Chapter 5

Applications: CARMA Mosaic Observations of Young, Massive Protostars in NGC 7538

Abstract

CARMA mosaic observations of a $2.5' \times 3.5'$ region in the nearby star-forming region NGC 7538 are presented here. The improved imaging capability has enabled the detection of infall signatures towards the central engines of the two most massive outflows in the region mapped, NGC 7538Sa and NGC 7538-IRS1, and several new outflows are also identified and characterized. Accretion rates are quite rapid for both the older, northern source, IRS1, and the younger, more embedded source, NGC 7538S, of the order 10^{-3} to $10^{-4}\,M_\odot$ yr^{-1}. For the first time, a complex of continuum clumps is resolved in the vicinity of NGC 7538S, suggesting that a cluster of stars is forming. Formation activity appears to be proceeding sequentially across the clump, due to a dynamical trigger from the northwest. Several of the young cluster members power outflows. Overall, the observations support earlier suggestions that mass accretion disks still exist around IRS1 and NGC 7538S, as expected in the monolithic collapse scenario for massive star formation.

5.1 Introduction

The births, lives and deaths of massive stars ($>8\,M_\odot$) impact the energetics, composition and visible to ultraviolet light production of the universe in fundamental ways. During their brief lives (10^{6-7} years), the ultra-violet, ionizing luminosity of these rare objects dominate over the luminosity output of all stars and generate ionization fronts and outflows that may trigger further star formation but can also disrupt a star-forming region completely. At the end of their lives, massive stars produce supernova which are visible at high redshift and allow distance determinations, produce the metals which eventually find their way into dust grains and pre-biotic molecules and may trigger additional waves of star formation (Kennicutt, 2005; Zinnecker & Yorke, 2007).

Nevertheless, the mechanism by which massive stars form remains poorly understood and has historically presented serious problems for theoretical models. Spherically symmetric collapse models indicate that radiation pressure terminates accretion at a stellar mass of about $\sim 40\,M_\odot$. This difficulty can be alleviated by invoking an accretion disk and envelope that redirect the stellar radiation field (Yorke & Bodenheimer, 1999; Krumholz, McKee, & Klein, 2005a). Rayleigh-Taylor or photon-bubble instabilities in the radiation/accreting mass boundary also allow enhanced accretion rates (e.g. Krumholz, Klein, & McKee, 2005b; Turner, Quataert, & Yorke, 2007). However, models still indicate a poorly constrained upper-limit ($\sim 100\,M_\odot$) that can be exceeded only by appeals to stellar coalescence (Zinnecker & Yorke, 2007, and references therein).

Recent debate has centered around three distinct models of massive star formation. The first, monolithic collapse of massive pre-stellar cores, follows the standard model of low-mass star formation (Yorke & Sonnhalter, 2002; Krumholz & Klein, 2007) and asserts that massive stars can form from the monolithic collapse of massive, prestellar cores. The second, competitive accretion (Bonnell et al., 1997; Bonnell & Bate, 2006), invokes Bondi-Hoyle accretion and expects that massive protostars will attract the necessary additional mass through an enhanced gravitational potential.

The final model relies on the coalescence of lower mass stars (e.g. Bonnell & Bate, 2005). Competitive accretion and coalescence require formation in clustered environments, while monolithic collapse allows for the possibility of truly isolated massive star formation. Competitive accretion and monolithic collapse require the presence of circumstellar or circumsystem disks to dissipate angular momentum and/or redirect the radiation field. Initially, the larger binary fraction for high-mass stars was used as evidence against monolithic collapse, but it has been shown that the collapse of a massive core will often lead to the formation of multiple systems (Krumholz et al., 2007).

Beyond these competing models, open questions remain at every step of early massive star evolution, be it the initial mass function of star forming clumps and cores,[1] or the infall, accretion, outflow, clustering, and feedback processes. Accretion rates onto massive stars are at best uncertain and appeals to estimates of infall rate from outflow rate are usually made. A better understanding of the relationship between outflow and infall is badly needed and could help calibrate the conversion factor between outflow mass and accretion rate (Tomisaka, 1998; Richer et al., 2000; Beuther et al., 2002).

This uncertainty in the conversion factor in part stems from the fact that the outflow ejection method is not well understood for high-mass stars, although recent simulations (Pudritz & Banerjee, 2005) and observations (Zhang et al., 2002; Beuther et al., 2004) suggest that the high-mass stellar outflows may be scaled up versions of the outflows from their low-mass counterparts. Indeed, Beuther & Shepherd (2005) suggest an evolutionary sequence for outflows from massive stars that explains the decrease in collimation (the ratio of length to width) with earlier and earlier spectral types. The sequence begins with the same outflow mechanism as for low-mass stars but includes the greater effect the central star has on the surrounding medium. It is clear, however, that the massive outflows cannot be driven by radiation pressure from the star because in general $L_*/c \ll \dot{M}_f v_f$, where L_* is the stellar luminosity, c

[1]Here and in what follows I utilize the following nomenclature. Clouds refer to entire complexes, i.e. Taurus, NGC 7538, etc. Clumps refer to the next level of substructure within the cloud. Clumps are further divided into cores which then contain protostellar objects and their envelopes and disks.

is the speed of light, $\dot{M}_f$ is the mass ejection rate of the outflow, and v_f is the outflow velocity (Churchwell, 2002). There is significant evidence that magnetic fields play a crucial role in determining the collimation factor of the outflow, but the detailed models of the jets which then entrain the material of the outflow are still varied with wind-driven shells, turbulent jets, and jet bow shocks all providing possible models. An additional possibility is that the molecular material is not entrained by the jet but it instead has its origin in disk material deflected towards the polar axis by the accretion process (Arce et al., 2007, and references therein).

Since infall signatures are rare even among low-mass protostars, it is not surprising that only a handful of definitive signatures of infall around massive stars have been reported (Ho & Haschick, 1986; Welch et al., 1987; Rudolph et al., 1990; Maxia, C. et al., 2001). Of these, several have been disputed leaving several subregions in W51 (Ho & Young, 1996; Zhang et al., 1998; Young et al., 1998; Zapata et al., 2008) and G10.62 (Keto et al., 1987, 1988) as the only regions with conclusive evidence. A variety of other possibilities have been identified (Wu & Evans, 2003). Details of the effect of massive star feedback on the natal cloud are also poorly understood. It is unclear if the associated outflows provide enough energy and couple sufficiently well to the surrounding cloud to drive cloud supersonic turbulence (Li & Nakamura, 2006; Banerjee et al., 2007). High resolution observations of outflows in clustered environments are required to constrain models of the process involved in this feedback.

Acquiring the necessary observations in massive star-forming regions is made difficult by several factors. First among these is that, despite their dominant role in producing ionizing radiation, high-mass stars are quite rare. From the initial mass function (IMF) $N(M) \propto M^{-\alpha}$ where α is $\sim$2.35 for stars more massive than about a solar mass (Salpeter, 1955), only 6% of stars are more massive than $4\,\mathrm{M}_\odot$. Early B to O stars represent less than 1% of all stars and only seven or eight groups are found within 500 pc. Of these, only two show evidence for recent and ongoing star formation. As a result, opportunities for high spatial resolution observations are limited compared to young, low-mass stars. In addition, the vast majority of massive stars form in binaries, higher-order multiple systems/clusters or unbound associations. If,

as has been suggested, a large fraction of the OB field star population is composed of ejected members of multiple systems, isolated massive star formation may be either rare or impossible (Zinnecker & Yorke, 2007, and references therein).

Due to the large distances of the appropriate star-forming regions, observations of such clustered star formation require high angular resolution. Additional complications arise because high-mass star-forming regions can emit radiation on angular scales ranging from point sources to the parsec sizes of entire clouds with fluxes from <0.01 Jy to >1 Jy. Extended emission often dominates and can often be recovered only by adding low resolution, single-dish data to high resolution array measurements to recover the largest angular scales. High fidelity and dynamic range, exceeding 300 in many cases,[2] are required to characterize substructure in the faint extended emission correctly and recover the flux of faint compact sources accurately. Scientifically, this translates into proper characterization of the properties of the outflow, the outflow-cloud interface, the infall signatures, and the star forming clump/core mass function in high-mass star forming regions.

Millimeter-wave array observations that are sensitive to gas and cold dust can provide the resolution needed to resolve structures down to the typical sizes of the fundamental unit in this case, the protostellar envelope scale (10,000 AU). Since many of the nearest active, massive star forming regions are at a distance of $\sim$2-3 kpc, resolutions of approximately 3-5$''$ are required, although higher resolution is required to definitively resolve individual protostellar envelopes. Measurements of the dynamics of any infall motion and outflow would also benefit from this resolution. As noted above, however, determination of the energetics and multiplicity of outflows or filaments and the interaction of the H II region and the cold cloud requires sensitivity to extended flux. These features can be large, spanning 1-2$'$ or more at these distances (e.g. Arce et al., 2007, and references therein) and the clouds as a whole can cover many square arcminutes or more.

Mosaiced array observations in the 1- or 3-mm continuum band and spectra of

[2]The value 300 is derived from 3×1 Jy/0.01 Jy, i.e. to see a 10 mJy source in the region of a 1 Jy source with 3σ confidence, the dynamic range must be at least 300

molecular lines with the addition of relevant single dish data are needed to satisfy the requirements outlined above. In this way, angular scales from an arcsecond to several arcminutes become accessible. However, the image fidelity and dynamic range required present a technical challenge. CARMA, with its unparalleled *uv*-coverage at millimeter wavelengths and the improvements to image fidelity described in Chapters 3 and 4 is ideal for these kinds of observations and provides a prime chance to disentangle the outflows and any infall while also resolving the individual cores. NGC 7538, where several epochs of star formation appear to be underway (Sandell & Sievers, 2004), is relatively nearby, 2.8 kpc (Crampton et al., 1978), and presents a excellent opportunity to test the CARMA capabilities. Each of the sub-regions within the main cloud may eventually form a group of stars rather than a single object assuming the dusty cores seen collapse to form stars. Two young stars show some evidence of infall.

CARMA mosaic imaging of an approximately 2.5′ by 3.5′ region centered on the two massive, young stars NGC 7538-IRS1 and NGC 7538S was therefore undertaken. Spectral lines HCO^+(1-0), ^{13}CO(1-0), $C^{18}O$(1-0) and ^{12}CO(1-0) along with 3.3 and 2.7 mm continuum emission were observed. Continuum and $C^{18}O$ observations trace the dense cores in dust and gas, respectively. The ^{13}CO and HCO^+ lines can reveal low velocity outflow emission in dense regions while ^{12}CO emission traces the high velocity components of the outflows. The HCO^+(1-0) transition, with its relatively high critical density, was also selected to trace any infall. The known structure and properties of NGC 7538 are discussed in §5.2. Data collection and reduction methods are described §5.3. In §5.4, the equations used to derive the properties of the outflows and dense cores are presented along with the resulting images and spectra. Discussion of these results is provided in §5.5, while §5.6 gives the conclusions.

5.2 NGC 7538

The massive star forming complex in the southern portion of NGC 7538 (also known as Sh2-158, G111.53+0.82; (α,δ)=(23:13:45.7,+61:28:21 J2000) is an ideal laboratory

for studying infall and outflows. The consensus distance is 2.8 kpc and is determined from the photometric properties of unobscured O stars in the area (Crampton et al., 1978). The uncertainty is rather large, 0.9 kpc (Blitz et al., 1982), and distances ranging from 2.2 kpc (Moreno & Chavarria, 1986) to 3.5 kpc (Israel et al., 1973) are found in the literature. The 2.8 kpc distance will be adopted here with the caveat that all quoted luminosities, and thus masses, can easily be in error by a factor of 70% while physical sizes are uncertain at the 30% level.

Figure 5.1 displays the entire region in 850 μm continuum emission (Sandell & Sievers, 2004). A cluster of massive stars excites an H II region (Schraml & Mezger, 1969) which appears to be impacting this dense molecular region, possibly exciting the star formation there (Martin, 1973). In the 850 μm image, the front is the northern boundary of the continuum emission.

Early infrared to radio studies of NGC 7538 revealed that there are several sites and possibly several epochs of star formation present in the regions south of the main H II region (Werner et al., 1979, and references therein). Since then, four regions of star formation associated with NGC 7538 have been identified. A north-central region can be seen in the 850 μm map of Figure 5.1, and includes the widely studied IRS1-3 (e.g. Keto et al., 2008); a south-central region encompasses NGC 7538S and IRS11 (Sandell & Sievers, 2004); an eastern region is associated with IRS9 (Sandell et al., 2005), and a less active western region contains IRS4-8. These regions are clearly identified in the 850 μm map of Figure 5.1. Observations described here focus on the regions surrounding the IRS1-3 and NGC 7538S complexes and Table 5.1 summarizes their properties.

5.2.1 IRS1-3

The IRS1 star-forming complex has been observed extensively from the near-infrared to the radio, and appears to power an ultracompact H II (UCH II) region with luminosity $1.5\times10^5\,L_\odot$, implying that it is rather young (Thronson & Harper, 1979; Werner et al., 1979; Sandell & Sievers, 2004). The continuum morphology is com-

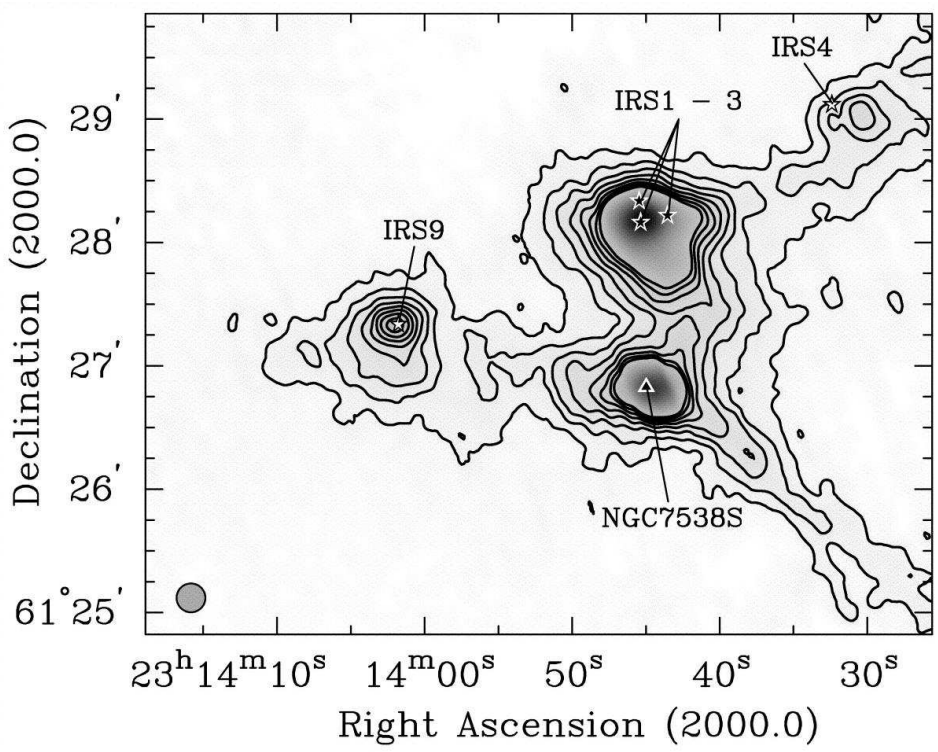

Figure 5.1 NGC 7538 is shown in submillimeter continuum emission (Sandell & Sievers, 2004). The sources IRS1, NGC 7538S, IRS9, and IRS4 are directly labeled on the image.

Table 5.1. Properties of Young Stars Associated with IRS1-3 and NGC 7538S Complexes

Property	IRS1	IRS2	IRS3	NGC 7538S	NGC 7538Sa	NGC 7538Sb	NGC 7538Sf	References[c]
$\Delta\alpha$ ($''$)[a]	2.7	3.05	-9.7	-2.3	0.16	-2.0	-6.6	0
$\Delta\delta$ ($''$)[a]	40.4	49.81	42.2	-41.1	-40.37	-41.7	-39.97	0
$V_{systemic}$ (km s^{-1})	-58.4?	U	U	-56.0	-56.3	-56.0	-59.4/-55.4?	1,U,U,2,0,2,0
Spectral Type	B0-O9?	B0-O9	B2	NA	U	U	U	3,3,3,NA,U,U,U
L_{bol} (10^4 $L_\odot$)	5-20	4-5	0.7-1	1.8?	U	U	U	4/5/6,6,6,7,U,U,U
Mass ($M_\odot$)[c]	20-30?	20?	10?	NA	U	U	U	3,3,3,NA,U,U,U
β_{dust}	U	U	U	1.8-2	1.0	2+?	1-2?	U,U,U,0+4,0,0+4,0
$T_{dust/core}$ (K)	20	U	U	25	30?	25?	30?	8,U,U,8,0+4,0+4,0+4
$T_{outflow}$(K)	100?	NA	NA	100?	100?	100?	100?	9,NA,NA,9,9,9,9

[a]Offsets are relative to the mosaic center at (α,δ)=(23:13:45.00,+61:27:30).

[b]Mass described here is the inferred mass of the protostar.

[c]A single reference indicates all information was derived from a single work, otherwise a reference per source is indicated. References: 0: this work, 1: Henkel et al. 1987, 2: Sandell, Wright & Goss, submitted, 3: Schmidt-Kaler 1982, 4: Sandell & Sievers 2004, 5: Werner et al. 1979, 6: Campbell & Thompson 1984, 7: Thronson & Harper, 1979, 8: Zheng et al. 2001, 9: Sandell, private communication

Note. — V_{lsr} for the observations was set to -56.0 km s^{-1}. A $\kappa_{1.3\,mm}$ of 1 cm^2 g^{-1} and a gas to dust mass ratio of 100 are assumed for all sources. Fields with U indicate that the quantity is unknown. IRS11 is not included in this table because no millimeter emission was found for this source in this study. Poorly known values are marked with the value and a ?. Certain parameters have no meaning for a particular source and these are denoted with NA. Values for other cores in NGC 7538S are taken as the values of the cloud.

plex, breaking into two lobes separated by 0.2-0.4″ with further structure present on even smaller scales (Gaume et al., 1995; Campbell, 1984). The pinched shape of the free-free lobes has led to speculation that a massive accretion disk is present. Radio recombination lines indicate an equally complex dynamical structure, including an outflow, circumstellar disk and wind (e.g. Keto et al., 2008; Gaume et al., 1995, and references therein). Maser emission from OH and H_2O (Downes, 1970; Kameya et al., 1990; Argon et al., 2000; Sandell et al., 2009), CH_3CN (e.g. Pestalozzi et al., 2004, 2006; Minier et al., 2000, 2001), H_2CO (Rots et al., 1981), and NH_3 (Johnston et al., 1989) is also associated with this source. CS (Kawabe et al., 1992) and methanol masers (Minier et al., 2000; Pestalozzi et al., 2004, 2006) have been used to model the dynamics of the region with a disk but these are possibly confused with the ambient cloud and outflow, respectively. The systematic velocity of IRS1 is thought to be -58 km s^{-1} (Sandell, private communication), although this value is uncertain due to confusion with outflowing, infalling and unassociated emission (e.g. Wilson et al., 1983).

Near-infrared imaging (Wynn-Williams et al., 1974; Werner et al., 1979; Ojha et al., 2004) and spectral (e.g. Gibb et al., 2004; Willner, 1976) studies of IRS1-3 date from the 1970's. Speckle interferometry reveals a complicated inner morphology with evidence for a processing outflow (Kraus et al., 2006) similar to that seen in the protostars IRAS04239+2436 (low-mass, Arce & Goodman, 2001) and IRAS 20126+4104 (high-mass, Cesaroni et al., 2005). Narrow-band imaging and spectra have revealed the presence of a variety of shocks near IRS1 and the surrounding filaments (Davis et al., 1998).

The (sub)millimeter continuum emission in the vicinity of the source has been mapped over wide-fields with modest resolution ($\geq$8″ Sandell & Sievers, 2004; Reid & Wilson, 2005), but this is insufficient to disentangle the complex source morphology known to exist at lower frequencies. Recent, 1.3 mm observations reveal an extremely compact source which is dominated by free-free emission, however, the flux is low compared to other, millimeter flux estimates (Keto et al., 2008; Akabane et al., 2001). A spectral index of $\sim$1 persists over too wide a frequency range to be explained by

simple passage from optical thick to thin free-free emission plus dust emission, but the exact interpretation of the behavior is varied (e.g. Henkel et al., 1984; Woody et al., 1989; Reynolds, 1986; Keto et al., 2008; Lugo et al., 2004; Akabane et al., 1992; Wood & Churchwell, 1989). However, the increase in flux at short submillimeter wavelengths is certainly consistent with strong thermal dust emission surrounding IRS1 (Sandell & Sievers, 2004)

It is likely that IRS1 powers one or two molecular outflows (Scoville et al., 1986; Dickel et al., 1981; Kameya et al., 1989) and may still be accreting material. Variability of the continuum flux at 2 and 6 cm indicates that the accretion may be variable (Franco-Hernández & Rodríguez, 2004). Based on observations of self-absorbed molecular line profiles, there is some suggestion of large-scale infall (Zhang et al., 2005; Wilson et al., 1983; Henkel et al., 1987; Xu et al., 2003). High-resolution, high-fidelity imaging over the $4''^2$ region is critically needed to disentangle the various components.

About $10''$ north of IRS1 is IRS2. This source was resolved in early observations and is subject to less detailed analysis because it is less active (Martin, 1973). IRS3 is located about $12''$ west of IRS1 and is also much less active than IRS1. Both of these sources power well-resolved H II regions that are dominated by free-free emission in the millimeter regime.

5.2.2 NGC 7538S

The dense region immediately adjacent to IRS11, NGC 7538S, was identified in early studies (Werner et al., 1979) and is thought to contain at least one heavily embedded, massive protostar based on the bolometric luminosity. It contains a very faint infrared counterpart, suggesting it is a younger counterpart to IRS1 (Sandell et al., 2003; Sandell & Sievers, 2004). This embedded object may harbor a massive circumstellar disk (Sandell et al., 2003, 2008), although there is substantial debate as to whether this is a circumstellar disk or a circumstellar torus (see, e.g. Cesaroni et al., 2007). The rotation curve of the presumed disk yields an enclosed mass of $40\,M_\odot$ but this is the mass of the disk plus star and the exact stellar mass cannot be easily determined.

The NGC 7538S clump is the brightest submillimeter source in the entire southern portion of NGC 7538 and has been studied predominately at $\sim 8''$ resolution (Sandell & Sievers, 2004; Reid & Wilson, 2005). Several maser sources are associated with the clump and the surrounding area (Kameya et al., 1990; Pestalozzi et al., 2006). The systemic velocity of the source is thought to be -56 km s^{-1} (Sandell et al., 2008). Far higher resolution is needed to determine the structure of this dense clump, while the location of NGC 7538S, $\sim 80''$ south of IRS1, requires high fidelity and dynamic range.

5.2.3 The Cloud

Filaments of dust and gas extend between IRS4 to IRS1-3, the two older regions, and from IRS9 in the direction of NGC 7538S, the two younger regions (Zheng et al., 2001; Sandell & Sievers, 2004; Reid & Wilson, 2005). These filaments do not completely link the sites of star-formation but visually suggest a connection. Morphologically, the filament connecting IRS1-3 and IRS4 appears to be related to the expanding, NGC 7538 H II region. An additional filament is seen extending away from NGC 7538S to the southeast. The main velocity component of the cloud peaks between -58 and -56 km s^{-1}, depending on position within the overall cloud. However, single dish spectra in the CO(2-1) line show that there is a secondary velocity component occurring at 49 km s^{-1}, suggesting the presence of a second cloud (Sandell, private communication).

5.3 Observations and Data Reduction

5.3.1 Interferometric Observations

All interferometric observations of NGC 7538 made at CARMA were taken during the calendar year 2007. CARMA is a 15 element, heterogeneous (six 10.4 m and nine 6.1 m diameter antennas) millimeter interferometer located at Cedar Flat (elevation 2200 m) in the Inyo Mountains of California. The array operates at 85-116 GHz

(the 3-mm band) and 215-270 GHz (the 1-mm band). At the time of observation, the SIS receivers were single polarization with IF spanning from either 1-4.5 GHz (10.4-m antennas) or 1.1-2.4 GHz (6.1-m antennas). Three tunable modules are provided to allow either wide-band (15-31.25 MHz channels), continuum observations of 468.75 MHz bandwidth or 63 channel spectral observations with per channel widths of 0.977, 0.488, 0.122, or 0.0305 MHz. These modes are nominally referred to as 62, 31, 8 and 2 MHz modes, respectively, reflecting the approximate integrated bandwidth.

Observations of the HCO^+(1-0), ^{12}CO(1-0), ^{13}CO(1-0), and $C^{18}O$(1-0) transitions were made of NGC 7538-IRS1, NGC 7538S, and surrounding regions. Simultaneous, single module, continuum observations provided measurement of the continuum flux. The ^{12}CO and HCO^+ observations each used a 32 MHz bandwidth module providing velocity resolutions of 1.641 and 1.270 km s^{-1} and coverages of 101 and 79 km s^{-1}, respectively. All spectral lines were observed in an 8 MHz mode, providing 0.410, 0.333, 0.332, and 0.317 km s^{-1} velocity resolution for HCO^+, ^{13}CO, $C^{18}O$, and ^{12}CO, respectively, with ^{13}CO and $C^{18}O$ being observed simultaneously. The velocity coverage in these high resolution modules ranges from 25 to 20 km s^{-1}. Table 5.2 summarizes the typical properties of datasets used in the production of the continuum images and spectral cubes.

Table 5.2. NGC 7538 Data Sets

Date	Line	Config	SSB Tsys 6-m/10-m	Pointing	Peak to Peak Amp Scatter %	0019+734 Flux Jy	Flux Cal	0102+584 FWHM ″	Measured/Theoretical RMS Continuum mJy
2007nov23	HCO+	B	145/250	Radio	16	1.512	Uranus	0.26	10.1/2.3
2007nov24	HCO+	B	140/220	Optical	7	1.512	None	0.13	11.2/4.5
2007nov29	HCO+	B	140/240	Optical	8	1.522	Uranus	0.33	9.8/2.0
2007jan16	HCO+	C	125/220	Mixed	9	1.996	None	0.14	9.3/10.8
2007feb18	HCO+	C	300/400	Radio	18	1.995	Uranus	0.44	16.7/16.3
2007mar22	HCO+	C	150/300	Radio	11	1.865	Uranus	0.68	17.3/11.9
2007apr05	HCO+	C	170/280	Radio	15	1.748	Uranus	0.56	18.7/15.5
2007nov01	HCO+	C	170/280	Optical	8	1.585	Uranus	0.44	8.3/4.9
2007jun02	HCO+	D	200/270	Radio	9	1.364	MWC349	1.08	8.5/4.8
2007jul19	HCO+	D	140/275	Optical	4	1.346	MWC349	1.25	14.3/10.0
2007jul28	HCO+	D	275/350	Radio	8	1.355	Mars	0.91	12.6/10.1
2007aug11	HCO+	E	140/265	Optical	5	1.30	None[a]	Neg	16.9/6.1
2007aug12	HCO+	E	135/240	Optical	5	1.30	None[a]	1.33	17.2/5.4
2007dec01	13CO	B	180/220	Mixed	11	1.276	Uranus	0.39	26.7/1.1
2007dec10	13CO	B	170/240	Optical	7	1.246	Uranus	0.10	13.3/1.7
2007dec13	13CO	B	160/250	Optical	15	1.332	Uranus	0.12	15.4/1.4
2007mar10	13CO	C	180/240	Radio	16	1.777	Neptune	0.85	35.9/12.7
2007oct21	13CO	C	170/250	Optical	8	1.520	Uranus	0.73	49.1/12.4
2007oct28	13CO	C	350/450	Mixed	13	1.426	Uranus	0.48	17.6/9.5
2007nov02	13CO	C	200/280	Radio	15	1.528	Uranus	0.83	27.2/8.2
2008may17	13CO	C	180/210	Optical	10	0.978	Uranus	0.38	20.1/1.3
2007jun08	13CO	D	200/240	Mixed	7	1.325	MWC349	0.22	13.5/10.8
2007jun18	13CO	D	200/275	Optical	5	1.680	MWC349	0.50	14.2/9.4

Table 5.2 (cont'd)

Date	Line	Config	SSB Tsys 6-m/10-m	Pointing	Peak to Peak Amp Scatter %	0019+734 Flux Jy	Flux Cal	0102+584 FWHM ″	Measured/Theoretical RMS Continuum mJy
2007jul27	13CO	D	340/450	Radio	8	1.304	Mars	0.90	15.7/10.1
2007aug15	13CO	E	300/350	Optical	8	1.242	Mars	0.71	16.8/7.8
2007aug25	13CO	E	250/400	Radio	7	1.292	Mars	0.77	17.3/8.7
2007sep10a	13CO	E	250/320	Optical	7	1.284	Mars	1.10	15.1/8.1
2007sep10b	13CO	E	300/350	Optical	8	1.284	None	0.32	15.9/10.8
2007sep11	13CO	E	280/330	Optical	9	1.284	None	0.10	14.7/7.3
2007oct23	12CO	C	400/500	Optical	12	1.412	Uranus	0.23	13.8/7.4
2007nov03	12CO	C	350/450	Optical	10	1.418	Uranus	0.28	20.8/8.9
2007nov10	12CO	C	350/450	Optical	17	1.362	Uranus	0.57	21.1/9.8
2007jun10	12CO	D	400/500	Radio	15	1.28	None[a]	0.72	26.4/9.6
2007jul26	12CO	D	550/650	None[b]	25	1.326	Mars	0.55	13.1/9.1
2007sep02	12CO	E	550/650	Radio	14	1.360	Neptune	0.85	17.0/11.7
2007sep03	12CO	E	550/650	Optical	13	1.360	None	0.24	16.6/12.4

[a]Flux was determined from an observation separated by less than 5 days but at a different frequency. The regularity of the data collection allows an estimate of the frequency scaling, 0.4% per GHz, which has been included here.

[b]No pointing of any kind was available.

Note. — B array and 2008 data contains only two pointing positions. The precision in the flux estimate reflects the statistical uncertainty in the measured flux, which is typically ±0.01 Jy.

All continuum observations and all spectral lines with the exception of ^{12}CO(1-0) were made in E, D, C and B arrays, which span baselines from 8 to 800 m, two orders of magnitude in spatial dynamic range. ^{12}CO(1-0) observations did not include B array and have a maximum baseline of 350 m. Observations of the quasar 0019+734, made every 10-25 minutes depending on configuration, were used to calibrate instrumental phase and amplitude gains. Quasar 0102+584 was also often observed to assess the quality of the resulting data and determine the typical seeing disk. Due to the northern declination of NGC 7538, observations were made over a variety of hour angles resulting in a combination of passband calibrators. Quasars 3C84, 3C454.3, 1751+096, BLLac, and 0102+584 were used at various times for this purpose. Mars, Neptune, Uranus, and MWC 349 were used as flux calibration sources as appropriate.

B-array observations were limited to two single pointings roughly centered on IRS1 and NGC 7538S. Other configuration observations consisted of four right ascension pointings by seven declination pointings, Nyquist-sampled at the 2-dimensional rate for the 10-m antennas. The mosaic was centered on (α,δ)=(23:13:45.00,+61:27:30 J2000), approximately halfway between IRS1 and NGC 7538S. The entire mosaic was typically visited once in a gain calibrator cycle to limit overhead. The *uv*-samples for individual pointings were filled in by repeated observations in the same configuration for a given spectral line. In B-array observations the two positions were alternated every 2.5 minutes. The mosaic does not include the areas of IRS4 or IRS9. When possible, the observations utilized optical offset guiding (see Chapter 4). Some tracks without guiding are included because most data taken in some configurations and/or lines were during the summer. Daytime optical guiding was made available near the end of these observations.

All data flagging, reduction and imaging were performed using MIRIAD (Sault, Teuben, & Wright, 1995). At present, there is no standard pipeline for calibration of CARMA narrow band data and the details of the general calibration are described in Appendix E.

5.3.2 Single-dish Observations

The observations were carried out on November 9, 2004 by Dr. Mark Heyer on behalf of Dr. G. Sandell with the 14-m Five College Radio Astronomy Observatory (FCRAO) telescope using the SEQUOIA 16 beam array receiver. Typical system temperatures were $T_{sys} \sim 120\,K$. They used the dual channel correlator (DCC) with a 50 MHz bandwidth and a spectral resolution of 48.8 kHz (0.16 km s^{-1}). The DCC was configured to simultaneously cover $H^{13}CN$(J=1-0) and HCO^+(1-0). At 86 and 89 GHz the half-power beam width (HPBW) is 58″ and 57″, respectively, while the main-beam efficiency, $\eta_{mb} \sim 0.50$. The observations were performed using on-the-fly (OTF) mapping, covering a $9' \times 9'$ area centered at (α,δ)= (23:13:45.4,+61:28:10.5 J2000), and covering the whole molecular cloud associated with NGC 7538. For further information regarding the single-dish data, see Sandell et al. (2008).

5.3.3 Imaging

5.3.3.1 Continuum Imaging

Imaging was carried out in several steps. The initial, dirty maps of each continuum dataset were constructed using the standard MIRIAD task **invert**. MIRIAD was allowed to select the cell size, which is typically a factor of three smaller than the resolution of the dirty map assuming uniform weighting. The value of **imsize** was selected so that the pixels sizes multiplied by the number of pixels was at least as large as the width of the 6-m antenna primary beam pattern at the 5% level.[3] Sidelobes were suppressed, in a least-squares sense, over a region approximately equal to twice the pointing sampling size, or 65″. The **robust** parameter was then used to tune the image resolution to values near 7.0, 4.5, 2.8, 2.2, and 1.25″. In addition to the weightings associated with sidelobe suppression (**sup**) and robust, the visibilities were also weighted by system temperature. Finally, the option **mosaic** was selected to interpret different pointing offsets as different phase centers. The line parameter

[3]MIRIAD pads the FFT in invert to the next largest $2^n + 1$ so the exact value is irrelevant.

was set to 30 channels and multi-frequency synthesis was used. This minimizes the effects of bandwidth smearing.

Initially, an estimate of the size and flux of the continuum emission from IRS1 was needed to both characterize the flux of IRS1 and to subtract the emission from the map. This was accomplished by using the MIRIAD task **mossdi** applied over a small region centered on IRS1. Due to the variable *uv*-coverage across the image, the point-spread-function (PSF) can vary with position. The task **mospsf** was used to estimate the average point-spread-function. The resulting PSF file was fit with a Gaussian of peak 1 and zero positional offset to determine the image resolution. Finally, the routine **restor** was used to convolve the clean components from **mossdi** and add them to the residuals from the cleaning process. Fits to the size and flux of IRS1 were done in the resulting images. In the end, the robust parameters yielding higher-resolution images were used to resolve-out the contribution from the extended emission known to be associated with IRS2.

IRS1 dominates the dynamic range in the resulting images and has a flux of 1.4 Jy or more at the wavelengths in question. Given the final maps should have an RMS in the neighborhood of the theoretical value, $\sim$3 mJy, the required dynamic range is on the order of 500. The goal is then to subtract the contribution from IRS1 using traditional methods and then compare the results to those using the method described in Chapter 2. Appendix F provides the script for using the measured voltage patterns. An additional motivation for this step is that IRS1 is rather compact while the remaining structures either in continuum or spectral lines appear to be extended. Compact sources are in the purview of the clean algorithm while the extended emission is best addressed using maximum entropy methods. Given I have limited numbers of point-like sources, it is advisable to remove the point sources first and then deconvolve the dirty images using maximum entropy methods.

Subtraction of the compact source was done in one of two ways. The quicker, but less accurate approach, utilizes the MIRIAD routines **demos** and **uvmodel**. In this case a model of IRS1 and the relevant *uv*-dataset to be compact source subtracted is fed to a Python wrapper to these MIRIAD routines. The Python code determines the

pointing centers by parsing the output of **uvindex**, determines the pointing centers and then uses **demos** to deconstruct the model into a similar mosaic pattern. If the model is truly point-like, the now primary beam attenuated model images are searched for the peak and offset relative to the observing center and then the call to **uvmodel** uses this flux and offset position. If the model is reasonably well resolved on the pixel scale of the model, the **demos**, primary beam modified image is fed directly to **uvmodel**. The calls to **uvmodel** are made using the option **subtract** which uses the input visibility file to determine what its response to the model would be and then subtracts this from the visibilities actually present in the visibility dataset. Only visibilities for the specific pointing are allowed to be used in the model (using the option **selradec**). A line argument is provided to **uvmodel** so that the output dataset will retain the spectral characteristics of the input visibility dataset and not the image model.

The second approach uses the visibility dataset to determine the pointings and hour angle coverage of the dataset. The program then proceeds to divide the hour angle coverage into a user defined bins. The provided model is then illuminated on a baseline by baseline basis similar to the simulations of Chapter 2, taking into account the parallactic angle. Again, the relevant visibilities are subtracted from the input dataset. In the end, the resulting visibilities are concatenated. The result should be an observation free of the compact source and free of artifacts associated with primary beam patterns (see Appendix F for details).

After the visibilities associated with IRS1 were subtracted from the continuum data, new images were constructed.[4] The reconstruction of the continuum images was necessary to obtain estimates of the continuum fluxes associated with the remaining sources, determine the quality of the visibility subtraction, and provide continuum images to subtract from the spectral line data cubes. These continuum images were then deconvolved, using **mossdi**, over small regions centered on IRS2 and NGC 7538S.

[4]The model used for IRS1 is discussed in §5.4.5.1. It is marginally resolved in the B-array data. In pointings far separated from the location of IRS1, imaging far out in the beam reveals IRS1 to be a double source. This is almost certainly a software bug. Given pointings near the source dominate the resulting morphology, this error, while intriguing, has little effect on the final image.

A template image of the entire region was made using only a single clean iteration. The regions associated with IRS2 and NGC 7538S were cleaned with 3000 iterations independently. The independent regions were then gridded onto the template image using the MIRIAD task **regrid**. The resulting clean component images were added together and then restored using **restor** to the resolution determined by Gaussian fits to the output of **mospsf**. This complicated method was required to deconvolve the two regions to different flux limits, a situation required to handle the variable sensitivity across the map due to the artifacts associated with IRS1.[5]

After the images were constructed using **restor**, final continuum images were generated by an additional convolution with a Gaussian determined so that the resulting image would have resolutions of exactly 7.0, 4.5 and 2.8″ for images without B-array and 2.2 and 1.25″ for images with B-array data. This put all data on a common scale. The images were then regrided onto a pixel scale which was consistent.[6]

5.3.3.2 Spectral Line Imaging

The model of IRS1 was subtracted from the *uv*-plane in the spectral line datasets in a manner similar to that described above. The dirty maps were constructed as above except that for the spectral line data, which were not imaged with multi-frequency-synthesis, had a line argument which provided either 57 or 63 spectral channels. The robust parameter was then selected to provide dirty maps with approximate resolutions of 7.0″, 4.5″, and 2.8″ for maps excluding B-array data. The parameter was tuned to obtain resolutions of approximately 2.2″ and 1.25″ when B-array was included. The resolution was obtained as described above.

The resulting spectral images were free of significant point-like features and image deconvolution was accomplished by maximum entropy methods. These generally

[5]The **restor** program takes the model, either the output of **mossdi** or **mosmem**, and convolves it by both the dirty beam and the clean beam, i.e. the provided FWHM Gaussian. The original map then has the model times the dirty beam subtracted and then the model times the clean beam added back in.

[6]This consistency was enforced among all datasets with B-array data and among all datasets without B-array data. Given the difference in on-the-sky size of the images, regriding the images without B-array data to the B-array image scale would have resulted in inhibitively large images.

converged after 100-200 iterations on the entire field and required 0.5-2 days per spectral line image to converge to the appropriate noise levels, depending on the resolution and size of the field. The routine **mosmem** was used with 300 iterations per spectral plane, although the image converged to the nominal noise level in fewer than 300. As was the case with the continuum images, **restor** was used along with a subsequent convolution with an additional Gaussian to provide a final resolution of 7.0, 4.5, 2.8, 2.2 or 1.25″. The images were then put onto a common pixel scale, using **regrid**, and the relevant continuum data, depending on frequency, were appended to the spectral line cubes using the task **imcat**. The task **avmaths** was then used to subtract the values of the last plane, now the continuum data, from the spectral line data. The last plane was then discarded.

The only remaining image manipulation required is the addition of the single-dish data to the now continuum-free HCO^+(1-0) data. The single-dish, OTF map discussed above was rescaled to the pixel and velocity scale of the CARMA HCO^+(1-0) image and then the single-dish and interferometer data were combined using the MIRIAD task **immerge**. The relative flux scale is determined internally by Fourier transforming the two datasets and plotting the flux on the overlapping spatial scales, 8.5 to 12 m in the case of CARMA+FCRAO data, and channels with significant flux. The FCRAO image needed to be multiplied by 0.8 to match the flux of the CARMA data over comparable scales. The resulting images are merged in the Fourier plane and reimaged with the resolution of the input interferometric dataset.

At this point, all of the spectral line data are free of continuum emission and the available single-dish data have been combined with the interferometric observations. The range of spatial scales sampled is similar for all CO lines. Table 5.3 describes the resulting maps in terms of spatial resolution, velocity resolution, map RMS and map peak flux. In the higher spectral resolution maps, it is sometimes difficult to find channels in the CO cubes which do not have flux and the resulting RMS estimates are likely to be higher than the true noise level.

The CO data may have further limits beyond the quoted noise levels. Despite my utilization of E-array, a compact configuration that contains several baselines down

Table 5.3. NGC 7538 Images

Line	Resolution Angular $''$	Resolution Velocity km s^{-1}	RMS Jy beam^{-1}	Peak Jy beam^{-1}
HCO+	7.0	1.641	0.030	4.254
HCO+	7.0	0.410	0.064	5.005
HCO+	4.5	1.641	0.032	2.230
HCO+	4.5	0.410	0.065	2.533
HCO+	2.2	1.641	0.022	0.835
HCO+	2.2	0.410	0.026	0.377
HCO+	1.25	1.641	0.050	1.044
HCO+	1.25	0.410	0.055	0.568
13CO	7.0	0.332	0.157	9.362
13CO	4.5	0.332	0.123	5.700
13CO	2.2	0.332	0.112	1.672
13CO	1.25	0.332	0.118	0.850
C18O	7.0	0.333	0.110	2.222
C18O	4.5	0.333	0.127	1.359
C18O	2.2	0.333	0.080	0.602
C18O	1.25	0.333	0.099	0.843
12CO	4.5	1.270	0.141	12.719
12CO	4.5	0.317	0.414	13.488
12CO	2.8	1.270	0.174	5.491
12CO	2.8	0.317	0.373	6.400
CONT	7.0	91.4	4.62e-3/2.45e-3	0.447
CONT	7.0	108.1	7.58e-3/4.50e-3	0.527
CONT	4.5	91.4	3.58e-3/2.21e-3	0.254
CONT	4.5	108.1	5.22e-3/2.85e-3	0.309
CONT	2.8	91.4	4.62e-3/2.79e-3	0.132
CONT	2.8	108.1	6.27e-3/3.16e-3	0.175
CONT	2.2	91.4	3.76e-3/1.25e-3	0.088
CONT	2.2	108.1	6.16e-3/1.54e-3	0.114
CONT	1.25	91.4	4.86e-3/1.91e-3	0.050
CONT	1.25	108.1	7.49e-3/2.03e-3	0.057

Note. — With the exception of the HCO^+ data, the images span ranges of uv-space from either 2.7 to 110 or 2.7 to 250 kλ. Multiple noise estimates are for the regions around IRS1 (left) and around NGC 7538S (right).

to the collision limit at CARMA, there is obviously significant flux on larger scales. The minimum baseline in each case is $\sim$2.6 kλ, which corresponds to angular scales of 80″. The *uv*-coverage is dense only on scales smaller than 75″. The morphology on sizes larger than this are suspect.

In what follows, flux estimates reported were measured from images made using the standard, uniform-beam-model, *uv*-plane subtraction methods. The computational time required for the current implementation of the methods that utilize the measured primary beam patterns is prohibitive for these large datasets and subsets must be used.

Uncertainty in the flux calibration scale based on models of the calibrators is assumed to be 10% based on the comparisons of the flux derived for CARMA observations of Neptune, Uranus, and Mars at similar airmass over a short period of time (Wright, private communication). Little variation in the flux of 0019+734 was seen on timescales of less than a week. Repeatability of flux measurements over these scales gives an RMS of 5% giving a total calibration uncertainty of 11%. Uncertainty in individual source measurements is based on either the residuals in Gaussian fits to smooth features or the integrated RMS in regions whose flux is determined by summing over regions. The calibration uncertainty is not included in the estimates of uncertainty. Therefore all flux estimates which follow carry an additional uncertainty of 11%.

5.4 Analysis & Results

5.4.1 Opacity & Mass Determination

In the CARMA data, continuum emission presents the best measure for the mass of dense structures when the spectral slopes are consistent with thermal dust emission.[7]

[7]Dust emission, in the optically thin limit, is expected to have spectral slope anywhere between 2 and 4 or more depending on the dust grain population (e.g. Hildebrand, 1983). The spectral index of free-free emission, on the other hand, is marginally flat (-0.1) in the optically thin limit but should be 2 or less in the optically thick or transition region (e.g. Rybicki & Lightman, 1979). Ionized winds typically have spectral slopes from -0.1 to 1 (Reynolds, 1986).

The dust mass is determined by

$$M_{dust} = R_{gd} \frac{d^2 F_\nu}{B_\nu(T_D, \nu)\kappa_\nu}, \tag{5.1}$$

where R_{gd} is the gas to dust mass ratio, d is the distance, F_ν is the flux, B_ν is the black body equation for dust at a temperature of T_{dust} and a frequency ν, and κ_ν is the opacity. An implicit assumption is that the dust emission is optically thin, an assumption that is likely invalid in the densest regions near the protostars. Additionally the dust opacity is assumed to scale as

$$\kappa_\nu = \kappa_{230\,\mathrm{GHz}} \left(\frac{\nu}{230\,\mathrm{GHz}} \right)^\beta, \tag{5.2}$$

where several of the parameters are poorly constrained. The value of $\kappa_{230\,\mathrm{GHz}}$ changes with environment but in dense cores a value of $1\,\mathrm{cm}^2\ \mathrm{g}^{-1}$ has been found. Values of β can span 0 to 2 or more (Ossenkopf & Henning, 1994). The dust temperature is often poorly known, but is likely to be very low ($\sim$10-30 K) in dense cores. A value of 100 is typically assumed for R_{gd}, but this is also uncertain at the 30-50% level. The combined uncertainty in total mass estimated by this method is a factor of several.

The properties of the gas emission from dense cores and outflows are determined assuming the emission arises from the rotational transitions of rigid rotor molecules. Two equations are required: the equation for optical depth correction and the equation for the gas mass in the optically thin regime. The opacity correction has a much stronger dependence on velocity than on position so often regional averages as a function of velocity channel are derived. In cases were the opacity correction cannot be derived, it is extrapolated from the nearest velocity channels that have valid estimates. If such information is still not available, as is the case for HCO^+, reasonable assumptions about the optical depth are made with the caveat that factors of several error can be introduced.

Under reasonable approximations, a line is optically thick if the ratio of the emission from that line to the emission from a less abundant isotopologue is less than

the abundance ratio of those two isotopologues, i.e. $F_x/F_y < A_x/A_y$ where F is the flux and A is the abundance. More specifically, the measurement equation gives the brightness temperature, T_{br}, of the emitting region

$$T_{br} = f(S(T_{ex}, \nu) - S(T_{2.73}, \nu))(1 - \exp(-\tau)), \tag{5.3}$$

where T_{ex} is the excitation temperature, τ is the optical depth, f is the beam filling factor, and $S(T, \nu)$ is the blackbody function in temperature units, i.e.

$$S(T, \nu) = \frac{h\nu}{k}(\exp(h\nu/kT) - 1)^{-1}. \tag{5.4}$$

Ratios of the measurement equation can provide estimates of the optical depth directly. To provide a function strictly of a single optical depth, a ratio of optical depths, $r = \tau_i/\tau_j$, must be constructed from knowledge of the isotopic ratio, a, correcting for differences in rotational constants, B, and frequency, ν (e.g. Garden et al., 1991)

$$r = a\frac{1 - \exp(-h\nu_i/kT_{ex})}{1 - \exp(-h\nu_j/kT_{ex})}\frac{kT_{ex}/hB_j + 1/3}{kT_{ex}/hB_i + 1/3}, \tag{5.5}$$

where the second term results from the differences in partition functions for the two lines. The equation for strictly τ_i is now given by the relation

$$\frac{1 - \exp(-\tau_i/r)}{1 - \exp(-\tau_i)} = \frac{(S_i(T_{ex}, \nu_i) - S_i(2.73, \nu_i))}{(S_j(T_{ex}, \nu_j) - S_j(2.73, \nu_j))}\frac{T_{j,br}}{T_{i,br}}, \tag{5.6}$$

and values of τ_i can be interpolated from line ratios.

In the optically thin regime, the measurement equation is reduced to

$$T_{br} = (S(T_{ex}, \nu) - S(T_{2.73,\nu}))\tau \tag{5.7}$$

and τ becomes a normalized brightness temperature. Quantum mechanics and local thermodynamic equilibrium provide that the column density, N, in terms of the

opacity (e.g. Garden et al., 1991):

$$N = \frac{3k}{8\pi^3\mu^2 B}\frac{\exp(hBJ(J+1)/kT_{ex})}{J+1}\frac{T_{ex}+hB/3k}{1-\exp(-h\nu/kT_{ex})}\int \tau\, dv, \qquad (5.8)$$

where ν is the frequency, B is the rotational constant in Hz, μ is the dipole moment, J is the quantum number associated with the lower level, dv is the velocity over which the gas is emitted and k and h are the Boltzmann and Plank constants, respectively. This equation can then be integrated over velocity and over the source size to obtain a mass estimate.

The assumption of optical thinness introduces an error, the correction, C, for which is easily defined:

$$C = \frac{\tau}{1-e^{-\tau}}. \qquad (5.9)$$

In the end, the mass is given by

$$M(x,y,v) = C(v)\frac{3k(T_{ex}+hB/3k)}{8\pi^3\mu^2 B(J+1)}\frac{\exp(E_j/kTex)}{1-\exp(-h\nu/kT_{ex})}\times \qquad (5.10)$$

$$\frac{[H_2/X]\mu_m m_H T_B(x,y,v)}{S(T_{ex},\nu)-S(2.73,\nu)}dxdydv, \qquad (5.11)$$

where the only new quantities introduced are the mean molecular weight, μ_m, in units of the mass of a hydrogen atom, m_H, and the abundance of the species in question relative to molecular hydrogen $[H_2/X]$. Opacity corrections for both ^{13}CO and C^{18}O are determined by comparing the relative emission in the lines over an identical beam and area. ^{12}CO opacities are determined by comparison to ^{13}CO. For high velocities, no direct means of calculating the opacity correction is available. In these cases, an extrapolation is made from the lower velocity channels. The abundance ratios and molecular properties used here are described in Table 5.4.

Gas mass estimates, and subsequent estimates of momentum, momentum flux, energy and mechanical luminosity are determined by taking velocity moments of Equation 5.11, integrating over relevant channels and regions of the map and normalizing by the appropriate constants and length scales. Outflow velocities are determined

Table 5.4. Molecular Constants

Species	μ Db	[H_2/X]	Rot. Const. (B) GHz
^{12}CO(1-0)	0.110[a]	10^{-4}	57.6356
^{13}CO(1-0)	0.110[a]	2.5×10^{-6}	55.1007
C^{18}O(1-0)	0.110[a]	2×10^{-7}	54.8911
HCO$^+$(1-0)	3.90[b]	2.8×10^{-9}[c]	44.5943

[a]Hellwege 1982

[b]Botschwina et al. 1993

[c]Value valid only for dense regions not outflows.

Note. — Abundance ratios taken from Blake et al. 1987 with the exception of C^{18}O, which was taken from Wilson & Rood 1994. The ratio of ^{12}CO to ^{13}CO has been determined to be more on the order of 60 in nearby star-forming regions, but I use the Blake et al. values since these were determined in a massive star forming region and single dish observations of these lines in NGC 7538 indicate that the ratio is likely significantly less than 60 (Sandell, private communication). Critical densities for molecules are 1×10^3 cm^{-3} for CO and 1×10^5 cm^{-3} for HCO$^+$.

by weighting by the mass. While the highest spatial resolution images are used to disentangle the morphology, the lowest resolution image which allows an independent measurement of outflow properties will be used to determine outflow/core flux. The flux on the largest scales is obviously missing from this discussion because the CO data do not have single dish corrections. However, it is the outflow mass alone that is desired so the interferometric observations serve to determine the outflow mass specifically, without contamination by the surrounding cloud.

5.4.2 Infall Determination

There are three possible methods for measuring the mass infall rate. The first assumes steady-state accretion and matter moving at near the free-fall speed so the mass accretion, $\dot{M}_{acc}$, is given by

$$\dot{M}_{acc} = 2\pi\Sigma R v_{in}, \tag{5.12}$$

where Σ is the surface density, R is the size scale and v_{in} is the infall velocity. The second method involves calculating the outflow mass (as described above), determin-

ing the age of the outflow and assuming that the outflow mass rate represents some fraction of the overall accretion, i.e.

$$\dot{M}_{acc} = \frac{f_{outflow} M_{outflow}}{t_{outflow}}. \tag{5.13}$$

The value of $f_{outflow}$ is given by models and is typically 2-3 (Tomisaka, 1998; Richer et al., 2000), although it is only strictly bounded below by one and values as large as 10 have been suggested. A value of 3 will be adopted here. A lower limit on the age of the outflow is typically determined by taking the extent of the outflow lobe and divide this by some representative velocity.[8] Finally, in the presence of strong self absorption from a given spectral line or absorption of a strong continuum source, an absorbed mass along the line of sight can be calculated. If an optically thin isotopologue of the absorbed species is available, the center position and width of this line can be used to fit the blue shifted side of the absorbed profile. The ratio of the amplitude of these profiles gives an estimate the opacity correction as described above. Unfortunately, such an optically thin tracer with comparable resolution is not available for NGC 7538. A best guess of the opacity must be made from a Gaussian fit to the blue shifted emission, fixing the systemic velocity at the adopted value. The measured profile which includes the absorption feature is subtracted from the Gaussian fit and the mass is determined as described above now using absorption instead of emission. The resulting mass must be doubled to account for infalling mass from the blue shifted side which is not absorbed. Slower moving gas farther from the line of sight to the main core can also be added. It should also be noted that the presence of an inverse P-Cygni profile against a continuum source provides definitive and conclusive evidence of significant infall because the continuum source allows localization of the infalling material.

[8]While many authors choose the maximal velocity, here a mass averaged velocity is used. Given the total mass is being used, a mass averaged velocity is more representative.

5.4.3 General Morphology

Figures 5.2, 5.3, 5.4 and 5.5 provide an overview of the morphology of the NGC 7538 region. Figure 5.2 shows CARMA contours of 91.4 GHz continuum emission overlaid on a *Spitzer* 8 μm false-color image. The only major features visible are a dense clump associated with NGC 7538S, seen in the south-central portion of the map, and a single, circular feature (IRS2), seen in the northern portion of the map. The remaining, small-scale features visible in the northern half of the map are probably artifacts associated with the subtraction of the IRS1 emission, which was performed in the *uv*-plane before generation of the continuum image. IRS1 occupies the white region in the lower portion of the central blue feature.

Figure 5.3 shows the high-velocity, ^{12}CO emission overlaid on the same *Spitzer* image. The image reveals that the high-velocity, gas dynamics of the IRS1 and NGC 7538S region is complex.[9] The red-shifted (red) and blue-shifted (black) contours indicate that gas is clearly associated with IRS1 and NGC 7538S and perhaps a number of other features. Lower velocity, C^{18}O and ^{13}CO emission is displayed in Figure 5.4, where IRS1 is indicated by a plus sign. In both spectral line figures, signatures of multiple outflows and filaments are seen. A number of features are immediately clear: 1) a number of outflows are associated with NGC 7538S, with bright, compact, red contours appearing very close to bright, compact, blue shifted contours in the high velocity map. 2) In the IRS1 region arc-like structures follow the bright, 8 μm lobe. 3) At lower velocities a two filaments are visible: a slightly blue-shifted filament extends from IRS1 towards IRS4 and another blue-shifted filament extends from NGC 7538S to the northwest and southeast. Both the large red shifted feature seen in low velocity gas in the extreme southwest of the image and the low velocity blue-shifted lobe northeast of IRS1 which curves to the northern edge of the map are thought to be associated with IRS1. Figure 5.5 displays the CARMA channel maps of HCO$^+$. One obvious result is that near the cloud velocity (3^{rd} row middle

[9]The use of term high velocity refers to the region over which there is only wide-band HCO$^+$ and ^{12}CO(1-0) data. Velocity is referred to as high velocity if it is blue of -64.21 km s^{-1} or red of -45.76 km s^{-1}.

four panels), the filamentary structure is visible in HCO^+(1-0), a transition with a critical density of 10^5 cm^{-3}. Detailed analysis of much of this complex structure will be followed up with the addition of single dish CO data.

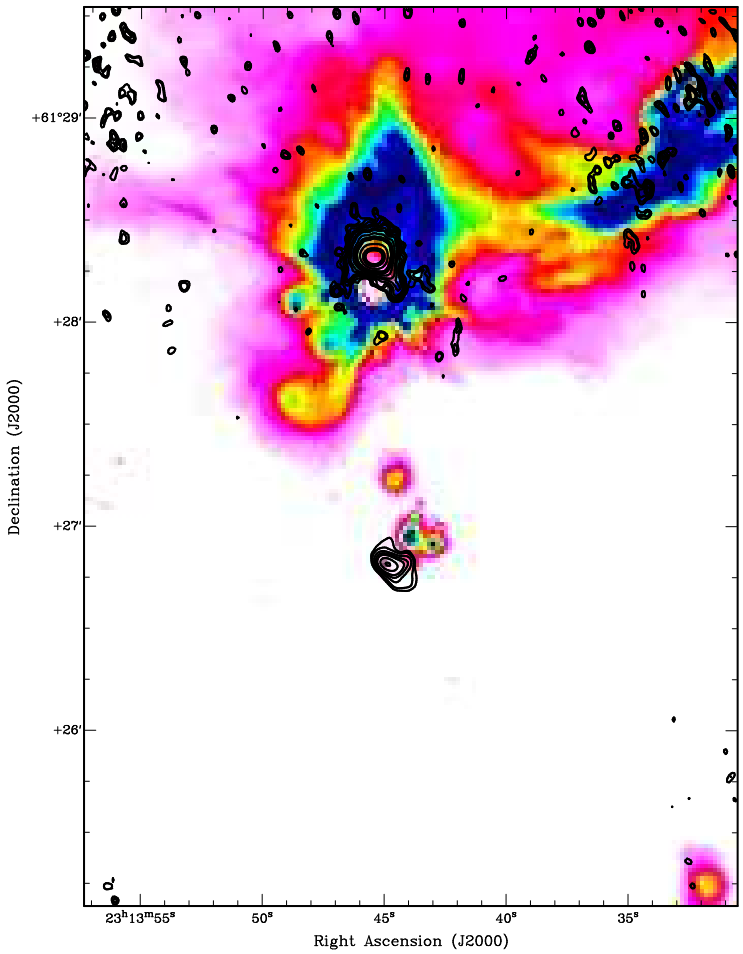

Figure 5.2 The 91.4 GHz continuum emission from the southern portion of NGC 7538 is shown as black contours (4.5″ resolution), beginning at 12 mJy. In this and all subsequent continuum figures (except where noted), the lowest level contour and the significance of that contour are quoted. The remaining contours are spaced according to the prescription: 5, 6, 8, 10, 12, 15, 20, 25, 30, 40, 50, 70, 100, 150, 200, and 300 mJy increasing at 100 mJy thereafter, where for a given image the contours begin at the quoted level and each subsequent contour is given as in this list. In this particular figure the 12 mJy lowest contour is roughly at the 3 and 5σ level in the northern and southern regions, respectively. The colorscale shows 8 μm emission from NGC 7538 taken with *Spitzer*. Emission from IRS1 is saturated in the 8 μm images and has been removed. It would have appeared as the white region in the southern part of the large, blue region in the north. Here the color stretch is such that blue is bright and red/pink is faint and white largely is emission free.

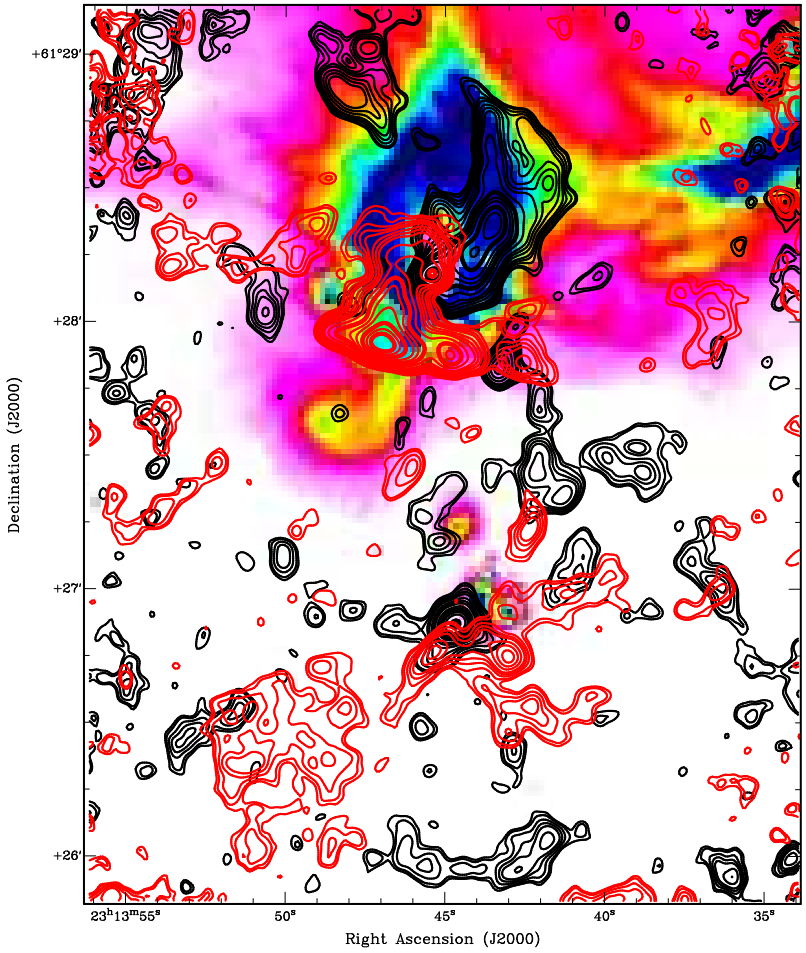

Figure 5.3 Contours of ^{12}CO emission are overlaid on the same *Spizter* image as in Figure 5.2. The velocity ranges from -95.39 km s^{-1} to -64.21 km s^{-1} in the blue and -45.76 km s^{-1} to -16.63 km s^{-1} in the red. In this and all subsequent integrated gas emission maps, the lowest contour level and the significance of that contour are given. The contours then increase according to: 0.1, 0.25, 0.5, 0.75, 1, 1.5, 2, 3, 4, 5, 7, 9, 11, 15, 20, 25, 30, 40, 50 and 60 Jy km s^{-1}, where a given image begins contour levels at the quoted minimum level. Here, high velocity blue-shifted contours are shown in black (to contrast them from the blue lobe of the 8 μm emission) and red contours show high velocity red-shifted emission. Contours begin at 1.5 Jy km s^{-1}, roughly $3\sigma_{rms}$.

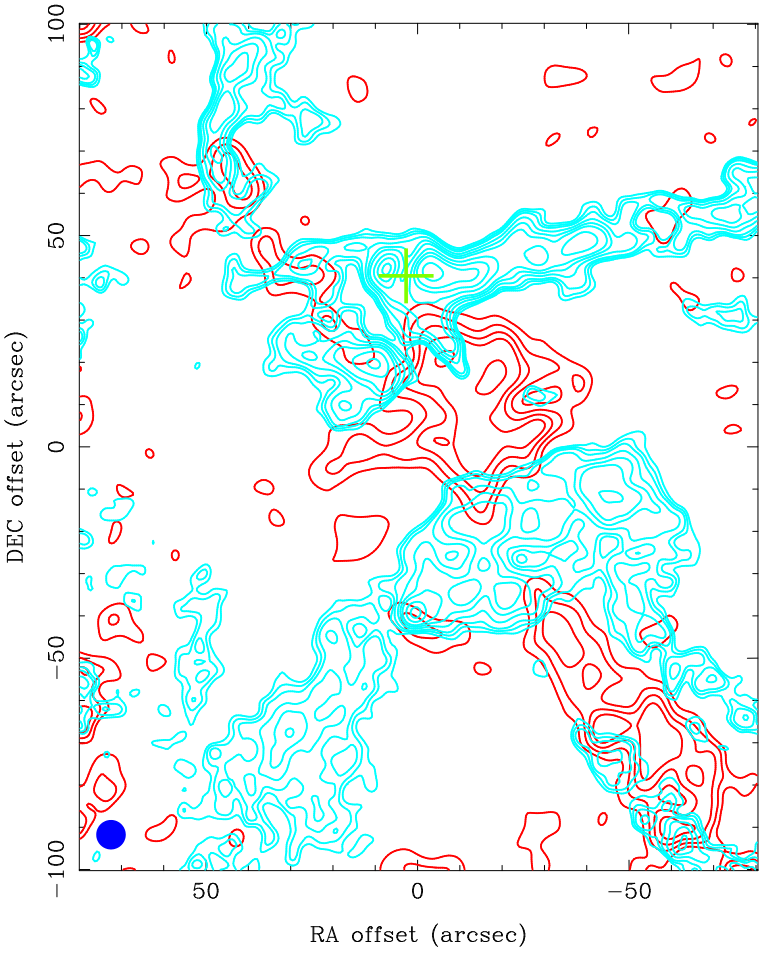

Figure 5.4 The blue contours show low-velocity (-64 km s^{-1} to -59 km s^{-1}) blue-shifted emission from ^{13}CO. The red contours depict $C^{18}O$ emission on the red-shifted side (-54 km s^{-1} to -51 km s^{-1}). Contours begin at 0.5 Jy km s^{-1} and 1.0 Jy km s^{-1} for the $C^{18}O$ and ^{13}CO, respectively. This is approximately 2.5σ and 3.5σ. IRS1 is indicated by the plus sign near position (0,40). See Figure 5.3 for further description of contours.

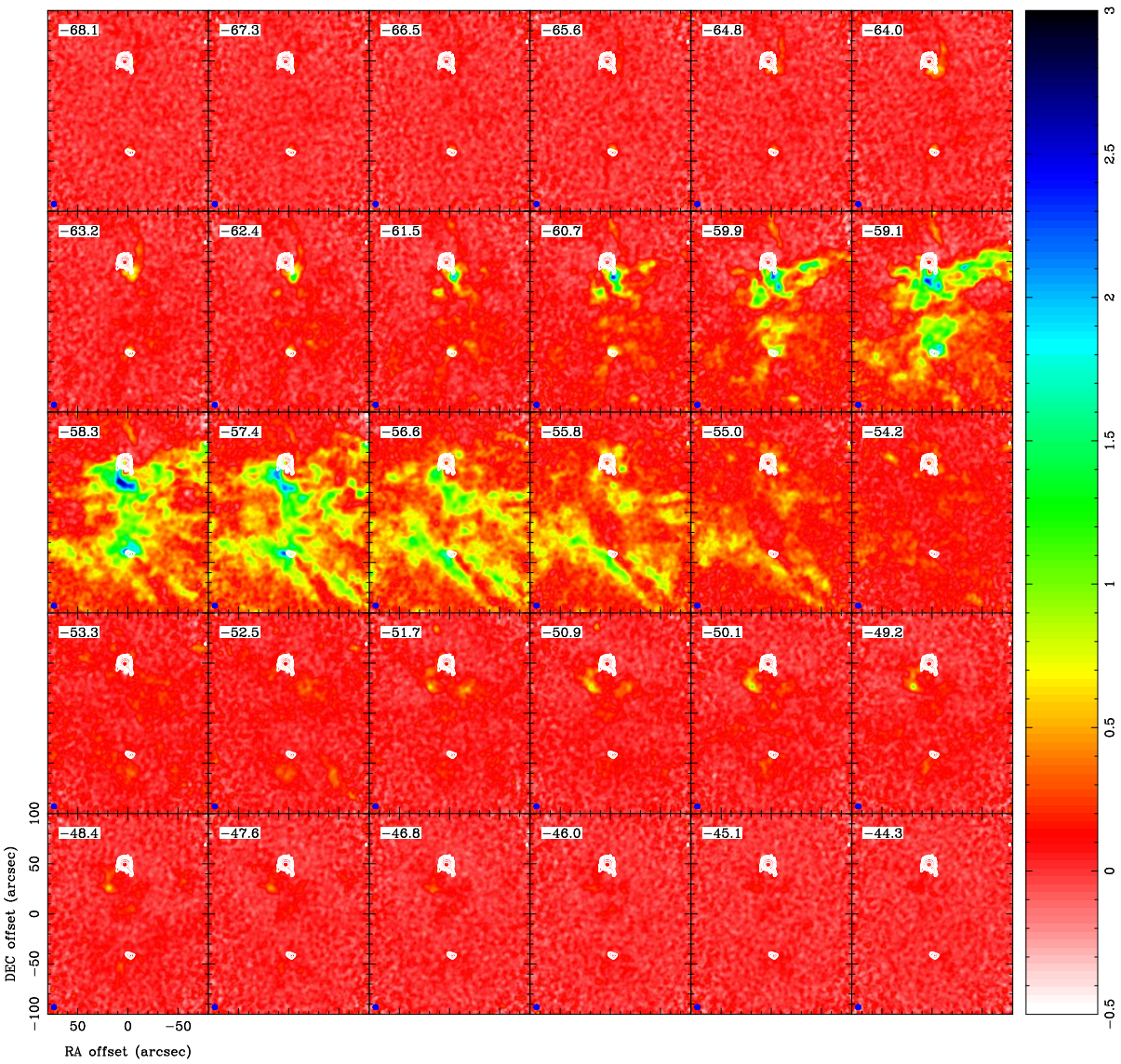

Figure 5.5 Individual velocity channels of the continuum-subtracted, single-dish corrected HCO^+ emission are shown. The velocity of the top-left panel is -68.1 km s^{-1} and the channel spacing is 0.82 km s^{-1}. Velocity increases left to right. The end channel (bottom-right) has a velocity of -44.3 km s^{-1}. The beam is shown in the lower left of each panel and is 4.5″ in diameter. The colorscale is shown on the right. Each panel is actually the average of two channels to reduce the number of panels provided. The white contours are 91.4 GHz continuum emission beginning at 25 mJy which is more than 6σ in the northern part of the image and more than 10σ in the south. See Figure 5.2 for further discussion of the contours.

5.4.4 NGC 7538S

5.4.4.1 Dense Structures: Continuum and $C^{18}O$

Figure 5.6 displays details of the continuum emission from NGC 7538S. Table 5.5 summarizes the bulk properties of the region. The measured position of NGC 7538S is $(\Delta\alpha, \Delta\delta) = (-2.4'', -41.2'')$. The source is well resolved in both the 7.0 and 4.5″ images and Gaussian fits reveal comparable sizes at both frequencies, 12″ by 7.4″ at a position angle of 60°. The position angle and size change slightly from the 7.0 to 4.5″ images mostly due to the northeastern extension fading at 91.4 GHz from the top panels of Figure 5.6.

The integrated flux in a region around the source, masked to exclude pixels below 4σ is 0.218±0.007 Jy at 91.4 GHz and 0.407±0.016 Jy at 108.1 GHz. This provides a spectral slope, defined so that $F(\nu_1)/F(\nu_2) = (\nu_1/\nu_2)^{slope}$ where ν_1 and ν_2 are frequencies and $F_{1,2}$ is the flux at the corresponding frequency, of 3.8±0.5 and is consistent with thermal emission from dust. This integrated flux for the continuum source suggests a mass of 700 $M_\odot$ for the clump. The FWHM of the elliptical Gaussian fit to the clump is 34,000 by 20,000 AU. However, even on 7″ scales, NGC 7538S shows evidence of more complicated structure. To the northeast, there is an extension seen both in the 91.4 and 108.1 GHz emission. Figure 5.7 provides an indication of where the additional sources are most likely located. The image is of 91.4 GHz emission but the white contours show the 2.2″ resolution image embedded in the 7″ image. Additional structure is revealed at every increase in resolution with the 1.25″ image showing that the central region of NGC 7538S breaks down into two, probably three, peaks.

Table 5.5. NGC 7538 Continuum Fluxes

Source	Resolution ″	Frequency GHz	Flux Jy	Size ″ × ″@°	Position $\Delta\alpha, \Delta\delta$
IRS1	NA	91.4	1.413(0.011)	0.5(0.1)x0.3(0.1)@-1(10)	2.7(0.1),40.4(0.1)
IRS1‘	NA	108.1	1.618(0.018)	0.4(0.2)x0.1(0.1)@20(90)	2.6(0.1),40.3(0.1)
IRS2	7.0	91.4	1.016(0.012)	7.9(0.3)x7.8(0.4)@70(90)	3.07(0.14),49.91(0.15)
IRS2	7.0	108.1	1.31(0.02)	8.6(0.6)x8.3(0.4)@-60(90)	2.9(0.2)0,49.8(0.2)
IRS2	4.5	91.4	1.031(0.013)	8.1(0.3)x8.0(0.3)@80(90)	3.07(0.13),49.77(0.13)
IRS2	4.5	108.1	1.22(0.02)	8.5(0.5)x7.0(0.4)@-50(90)	3.05(0.18),49.81(0.17)
IRS2	2.8	91.4	1.00(0.02)	8.0x8.0@0	3.0,49.9
IRS2	2.8	108.1	1.13(0.04)	8.0x8.0@0	3.0,49.9
IRS2	2.2	91.4	1.05(0.02)	8.0x8.0@0	3.0,49.9
IRS2	2.2	108.1	1.25(0.05)	8.0x8.0@0	3.0,49.9
IRS2(SE)	2.8	91.4	0.034(0.013)	point	4.4(0.6),48.0(0.6)
IRS2(SE)	2.8	108.1	0.033(0.022)	point	4.4(1.2),48.1(1.1)
IRS2(SE)	2.2	91.4	0.038(0.009)	point	4.4(0.3),47.9(0.3)
IRS2(SE)	2.2	108.1	0.051(0.016)	point	3.9(0.4),48.6(0.4)
IRS3[a]	4.5	112.5	0.059(0.010)	point	-9.7(0.3),42.2(0.2)
IRS1a	7.0	91.4	0.041(0.013)	point	-5.4(1.7),41.3(1.4)
IRS1a	7.0	108.1	0.097(0.022)	point	-6.6(1.4),41.5(1.1)
IRS1a	4.5	91.4	0.033(0.011)	5.0(2.8)x4.5(2.5)@10(90)	-3.8(1.0),40.4(1.1)
IRS1a	4.5	108.1	0.076(0.017)	4.8(1.7)x4.5(1.6)@-12(90)	-4.9(0.7),42.5(0.7)
NGC7538S	7.0	91.4	0.218(0.007)	12.2(0.7)x7.6(0.5)@55(6)	-2.5(0.3),-41.3(0.2)
NGC7538S	7.0	108.1	0.407(0.016)	12.0(0.6)x7.2(0.4)@63(5)	-2.3(0.2),-41.1(0.2)
NGC7538S	4.5	91.4	0.204(0.009)	11.2(0.9)x6.8(0.6)@50(7)	-2.4(0.3),-41.4(0.3)
NGC7538S	4.5	108.1	0.394(0.013)	11.0(0.8)x6.4(0.5)@61(6)	-2.1(0.3),-41.1(0.2)
NGC7538S	2.8	91.4	0.191(0.018)	NA	NA,NA
NGC7538S	2.8	108.1	0.35(0.02)	NA	NA,NA
NGC7538S	2.2	91.4	0.178(0.007)	NA	NA,NA
NGC7538S	2.2	108.1	0.377(0.014)	NA	NA,NA
NGC7538S	1.25	91.4	0.18(0.02)	NA	NA,NA
NGC7538S	1.25	108.1	0.21(0.03)	NA	NA,NA

[a]IRS3 was seen only in the 112.5 GHz data.

Note. — Quoted fluxes are integrated. Source sizes are deconvolved. Offsets are with respect to the mosaic pointing center, (α,δ)=(23:13:45.00,+61:27:30). The bulk of IRS2 in the two higher resolution images was subtracted by fitting a Gaussian of a size and position consistent with the fits at lower resolution. The fine-scale structure of NGC7538S is far more complex and is presented elsewhere. The previously unidentified continuum source is labelled as IRS1a here.

Table 5.6. NGC 7538 High Resolution Continuum Fluxes

Source	Resolution $''$	Frequency GHz	Peak Flux Jy	Total Flux Jy	Mass $M_\odot$	Size $'' \times ''@^\circ$	Position $\Delta\alpha, \Delta\delta$
NGC7538Sa	1.25	91.4	0.0144(0.0019)	0.045	61	2.3(0.5)x1.4(0.3)@60(20)	0.00(0.19),-40.35(0.13)
NGC7538Sa	1.25	108.1	0.0229(0.0018)	0.075	61	2.3(0.3)x1.5(0.2)@78(11)	0.16(0.11),-40.37(0.07)
NGC7538Sb	1.25	91.4	0.0102(0.0016)	0.0102	34	point	-2.18(0.12),-41.56(0.14)
NGC7538Sb	1.25	108.1	0.016(0.004)	0.016	34	point	-2.0(0.2),-41.7(0.2)
NGC7538Sa	2.2	91.4	0.0221(0.0015)	0.055	111	3.2(0.5)x2.2(0.3)@51(17)	0.10(0.19),-40.45(0.13)
NGC7538Sa	2.2	108.1	0.043(0.004)	0.136	111	3.7(0.6)x2.8(0.4)@60(20)	0.16(0.11),-40.37(0.07)
NGC7538Sb	2.2	91.4	0.011(0.005)	0.011	49	point	-2.18(0.12),-41.56(0.14)
NGC7538Sb	2.2	108.1	0.023(0.007)	0.023	49	point	-2.0(0.2),-41.7(0.2)
NGC7538Sc?	2.2	91.4	0.0120(0.0019)	0.0120	22	point	-4.3(0.2),-42.2(0.2)
NGC7538Sc	2.2	108.1	0.0104(0.0015)	0.0104	22	point	-3.7(0.2),-43.0(0.3)
NGC7538Sd	2.2	91.4	0.010(0.002)	0.010	30	point	-3.9(0.4),-47.2(0.4)
NGC7538Sd	2.2	108.1	0.014(0.003)	0.014	30	point	-3.6(0.6),-46.8(0.6)
NGC7538Se	2.2	91.4	0.008(0.002)	0.008	34	point	-7.6(0.5),-47.4(0.7)
NGC7538Se	2.2	108.1	0.016(0.003)	0.016	34	point	-6.9(0.6),-47.3(0.6)
NGC7538Sf?	2.2	91.4	0.0077(0.0014)	0.0077	35	point	-7.9(0.4),-40.2(0.2)
NGC7538Sf[a]	2.2	108.1	0.0163(0.0015)	0.096?	35	5.0(0.7)x4.7(0.7)@-84(90)	-6.59(0.19),-39.97(0.18)

[a]Flux is calculated assuming a point source since the size of the model fit is highly uncertain and marginally consistent with a point source.

Note. — Source sizes are deconvolved. Offsets are with respect to the mosaic pointing center, (α,δ)=(23:13:45.00,+61:27:30). Positions for cores a and b are fixed from the determination at the highest resolution because these sources are rather blended in images with poorer resolution. A total of 9 independent clumps can be identified visually with some level of confidence but only the clumps which appear at a consistent position between the two frequencies are identified here. The integrated flux for the entire NGC 7538S clump at $2.2''$ results in a mass of 650 $M_\odot$ (more than 90% of the mass determined from lower resolution data). Masses were calculated from 108.1 GHz continuum emission. The mass of core f was calculated assuming the source was unresolved.

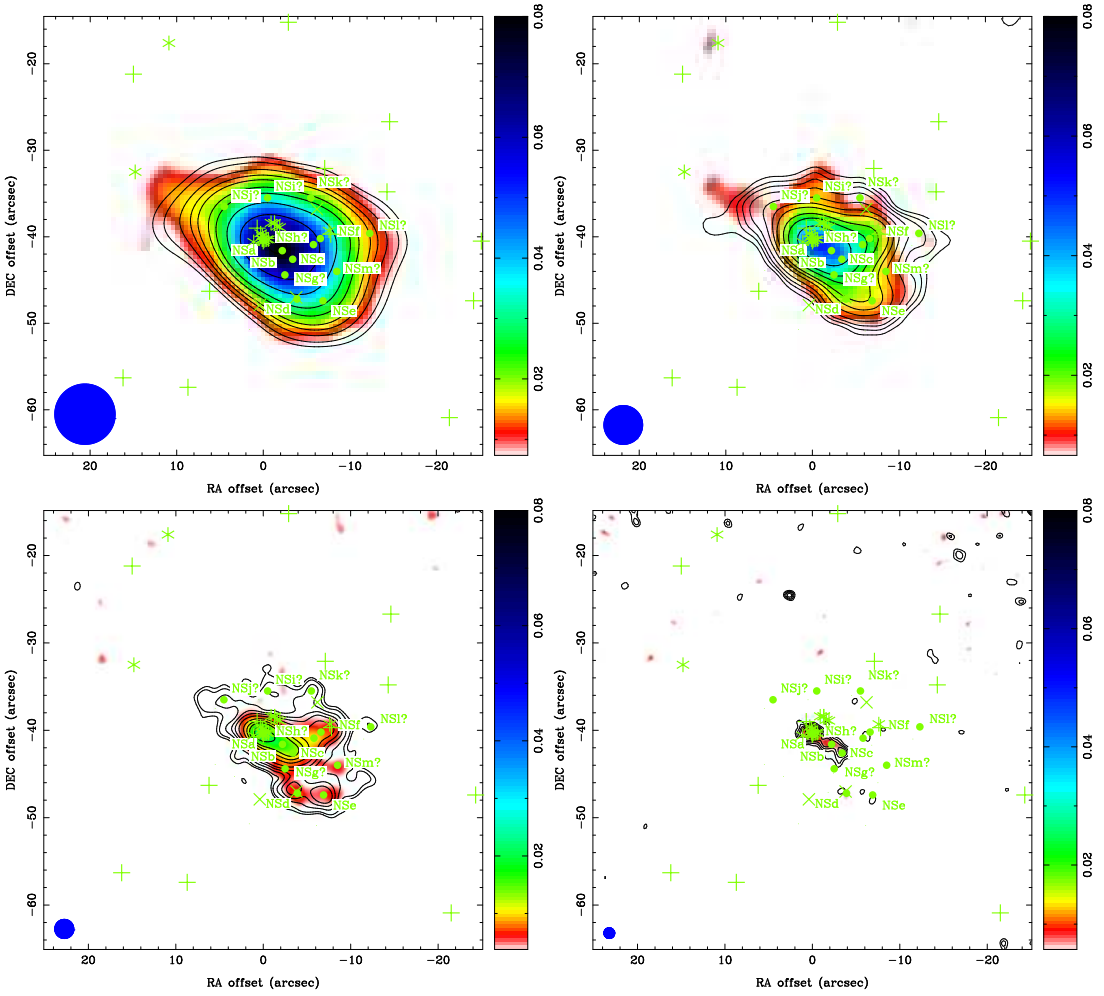

Figure 5.6 NGC 7538S continuum emission is shown at different resolutions, 7.0, 4.5, 2.2, and 1.25″ for the top-left, top-right, bottom-left and bottom-right panels, respectively. The beam size is in the bottom left of each panel. Each image covers the same sized region of NGC 7538S. Contours begin at 12, 8, 5 and 6 mJy, about 3σ, for the 7.0, 4.5, 2.2 and 1.25″ images, respectively. Colorscale is logarithmically stretched 91.4 GHz emission while the contours show 108.1 GHz emission. Minimum displayed flux is 3σ. See Figure 5.2 for further information regarding the contours. The labels NSx are short for NGC 7538Sx, the identifier in the table. Plus signs indicate infrared sources determined from Werner et al. (1979) and the *Spitzer* image, dots are the locations of the continuum sources determined in this work, and crosses and stars report the location of masers.

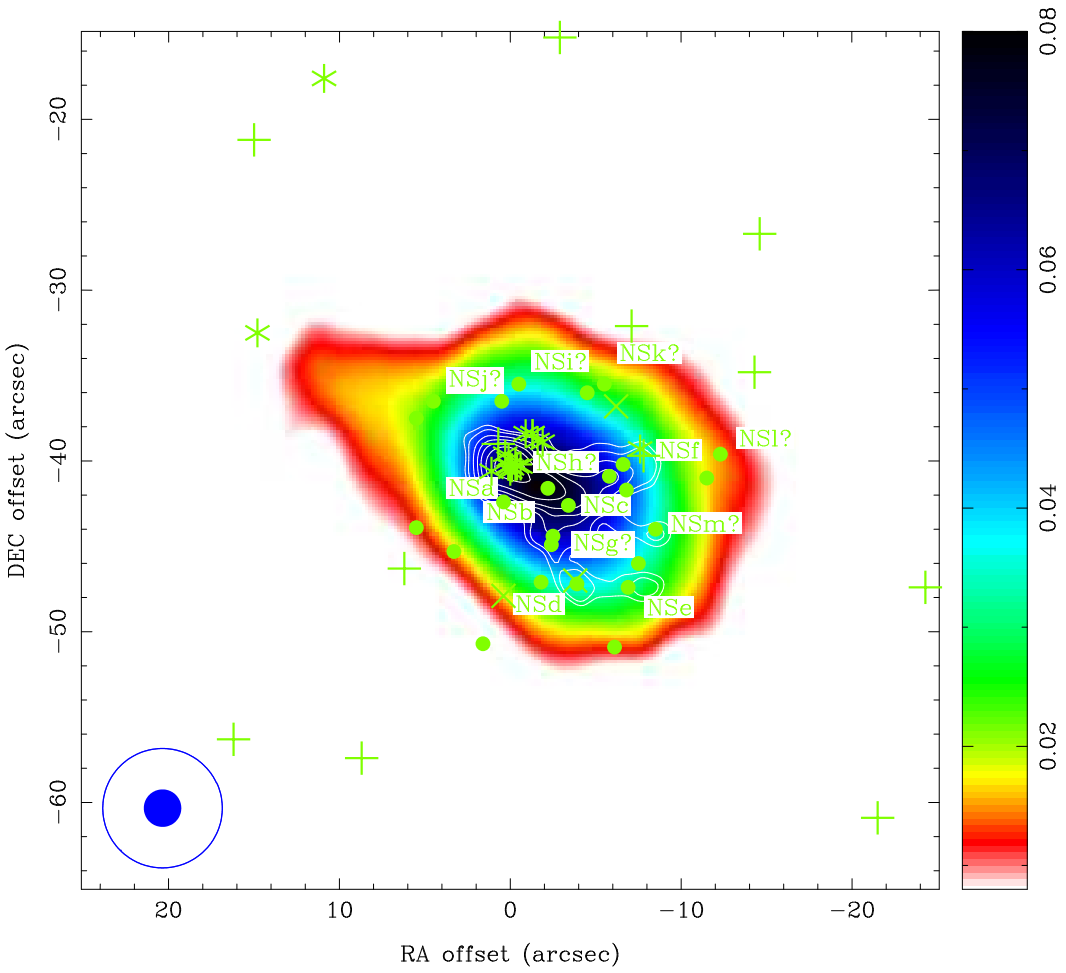

Figure 5.7 The 91.4 GHz image of NGC 7538S is show with the 7.0″ image in color and the 2.2″ image show in contours. Contours begin a 5 mJy and color begins at 8 mJy, effectively 3σ. Both beams are shown in the lower left corner with the 2.2″ beam being a solid circle. Labels are as in Figure 5.6. Contours are as in Figure 5.2.

In an attempt to disentangle the structure seen in the NGC 7538S images, Gaussian or point source fits to the structures seen in the 1.25″ images were made. Only peaks above 4σ were fit. After the peaks at 1.25″ had been characterized, fits at 2.2″ were done in an attempt to characterize some of the lower surface brightness features. In these images, the brightest peak was first fit, sometimes restricting the position to that determined by the 1.25″ images in the case of marginally blended sources. The source was then subtracted and a series of objects were extracted in this manner. In

all, six components containing nearly 60% of the total mass for the clump at 2.2″ resolution were identified in both the 91.4 and 108.1 GHz images.

There is evidence from the 2.2″, 91.4 GHz image that an additional two structures may be present but these sources are not seen with high confidence in the 108.1 GHz maps. Beyond the two structures, an additional two sources are apparent in the 4.5″ images. These sources are almost certainly resolved which explains their absence in higher resolution images. Their blended nature in the low resolution maps makes identification of a common position and flux estimate impossible.

The positions of all 10 possible cores are indicated on Figure 5.6 and 5.7. All assumed dust properties are described in Table 5.1. The brightest core, NGC 7538Sa, is located at $(\Delta\alpha, \Delta\delta) = (0.16'', -40.37'')$ in the 108.1 GHz map at 1.25″ resolution, well separated from the center of the clump derived from low resolution data. Even at this resolution the source NGC 7538Sa is extended with a deconvolved FWHM of 2.3×1.5″ at a position angle between 65-85° but there is 0.2-0.3″ uncertainty in the length of the deconvolved axes. The integrated flux based on the Gaussian fit is 0.075 Jy at 108.1 GHz. The spectral slope when compared to the 91.4 GHz data is 3.0. NGC 7538Sa is spatially coincident with the weakly detected (2.8 mJy at 6 cm) free-free emission peak (Sandell et al., 2003) and a faint *Spitzer* detection at 8 μm. The presumed mass of the cold material in this most prominent peak is 61 $M_\odot$ and it has an extent of 6400 by 4200 AU. It should be noted that the flux of that prominent peak in the 2.2″ images increases by a factor of two over the 1.25″ image at 108.1 GHz, further indicating that the source is resolved.

The central ridge of NGC 7538S contains two additional sources, NGC 7538Sb and NGC 7538Sc. Source b is visible at both frequencies in the highest resolution image. The position of b in the 108.1 GHz map is $(\Delta\alpha, \Delta\delta) = (-2.0'', -41.7'')$ and the position in the 91.4 GHz map is consistent within the uncertainties. This position is consistent with the central position of the clump. The source is unresolved at 1.25″ resolution and has flux of 0.016 Jy at 108.1 GHz, yielding a mass of 30 $M_\odot$. Object c does not quite reach detection criteria in the 1.25″ 91.4 GHz image but its presence is required to match the 2.2″ images. At 2.2″, sources a and b have integrated fluxes of

0.136 and 0.023 Jy, respectively, at 108.1 GHz. The deconvolved sizes of NGC 7538Sa increases slightly when measured in the poorer resolution map. The spectral slope of the integrated emission is much steeper, but the spectral slope calculated from the measured *peak* fluxes is consistent with the previously quoted value for NGC 7538Sa.

At 2.2″ resolution, NGC 7538Sb continues to be a point source with a flux that is consistent with the estimates at 1.25″. Like all of the other sub-structures detected in NGC 7538S, the signal-to-noise is not sufficient to allow estimates of the spectral slope. The NGC 7538Sc is detected as a blended source in both 2.2″ images. Its flux is between 10 and 18 mJy depending on which resolution and frequency is used. NGC 7538Sd has flux between 10 and 14 mJy and the nearby NGC 7538Se is between 8 and 16 mJy. NGC 7538Sf has peak flux between 7.7 and 16.3 mJy. The 7.7 mJy flux is only slightly above the detection threshold at 91.4 GHz and the counterpart in the 108.1 GHz image is displaced slightly and is resolved. The position of NGC 7538Sf varies more with frequency than did the positions of NGC 7538Sa, b, c, d or e. The poor quality detection of f at 91.4 GHz may be the result of the likely extended nature of NGC 7538Sf. Despite the marginally consistent positions at multiple frequencies, NGC 7538Sd, e, f, and h have single contours of 108.1 GHz emission detected at 1.25″. Sources NGC 7538Sa and f are associated with 8 μm detections. A summary of the source properties is provided in Table 5.6.

Table 5.7. NGC 7538 $C^{18}O$ Fluxes

Source Id	Resolution $''$	Velocity Width km s^{-1}	Integrated Flux Jy km s^{-1}	Peak Flux Jy km s^{-1}	Mass $M_\odot$	Position $\Delta\alpha''$, $\Delta\delta''$	Size(major,minor,pa) $''$, $''$, degree
NGC7538S	7.0	-53.3,-60.0	21.6(1.1)	6.4	160(8)	-0.7(0.5),-39.2(0.3)	11.0(1.4)x6.6(1.0)@90(11)
NGC7538S	4.5	-53.3,-60.0	20.8(1.0)	4.1	154(7)	-0.6(0.4),-39.9(0.2)	9.6(1.0)x4.6(0.6)@80(7)
NGC7538Sa	2.2	-53.3,-60.0	8.3(0.9)	1.7	61(7)	-0.1(0.3),-40.22(0.15)	8.4(0.7) x3.0(0.3)@73(3)

Note. — Offsets are with respect to the mosaic pointing center, (α,δ)=(23:13:45.00,+61:27:30). Peak fluxes are determined from the zeroth moment map. Total flux is calculated in a region masked at 3σ. Mass uncertainty includes only the contribution from statistical uncertainty, i.e. there is an additional factor of 11% uncertainty in the total flux. Center position and size are determined from a Gaussian fit with an additional DC level.

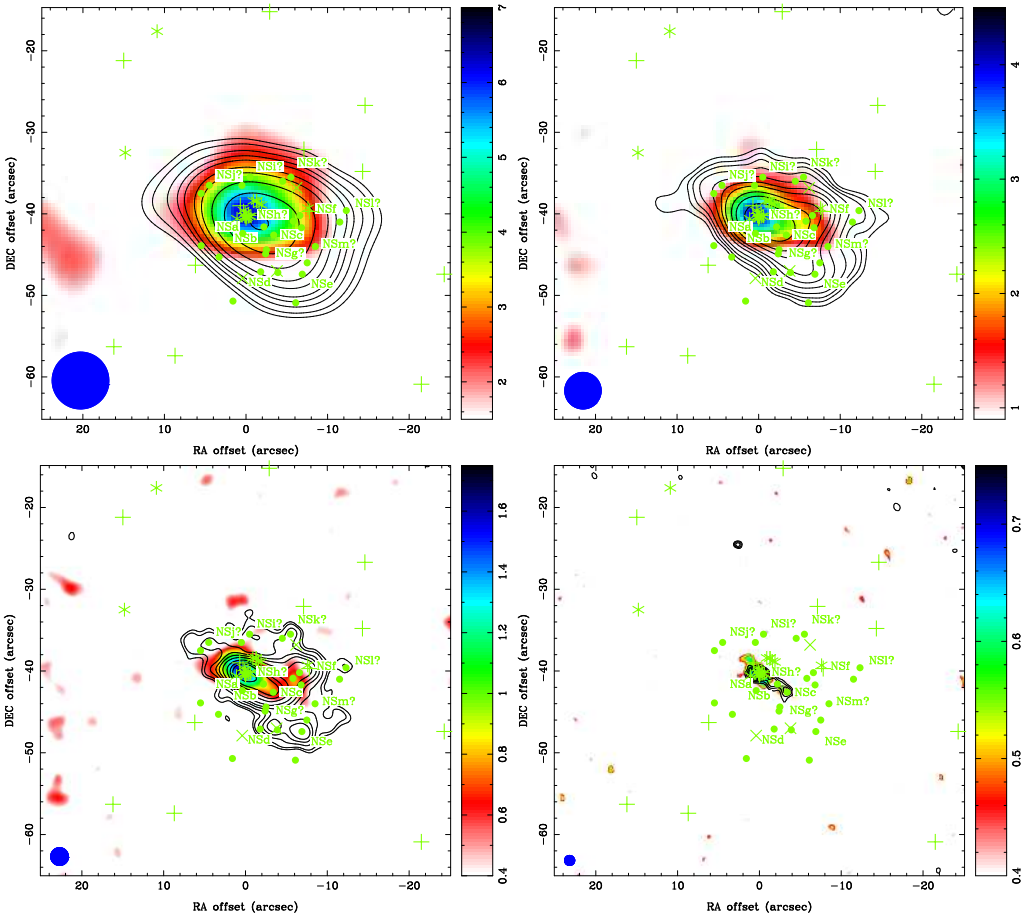

Figure 5.8 NGC 7538S is shown with $C^{18}O$ emission shown in color and continuum at 108.1 GHz shown as contours. The top two panels are 7.0″ (left) and 4.5″ (right) resolution. The lower panels show 2.2″ (left) and 1.25″ (right) resolutions. Contours begin at 12, 8, 5, and 6 mJy with improving resolution and continue according to Figure 5.2. Colorscale is linearly stretched. Minimum displayed flux is typically about 2σ. The beam size is shown in the bottom left of each panel for reference. The size scales of the images are the same in each instance. Symbols are as in Figure 5.6.

Figure 5.8 shows the integrated $C^{18}O$ emission from NGC 7538S at four different resolutions. From the 7.0″ image, it is obvious that the bulk of the $C^{18}O$ emission is not necessarily associated with the NGC 7538S clump. Gaussian fits to the emission reveal that peak is 1.54″ from the high resolution position of NGC 7538Sa and offset in the opposite sense of the offset between NGC 7538Sa and the center of the NGC 7538S clump. At 4.5″ resolution, the position of the $C^{18}O$ emission is aligned with NGC 7538Sa, with some additional flux at low significance.

At 2.2″ resolution, there is low level emission associated with NGC 7538Sf or h. Given the confirmed continuum detection of f and the proximity to an infrared source, the $C^{18}O$ clump is assumed to be associated with f. There is also extended emission along the ridge of NGC 7538S which might be associated with NGC 7538Sb or c. At 1.25″ resolution, the emission seems localized to NGC 7538Sc but the detection is marginal in any case. But, even in the highest resolution images, the bulk of the emission is still dominated by NGC 7538Sa. The source properties are summarized in Table 5.7.

The emission associated with NGC 7538Sa in the 2.2″, $C^{18}O$ image shows a noticeable gradient. The gradient is strongest along a position angle of approximately 60°. Figure 5.9 shows the spectrum of the emission centered on NGC 7538Sa and offsets along this position angle to the northeast and southwest. The northeastern component has a 0.5-1 km s^{-1} velocity shift relative to the center position. The southwestern component shows a similar shift in velocity. Unfortunately the identification of the gradient is somewhat confused by the cloud, as self-absorption is seen in the $C^{18}O$ data. Higher velocity resolution is required to definitively measure the velocity gradient.

5.4.4.2 Outflows

Three distinct outflows are detected in the NGC 7538S clump. Figures 5.10 and 5.11 show the high velocity blue- and red-shifted contours of HCO^+ and ^{12}CO emission, respectively. The colorscale is the relevant resolution continuum image. The highest resolution images in either case are remarkably similar, although the HCO^+

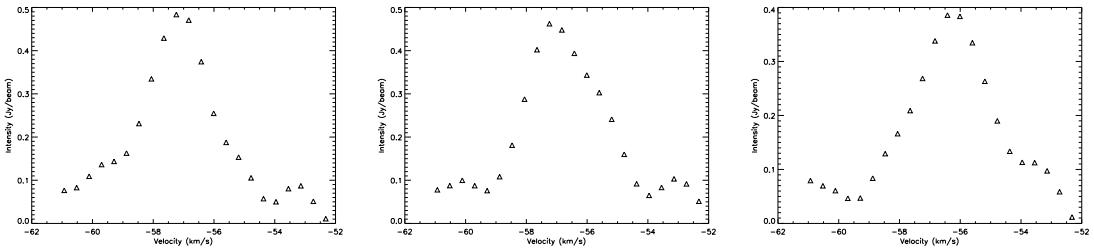

Figure 5.9 Three $C^{18}O$ spectra of NGC 7538Sa are shown. The left most panel is northeast of NGC 7538Sa, while the center and right panels are centered on NGC 7538Sa and on a position southwest of NGC 7538Sa, respectively. The step between positions is 1.1″, half the resolution of the data cube used to make the spectra.

emission is obviously lower signal-to-noise. There is a large blue-shifted lobe to the north-north-west of NGC 7538Sa. Near the peak of this lobe several maser spots are seen. Maser spots are also seen on NGC 7538Sa and a single maser is seen towards NGC 7538Sf. There is also significant structure in the lower 2-4 contours of the ^{12}CO map, with extensions to the north-northeast of the blue-shifted peak and extensions to the southwest and northeast of the peak. Red-shifted emission is seen to the southeast of NGC 7538Sa, to the south of NGC 7538Sb/c, and to the southwest of NGC 7538Sf. These features are seen only in the lowest contours of HCO^+, but they are seen with higher significance in the ^{12}CO image. The positions and integrated fluxes of the lobes are given for both spectral lines but only CO lines are used to derive the masses and mass moments in Table 5.8, 5.9, and 5.10.

In all, there is evidence for high-velocity outflow activity from NGC 7538Sa, b and f, but, since the blue shifted lobes of these sources are roughly coincident, it is impossible to disentangle the high-velocity emission. Accurate partitioning of the outflow flux requires far higher velocity resolution. The bulk of the flux is assigned to the NGC 7538Sa outflow lobe due to the proximity of the lobe to the driving source and the presence of copious maser activity. NGC 7538Sa is assigned 80% of the blue lobe flux, with 20% assigned to NGC 7538Sf.

Table 5.8. NGC 7538 Outflow Properties I

Source Id	Line	Resolution “	Velocity Range km s^{-1}	Peak Flux Jy km s^{-1}	Flux Jy km s^{-1}	Peak Position “	Width “	Length “	Position Angle degrees
IRS1	^{12}CO	2.8	-95.39,-78.98	17.8(0.5)/18.4(0.9)	17.8(0.5)/18.4	2.70(0.08),40.67(0.08)	NA	NA	NA
IRS1	^{12}CO	4.5	-95.39,-78.98	17.6(0.4)/17.4(0.6)	17.6(0.4)/17.4	2.69(0.10),40.72(0.09)	NA	NA	NA
IRS1	^{12}CO	2.8	-29.75,-16.63	9.2(0.4)/9.0(0.9)	10.0(1.0)/11.4	2.93(0.16),40.43(0.13)	0.6(0.3)	2.1(0.4)	-80(20)
IRS1	^{12}CO	4.5	-29.75,-16.63	10.0(0.4)/10.4(0.7)	10.0(0.4)/10.4	3.06(0.17),40.59(0.17)	NA	NA	NA
IRS1	^{12}CO	4.5	-78.98,-64.22	58.9(0.4)/??	918(4)/??	NA,NA	$\sim$70	$\sim$85	$\sim$40
IRS1	^{12}CO	4.5	-45.75,-29.75	72.3(0.4)/??	698(3)/??	NA,NA	$\sim$36	$\sim$24	$\sim$0
IRS1	^{12}CO	2.8	-78.98,-64.22	27.2(0.5)/??	710(5)/??	NA,NA	$\sim$62	$\sim$75	$\sim$40
IRS1	^{12}CO	2.8	-45.75,-29.75	34.6(0.5)/??	559(4)/??	NA,NA	$\sim$30	$\sim$18	$\sim$0
IRS1	HCO$^+$	4.5	-74.06,-64.22	1.71(0.08)/??	37.1(0.6)/??	NA,NA	$\sim$30	$\sim$60	$\sim$15
IRS1	HCO$^+$	4.5	-45.76,-37.96	1.57(0.07)/??	25.1(0.5)/??	NA,NA	$\sim$45	$\sim$20	$\sim$0
IRS1	HCO$^+$	4.5	-64.21,-59.50	7.2(0.2)/??	65.7(1.3)/??	NA,NA	$\sim$45	$\sim$50	$\sim$10
IRS1	^{13}CO	4.5	-64.21,-59.50	7.6(0.4)/??	113(2)/??	NA,NA	$\sim$25	$\sim$65	$\sim$40
IRS1	^{13}CO	4.5	-56.01,-51.09	8.5(0.4)/??	312(4)/??	NA,NA	$\sim$40	$\sim$160	$\sim$30
IRS1	^{13}CO	4.5	-49.86,-45.76	4.9(0.4)/??	24.2(1.1)/??	NA,NA	$\sim$12	$\sim$30	$\sim$-35
NGC7538Sa[a]	^{12}CO	2.8	-78.98,-64.22	24.3(0.4)/21.5(1.5)	79.1(1.8)/76	-2.24(0.16),-37.90(0.16)	3.9(0.4)	4.9(0.5)	-49(90)
NGC7538Sa[b]	^{12}CO	2.8	-45.75,-37.96	5.8(0.4)/5.2(0.6)	15.7(0.9)/15.3	2.0(0.4),-43.8(0.3)	2.1(0.8)	6.0(0.9)	-49(9)
NGC7538Sa[b]	^{12}CO	2.8	-45.75,-37.96	NA/2.3(0.5)	NA/4.3	6.7(0.7),-48.3(0.7)	2(2)	3(2)	-33(90)
NGC7538Sb	^{12}CO	2.8	-45.75,-41.24	3.1(0.3)/2.9(0.5)	5.0(0.4)/7.4	-2.9(0.3),-43.9(0.4)	3.2(1.1)	3.7(1.2)	63(90)
NGC7538Sf	^{12}CO	2.8	-45.75,-31.38	7.0(0.4)/5.7(0.9)	36.0(1.4)/34.6	-13.7(0.6),-44.7(0.5)	4.7(1.1)	8.1(1.9)	55.8(90)
NGC7538Sa[a]	HCO$^+$	4.5	-77.45,-64.22	4.48(0.09)/4.0(0.4)	11.4(0.3)/11.6	-2.2(0.3),-38.0(0.3)	5.9(1.8)	6.5(1.9)	-51.8(90
NGC7538Sa[b]	HCO$^+$	4.5	-45.75,-39.60	0.96(0.03)/0.76(0.13)	3.02(0.17)/2.8	2.7(1.2),-45.6(1.2)	6.4(1.8)	8.3(3.2)	-61.7(90)
NGC7538Sa[b]	HCO$^+$	4.5	-45.75,-39.60	NA/0.57(0.17)	NA/1.4	7.0(1.2),-53.5(0.9)	9(5)	3(4)	66.6(90)
NGC7538Sb	HCO$^+$	4.5	-45.75,-41.24	0.56(0.06)/0.71(0.11)	0.56(0.06)/0.71	-2.2(0.5),-44.7(0.4)	NA	NA	NA

Table 5.8 (cont'd)

Source Id	Line	Resolution “	Velocity Range km s^{-1}	Peak Flux Jy km s^{-1}	Flux Jy km s^{-1}	Peak Position “	Width “	Length “	Position Angle degrees
NGC7538Sf	HCO^+	4.5	-45.75,-36.32	1.17(0.08)/1.08(0.13)	3.6(0.2)/5.0	-13.0(0.5),-44.0(0.5)	7.3(1.0)	8.9(1.3)	38.1(90)
NGC7538Sa[a]	^{12}CO	4.5	-83.91,-64.22	42.6(0.4)/40(2)	87.6(1.1)/88	-2.38(0.14),-37.82(0.14)	4.0(0.6)	5.8(0.7)	-55(90)
NGC7538Sa[b]	^{12}CO	4.5	-45.75,-37.96	9.5(0.3)/8.2(1.0)	25.1(0.8)/20.0	1.6(0.4),-43.6(0.3)	2.4(0.5)	8.7(1.3)	-53(6)
NGC7538Sa[b]	^{12}CO	4.5	-45.75,-37.96	NA/2.7(0.4)	NA/14.9	9(2),-54(2)	4.4(1.7)	17.1(8.9)	-33(11)
NGC7538Sf[b]	^{12}CO	4.5	-45.75,-33.04	12.2(0.4)/11.2(1.3)	38.4(1.0)/34.5	-13.5(0.5),-44.6(0.4)	6(2)	7.1(1.9)	65(90)
NGC7538Sf[b]	^{12}CO	4.5	-45.75,-33.04	NA/6(2)	NA/6	-7.5(1.0),-41.0(0.8)	NA	NA	NA
NGC7538Sa[a]	HCO^+	4.5	-64.21,-62.57	1.22(0.13)/1.19(0.06)	2.6(0.2)/4.0	-1.28(0.18),-37.70(0.2)	5.9(0.4)	8.0(0.6)	-33(12)

[a]The blue lobes of NGC 7538 Sa, b and f are largely blended making individual idenfitication of flux characteristics difficult at the resolution of these observations.

[b]Multiple components have been fit. The integrated and image peak values reflect the entire region while the Gaussian fits are component based.

Note. — Offsets are with respect to the mosaic pointing center, (α,δ)=(23:13:45.00,+61:27:30). -64.21km s^{-1} is the dividing line between high and low velocity emission on the blue-shifted side. -45.76km s^{-1} provides the same limit on the red-shifted side. Systemic velocity depends on the source in question. The double values of flux are the integrated in the region compared and the integrated flux of a Gaussian fit. Similarly, the two values of peak flux are in the map and of the best-fit Gaussian. Gaussian fits to peaks may show larger flux than the map integrated flux due to the fact that the Gaussian may have significant flux off the map, i.e. the Gaussian fit may recover flux which was excluded from the fit because of a blended source. In instances where Gaussians did not well approximate the structure, the position was determined by the centroid and the width and length were measured at the 4σ position. The best-fit Gaussian peak and integrated flux are indicated by ?? in these cases.

Table 5.9. NGC 7538 Outflow Properties II

Source Id	Line	Resolution “	Velocity Range km s^{-1}	Mass $M_\odot$	Momentum $M_\odot$ km s^{-1}	Energy 10^{45}ergs	3^{rd} Moment 10^{51} ergs cm s^{-1}
NGC7538Sabf	^{12}CO	2.8	-78.98,-64.21	2.66	33.5	4.64	14.1
NGC7538Sa	^{12}CO	2.8	-45.75,-37.96	0.216	2.80	0.382	1.08
NGC7538Sb	^{12}CO	2.8	-45.75,-41.23	0.065	0.74	0.087	0.22
NGC7538Sf	^{12}CO	2.8	-45.75,-31.38	0.447	6.62	1.07	3.76
NGC7538Sabf	^{12}CO	4.5	-83.91,-64.21	3.02	39.5	5.83	19.6
NGC7538Sab	^{12}CO	4.5	-45.76,-37.96	0.865	10.5	1.32	3.48
NGC7538Sf	^{12}CO	4.5	-45.76,-33.04	1.33	18.1	2.62	8.23

Note. — Offsets are with respect to the mosaic pointing center, (α,δ)=(23:13:45.00,+61:27:30). -64.21km s^{-1} is the dividing line between high and low velocity emission on the blue-shifted side. -45.76km s^{-1} provides the same limit on the red-shifted side. Systemic velocity depends on the source in question. The double values of flux are the integrated in the region compared and the integrated flux of a Gaussian fit. Similarly, the two values of peak flux are in the map and of the best-fit Gaussian. Gaussian fits to peaks may show larger flux than the map integrated flux due to the fact that the Gaussian may have significant flux off the map, i.e. the Gaussian fit may recover flux which was excluded from the fit because of a blended source. In instances where Gaussians did not well approximate the structure, the position was determined by the centroid and the width and length were measured at the 4σ position. The presence of multiple identifying cores indicates that the measurement is of the combined outflow lobes. Blended blue-shifted emission is assigned in the proportion 20% to Sf and 80% to Sa.

Table 5.10. NGC 7538 Outflow Properties III

Property	NGC 7538Sa	NGC 7538Sf
$M_{Red}/M_{Blue}/M_{Total}$ ($M_\odot$)	0.87/2.42/3.29	1.33/0.60/1.93
$P_{Red}/P_{Blue}/P_{Total}$ ($M_\odot$ km s^{-1})	10.52/31.58/42.10	18.08/7.89/25.97
$E_{Red}/E_{Blue}/E_{Total}$ (10^{45}ergs)	1.32/4.67/5.99	2.62/1.17/3.79
L_{Red}/L_{Blue} (pc)	0.15/0.18	0.16/??
W_{Red}/W_{Blue} (pc)	0.11/0.14	0.12/?
V_{max} (Red/Blue) (km s^{-1})	18.04/-22.98	22.96/-22.98
V_{avg} (km s^{-1})	13	13
Time Scale (10^4 years)	1.3	1.2[b]
Position Angle (degrees)	-35	47

[a]Calculated using the longer length scale only. The outflow is almost certainly larger so the timescale would then be larger.

[b]A blue lobe size estimate is not possible so the red-side is used in these calculations.

Note. — M, P, E, L, and W are the mass, momentum, energy, length, and width. Values for the blue lobes of NGC7538Sa and f are estimated from the proportions of momentum in the red of the ^{12}CO, 2.8″ images over the extreme velocity channels. Insuffient information is available to disentangle the properties of NGC7538Sa and b although it is clear that two outflow are present. The estimates of total properties include emission near the systemic velocity of the source which is not easily assigned to the red or blue lobe in terms of velocity. This flux is certainly related to the outflow though the emission may be inflated by cloud emission and these numbers should be regarded with some skepticism. The emission arising from the blue lobe of NGC7538Sf cannot be easily disentangled from the flux of Sa, which dominates at velocities in the region -64 to -59.5 km s^{-1}. Here, I assume the extreme velocity proportion applies but only to flux near the core while extended emission is assigned exclusively to Sa. Sf appears to have a different systemic velocity than Sa or b though this velocity is highly uncertain. Momentum and luminosity, which depend on the sign of the velocity component do not have these cloud like components added as they are relatively meaningless over regions where the sign of velocity is not well constrained. The inclusion of near cloud velocities was made to allow maximal properties to be determined but these results can vary strongly with choice of systemic velocity and opacity correction which is somewhat uncertain given the lack of single dish data. The use of the redder velocity for NGC7538Sf results in little change to the values whereas use of the blue-shifted velocity balences the mommentum on the red and blue side and would provide substantially less energy on the blue side resulting in a less luminous outflow overall, however, given the blended nature of the blue side such an approach is not possible.

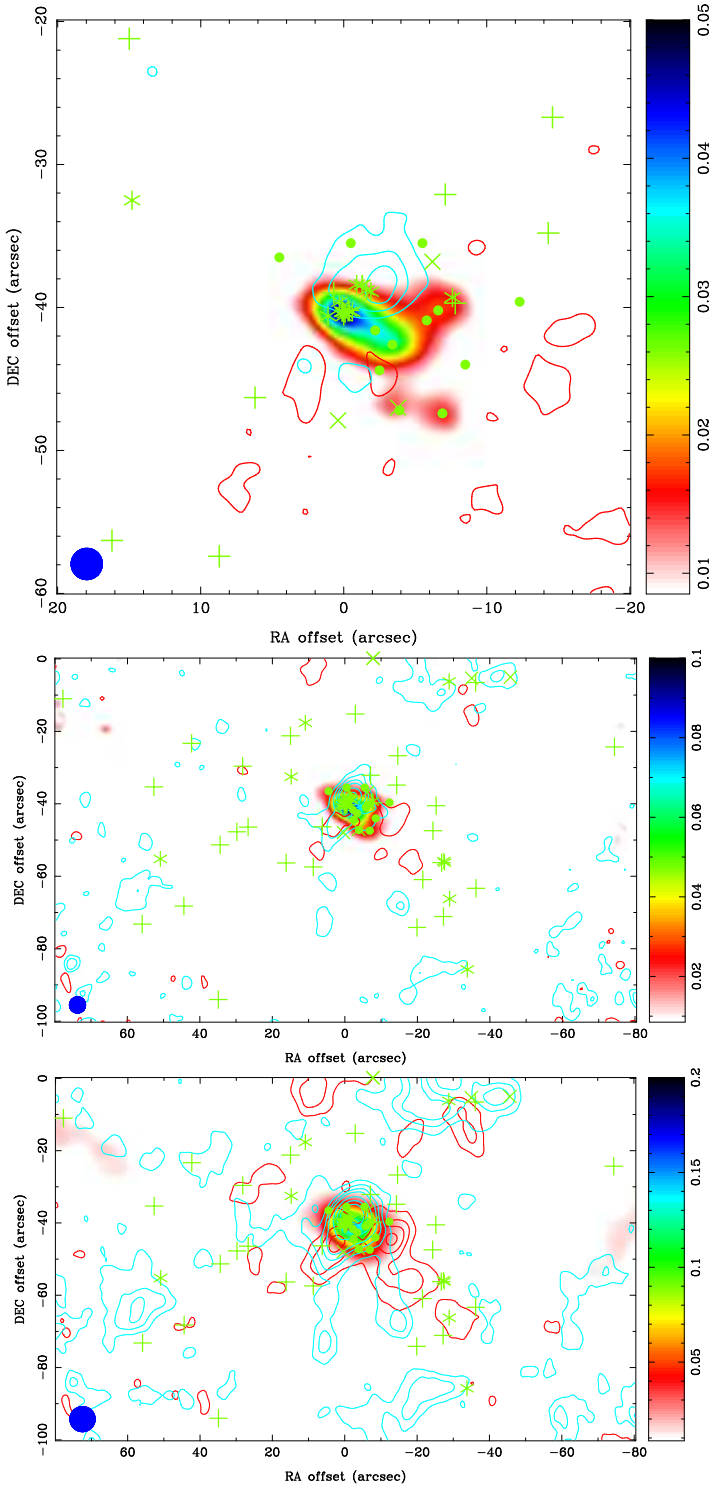

Figure 5.10 NGC 7538S and vicinity are shown. The contours of very high velocity blue- and red-shifted HCO^+(1-0) emission are shown in blue and red, respectively. The top, middle and bottom panels show the 2.2″, 4.5″, and 7.0″ images, respectively. The background color image is the relevant resolution continuum image. Contours begin at 0.5 Jy km s^{-1} except in the 2.2″ red-shifted contours, which start at 0.25 Jy km s^{-1}. Emission is at 4σ or higher. Continuum emission begins at 8.5 mJy. Contours are as described in Figure 5.3.

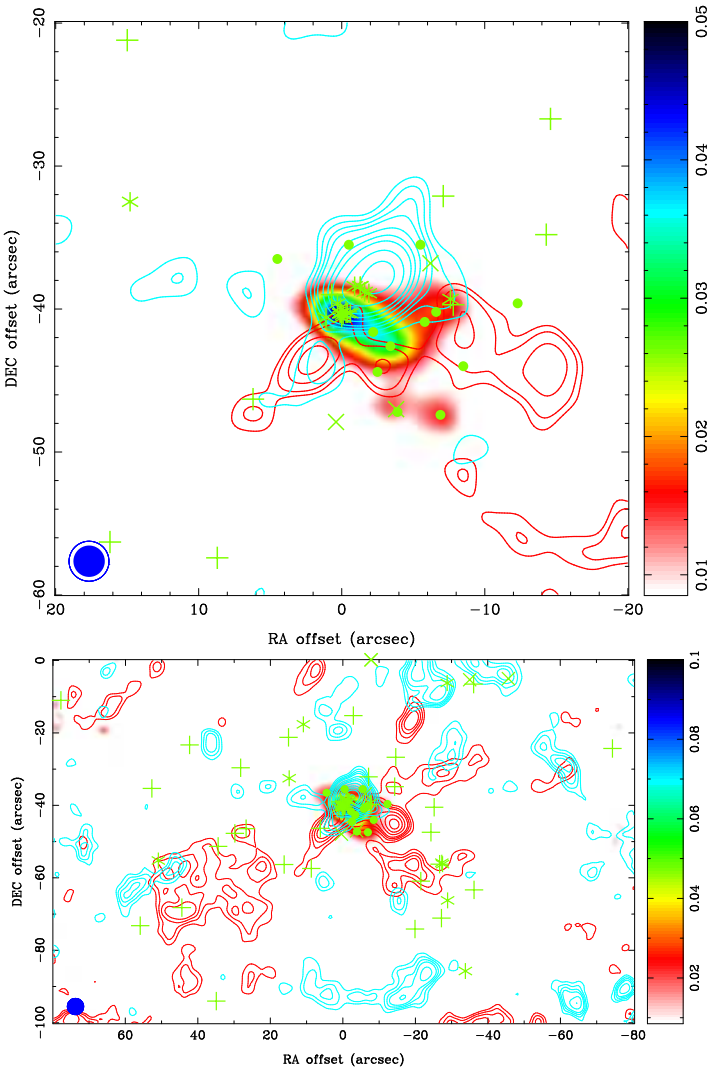

Figure 5.11 NGC 7538S and vicinity are shown. The contours of very high velocity blue- and red-shifted ^{12}CO(1-0) emission are shown in blue and red, respectively. The top panel shows the 2.8″ resolution image while the bottom panel shows 4.5″ resolution. The background color image is the relevant resolution continuum image. Contours begin at 2 and 1.5 Jy km s^{-1} for blue-shifted and red-shifted contours, respectively. Emission is at 4σ or higher. Continuum emission begins at 8.5 mJy. Contours are as described in Figure 5.3. Symbols are described in Figure 5.6

The picture at high spatial resolution was rather clean with clear association of outflow feature with continuum and/or $C^{18}O$ core. In the vicinity of NGC 7538S, the morphology is quite similar at lower resolution. There is still evidence of outflow activity from NGC 7538Sa, b/c, and f, with the red-shifted lobe of NGC 7538Sb now being blended with the NGC 7538Sa lobe. The red shifted lobe of the outflow from NGC 7538Sf is more extended than at high resolution, suggesting that the distant red shifted peak seen in the high resolution data is indeed associated with the outflow. If the larger scale emission that extends from the bright, red-lobe of NGC 7538Sf in Figure 5.11 to the southwest and northwest is associated with the outflow, it indicates that the NGC 7538Sf outflow is far less collimated, and therefore likely older than the NGC 7538Sa and b flows.

At low velocities, the morphology at low emission levels becomes extremely complicated and the outflow emission begins to be blended with filaments, confusing the interpretation. The structure of these features is highly uncertain given the lack of large angular scale information, and further discussion of the origin or properties of these features awaits single dish data.

5.4.4.3 Infall

NGC 7538Sa lends itself to calculation of infall mass via all three methods described in §5.4.1. Taking the infall velocity to be approximately the rotational velocity measured above in $C^{18}O$, the radius at the location where the velocity shift appears to flatten, and the density derived from the continuum mass towards the source, the mass accretion rate appears to be approximately 1.5×10^{-3} $M_\odot$ yr^{-1}. The infall mass can also be calculated from the size and velocity of the outflow lobe from NGC 7538Sa. The characteristic length and velocity of the outflow lobes are 0.17 pc and 13 km s^{-1}, respectively. This gives an accretion rate of 8×10^{-4} $M_\odot$ yr^{-1}.

Finally, the accretion rate is calculated from the absorption spectra. Figure 5.12 shows the HCO^+ spectral line. The systemic velocity is determined from a variety of optically thin or near optically thin tracers (e.g. $H^{13}CN$, DCN, $H^{13}CO+$, Sandell et al., 2008). A Gaussian, fixed to the systemic velocity, is fit to the blue side of the

line. The data are subtracted from this line to provide an absorption profile. The only remaining difficulty is the correction for optical depth which is then integrated and converted to a mass. A comparison of the $H^{13}CO^+$ peak and the HCO^+(1-0) peak reveal that the optical depth between the core and the front edge of the cloud is $\sim$6. Assuming the optical depth falls off as a Gaussian of width similar to the cloud component and that equal quantities contribute from the back of the cloud, the total infalling mass is then 12.1 $M_\odot$. Using the free-fall rate as the infall timescale, the accretion rate is 6×10^{-4} $M_\odot$. A correction for the fact that the low velocity infalling mass occupies a larger volume can be made and this results in accretion rates larger by a factor of 1.5, i.e. 9×10^{-4} $M_\odot$ Table 5.11 summarizes all the infall calculations. For NGC 7538Sa, the accretion rates are within a factor of 2. Given the uncertainties involved, this is excellent agreement.

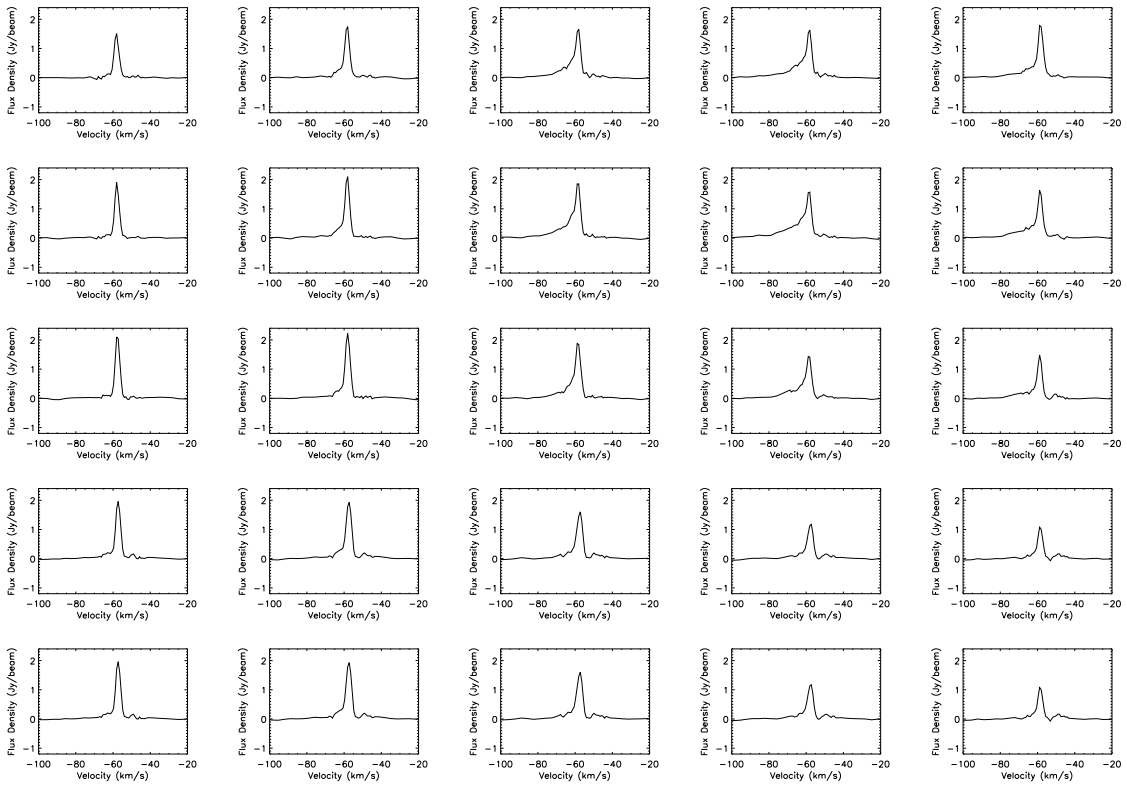

Figure 5.12 HCO^+ self absorption profile toward 25 positions centered on NGC 7538Sa. Asymmetric line profiles are seen in every panel.

Table 5.11. NGC 7538 Infall Estimates

Source Id	Method	Velocity km s^{-1}	Mass $M_\odot$	Timescale years	Accretion Rate 10^{-4} $M_\odot$ yr^{-1}
IRS1	Absorption	-60,-52	6.8	30000	2
NGC7538Sa	Absorption	-61,-35	12.1	21000	6-9
NGC7538Sa	Rotation	∼0.5	111[a]	NA	15
NGC7538Sa	Outflow	∼13	3×3.29[b]	13000	8
NGC7538Sf	Outflow	∼1.7	3×1.93[b]	12000	5

[a]The continuum mass of the NGC 7538Sa core is converted to a surface density for use in Equation 5.12 assuming the size determined for the core in Table 5.6.

[b]A factor of three is assumed to convert the outflow mass to accretion mass.

Note. — Offsets are with respect to the mosaic pointing center, (α,δ)=(23:13:45.00,+61:27:30). Fits to the blue side of the profiles are made assuming a fixed central velocity equal to the systemic velocity of the system. All HCO^+, 4.5″ spectra were taken towards the central position of the source given in Table 6.1. The uncertainty in the mass and accretion rate estimates is a factor of a few.

5.4.5 IRS1-3

5.4.5.1 Dense Structures

Continuum fluxes for IRS1 were obtained by fitting compact sources to the IRS1 region in the image plane and verified to be consistent with *uv*-plane fits to individual pointings of the mosaic. IRS1 was then subtracted in the *uv*-plane. The integrated flux associated with IRS1 is 1.46 and 1.62 at 91.4 and 108.1 GHz, respectively. This is consistent with a spectral index of 0.8 though with rather large error bars, 0.4, owing to the rather small frequency difference. The source may be resolved in the 108.1 GHz images with elongation to the north/south in the deconvolved images. A summary of the measured IRS1 properties is given in Table 5.5.

Figure 5.13 displays the various images associated with the continuum emission from IRS2 and an additional source, called IRS1a. Table 5.5 describes the flux and size of IRS2 and 1a in the 91.4 and 108.1 GHz images at a variety of resolutions. At 4.5″ and poorer resolution, IRS2 has rather simple structure. IRS1a, seen only in the top two panels of Figure 5.13, is the south-west extension of the main lobe of emission which is IRS2. The flux of IRS1a is difficult to estimate given the proximity to IRS2 and the likelihood of contamination from the subtraction of IRS1. However,

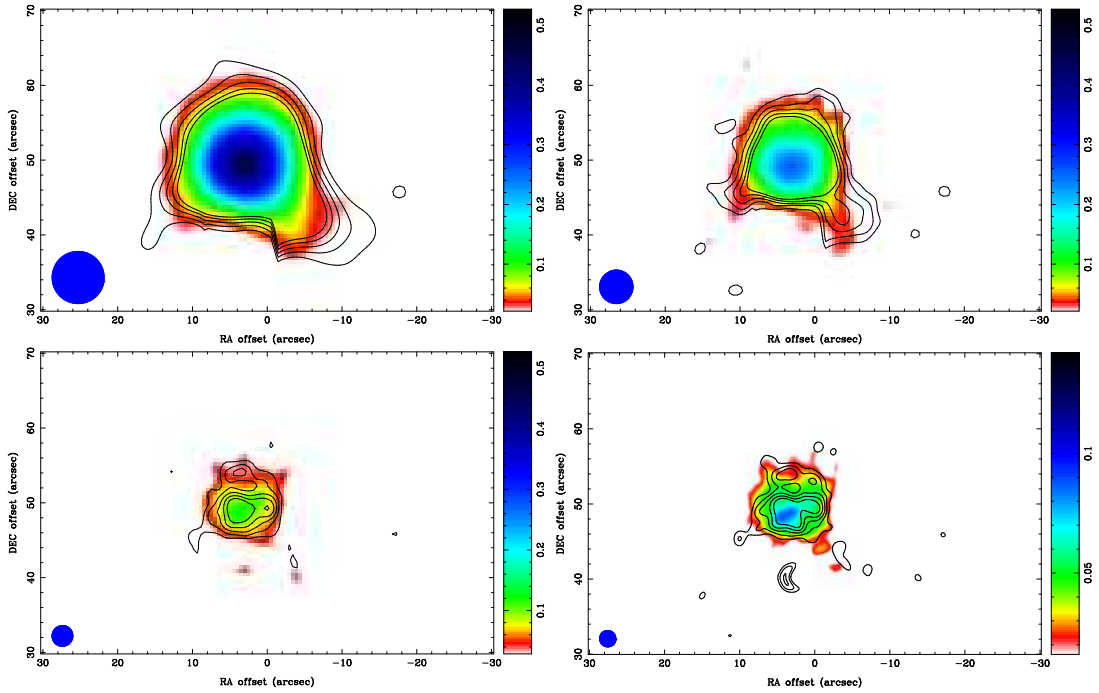

Figure 5.13 IRS2 and 1a are shown. IRS1a is the southwestern extension of IRS2 seen in the top two panels. Contours begin at 4σ and increase in steps of 2σ, where σ is given in Table 5.3. Colorscale is logarithmically stretched 91.4 GHz emission while the contours show 108.1 GHz emission. Minimum displayed flux is 4σ. The four panels show increasing resolution. With resolution of 7.0, 4.5, 2.8 and 2.2″ for the top-left, top-right, bottom-left and bottom-right panels, respectively. The beam size is shown in the bottom left of each panel for reference. The size scales of the images are the same in each instance.

the level of contamination can be seen from the degree of extension on the eastern side of IRS2 and the flux from the presumed location of IRS1a greatly exceeds the western extension.

Gaussian fits to IRS1a yield an offset from the mosaic center of $(\Delta\alpha, \Delta\delta) = (-4.35'', 41.45'')$ and deconvolved size of approximately 5.0″. Given the detection at 91.4 GHz is marginal, the measured spectral spectral slope is highly uncertain. The lack of detection at longer wavelengths, however, suggests that the emission may be from thermal dust emission.

The position of IRS2 at both frequencies is consistent within the uncertainties, $(\Delta\alpha, \Delta\delta) = (3.07'', 49.9'')$. The integrated flux is 1.016 ± 0.012 Jy at 91.4 GHz with a

spectral slope of $1.43^{+0.2}_{-0.4}$, consistent with a transition from optically thick to optically thin free-free emission or a combination of multiple regions. IRS2 quite circular on large scales with a size of $8.0\pm0.5''$. Gaussian fits produce completely unconstrained position angles while axis lengths are consistent to within 2σ in the 4.5 and $7.0''$ images at 91.4 and 108.1 GHz.

At higher resolution, however, the simple structure of IRS2 breaks down. This is not surprising given centimeter-wave observations have also shown complex morphology (Campbell, 1984; Gaume et al., 1995). For the most part, the 91.4 GHz images show less structure than the 108.1 GHz contours. This may be because the structures are brighter at 108.1 GHz or because of increased phase error associated with 108.1 GHz images. Given the features are not reproducible at both frequencies, their detailed properties are not confirmed, although the 108.1 GHz emission shows 4 individual peaks in the $2.2''$ image.

There is one common theme at both frequencies: a progression of the peak to the southeast and the appearance of an additional peak to the west of the low resolution center. Fits of three independent Gaussians reveal that the western peak is not statistically significant upon subtraction of the main emission and the southeastern peak (IRS2SE). In the $2.2''$ image, which is the most sensitive of the high-resolution images, IRS2SE has a flux between 38 and 51 mJy. The peak above the cloud is significant at the 3-4σ level in both frequencies so an estimate of the spectral slope has little meaning. No additional dense peaks are detected in both frequencies.

The $C^{18}O$ emission in the IRS1-3 complex is associated in some way with either filamentary structures or outflows. These structures will be discussed in the following section.

5.4.5.2 Continuum With Measured Primary Beam Correction

There are obvious, significant artifacts in the continuum emission surrounding IRS1. Given the brightness of IRS1, it is likely that the artifacts are due to improper pointing or primary beam correction. This is an ideal case for attempting to reduce the

residuals by use of the measured primary beam profiles (see Chapter 3) via the method discussed in Chapter 2.

Unfortunately the application of the primary beams to the entire dataset requires prohibitively long to execute given the current implementation. Therefore, only a select number of baselines, spanning a representative range in properties were selected. Baselines 1-4 and 5-9 were selected because these baselines have the largest phase gradients in the primary beam pattern. Baseline 2-3 was selected because it has little phase gradient and good pointing. Baseline 7-8 has very poor pointing but no phase gradient. Visibilities around transit were selected to limit the impact of parallactic angle rotation and pointings near IRS1 were selected because this is the most likely source of image degradation given its brightness.

The use of the measured voltage patterns results in a measurable change in only one of the four baselines tested, 1-4. For the pointing roughly centered on IRS1, there was no obvious change. This was expected because the contribution from the imaginary components is vanishingly small near the center of the beam. For pointings that placed IRS1 near the 60-70% point in the primary beam, a $\sim$20% change was made to the resulting visibilities, with the measured beam producing lower flux. This is also consistent with expectation. The goal was to subtract IRS1 from the dataset and the lower visibility amplitude is consistent with the measured profile resulting in better subtraction. For the pointing with IRS1 at the 20% point, generally poor subtraction was seen. This echoes the low signal-to-noise that results from observing sources well separated from the pointing center. The lack of changing visibility amplitudes on baseline 5-9 was initially somewhat surprising, but an examination of the directions of the pointing offset and the imaginary gradient reveals that the imaginary component would have little influence in this direction.

Further application of the method awaits better implementation of the algorithm but the initial results are promising. Several possibilities exist to improve the speed of function. First, the baselines that have fairly common primary beams could be processed in batch, rather than singularly. Given the uniform nature of the majority of the 6-m voltage patterns, it is possible that a factor of several reduction in run-

time could be generated in this way. Also, storing the baseline-based primary beam in memory and processing all the pointings at the same time would result in an additional factor of a few. Finally, the method lends itself well to parallelization. A reduction of a factor of 10 or more could be gained in this way. Together, the run-time could be reduced by at least two orders of magnitude.

5.4.5.3 Outflows

The region surrounding IRS1 is filled with a variety of structures. None of these structures appear to be associated with IRS2, IRS2SE, IRS1a or IRS3. At very high velocities in the ^{12}CO images, a compact source is clearly visible toward the IRS1 core. Figure 5.14 displays the integrated, very-high velocity contours towards IRS1. The position of IRS1 is indicated by the plus sign. There is a hint of displacement of red and blue shifted contours to the east and west and of a gradient in the velocity map in a similar direction. The velocity map was masked between -70 and -30 km s^{-1} so the velocities in the map represent averages of extreme velocity emission. The positions of the two lobes are only different at the two sigma level. It is also important to note that the detected emission extends to the edges of the band, implying that still higher velocity emission is probably present. The origin of this emission is either in the outflow or in the presumed disk. Spatial resolution of the emission is required to determine the gradient and offset position definitively.

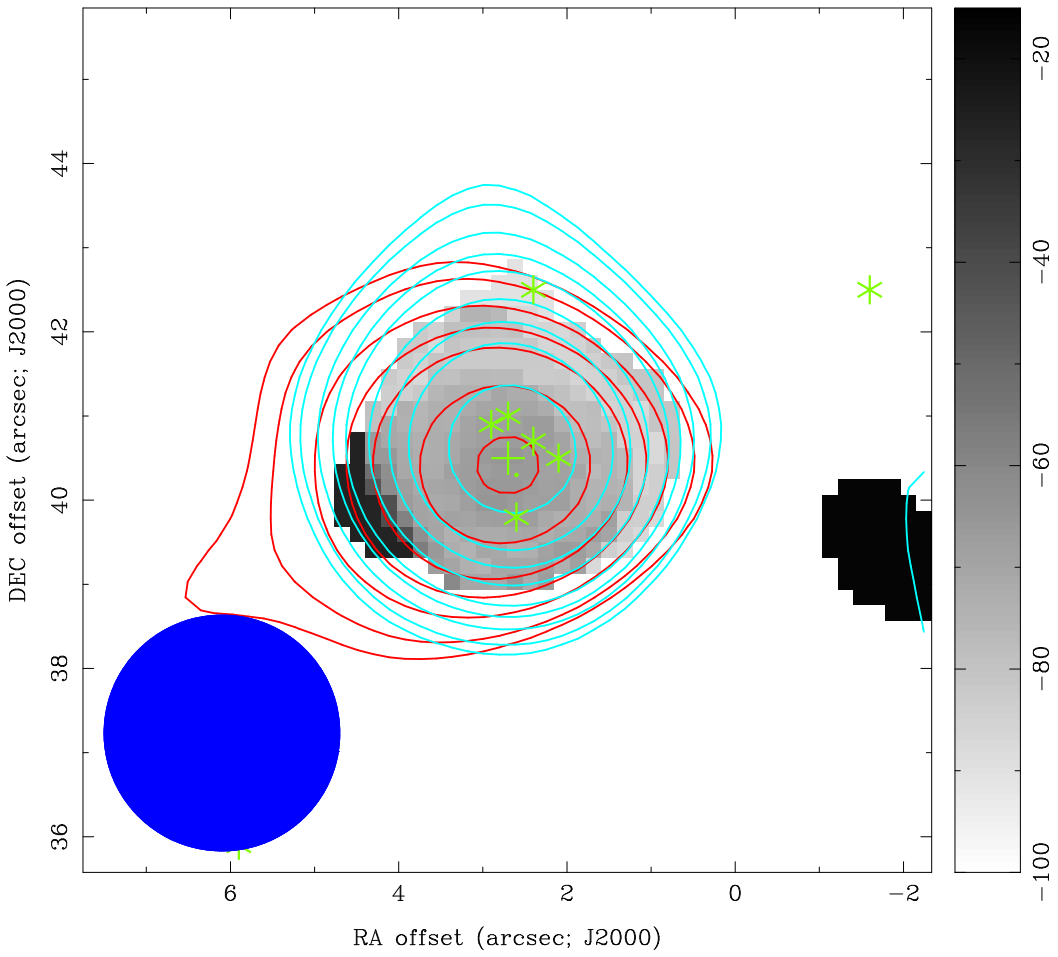

Figure 5.14 The first moment map of the ^{12}CO, 2.8″ image of IRS1 only in the highest velocity channels is shown. Intervening channels have been masked. Contours are red and blue-shifted emission from the same map. The lowest contour is 1.5 Jy km s^{-1} which is approximately 3σ in each case. The IRS1 position is indicated by the plus sign. Masers are indicated with star symbols. Blue shifted emission ranges from 21 to 37 km s^{-1} from the systemic velocity. On the red side, the emission ranges from 28 to 41 km s^{-1} with respect to the systemic velocity. Details of the contour intervals are found in Figure 5.3.

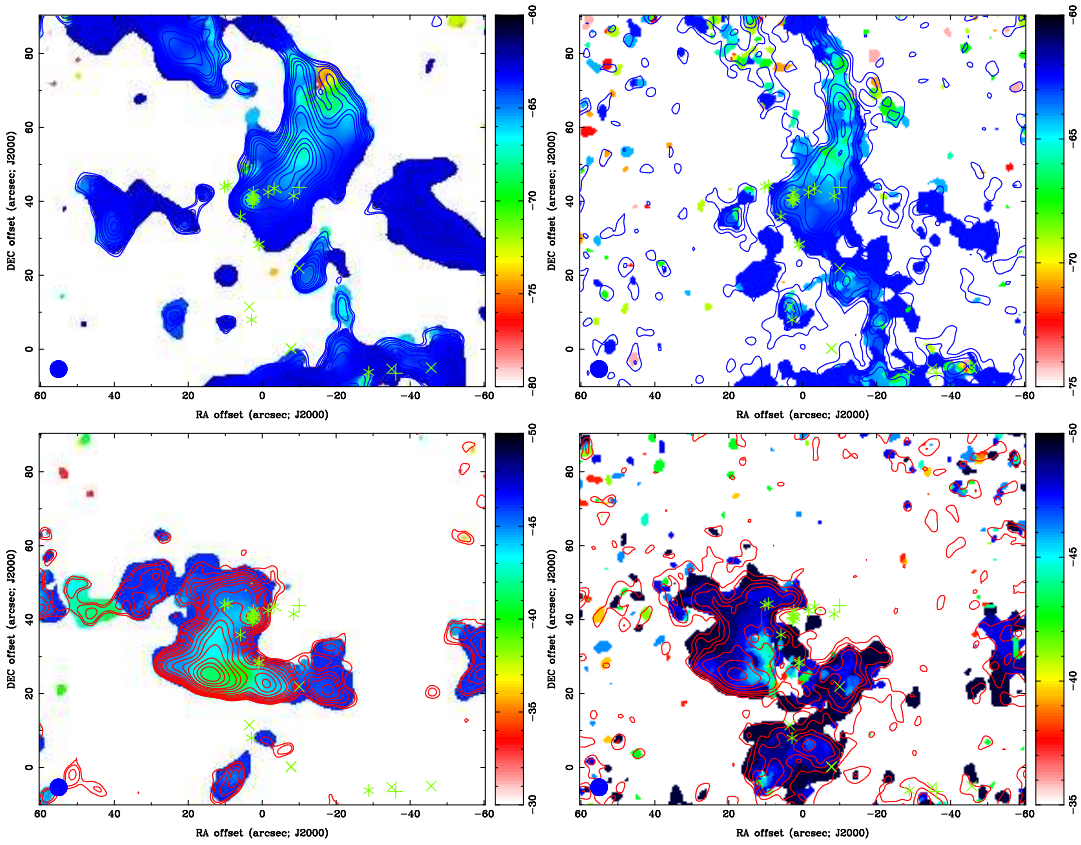

Figure 5.15 The first moment maps of IRS1 in ^{12}CO (left side) and HCO$^+$ (right side) are shown in color. Contours are the zeroth moment map. The top row shows blue shifted emission while the bottom row displays the red shifted emission. Contours of ^{12}CO begin at 1.5 Jy km s^{-1} while the HCO$^+$ contours begin at 0.25 Jy km s^{-1}. These levels are approximately 3σ. Details of the contour intervals are found in Figure 5.3.

At less extreme velocities, the outflow lobes become quite prominent. Figure 5.15 shows velocities ranging from 21 and 6 km s^{-1} on the blue side and 12 to 28 km s^{-1} to the red, where the velocities are now relative to the systemic velocity (-58 km s^{-1}). The top panels show blue shifted emission from ^{12}CO (left) and HCO$^+$ (right). The bottom panels show red shifted emission. Very extended features are revealed. On the blue side, the velocity with respect to IRS1 peaks near the position $(\Delta\alpha, \Delta\delta) = (-20'', -70'')$ and then decreases both to the north and south of that position. The trend in velocity on the red-shifted side is somewhat different. Here the peak velocities

are almost directly south if IRS1 and there is an east to west velocity trend along the lobe.

At lower, red shifted velocities, there is a large outflow lobe to the southwest of IRS1. The physical extent of this outflow lobe, as seen in red-shifted emission of Figure 5.4 is quite large, over 2 pc. It is unclear if the outflow lobe continues to still greater distances because it terminates near the edge of the image where the sensitivity is falling off. Along a line extending the red outflow lobe to the northeast of IRS1, blue shifted emission is seen. This emission serves as a northern counterpart to the higher velocity, blue-shifted lobe seen to the north-northwest of IRS1 in Figure 5.15. Again, the extent of the outflow lobe reaches the edge of the image suggesting that the full extent is not measured. If the blue-shifted emission from the IRS1 outflow is present on both sides of IRS2, it is possible that the high-velocity, red-shifted emission feature seen in Figure 5.15, is the eastern counterpart to the long, red-shifted outflow lobe seen in Figure 5.4. In any case, the outflow is oriented north-south or has a position angle of at most 10-20°. The properties of the outflows are summarized in Table 5.8. The mass and mass moments are not provided for IRS1. The emission in the dense regions well separated from the driving source are likely at a lower temperature than the 100 K assumed here. An assumption of cold gas at 20 K, would reduce the mass by a factor of 4 in those cases. Given this extended emission likely represents the bulk of the outflow mass, no estimate is given rather than providing an erroneous estimate. No data are available to determine the temperature in these extended regions.

5.4.5.4 Infall

The presence of an inverse P-Cygni profile, shown in Figure 5.16, requires a significant infall rate onto IRS1. The image reveals that the absorption profile has two components. At higher spatial resolution, this double peaked absorption spectrum persists, suggesting that there are two velocity components in the absorption. Unlike NGC 7538S, the outflow mass cannot be accurately measured due to its large extent compared to the size of the map. However, the accretion rate from the absorption spectrum can be calculated. The presence of two distinct velocity components in the

emission profile somewhat complicates the calculation. At the poorest spatial resolution, the component associated with the lower velocity emission dominates, consistent with low velocity gas being present over a larger area and the high velocity emission perhaps being associated with the outflow.

A Gaussian spectrum was fit to the lower velocity component of the emission profile assuming a systemic velocity of -58 km s^{-1}. An optical depth correction is clearly needed otherwise the HCO^+ would not have been seen in absorption. However, even $C^{18}O$ shows severe self absorption towards the position of IRS1. Unfortunately, unlike the case for NGC 7538S, there are no available $H^{13}CO^+$ data to make an optical depth estimate. The fit to the HCO^+ profile has lower amplitude than that seen in NGC 7538S, suggesting that the opacity may be lower in IRS1. The peak of the correction is assumed to scale with correction used on NGC 7538S. With all these caveats, the infalling mass is found to be 6.8 $M_\odot$. This results in an accretion rate of 2×10^{-4} $M_\odot$ yr^{-1}.

5.4.5.5 Other Regions

The region to the southeast of IRS1 has been assumed part of the outflow in this discussion. However, it is likely that there is an additional source in this region given the complex velocity structure seen in Figure 5.15. This structure is the subject of future work with higher velocity resolution. To the west, there is a filament connecting IRS1 to IRS4. This filament basically represents the cloud boundary (Davis et al., 1998). A detailed discussion of these regions is also the subject of further study.

5.5 Discussion

NGC 7538S appears to have an age gradient with older objects being to the northwest of the NGC 7538S clump. The *Spitzer* image shows that infrared bright sources like IRS11 dominate to the northwest of NGC 7538S. These sources are not as embedded as the sources to the southeast, as seen from the millimeter continuum map. The source NGC 7538Sf appears to be at an intermediate stage, with less accretion and

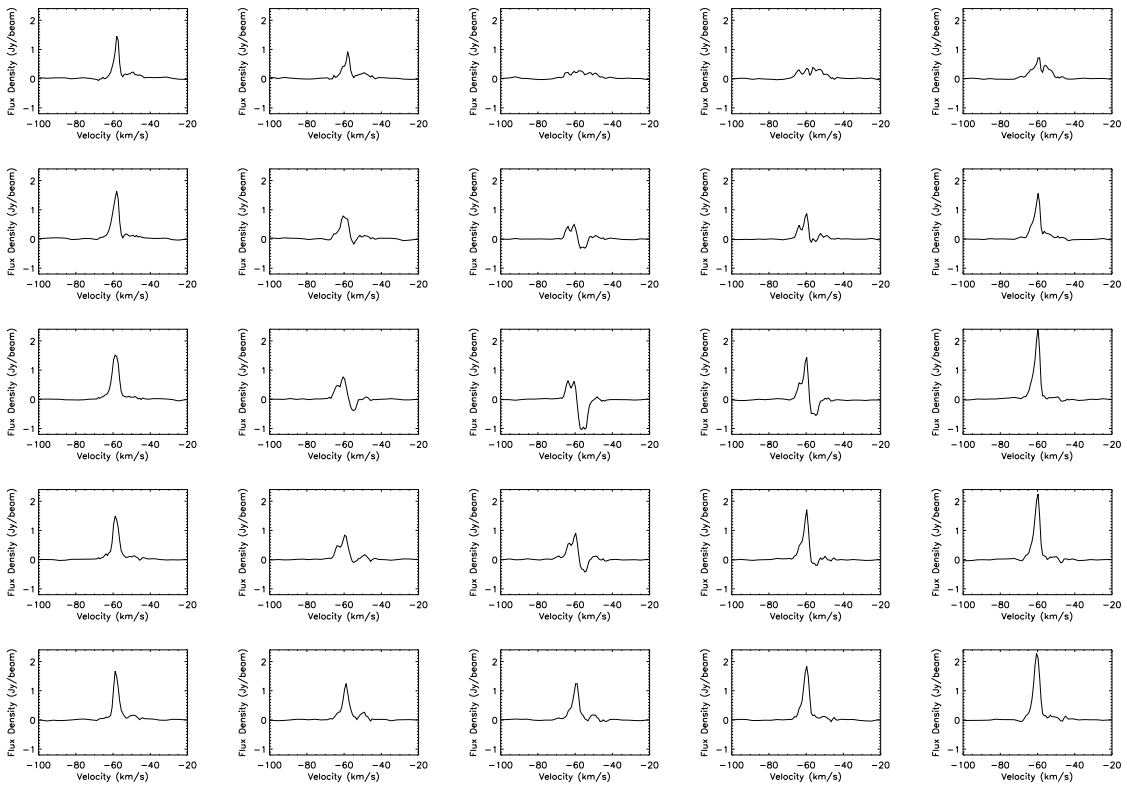

Figure 5.16 Inverse P-Cygni profile toward 25 positions centered on NGC 7538-IRS1 in the HCO^+ line.

a possibly less collimated outflow when compared to NGC 7538Sa. However, both of these sources are detected in the *Spitzer* image, albeit at low levels compared with IRS11.

IRS1, NGC 7538Sa, and NGC 7538Sf all exhibit signatures of significant mass accretion. The accretion rate onto IRS1 is a factor of 2.5 less than that of NGC 7538Sf and a factor of 4-5 less than NGC 7538Sa. Given the methods of mass measurement for the outflows are similar the difference in accretion rate predicted for NGC 7538Sa and f, approximately a factor of two, is likely real, although not particularly significant. Similarly, differences in accretion rates determined via absorption profiles also likely represent a true difference.

In the case of NGC 7538Sa, there is only a weak detection of free-free emission from the stellar position and there clearly is not an UCH II region. The accretion rate towards NGC 7538Sa is sufficiently large as to quench the formation of any significant

H II region (Churchwell, 2002, and references therein) given the stellar mass predicted for the source, $\sim$8 $M_\odot$ (Sandell et al., 2003). The free-free emission properties of the source are not well known and further observations are required to determine its exact nature.

NGC 7538Sf, on the other hand, shows no free-free emission. Since star formation seems to be proceeding northwest to southeast in the clump, the position of NGC 7538Sf suggests that this may be a more well evolved object, further suggesting it should show stronger free-free emission. The lack of such free-free emission from NGC 7538Sf then seems to imply that the object may be of somewhat lower mass and may not be capable of powering an H II region.

The situation with IRS1 is somewhat more complicated. The sources has been suggested to be a combination of two UCH II regions (e.g. Akabane et al., 1992; Wood & Churchwell, 1989) and an ionized wind (Reynolds, 1986; Sandell et al., 2009). Regardless of the nature of the free-free emission, what is clear is that the source is still experiencing accretion at a rate sufficient to quench the expansion of the classical H II region, which is 10^{-5} $M_\odot$ for the spectral type of IRS1 (Churchwell, 2002). However, such quenching predicts little to no free-free flux, but IRS1 is a strong free-free source.

If the radio emission is due to an UCH II region, the question is two fold. How is it that free-free emission is seen in the presence of such rapid accretion and why has the UCH II region not expanded given the time scale for expansion to a classical H II region is on the order of 100 years or less (Stahler & Palla, 2004)? The first would require that the spectral type, and therefore ionizing luminosity, is significantly in error. To exceed the quenching accretion rate the star would need to be an O4 or O5 star, not a O9/B0. If this were the case, then gravitational forces result in the compact size of the resulting H II region. Keto (2002) has shown that initially, the UCH II region cannot expand because the sound speed of the ionized gas does not exceed the escape velocity of the star. Their models predict that the evolution of the UCH II region is significantly slowed until the radius reaches a point where the sound speed reaches the escape velocity. However, it seems unlikely that the spectral type

is so significantly in error suggesting that the free-free emission is the result of an ionized wind.

The accretion rates of IRS1 and NGC 7538Sa differ by a factor of 3-4, suggesting that accretion onto IRS1 is either intrinsically slower or that accretion has slowed somewhat. The accretion luminosity, calculated from $L_{acc} = GM_*\dot{M}/R_*$ where M_* is the stellar mass, $\dot{M}$ is the accretion rate and R_* is the stellar radius, is $1.9{\times}10^4\,L_\odot$ for IRS1, less than 40% of the lower end of the range reported for the bolometric luminosity. This indicates that reprocessed stellar luminosity dominates the emission. However, Franco-Hernández & Rodríguez (2004) have reported variability in the free-free emission from IRS1 at 2 and 6 cm. The multiple absorption peaks in the IRS1 spectrum suggests that the variability may be due to episodic accretion. Variable accretion rates indicate that instabilities may play a vital role in the accretion process.

NGC 7538S has a bolometric luminosity of $1.8{\times}10^4\,L_\odot$, of which NGC 7538Sa likely contributes some fraction. The accretion luminosity for NGC 7538Sa is $\sim 5{\times}10^4\,L_\odot$ with factors of several uncertainty arising from the unknown stellar mass and radius. Also, this is an upper limit on the accretion luminosity because the material may not fall to the stellar surface. With those caveats, it appears as though NGC 7538Sa is dominated by accretion luminosity.

Regardless of the scatter in the accretion rate measures, all three major sources exhibit significant accretion. The outflow from NGC 7538Sa appears to be well collimated suggesting that it is a single source or a low order multiple system, not a cluster or association. The rapid accretion onto already massive protostars indicates that the massive stars in this region are not formed via collisions. The three accretion rates for NGC 7538S are consistent but suggest that the multiplier for converting mass outflow rate to mass infall rate should be 3 or perhaps greater.

The continued infall in the presence of an already massive protostar (IRS1) seen in this CARMA data casts doubt on star-star collisions as the source of this protostar. The observed accretion rate along with the estimated age of the outflow,

100,000 years,[10] suggests that the star could have formed from accretion given the $2\times10^{-4}\,M_\odot$ year^{-1}. This, of course, does not completely rule out the possibility of collisions very early in the evolution of IRS1. The collimated and extended outflow from IRS1 argues against a cluster powering the free-free emission from IRS1. Any group of stars would disrupt accretion disks and thus outflows periodically via interactions. The IRS1 outflow does not appear to have experienced any significant such event in the last ∼100,000 year given its rather smooth appearance. This all suggests that IRS1 formed via monolithic collapse.

However, these observations can by no means rule out competitive accretion as a mechanism. The best test to determine if star formation at high masses is a continuation of low mass star formation is a measurement of the core/clump initial mass function as a function of environment. Competitive accretion models predict that in denser clouds will form a higher fraction of lower mass cores than will less dense clouds. On the other hand, monolithic collapse predicts an initial mass function for cores which follows the stellar initial mass function. Both models predict a similar initial mass function for stars, but competitive accretion requires lower mass stars to accumulate mass via Bondi-Hoyle accretion to flatten out the stellar initial mass function and remove the excess of initially low mass cores.

To this end, this study serves as a cautionary tale. Recent surveys of the clump/core initial mass function in high-mass star-forming regions (Reid & Wilson, 2005, 2006a,b) have insufficient resolution to resolve the individual cores seen in NGC 7538S and they assume a constant temperature and opacity throughout the cloud. However, it is likely that NGC 7538Sa and f have higher temperatures when compared to other sources in NGC 7538S due to their outflows. Also, NGC 7538Sa contains free-free emission of unknown slope. This will alter the determination of the submillimeter slope. Therefore, a combination of long wavelength and submillimeter wavelength observations with resolution ∼1″ are needed so that individual cores can be resolved

[10]This is the lower limit derived by the velocity of the IRS1 outflow and its extent. The full extent of the outflow could not be determined from this study.

and accurate determinations of spectral index and free-free contamination can be made.

High fidelity images are needed to accurately extract the mass of clumps in such massive star-forming regions. Sandell & Sievers (2004) found evidence for several continuum clumps which are not seen in this work. This could be an indication of poor fidelity in the continuum images of either Sandell & Sievers (2004) or of the images presented here. However, using reasonable values for the frequency scaling of the flux, the additional sources detected at 450 μm are expected to be at best marginally detectable in the 108.1 GHz images. This is further evidence to the fact that high resolution, high fidelity, and high sensitivity observations are needed to accurately assess the mass functions.

These observations, while not able to conclusively show the presence of circumstellar disks, do support previous claims of a disk in NGC 7538S (Sandell et al., 2003, 2008), and, at a minimum, do not provide counter evidence to the claim that a disk surrounds IRS1 (Minier et al., 2000; Pestalozzi et al., 2004, 2006). Despite the $C^{18}O$ mass determined for NGC 7538S being lower by a factor of several when compared to the continuum mass estimate, the association of the bulk of the $C^{18}O$ emission with NGC 7538Sa supports the idea that NGC 7538Sa harbors a disk or at least a rotating envelope. The mass differential is almost certainly due to a combination of errors in the optical depth determination and freeze out of CO onto dust grains (Bergin et al., 2002). The gradient in $C^{18}O$ also supports the idea of a disk.

However, the pictures provided by these authors are very likely too simple. The kinematic signatures seen in IRS1 are suggestive of infall, outflow, disk and velocity structure within the outflow lobes. In NGC 7538S, the previously identified disk was quite large, covering the region now known to contain NGC 7538Sa, b, and c. Given that optically thin tracers show rotation signatures consistent with a disk across the NGC 7538S ridge (Sandell et al., 2008), this may be a signature of the massive, NGC 7538S clump rotating and then fracturing into several different objects (Krumholz et al., 2007).

The mass of the NGC 7538Sa and f outflows are on the order of 2-3 $M_\odot$, while the

momentum of the NGC 7538Sa outflow is $42\,M_\odot$ km s^{-1}. The NGC 7538Sf outflow has momentum of $26\,M_\odot$ km s^{-1}. The collimation factors (length divided by width) are approximately 1.3 but the outflows are not particularly well-resolved in width. All of the properties, including outflow length and energy, are at the lower end of the values typically seen for outflows from massive protostars (Beuther et al., 2002). Compared to typical properties of low mass stellar outflows, these two outflows are on the high end, especially considering the mass outflow rate (Arce et al., 2007). IRS1, on the other hand, is more consistent with typical properties of these massive star outflows (Beuther et al., 2002). The length is larger then the extent of the map and is therefore a parsec or longer. The mass from the emission within the map is likely to be on the order of 50 to $100\,M_\odot$, given the outflow fluxes seen in ^{13}CO. The relative sizes are a further indication that the outflows associated with NGC 7538S are younger than the outflow from IRS1, supporting the claim that the southern region is indeed younger than IRS1.

The IRS1 outflow position angle has been reported as $\sim$130-140° (Scoville et al., 1986). However, the observations presented here reveal that at higher resolution, the blue-shifted emission curves around to the north. There is also evidence of a southwestern lobe which is a counterpart to the previously identified red-shifted lobe to the southeast. The outflow presented here has a position angle more consistent with a position angle of 10-20°. This interpretation is more in agreement with the free-free morphology which reports the UCH II region or wind driven ionized cavity as being orientated north-south. This result emphasizes the importance of obtaining observations of lines less optically thick than ^{12}CO so that the dense regions can be probed for massive, slow moving components. In general, care should be taken to obtain truly optically thin tracers. Here, traditionally optically thin tracers like C^{18}O and HCO$^+$ are decidedly optically thick even in regions well separated from the dense clumps within the cloud.

5.6 Conclusions & Future Work

The results presented here represent the beginning of a study of NGC 7538 with observations of unprecedented fidelity and resolution. The new CARMA mosaiced observations reveal complex kinematics in NGC 7538-IRS1 and NGC 7538S, with NGC 7538S containing several outflows. Infall signatures are seen towards both IRS1 and NGC 7538S suggesting that rapid accretion, a few times 10^{-3} or 10^{-4} $M_{\odot}$ yr^{-1}, can occur across multiple evolutionary stages.

The morphology of the region is more complex than previously indicated. The outflow of IRS1 is orientated nearly 60° away from the previously reported position angle. This newly reported position angle is more consistent with the free-free morphology of IRS1. NGC 7538S contains at least three outflows whose blue-shifted lobes blend into the northwestern side of the clump. This northwestern edge is more evolved, containing several mid-infrared bright sources.

The NGC 7538S clump is not a monolithic object but instead breaks into several cores at high resolution. Nevertheless, NGC 7538Sa appears to support a massive disk. Future studies of the core initial mass function in massive star-forming regions and searches for disks around massive protostars should take care to consider the effect that the far greater distances have on the interpretation of the data.

The measured primary beams were used to subtract a source model for IRS1. On the most extreme baselines, the residuals were reduced. Application of the method to a far larger fraction of the dataset is required to definitively measure the overall improvement. The precise fidelity of the continuum image cannot be measured without an image model of the region, but it is likely on the order of 100 when considering the peak to residual noise level in the region around IRS1. This is at the lower end of the target fidelity. The fidelity of the spectral line images difficult to estimate in the absence of a model, however, the fidelity was sufficient so that the HCO^{+} image does not contain significant negative features other than the inverse P-Cygni profile. This is not the case with previous maps of the region obtained with only BIMA. The fidelity in the CO maps is likely poor given the absence of single dish data.

These observations were not able demonstrate the validity of competitive accretion or monolithic collapse. Competitive accretion predicts more low mass cores ($\lesssim 1\,M_\odot$) in more dense environments whereas monolithic collapse predicts a mass function of cores which is independent of environmental differences. Massive cores of a few hundred solar masses likely to inhabit very dense star-forming regions. Free-free sources could be brighter by factors of 1000 or more. This makes detecting $\sim 1\,M_\odot$ cores difficult. In the 1-mm band, a detection threshold of a few mJy is required to detect these low mass cores. Over small mosaic fields this sensitivity limit is achievable with CARMA, especially when the new correlator comes online. However, fidelity of the order of 1000 or more in the 1-mm band is not achievable even with the new corrective measures of Chapter 2. In the 3-mm band, this fidelity might be achievable depending on the specifics of the source distribution but the sensitivity limits cannot likely be obtained in reasonable integration times. In the end, observations with ALMA will be required to settle the question of competitive accretion versus monolithic collapse. CARMA can, on the other hand, determine the shape of the low mass end of the clump initial mass function in lower mass star forming regions which are free of extremely bright free-free sources.

To further exploit the data presented here, single dish observations in the CO lines are needed. Such data would allow the absorption profiles of CO to be used and opacity corrections to be made more accurately. 1.3 mm observations at 1-2″ would also allow better determination of the clump/core mass function in the region, provided IRS1 can be appropriately subtracted and fidelity of 300-400 can be achieved for 1-mm band observations. Such observations would also allow an estimate of the gas temperature which is vital to the measurements of the IRS1 outflow properties. The presence of the additional cloud component at -49 km s^{-1} presents intriguing possibilities for a discussion of triggered star formation especially given this additional component peaks at the southern locations of star formation but is largely absent from the north. But this, too, requires single dish data in the CO lines. Still more optically thin tracers are needed to trace the densest regions and provide more accurate optical depth corrections. Such observations can be easily obtained in the 1- and

3-mm bands when the new CARMA correlator comes on-line; the new correlator will allow simultaneous mapping of many isotopologue pairs with finer velocity resolution. Overall, CARMA is well equipped to attempt such observations, in partial thanks to the work presented in Chapters 3 and 4.

Bibliography

Akabane, K., Matsuo, H., Kuno, N., & Sugitani, K. 2001, PASJ, 53, 821

Akabane, K., Tsunekawa, S., Inoue, M., Kawabe, R., Ohashi, N., Kameya, O., Ishiguro, M., & Sofue, Y. 1992, PASJ, 44, 421

Arce, H. G., Shepherd, D., Gueth, F., Lee, C.-F., Bachiller, R., Rosen, A., & Beuther, H. 2007, Protostars and Planets V, 245

Arce, H. G., & Goodman, A. A. 2001, ApJ, 554, 132

Argon, A. L., Reid, M. J., & Menten, K. M. 2000, ApJS, 129, 159

Banerjee, R., Klessen, R. S., & Fendt, C. 2007, ApJ, 668, 1028

Bergin, E. A., Alves, J., Huard, T., & Lada, C. J. 2002, ApJ, 570, L101

Beuther, H., Schilke, P., Sridharan, T. K., Menten, K. M., Walmsley, C. M., & Wyrowski, F. 2002, A&A, 383, 892

Beuther, H., Schilke, P., & Gueth, F. 2004, ApJ, 608, 330

Beuther, H. & Shepherd, D. 2005, Cores to Clusters: Star Formation with Next Telescopes, 105

Blake, G. A., Sutton, E. C., Masson, C. R., & Phillips, T. G. 1987, ApJ, 315, 621

Blitz, L., Fich, M., & Stark, A. A. 1982, ApJS, 49, 183

Bonnell, I. A., Bate, M. R., Clarke, C. J., & Pringle, J. E. 1997, MNRAS, 285, 201

Bonnell, I. A. & Bate, M. R. 2006, MNRAS, 370, 488

Bonnell, I. A. & Bate, M. R. 2006, MNRAS, 370, 488

Bonnell, I. A. & Bate, M. R. 2005, MNRAS, 362, 915

Botschwina, P., Horn, M., Flugge, J., & Seeger, S. 1993, J. Chem. Soc., 89, 2219

Churchwell, E. 2002, ARAA, 40, 27

Hellwege, K. H. Landolt-Bornstein, Numerical Data and Functional Relationships in Science and Technology, Group II, Vol 14, subvolume a, Springer-Verlag, Heidelberg, 1982

Crampton, D., Georgelin, Y. M., & Georgelin, Y. P. 1978, A&A, 66, 1

Campbell, B. 1984, ApJ, 282, L27

Campbell, B. & Thompson, R. I. 1984, ApJ, 279, 650

Cesaroni, R., Galli, D., Lodato, G., Walmsley, C. M., & Zhang, Q. 2007, Protostars and Planets V, 197

Cesaroni, R., Neri, R., Olmi, L., Testi, L., Walmsley, C. M., & Hofner, P. 2005, A&A, 434, 1039

Davis, C. J., Moriarty-Schieven, G., Eislöffel, J., Hoare, M. G., & Ray, T. P. 1998, AJ, 115, 1118

Dickel, H. R., Dickel, J. R., & Wilson, W. J. 1981, ApJ, 250, L43

Downes, D. 1970, Astrophys. Lett., 5, 53

Franco-Hernández, R., & Rodríguez, L. F. 2004, ApJ, 604, L105

Garden, R. P., Hayashi, M., Gatley, I., Hasegaway, T., & Kaifu, N. 1991, ApJ, 374, 540

Gaume, R. A., Goss, W. M., Dickel, H. R., Wilson, T. L., & Johnston, K. J. 1995, ApJ, 438, 776

Gibb, E. L., Whittet, D. C. B., Boogert, A. C. A., & Tielens, A. G. G. M. 2004, ApJ, 151, 35

Henkel, C., Wilson, T. L., & Johnston, K. J. 1984, ApJ, 282, L93

Henkel, C.,Mauersberge, R., Wilson, T. L., Snyder, L. E., Menten, K. M., & Wouterloot, J. G. A. 1987, ApJ, 182, 299

Hildebrand, R. H. 1983, QJRAS, 24, 267

Ho, P. T. P. & Haschick, A. D. 1986, ApJ, 304, 501

Ho, P. T. P. & Young, L. M. 1996, ApJ, 472, 742

Israel, F. P., Habing, H. J., & de Jong, T. 1973, A&A, 27, 143

Johnston, K. J., Stolovy, S. R., Wilson, T. L., Henkel, C., & Mauersberger, R. 1989, ApJ, 343, L41

Kameya, O., Hasegawa, T. I., Hirano, N., Takakubo, K., & Seki, M. 1989, ApJ, 339, 222

Kameya, O., Morita, K.-I., Kawabe, R., & Ishiguro, M. ApJ, 355, 562

Kawabe, R., Suzuki, M., Hirano, N. Akabane, K., Barsony, M., Najita, J. R., Kameya, O., & Ishiguro, M. 1992, PASJ, 44, 435

Kennicutt, R. C. 2005, in IAU Symposium 227: Massive star birth: A crossroads of Astrophysics, editors R. Cesaroni, M. Felli, E. Churchwell, & M. Walmsley, p. 3

Keto, E., Zhang, Q., & Kurtz, Stanley. 2008, ApJ, 672, 423

Keto, E. 2002, ApJ, 580, 980

Keto, E. R., Ho, P. T. P., & Haschick, A. D. 1988, ApJ, 324, 920

Keto, E. R., Ho, P. T. P., & Haschick, A. D. 1987, ApJ, 318, 712

Kraus, S. et al. 2006, A&A, 455, 521

Krumholz, M. R., McKee, C. F., & Klein, R. I. 2005, ApJ, 618, L33

Krumholz, M. R., Klein, R. I., & McKee, C. F. 2005, in IAU Symposium 227: Massive star birth: A crossroads of Astrophysics, editors R. Cesaroni, M. Felli, E. Churchwell, & M. Walmsley, p. 231

Krumholz, M. R. & Klein, R. I. 2007, ApJ, 661, 1034

Krumholz, M. R., Klein, R. I., & McKee, C. F. 2007, ApJ, 656, 959

Li, Z.-Y., & Nakamura, F. 2006, ApJ, 640, L187

Lugo, J., Lizano, S., & Garay, G. 2004, ApJ, 614, 807

Martin, A. H. M. 1973, MNRAS, 163, 141

Maxia, C., Testi, L., Cesaroni, R., & Walmsley, C. M. A&A, 371, 287

Minier, V., Booth, R. S., & Conway, J. E. 2000, A&A, 362, 1093

Minier, V., Conway, J. E., & Booth, R. S. 2001, A&A, 369, 278

Moreno, M. A. & Chavarria, C. K. 1986, A&A, 161, 130

Ojha, D. K., et al. 2004, ApJ, 626, 1042

Ossenkopf, V. & Henning, Th. 1994, A&A, 291, 943

Pestalozzi, M. R., Elitzur, M., Conway, J. E., & Booth, R. S. 2004, ApJ, 603, L113

Pestalozzi, M. R., Minier, V., Motte, R., & Conway, J. E. 2006, A&A, 448, L57

Pudritz, R. E. & Banerjee, R. 2005, In IAU Symp. 227: "Massive Star Birth: A Crossroads of Astrophysics", eds. R. Cesaroni et al., 163

Reid, M. A. & Wilson, C. D. 2005, ApJ, 625, 891

Reid, M. A., & Wilson, C. D. 2006, ApJ, 650, 970

Reid, M. A., & Wilson, C. D. 2006, ApJ, 644, 990

Reynolds, S. P. 1986, ApJ, 304, 713

Richer, J. S., Shepherd, D. S., Cabrit, S., Bachiller, R., & Churchwell, E. 2000, Protostars and Planets IV, 867

Rots, A. H., Dickel, H. R., Forster, J. R., & Goss, W. M. 1981, ApJ, 245, L15

Rudolph, A., Welch, Wm. J., Palmer, P., & Dubrulle, B. 1990, ApJ, 363, 528

Rybicki, G. B. & Lightman, A. P. 1979, Radiative Processes in Astrophysics

Salpeter, E. E. 1955, ApJ, 121, 161

Sandell, G., Wright, M., & Forster, J. R. 2003, ApJ, 590, L45

Sandell, G. & Sievers, A. 2004, ApJ, 600, 269

Sandell, G., Goss, W. M., & Wright, M. 2005, ApJ, 621, 839

Sandell, G., Wright, M., & Goss, W. M. 2008, ApJ, submitted

Sandell, G., Goss, W. M., & Wright, M. 2009, in prep.

Sandell, G. private communication

Sault, R. J., Teuben, P. J., & Wright, M. C. H. 1995, ASPC, 77, 433

Schraml, J. & Mezger, P. G. 1969, ApJ, 156, 269

Scoville, N. Z., Sargent, A. I., Sanders, D. B., Claussen, M. J., Masson, C. R., Lo, K. Y., & Phillips, T. G. 1986, ApJ, 303, 416

Stahler, S. W. & Palla, F. 2004, The Formation of Stars, Wiley-VCH, Berlin

Tomisaka, K. 1998, ApJ, 502, L163

Turner, N. J., Quataert, E., & Yorke, H. W. 2007, ApJ, 662, 1025

Thronson, H. A. & Harper, D. A. 1979, ApJ, 230, 133

Welch, Wm. J., Dreher, J. W., Jackson, J. M., Terebey, S., & Vogel, S. N. Science, 1987, 238, 1550

Werner, M. W., Becklin, E. E., Gatley, I., Matthews, K., Neugebauer, G., & Wynn-Williams, C. G. 1979, MNRAS, 188, 463

Willner, S. P. 1976, ApJ, 206, 728

Wilson, T. L., Mauersberger, R., Walmsley, C. M., & Batrla, W. 1983, A&A, 127, L19

Wilson, T. L. & Rood, R. 1994, ARA&A, 32, 191

Wood, D. O. S. & Churchwell, E. 1989, ApJS, 69, 831

Woody, D. P., Scott, S. L., Scoville, N. Z., Mundy, L. G., Sargent, A. I., Padin, S., Tinney, C. G., & Wilson, C. D. 1989, ApJ, 337, L41

Wu, J. & Evans, N. J. 2003, ApJ, 592, 79L

Wynn-Williams, C. G., Becklin, E. E., & Neugebauer, G. 1974, ApJ, 187, 473

Yorke, H. W. & Sonnhalter, C. 2002, ApJ, 569, 846

Yorke, H. W. & Bodenheimer, P. 1999, ApJ, 525, 330

Young, L. M., Keto, E., & Ho, P. T. P. 1998, ApJ, 507, 270

Xu, Y., Zheng, X.-W., & Jiang, D.-R.

Zhang, Q., Hunter, T. R., Brand, J., Sridharan, T. K., Cesaroni, R., Molinari, S., Wang, J., & Kramer, M. 2005, ApJ, 625, 864

Zapata, L. A., Palau, A., Ho, P. T. P., Schilke, P., Garrod, R. T., Rodríguez, L. F., & Menten, K. 2008, A&A, 479, L25

Zhang, S. N., Yu, W., & Zhang, W. 1998, ApJ, 494, 91

Zhang, Q., Hunter, T. R., Sridharan, T. K., & Ho, T. P. T. 2002, ApJ, 566, 982

Zheng, X.-W., Zhang, W., Ho, P. T. P., & Pratap, P. 2001, ApJ, 550, 301

Zinnecker, H. & Yorke, H. W. 2007, ARA&A, 45, 481

Chapter 6

Summary and Future Work

6.1 Summary

This dissertation described the techniques I have developed to improve the image fidelity of the Combined Array for Research in Millimeter-wave Astronomy (CARMA). High image fidelity is particularly necessary to enable accurate astronomical imaging of sources in which the properties of faint emission must be distinguished in the presence of bright emission or in cases where the ratio of images needs to be determined accurately. Two common situations requiring high fidelity are:
(1) Initial mass function studies where the objects in question are expected to be clustered and the source intensities span several decades of flux.
(2) Observations where temperature, opacity, and spectral indices must be calculated from images.
While the science case for high image fidelity is not restricted to sources of any particular size scale, the deleterious effects on fidelity are larger for sources that are large compared to the primary beam. For this reason, I focused on improving the image fidelity of mosaiced observations.

Simulations were conducted to determine the effects of primary beam errors on mosaiced images. Pointing error provides the largest detriment to fidelity under typical assumptions about the primary beam. Relaxation of certain primary beam assumptions results in minimal reduction in fidelity. However, the presence of large surface inaccuracies can degrade fidelity significantly in a way which is not correctable

either at the time of observation or in post processing. If the beams are allowed to contain imaginary components, even greater reductions are made to fidelity.

To limit the influence of these surface errors, holographic data was obtained on all of the CARMA antennas. Surface corrections were applied to eight of the nine 6-m antennas, reducing the various surface RMS values from levels as high as 120 μm to 30-40 μm. The 10-m antennas were found to contain large illumination pattern offsets, which were corrected via optical path alignment. Beyond these corrections, repeated measurements of the primary beams, or, more precisely the antenna-based voltage patterns, were taken to determine the actual pattern shape. These patterns were applied to simulated data and it was found that incorrect assumptions about the primary beam shape result in factors of several reduction to image fidelity. A method was developed to correct these errors post observation. Symmetrized voltage pattern models were also constructed. These models can be directly imported into MIRIAD allowing factors of up to two improvement to image fidelity (see Chapters 2 and 3).

Reduction of the pointing errors was accomplished in two steps. First, the fit to the CARMA pointing model was improved by increasing the data collection rate by factor of four, i.e four times more points were available to constrain the fit. This resulted in approximately a factor of two reduction in the pointing RMS. Beyond this, a method was devised to allow optical pointing measurements within radio observations. The degree of improvement, especially to the 6-m antennas by day, is dramatic, with peak-to-peak pointing drifts reduced by factors of several. In addition to providing the opportunity to obtain high fidelity images, the method is also critical to obtaining 1-mm band, day-time observations. A specific example is presented which indicates that, in the absence of the optical corrections, the sensitivity of 1-mm band observations on the 6-m antennas can be reduced by up to a factor of two.

With methods to improve the sensitivity and image fidelity in hand, the new techniques were applied to the greatest extent allowable on observations of the massive star-forming complex NGC 7538. The aims of the study were to measure the properties of the various suspected outflows, determine the accretion rates of any massive

protostars detected and detect and possibly resolve any continuum structures in the region. High fidelity is required because continuum subtraction is required to see the absorption profiles which provide accretion measurements. It is also needed to resolve and detect continuum structures in the presence of the bright emission from the compact source, IRS1. Evidence that the presumed massive protostars are still accreting was found, suggesting that models of massive star formation that invoke stellar collisions do not apply in these cases. The presence of collimated outflows from these massive protostars suggests that single stars can be present over long time scales, a result which favors massive star formation via collapse of monolithic, massive cores. While the apparent fidelity of the resulting images was not as high as intended, probably $\sim$100 rather than 300 in the continuum image, the aims of the study were still met. Infall signatures were seen towards two protostars. The inverse P-Cygni profile seen towards IRS1 is certainly real and represents some of the best evidence to date of definitive infall onto a massive star. The southern clump, NGC 7538S, was resolved into several individual cores, three of which harbor outflows of varying ages.

Full application of the real voltage patterns and optical offset pointing on all tracks would likely have resulted in a continuum image with a factor of several greater fidelity, possibly as much as an order of magnitude greater. Most of this improvement comes from correcting for the offset in illumination patterns and deviations from the Gaussian profile, recall the combination results in a factor of five decrement in fidelity. The source structure in NGC 7538 is significantly more empty than the Cas A model, implying the higher fidelity can be achieved.[1]

On the other hand, if the holography adjustments had not been made the fidelity would likely have degraded by a factor of a few. The alignment errors were twice as large initially on the poorest performing antennas. In Chapter 2 it was shown that fixing one highly deviant baseline significantly improved the fidelity. Therefore, doubling the alignment offsets would likely resulted in a corresponding drop in fidelity of a factor of a couple. The amplitude scatter in the data is inconsistent with pointing drift, i.e. is it simply a scatter not a trend. The magnitude of this scatter is larger

[1]Gaussian models typically obtained fidelity of 1000 in the error free simulations.

than expected from typical pointing RMS suggesting that the amplitude scatter is dominated by something other than pointing and it is then difficult to estimate the the pointing error. However, doubling the pointing error, returning it to the historical levels, would have made 0.5% difference in the effective gain error and the fidelity could have been reduced by a factor of 1.5 or 2, but this was of course for the Cas A model. Finally, the surface adjustments reduced the effective gain error from surface errors slightly on average. The bulk of the gain was on a few particularly deviant antennas. The effect of large, single antenna deviations from the ideal surface was not simulated and the effects are difficult to predict.

The techniques developed and described here are applicable beyond CARMA. As the Atacama Large Millimeter Array (ALMA) is commissioned over the next few years, the number of projects which will be limited by image fidelity issues will grow. Successful (sub)millimeter astronomy research will depend on providing accurate and credible images to the astronomical community as a whole, not just to experienced radio interferometrists. It will be important that most of the time spent by the proposing scientist is used interpreting accurate images rather than reducing and imaging the data in a variety of ways to determine if specific structures are real or not. For this reason, it was an important part of this work to provide the optical offset pointing as a tool to the CARMA community in a way which requires minimal input from the user. The proposing scientist should not need to understand the details of how the pointing improvement is done, the pointing should simply be as good as possible. At CARMA, the user now sets a single flag and the software does the coordination of the antennas, selects appropriate sources and applies the proper corrections.

6.2 The Future

It is clear that there is much to be gained from imaging extended star-forming regions at high resolution with high fidelity. At CARMA, further improvements will continue

and new techniques will be required for use at ALMA to provide the greatest possible fidelity.

6.2.1 High Fidelity Science

6.2.1.1 Single Dish Correction with NGC 7538

The CARMA NGC 7538 HCO^+ data set was free of significant artifacts, indicating that the underlying agreement of the single dish and interferometric data was good. However, the CO observations displayed significant bowls around the more prominent features. Combination with single dish data will improve the quality of the image and allow the interface of the outflow and cloud to be measured. To date, little is known about the outflow cloud interface for high mass protostellar outflows. Nevertheless, the interface of the outflow and cloud measures the energy transfer from the outflow to the cloud and would provide important constraints to simulations which attempt to use outflow feedback as a means of continuing star formation.

In addition to single dish observations in the CO(1-0) transitions, single dish and array maps in 1.3 mm continuum emission will provide a better probe of thermal continuum sources and CO(2-1), combined with the CO(1-0) data, provides a measure of the temperature distribution to complement the density structure determined from the isotopologues of CO(1-0). Study of the nature of the filaments and the overall cloud morphology of NGC 7538 requires these additional data. These filaments could play an important role in star formation with over-densities in individual filaments collapsing into clumps like NGC 7538S which in turn collapse into cores which form stars.

6.2.2 Outflow Feedback in Nearby Star Forming Regions

The study of feedback need not be restricted to massive star forming regions. Wide-field, deep, single dish images of low mass star-forming regions in CO lines already exist. Along with H. Arce, I have begun a program to survey the denser portions of these regions with CARMA in CO lines. Observations of the Serpens star forming

cloud are in hand while observations of NGC 1333 are scheduled. Supplemental NGC 1333 data from BIMA and Serpens data from OVRO are also available.

6.2.3 Substructures in Disks

Comparisons of circumstellar disks at multiple submillimeter frequencies are becoming more available. Changes in the spectral index as a function of position reveals variations in the density structure and dust properties as a function of radius in the disk. At both CARMA (Isella) and the SMA (Andrews), large programs are underway to understand the radial structure of the continuum emission in these disks. Study of these steady-state disks is vital to determination of their detailed structure, which affects the models of planet formation around other stars by specifying the density and temperature distribution.

Gravitational instability in disks may also be of great importance to the formation of planets. While the possibility of detecting gravitational instability in the steady-state disks is unlikely, rapidly accreting disks may show signs of this behavior. Models and statistical analyses suggest that most if not all stars go through periods of enhanced accretion rate. If this is the case and gravitational instabilities play an important role in this outburst, rapid growth of planetesimals or direct planet formation can occur. Systematic observation of rapidly accreting protostars at high resolution awaits study. Such a study may reveal prominent infall signatures and possibly direct detection of spiral structures.

Finally, models have been proposed for determining the structure of a planetary system from the substructure in debris disks around nearby stars. With current interferometers and single dish telescopes these sources are far too faint to be subject to the concerns of image fidelity. However, ALMA combined with higher frequency observations will push the nearest such disks into the high fidelity regime. Given the study of these debris disks is the only way to detect ice-giant like planets around young stars, it is important to accurately represent their population from this method.

6.2.4 Enhancing Fidelity, Near Future

The voltage patterns of the 10-m antennas at CARMA still contain significant phase gradients across the beam. This is due to a combination of focus error in the plane perpendicular to the aperture and offset/misalignment of the receiver system. Further work on holography is being continued at higher resolution (Lamb & Corder, in prep). The alignment will hopefully be improved and the resulting voltage patterns will be used to correct future observations using methods similar to those proposed in Chapter 2. Eventually, the use of the measured primary beams should be integrated into the standard imaging pipeline, as long as sufficient improvements in speed can be made. The point here, like with the pointing, is to provide a means to improve the resulting images without the user having detailed knowledge of the underlying image restrictions.

The 3.5-m, SZA antennas have recently been moved to the CARMA site. When a 23-station correlator is available, these smallest antennas will provide measurement of baselines down to 3.5-4 m and increase the density of uv-points in the range 4-10 m. A challenge remains, however. While the sidelobes of the 10-m antenna voltage patterns are illuminated by the main beam wings of the 6-m patterns, the 3.5-m antennas will directly illuminate these sidelobes. In order to allow cross correlations of the 3.5- and 10-m antennas the shape and stability of the sidelobes must be determined. The basic analysis is outlined in this thesis but significant observational and modeling work remains.

6.2.5 Enhancing Fidelity, Far Future

ALMA will open new horizons for submillimeter astronomy. The improvement to sensitivity, wavelength coverage and resolution are so dramatic that the most influential science to come out of the array has probably not been considered yet. ALMA will bring with it increased difficulties because of its improved sensitivity. Astronomers will hope to push the instrument to its limit but for the theoretical limits to be reached new problems will need to be addressed.

In practice, the presence of phase gradients in the voltage patterns will cause time variable leakage terms in polarization studies. Polarization studies will be vital for understanding the structure of magnetic fields in the coming years. Given that the polarization signals are often 5% or less of the total signal and the variation in the leakage term will depend on the source strength itself, phase gradient effects could easily swamp the desired signal. The gradients must be minimized and the effects on the polarization term must be explored in more detail. The gradients may also be time variable due to gravitational stresses on the secondary mirrors. Active focus correction in three dimensions will need to be explored to obtain maximal fidelity.

The groundwork for high fidelity imaging at CARMA and beyond has been laid with this thesis. Short term improvements and long term directions have been discussed. Integrating submillimeter interferometric observations into astronomy at large requires that those with the specialized knowledge of the limitations and inner workings of these complex instruments provide the tools for the general user while pushing the frontier towards a deeper, broader, more fundamental understanding of the variety of sources which are observable.

Appendix A

Optical Alignment

The optical system[1] of the 10-m antennas consists of the 10.4 m primary surface of the antenna, a 0.61 m secondary mirror, and five additional reflections before the light path reaches the receiver feed horn. The five additional reflections are designed to create an image of the primary at the feed horn (Woody, private communication).

Any misalignment of these five mirrors or displacement of the secondary from the principal axis of the antenna will result in reduced aperture efficiency due to an improperly illuminated primary and phase gradients across the antenna voltage pattern on the sky. The alignment is altered by either adjusting the position of the secondary with respect to the plane perpendicular to the principal axis of the antenna, altering the set positions or orientations of any of the five mirrors between the secondary and the feed horn, and moving the entire cryostat.

All optical path adjustments were performed by David Woody over the course of April-May 2007 and April-June 2008. Adjustments were made for both the 3-mm and 1-mm receiver system. The basic approach to aligning the optics is as follows. A bright, optical light source is connected to a $\sim$1 cm bundle of optical fibers. The optical fibers are then mounted to the center of the secondary mirror as shown in Figure A.1. The precise orientation of the light source is irrelevant because the light source fully illuminates the tertiary mirror, however, there is a mounting feature on the secondary that roughly aligns the pointing of the fibers. The goal is then to create

[1]Here, optical system is meant in the sense of optics, i.e. the path the radio beam takes from the primary to the feed horn.

a sufficiently bright point on the secondary so that the point is visible in contrast to the rest of the secondary when viewed at the feed horn.

Figure A.1 A close up photo of the 10-m antenna secondary mirror is shown. The optical source is inside the black box mounted on the back side of the secondary mirror. The optical fiber connects the black box to a brass mounting tool shown at the center of the secondary. The resulting point of light is positioned at the center of the secondary and aimed towards the tertiary mirror.

The left panel of Figure A.2 shows an image of a piece of paper with cross hairs placed on the window to the cryostat at the feed horn. The right panel of Figure A.2 shows a close up of the same piece of paper now with the optical light source switched on. The goal of the alignment process is then to adjust the set position and orientation of the mirrors and the cryostat to center the bright point as closely as possible on the cross hairs.

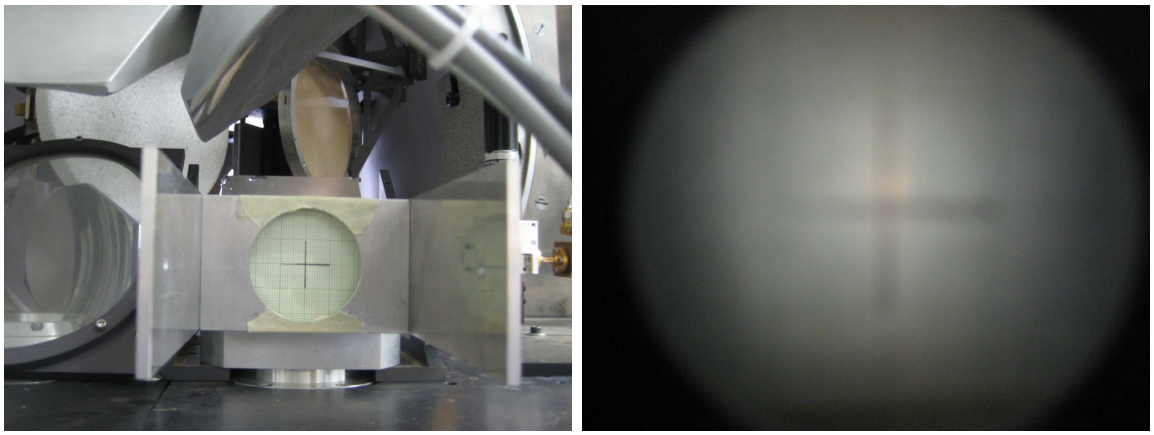

Figure A.2 The left panel shows a piece of paper with cross hairs drawn at the center of the feed horn. Ideally, the optical path is such that the bright point on the secondary will appear as a point at the center of the cross hairs. The right panel shows a close up of the cross hairs now with the optical source switched on. Here the alignment is seen to be reasonably good. The bright point may be slightly offset up and to the left but at the precision possible with this method, the alignment is acceptable.

Appendix B

Optical Telescope and Camera System

Each of the CARMA antennas is equipped with 102 mm refracting telescope. Each optical telescope is equipped with a motorized lens cap that can be opened or closed remotely using the CARMA control system. Figure B.1 shows the two optical telescopes used at CARMA.

A COHU 4910 Series, CCD video camera is mounted to each optical telescope. The cameras are focused by rotating the camera in or out along the threads of the C-mount. The combination of optical telescope and camera results in 1.25″ per pixel and a field of view of approximately 10′ by 15′. The camera is connected to a frame grabber card via a coaxial cable. The frame grabber can capture single frames of the digital video stream at a rate of 15 frames per second. The camera gain is adjusted automatically depending on light level, allowing function at day- and night-time.

The telescope and camera are mounted to the backing structure of the 10- and 6-m antennas. Figure B.3 shows the optical telescopes and cameras mounted to the radio antennas. The top panels show the mounting in the backing structure while the bottom panels show the opening in the primary. A small circular hole is seen on to the left (6-m antenna) or right (10-m antenna) of the opening in the primary. The telescope and camera occupy only a small fraction of the backing structure and are therefore subject to different gravitational stresses when compared to the radio surface.

The frame grabber card returns images in pnm (portable anymap) format. These images are then immediately converted to the Python image structure. The centroid is then calculated as follows. The entire image is cropped to exclude a user defined number of pixels on each side of the image to reduce edge effects. The brightest pixel in the cropped image is selected. If there are two equally bright pixels, the initial estimate of the center is taken to be the average of the pixel locations.[1] The RMS of the cropped image is calculated and the remaining image is masked so that pixels below $3\sigma_{rms}$ are not considered. Then, a region of 15 by 15 pixels around the peak is defined and pixels outside this box are also masked. Finally, the centroid position is determined via a center of mass type calculation, i.e. no Gaussian fitting is performed (original algorithm by P. Teuben).

At night, the centroids from 16 frames are calculated. If fewer than half of these contain valid data, then the centering attempt is abandoned. If half or more are valid, then the mean offset of the 16 centroid positions is applied to the antenna pointing model and a mean and uncertainty are reported for the applied offset. If the uncertainty in the centroid position was larger than $1.5''$ per axis, the offset is not applied. Uncertainties of successful centroids are typically on the order of 0.18 to $0.4''$ per axis. This process is repeated up to four times. For each cycle, the differential offset is compared to a convergence criteria which is based on the expected gain of the centroiding process. In early applications, if the applied offset was less than $4''$, the centroid is assumed converged. Since the camera rotations and inter-camera pixel scale variations have been accounted for, the gain is typically quite good and the limiting offset is now $10''$. The centroiding process is abandoned if the convergence criteria are not met in four attempts and any applied offsets are removed. Otherwise, the process is stopped when the convergence criteria are met.

By day, the process is slightly more complicated. Several frames must be added together and the background must be subtracted. Typically, 40 frames are coadded and then a single centroid is calculated. The background subtraction is done by

[1] This approach can cause significant problems if there are multiple stars in the field or the image suffers from saturation.

moving the telescope 2′ off from the nominal stellar position and integrating the same number of frames. Convergence is checked on the on-source, background-subtracted, coadded frames similarly to the method described above. A single background frame is used over the entire set of four cycles, i.e. at each of the possible four centroid calculations a common background image is used.

Figure B.1 The top panel shows the optical telescope used on the 6-m antennas. In the bottom panel, the 6-m antenna optical telescope is shown. The 10-m antenna telescope aperture is located behind the white cap on the left side of the image. The 6-m optical telescope is shown mounted to the antenna.

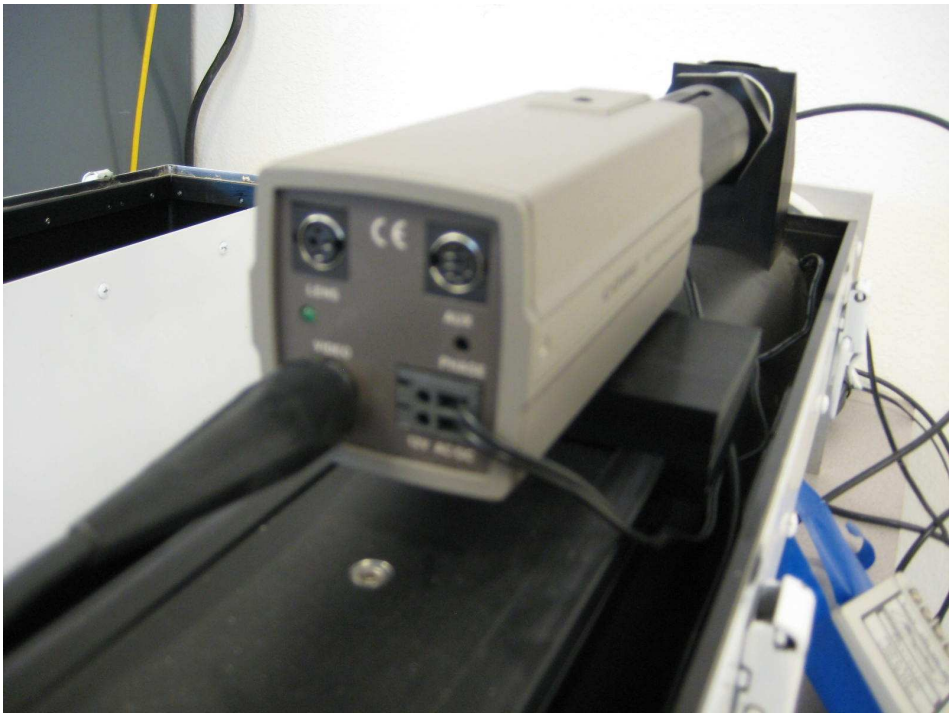

Figure B.2 The COHU 4910 digital (CCD) video camera is shown. The coaxial cable is shown connected on the left side of the camera. The other connection is the power supply (on the right side of the camera.)

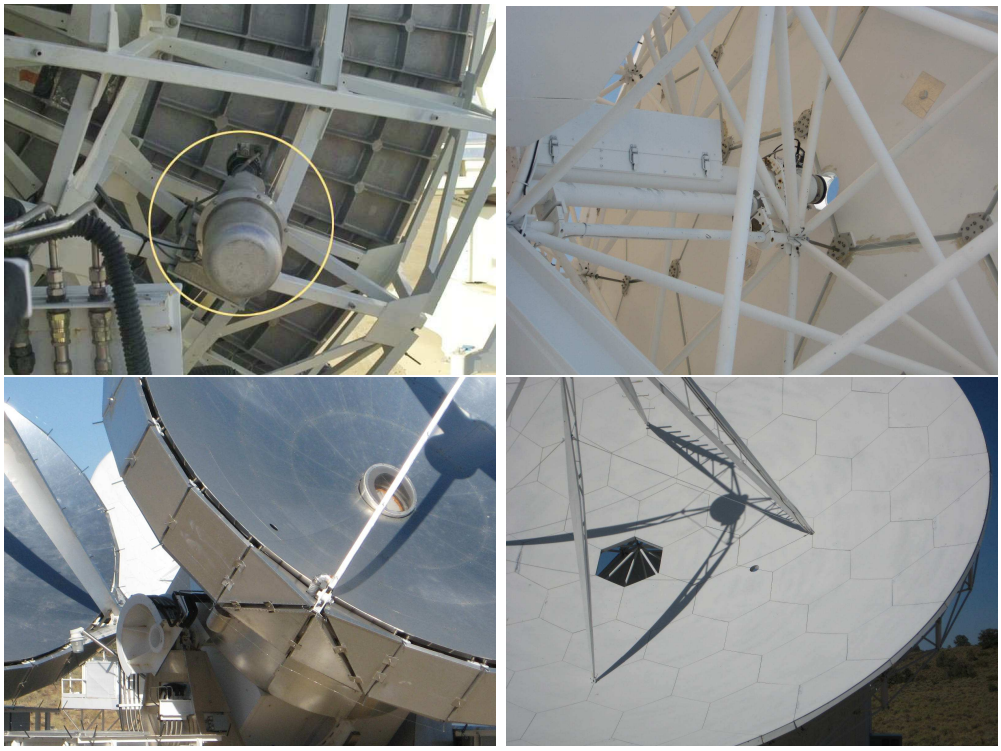

Figure B.3 The left panels show the optical telescope and camera used on the 6-m antennas. In the right panels, the 10-m antenna optical telescope and camera are shown. The top row shows images from the back of the radio surface while the bottom row shows the small hole in the primary through which the optical telescope is pointed. The opening for the optical telescope is located on the left side of the central hole in the primary for the 6-m antennas (left) and on the right side of the central hole in the primary for the 10-m antennas.

Appendix C

Implementation of Optical Offset Pointing

The centroiding, coaddition, and background subtraction are done in the antenna computers. A switch is set by the higher level interface to determine the number of coadditions to use. At night the default is one frame while by day this number is typically 40. The frames are obtained from the cameras at about 15 frames per second. Calls to the centroid routine are as follows. For night-time function, a series of 16 single frames are obtained and an average offset position is calculated. The telescope is offset by the proper amount. If fewer than 8 frames are valid or if the errors in the calculated offset are larger than $1''$, the fit is rejected. If the offset amount is less than $4''$, the gain of the centroiding routine, which is limited by the rotation of the cameras, is such that the expected residual error is less than $0.5''$. If the offset is larger than $4''$, the process is repeated until four cycles are performed or the offset becomes less than $4''$. If the four cycles complete without convergence, the original offsets are restored. For daytime function, the telescope is offset by a user defined quantity, typical $2'$, and 40 frames are obtained and coadded. This background image is stored temporarily. Then, 4 sets of 40 added frames are used to obtain a measure of the offset. Rejection and convergence criteria similar to the night-time approach are used.[1]

The bulk of the control system interface is contained in two commands, *opti-*

[1] As of 2008 June 18, offsets as large as $12''$ are considered to be converged because the true pixel scales and camera rotation angles are utilized when the correction is applied.

calGuideMain.deriveOptRadDiff and *opticalGuideMain.subOptical*. The purpose of these routines is to derive the optical to radio offset (*deriveOptRadDiff*) and apply pointing model changes to the telescopes based on the derived difference and the newly measured optical offset (*subOptical*). For the optical to radio difference, the user must provide a radio source and an optical counterpart. A call to *refPoint* is made to center the radio pointing model on a bright source. It is usually advisable to use the brightest radio pointing source available provided the elevation is reasonable (30° <el< 70°). This ensures good signal-to-noise in the fit to the radio offset. Then, relative to this newly centered pointing model, the nearby optical counterpart is selected to measure the optical to radio offset. Ideally, the source should be as close as possible to the radio source to minimize the influence of pointing model error field gradients over the separation. The output of this routine contains a python dictionary of telescopes and optical to radio azimuth and elevation offsets. These differences are assumed constant over the sky and in time until the offset is measured again, typically 6-8 hours later. The program *subOptical* takes this measured offset and a new optical source, typically near a flux calibrator, gain calibrator or science target, and reverses the process. The measured optical to radio offset is put into the system and the new star is centered. The change in the initial offset is recorded. If a new offset is not measured because of clouds or other failures, it returns to the initial offset and the change in offset is thus zero. Otherwise, the difference in the measured position and known offset is used to change the underlying pointing parameters such that the offset would be the same, i.e. the head of the vector defined by the optical to radio offset is used to reset the origin so that the head of the vector appears at the same location as before.

To utilize the speed benefits of optical to radio offset guiding, the telescopes must separate from their unified efforts of radio pointing and standard radio observing, and act individually to correct the pointing. To this end, I created a method which automatically launches copies of the control program. In the case of optical offset

guiding, 14 copies are launched, one for each antenna except one.[2] The nominal control program is used to control the remaining antenna. For the most part the 14 copies, each associated with a given antenna, spend their time watching the original control program which controls the radio observations. Eventually, this main program signals the watching programs that it is time to do optical pointing. At this point, all of the programs take control of their individual telescopes and speed off to a nearby optical target. When the main program is done observing its optical counterpart, it in turn watches the remaining programs to see when they report that they are done with their optical pointing. At this time, the main control program resets the parameters required to do regular radio observations and the other 14 copies return to their watching states. The extra windows which are launched automatically upon start-up are destroyed upon completion of the observation.

At the CARMA user interface, PI level (Carpenter) reasonable defaults and an additional utility *getNearest* (Corder) allow the use of optical offset guiding with the setting of a single parameter, *doOptPoint*. This is the switch telling the user script to utilize optical offset guiding. At any point at which the optical offset fails to satisfy certain convergence criteria, the offset is not applied. The default behavior, if this parameter is True, is as follows. Initially, radio pointing is done and an attempt is made to measure the optical to radio offset vector. The success or failure of this measurement depends both on the number of good radio pointing fits and optical offsets measured. If more than *nbadAnts* antennas (a user settable parameter which defaults to 3) fail to have radio or optical pointing, optical updates are not done and the standard radio pointing parameters are then enforced. Each time a radio pointing is attempted, the optical to radio offset is measured again.

A successful attempt of the measurement excites the use of optical updates to the pointing. If during optical updates the update fails for more than *nbadAnts* more than *nfailOpt* consecutive times, optical pointing is aborted until another attempt of radio pointing is done. Again, the user script defaults back to radio pointing parameters

[2]If antennas are missing from the observation for maintenance or transport, the program appropriate ignores such antennas.

set by the user. If successful, the pointing is updated every calibrator cycle by default though a time scale can be set with *intervalOpt*. Preferred sources can be selected with *optradPreferred* but the default behavior is to select the nearest source in coordinate space to the radio source in question. The default is also to do optical pointing updates near the calibrator but not the target, i.e. *optPointCal* is True but *optPointTarget* is False. If the calibrator and target are particularly separated then the user can make both of these true. Finally, *ncoadd*, *subtract*, *maxmag* default to different behavior by day and by night. The number of coadds is 1 at night and 40 by day, subtraction is True by day and False by night, and the magnitude limit is unlimited (full catalog) by day and $V_{mag} = 3$ by day.

Appendix D

Optical Offset Pointing Equation of Merit

The pointing accuracy is fundamentally limited by the rms of repeated radio pointing observations on the same part of the sky. This sets the floor of the pointing error, call it δR_p. There is also the random error associated with the measurement of the optical to radio offset vector δR_{ro} and individual optical pointing updates, δR_o. There are three additional sources of error which can contribute to the overall error in pointing. Errors in the pointing model give rise to gradients in the pointing error field. Typical values are provided in Table 4.1. The two major sources of error result from the time since the last pointing update and the distance from the target which that pointing update was done. These values are given by $\delta R_{time} = d\phi/dt\ dF/d\phi\ \delta T$ where δR_{time} is the systematic error introduced by time since the last measurement δT. The two derivatives present are the coordinate speed $d\phi/dt$ and the pointing error field gradient $dF/d\phi$ with respect to the coordinate. Additional systematic error comes from the distance to the pointing source, $\delta R_{pos} = DdF/d\phi$ where now D is the distance to the pointing source. Also, errors associated with changes in the optical to radio offset vector can also occur, call that error δR_{vec}. The functional form of δR_{vec} is not well known. The total error for optical and radio pointing is then:

$$\Delta P_{ro} = (\delta R_{ro})^2 + (\delta R_o)^2 + (\delta R_{time_opt})^2 + (\delta R_{pos_opt})^2 + (\delta R_{vec})^2 \qquad \text{(D.1)}$$

$$\Delta P_r = (\delta R_r)^2 + (\delta R_{time_rad})^2 + (\delta R_{pos_rad})^2 \qquad \text{(D.2)}$$

Table 4.1 shows the δR_o is small compared to δR_p suggesting that δR_{ro} will be much larger than (δR_o) and comparable to δR_p. Indeed, repeated calculations of RMS on sets of four or five consecutive points shows that the RMS is similar to the repeated radio observations indicating that the bulk of the error in the optical to radio offset determination over short time scales is dominated by the repeatability of the radio measures. Given this similarity, optical offset pointing will show a benefit provided:

$$(\delta R_{time_opt})^2 + (\delta R_{pos_opt})^2 + (\delta R_{vec})^2 < (\delta R_{time_rad})^2 + (\delta R_{pos_rad})^2 \tag{D.3}$$

or

$$(\delta R_{vec}) < |dF/d\phi| \sqrt{|d\phi/dt|(\delta T_{rad}^2 - \delta T_{opt}^2) + C^2(D_{rad}^2 - D_{opt}^2)} \tag{D.4}$$

Typical values for δT are 20-30 minutes for optical pointing and no less than 2 hours and 15 minutes for radio pointing while 4 hours is more typical at night. The difference here arises because of the time taken to slew to the radio pointing sources and the time associated with the actual measurement. The fact that pointing takes 10 minutes plus slew time implies that gain calibration must be done before and after the pointing. Also, retuning of the 1^{st} or 2^{nd} is often performed to optimize sensitivity. This can result in an amplitude jump, again requiring additional calibration observations. Together this indicates that pointing on less than 2 hour time scales would seriously hamper observing efficiency. The 20-30 minute time for optical pointing comes simply because this is the gain calibrator time scale and the measurement can easily be fit into observations on this time scale. The fundamental limit is more like 10 minutes by night and 20 by day from efficiency considerations.

Values D are far more variable. At night, the distance to optical pointing sources is usually 7° or less. By day this number is often greater, with distances more typically 10-15° due to the brighter magnitude limit. For radio source, of course, the distance is less dependent on position of the sun except in that phase stability is typically better by night. For the purposes of this calculation I will assume that the distance to a bright pointing source is 25°, though the number can sometimes be as large as 50.

The value C is a correction factor for the fact that the distances in question should be coordinate distances, not on the sky distances. However, $C \geq 1$ and taking $C = 1$ sets the most stringent limits on the value of δR_{vec}. C scales as $1/\cos(el)$ reduced by a factor which depends on the az differences between sources and has typical range of 1.05 to 4.

The presence of $d\phi/dt$ makes the relation somewhat complicated as the coordinate speed can change rather rapidly over the course of observations. It is limited to be greater or equal the sidereal rate of 15 coordinate arcseconds per second though it can grow large at high elevation, to 50-60. Typical values for $dF/d\phi$ can be taken from Table 4.1.

Appendix E

CARMA Narrow Band Calibration

The data for the gain calibrator and secondary calibrator were checked after each step. The cross-correlation spectrum of each baseline is divided by the geometric mean of the auto-correlation spectrum for the antennas that constitute that baseline on a record by record basis using the task **uvcal** with the fxcal option. This results in flatter passbands with less channel to channel variation in amplitude but has no effect on the phase information which is lost in the auto-correlation.

CARMA provides a measurement of the change in the fiber length from the control building to the telescope. This line-length measurement indicates a phase correction that should be applied to correct for changes in length from thermal effects. An effective gain solution for the line-length correction was derived using the task **lincal**. This gain table is then applied to the data using **uvcat**. In general, the application of the line-length data results in more slowly varying phase verses time in the resulting data. The line length correction was not available for the earliest datasets but divisions into comparable with line-length and without line-length datasets results in no difference in data quality.

The most relevant baseline solution was then applied to the data and the dataset was then divided into files based on source and spectral/continuum band. Once so divided, the file associated with the continuum portion of the passband source is used to derive a global passband solution for the continuum bands of all sources. The task **mfcal** was used with a very short interval for the gain solution interval, typically 15 seconds, and on a per channel basis. This optimizes the signal-to-noise

in the bandpass calibration. The passband solution for the 32 MHz spectral bands were similarly derived but averaging seven channels. 8 MHz modes are inherently low signal-to-noise and thus the spectrum is averaged over an entire sideband. This results in a passband which is simply a correction of the phase offset from upper to lower sideband and a constant amplitude factor. These passband solutions are then copied to files and applied to relevant files for the spectral/continuum band but the fine timescale gain solution was not applied.

At this point the spectral channels and the continuum band will be flat across the passband but there will be some average phase as a function of time, i.e. a traditional gain variation with time. The functional form should be the same in the continuum and spectral bands but there may be some constant offset. Therefore, a gain solution is derived for the continuum modules of the passband calibrator on a few minute time scales. This solution is then copied to the narrow band modes and applied. Now, the phase with time should be constant and the only residual phase in the narrow band should be the offset between the continuum and spectral bands. This difference has been shown to be constant on timescales of a few days[1], meaning that for a given dataset it can be taken as a constant. The offset phase is then calculated by doing another phase selfcal with a very long time scale but now on the narrow band data. The output gain table has a single phase per antenna. This difference is then applied to the spectral bands of the other sources. The phase zero point of the continuum and narrow bands is now the same.

Next, a phase selfcal on timescales of the calibrator cycles is derived on the continuum bands of the gain calibrator and then copied and applied to the other bands, including the narrow band modes. On the altered continuum dataset, a longer timescale amplitude selfcal is done to set the overall flux scale. This gain solution again is copied to the datasets which have already had the phase solutions applied. At this point the time variation has been removed by the continuum modes and the offsets between the continuum and spectral line has been removed.

[1]There are instances where this is obviously not the case but it appears as though the difference is constant in time except for random situations where it is not. The effect of a changing band to band phase offset is obvious and is checked in the final data.

MIRIAD's **bootflux** was used to calculate a flux on a continuum sideband module by continuum sideband module basis. The fluxes of both 0019+734 and 0102+584 were tracked over time. 0102+584 was found to be strongly time variable in terms of flux and by the end of the observation time frame, it fell below the 1 Jy mark and thus is of limited value as a calibrator. 0019+734 was on average fainter than 0102+584 but more constant, decaying at a fairly constant rate from 2 to 1.3 Jy. Most of the datasets contained flux calibrators, and there was typically an observation with a flux calibrator within a few days of every dataset.

Data were then flagged according to a number of criteria. Time periods with strongly deviant system temperature where flagged. Time periods of large tracking error were also flagged although most of such data were flagged on line by the CARMA pipeline system. The MIRIAD routine **closure** was also used to identify baseline based errors. For the most part, amplitude stability of the gain calibrator was used as the final discriminant of data to be flagged. Variation in the amplitude gain is typically in response to poor phase stability on long baselines or poor pointing. In either case, a decay in the amplitude indicates that the data are of limited utility especially given either of these conditions result in significant decrease in image fidelity. Estimates of the seeing disk were made using by fitting a Gaussian to the visibilities (**uvfit**) associated with the secondary calibrator 0102+584, when available. The size of the seeing disk is then used to correct the amplitudes of the target dataset as a function of uv-distance using **uvcal**, i.e. the amplitude visibilities were divided by a number for a given uv-distance associated with a Gaussian fit to the uv-data of the secondary calibrator. Table 5.2 describes the individual datasets and measurements of the quality.

Appendix F

Simulator and Using Measured Primary Beams

F.1 Overview

The MIRIAD Python scripts used to simulate observations and to subtract a model using the real primary beams are provided here. There are two principle routines, *uvsubtract.py* and *uvmodel.py*. The former is utilized to subtract an assumed model from a measured visibility file, i.e. to attempt to correct for the true primary beam shape. The latter is the simulator package. Each of these calls functions in other Python libraries. Chief among these are, *pymiriad.py*, *shortCuts.py*, *fileIOPython.py*, *makeBeams.py*. The package *fileIOPython.py* is described in detail on the CARMA observer web pages and is not included here. The package *pymiriad.py* is largely a set of Python wrappers to MIRIAD functions, i.e. *pymiriad.uvindexPy* is equivalent to a **uvindex** call with standard defaults. Only *pymiriad.py* routines that are more complicated than simple Python wrapers to single MIRIAD commands are described here.

In several locations, the lines had to be split up to fit on the page. Usually, this was done where Python would allow line continuation. However, in some instances, typically involving *os.system* calls to MIRIAD functions, the split was required but no reasonable location was available for breaking the line. These cases are noted and the

user needs to search for the word *compile*. In general, removal of the line continuation character, \, by the end user is advised to reduce the chance of compile errors.

While many of these routines can in theory be called individually, only *uvmodel.uvmodel_sim_wrap* and *uvsubtract.uvsubtract* are called directly in practice. The general approach is to define the relevant variables within the files are specified (i.e. frequency, simulation variables like configs, etc.) and then at the Python prompt, the user types

import uvmodel

uvmodel.uvmodel_sim_wrap()

or, for the uvsubtraction routine

import uvsubtract

uvsubtract.uvsubtract(parameters)

For the *uvmodel* call, the user should set any and all of the parameters given before the definition of *uvmodel_sim_wrap*. These values are described below. For the input parameters to *uvsubtract*, the user general sets the frequency and the illuminateType (see below) in the top portion of the file *uvsubtract.py* before importing the routine[1] and then in the parameter list, the user needs to provide: modelImage, inputUV, and source. These are given as a comma separated series of values. All of the inputs are strings and are the name of the model image (modelImage), the observed visibility file, i.e. the observations (inputUV) and the name of the source from which the model visibilities will be subtracted (source). The name of the source should match exactly the name in the MIRIAD file. Below is a more detailed description of the underlying code and the top level variables which the user can define.

F.2 *pymiriad.py*

The routines *pymiriad.getRaDec*, *pymiriad.getPointingOffsets* and *pymiriad.getMaxMinHa* are used to recover the source locations, mosaic pointings and the hour angle cov-

[1]Once a routine has been called with the import command, subsequent changes to the code require a reload(uvsubtract) command which recompiles the code.

erage. These functions return [ra,dec], [raOffsets,decOffsets], and [maxHa,minHa], respectively. These routines in turn call routines within *fileIOPython* (often called *fiop* for short) and other routines within *pymiriad.py*, e.g. *listobsPy* which is a simple wrapper to the MIRIAD routine **listobs**.

```
def getRaDec(uvfile,source) :
    os.system(``uvindex vis=%s | grep %s > uvindexFile'' % \
        (uvfile,source.upper()))
    tempCol = fiop.readcolPy('uvindexFile','s,s,s,f,f',\
        beStrict=True,startStrict=True)
    ra = tempCol[1][0]
    dec = tempCol[2][0]
    return [ra,dec]


def getPointingOffsets(uvfile) :
    os.system(``uvindex vis=%s  > uvlistFile'' % (uvfile))
    tempTab = fiop.fileToTable('uvlistFile')
    [retab,loco] = fiop.getRestrictTable(tempTab,0,'Source')
    raNums  = []
    decNums = []
    for i in range(len(tempTab)) :
        if i <= loco[0] : continue
        else :
            try:
                raNums.append(float(tempTab[i][-2]))
                decNums.append(float(tempTab[i][-1]))
            except:
                continue
    return [raNums[:-1],decNums[:-1]]
```

```
def getMaxMinHa(uvfile,doEasy=False) :
    if not doEasy : listobsPy(uvfile,log='listobsFile')
    lst = fiop.readcolPy('listobsFile',\
          's,f,f,f,f,i,i,i,i,i,i,i,i,i,i,i,i,i,i,i',\
          beStrict=True,startStrict=True)[2]
    secondListobsTable = fiop.readcolPy('listobsFile',\
                         's,s,i,i,f,i,i,f,f,f',\
                         beStrict=True,startStrict=True)
    raH = secondListobsTable[2][0]
    raM = secondListobsTable[3][0]
    raS = secondListobsTable[4][0]
    ra  = float(raH)+float(raM)/60.0+float(raS)/3600.0
    has = []
    for i in lst :
        ii = str(i)
        if len(ii) < 5 :
            lstH = 0.0
            lstM = 0.0
            lstS = float(ii)
        elif len(ii) < 7 :
            lstH = 0.0
            lstM = float(ii[:-4])
            lstS = float(ii[-4:])
        else :
            lstH = float(ii[:-6])
            lstM = float(ii[-6:-4])
            lstS = float(ii[-4:])
        lst = lstH+lstM/60.0+lstS/3600.0
        ha = (lst-ra)
        if ha > 12.0 : ha = ha  - 24.0
```

```
        if ha < -12.0 : ha = ha + 24.0
        has.append(ha)
    return [max(has),min(has)]
```

F.3 *makeBeams.py*

Routines in this package make baseline based primary beams (*makeBeams.makeBaseline*), alter the voltage patterns to the relevant frequency (*makeBeams.changeFreq*), alter the image header to reflect the source in the measured visibility file (*makeBeams.adaptToImage*), offset the beam center to the proper pointing position (*makeBeams.offsetPositions*), regrid the voltage pattern to the model resolution (*makeBeams.regridToImage*), and offset the header information to reflect a phase center at the new pointing location (*makeBeams.offsetCenter*). The package includes other functions which aid in making beam models for testing the simulator but these are not relevant here.

```
def makeBaseline(realIn1,realIn2,imagIn1,imagIn2,realOut,imagOut) :
    os.system(``rm -rf %s %s'' % (realOut,imagOut) )
    os.system(``maths exp='(<%s>*<%s>+<%s>*<%s>)' out=%s'' % \
         (realIn1,realIn2,imagIn1,imagIn2,realOut) )
    os.system(``maths exp='(<%s>*<%s>-<%s>*<%s>)' out=%s'' % \
         (realIn2,imagIn1,realIn1,imagIn2,imagOut) )


def changeFreq(outFreq,inFile,inFreq=100.2,outFile=None) :
    if outFreq == inFreq : return
    else :
        os.system(``rm -rf %s freqReset freqReset2'' % (outFile) )
        os.system(``cp -r %s freqReset'' % inFile)
        cdelt2=float(\
               os.popen(``gethd in=freqReset/cdelt2 format=arcsec'').read())
        cdelt1=float(\
```

```
            os.popen(``gethd in=freqReset/cdelt1 format=arcsec'').read())
        cdelt2 = cdelt2*inFreq/outFreq
        cdelt1 = cdelt1*inFreq/outFreq
        os.system(``puthd in=freqReset/cdelt2 value=%f,arcsec'' % cdelt2)
        os.system(``puthd in=freqReset/cdelt1 value=%f,arcsec'' % cdelt1)
        os.system(``puthd in=freqReset/cdelt3 value=%f'' % outFreq)
        if outFile <> None :
            os.system(``regrid in=freqReset out=%s tin=%s'' % \
                    (outFile,inFile) )
        else :
            os.system(``cp -r %s freqReset2'' % inFile)
            os.system(``regrid in=freqReset out=%s tin=freqReset2'' % \
                    (inFile) )

def adaptToImage(fileIn,dec='00:00:00,dms',ra='00:00:00,hms',freq=100) :
    os.system(``puthd in=%s/crval1 value=%s'' % (fileIn,ra))
    os.system(``puthd in=%s/crval2 value=%s'' % (fileIn,dec))
    os.system(``puthd in=%s/crval3 value=%f'' % (fileIn,freq))

def offsetPositions(fileIn,fileOut,raOff,decOff) :
    os.system(``rm -rf %s intermedFile'' % fileOut)
    sizer = float(os.popen(``gethd in=%s/naxis1'' % fileIn).read())
    increaseFactor = 4.0
    os.system(``imframe in=%s frame=%i,%i,%i,%i out=intermedFile'' % \
             (fileIn,-sizer*increaseFactor,sizer*increaseFactor-1,\
             -sizer*increaseFactor,sizer*increaseFactor-1))
    print 'offsetPositions',raOff,decOff,fileIn,fileOut
# USER: This command will not compile like this.  I needed to
# USER: break it up in such a way to make it fit on the page.
# USER: This was necessary to fit it on the page.
```

```
    os.system(``imdiff in2=intermedFile in1=intermedFile \
                options=noamp,noex,noof,noxshift,noyshift \
                xshift=%f yshift=%s adjust=%s guard=%f'' % \
                (raOff,decOff,fileOut,10.0*increaseFactor) )

def regridToImage(imIn,modelIn,fileOut) :
    os.system(``rm -rf %s'' % fileOut)
    os.system(``regrid in=%s tin=%s out=%s axes=1,2'' % \
              (imIn,modelIn,fileOut) )

def offsetCenter(fileIn,raOff,decOff) :
    if raOff <0.0 : raOff=raOff+1
    if decOff < 0.0 : decOff=decOff+1
    if raOff >0.0 : raOff=raOff
    if decOff > 0.0 : decOff=decOff
    crpix1=int(int(\
           os.popen(``gethd in=%s/crpix1'' % fileIn).read()[:-1])+raOff)
    crpix2=int(int(\
           os.popen(``gethd in=%s/crpix2'' % fileIn).read()[:-1])+decOff)
    os.system(``puthd in=%s/crpix1 value=%i'' % (fileIn,crpix1) )
    os.system(``puthd in=%s/crpix2 value=%i'' % (fileIn,crpix2) )
    os.system(``puthd in=%s/bunit value=JY/PIXEL'' % (fileIn) )
```

F.4 *uvsubtract.py*

The package *uvsubtract.py* is the base routine for subtracting a model illuminated by measured voltage patterns. Instead of commenting on the entire package, which is quite lengthy, comments on the function of this package are embedded within the code, given by lines preceded by the standard Python comment character '#' and the character string USER. Currently the script only works for continuum data.

```
# USER: These are standard Python import statements.
# USER: Reloads are for debugging purposes.
import os,sys,time
import random,math
import makeBeams
import fileIOPython
import pymiriad as pym
reload(makeBeams)
reload(pym)
reload(fileIOPython)
# USER: beamClip is used to define the lowest point in the resulting
# USER: baseline based primary beams that the image should utilize,
# USER: typically a value of 0.05 or None should be used.
beamClip   = None
# USER: The mean frequency must be provided here, one could in theory
# USER: get this from the header but I did not do that yet.
freq        = 108.1
# USER: If the model is a point source, the point source center is defined
# USER: here.  This has limited utility and is for special case use only.
raLocPoint  = 2.689
decLocPoint = 40.400
#
ovroAnts = range(1,7)
bimaAnts = range(7,16)
allAnts = range(1,16)
antTypes = ['carma','ovro','hatcreek']
# USER: Main routine begins here.  From the command line in Python type:
# USER: import uvsubtract
# USER: uvsubtract.uvsubtract(parameters)
# USER: where the parameters are the image model (in units of Jy/Pixel),
```

```
# USER: the input visibility dataset, i.e. your data,
# USER: the source name (needed for getting properties from the header),
# USER: the hour angle refinement interval (smaller is better but more
# USER:    expensive computationally),
# USER: iluminateType is the type of voltage pattern to use, types include
# USER:   'miriad', 'miriadStyle' and 'real' (i.e. measured voltage patterns),
# USER: doQuick should be false except for testing,
# USER: isPoint is True only if your source model is a point, and
# USER: line is None unless you want to specify it for special purposes.
def uvsubtract(modelImage,inputUV,source,chopInterval=0.5,\
               illuminateType='miriad',doQuick=True,isPoint=False,line=None) :
    if illuminateType == 'real' : isReal=False
    else : isReal=True
    dataFile = open('sourceFile','w')
# USER: pym.getRaDec gets the source ra and dec from the visibility file.
    [ra,dec]       = pym.getRaDec(inputUV,source)
    raCen          = convertSexToReal(ra)
    decCen         = convertSexToReal(dec)
# USER: pym.getPointingOffsets gets the mosaic pointings from the
# USER: visibility file.
    [raOff,decOff] = pym.getPointingOffsets(inputUV)
    nPoint = len(raOff)
# USER: pym.getMaxMinHa gets the hour angle coverage from the visibility file.
    [maxHa,minHa]  = pym.getMaxMinHa(inputUV)
    maxHa = math.ceil(maxHa/chopInterval)*chopInterval
    minHa = math.floor(minHa/chopInterval)*chopInterval
    Harange = makeHarange(minHa,maxHa,0.008,chopInterval)
    numStuff = 210*len(Harange)*nPoint
    if (not doQuick) :
# USER: The user is warned about the run time.  This can be removed.
```

```
        print 'You are going to have to run uvmodel and illuminate data: ',\
              numStuff,' times...this could take awhile.'
        print 'There are 210 baseline illuminations, ',nPoint,\
              ' different pointings and ',len(Harange),' hour angle divisions.'
        print 'To continue without interuption, press enter, else cntrl-c.'
        sys.stdin.readline()
# USER: Files from the previous run are removed to clear disk space.
        print 'Cleaning up before generating a million plus files.'
        cleanUp()
        print 'Now removing the old attempt to make the visibility file.'
        print 'This will certainly take awhile.'
        os.system("rm -rf HA*")
        print Harange
        sys.stdin.readline()
# USER: The loop over hour angle chunks (set with chopInterval) begins.
        for ii in range(len(Harange)) :
            os.system("mkdir HA%i" % ii)
            harange=Harange[ii]
            print harange
            haStart = float(harange.split(',')[0])
            haEnd   = float(harange.split(',')[1])
# USER: Subdirectories for visibility files are defined here.
            fileUv = "HA%i/%s" % (ii,inputUV)
            os.system("rm -rf %s" % fileUv)
            print inputUV,fileUv,haStart,haEnd
# USER: This {\bf uvcat} selects out a visibility range for faster run time.
            os.system("uvcat vis=%s out=%s select='ha(%f,%f)'" % \
                      (inputUV,fileUv,haStart,haEnd) )
            antsForHa = getAnts(fileUv)
# USER: getChi returns the average parallatic angle over the hour angle range.
```

```
            chiVal = getChi(fileUv,antsForHa[0],antsForHa[1])
            if chiVal == None :
                print 'what happened?  No chi...'
                continue
            chiVal  = int(round(chiVal/20.0))*20
            if chiVal > 340 : chiVal = 0
# USER: The loop over mosaic pointings begins here.
            for jj in range(nPoint) :
                print 'pointing: ',jj+1,' of ',nPoint+1
                pnt1 = raOff[jj]
                pnt2 = decOff[jj]
                print pnt1,pnt2
                os.system("mkdir HA%i/PNT%i" % (ii,jj))
# USER: The loop over baselines begins here.
                for ant1 in antsForHa :
                    for ant2 in antsForHa :
                        if ant1 < ant2 :
                            print 'ants: ',ant1,ant2
                            visFile = ("HA%i/a%i.a%i.vis" % (ii,ant1,ant2))
                            if jj==0 :
                                os.system("rm -rf %s" % visFile)
# USER: This line will not compile as is.
                                os.system("uvcat vis=%s out=%s \
                                   select='ant(%i)(%i)'" \
                                   % (fileUv,visFile,ant1,ant2))
# USER: illuminateData multiplies the baseline based primary beam and the model
# USER: and returns file names of the model times the real and imaginary
# USER: parts of the beam.
                            [fileIllumReal,fileIllumImag] = \
                                illuminateData(modelImage,visFile,ra,dec,ant1,\
```

```
                                ant2,[pnt1,pnt2],ii,jj,illuminateType,freq,\
                                isReal,chiVal)
# USER: uvmodel_data_single takes the primary beam times model and
# USER: samples it according to the input visibility file.
                            [fileModelImag] = \
                                uvmodel_data_single(visFile,fileIllumReal,\
                                fileIllumImag,ant1,ant2,ii,jj,[pnt1,pnt2],\
                                isReal,harange,line=line)
                            dataFile.write("%s\n" % (fileModelImag) )
        dataFile.close()
        catFile = '%s.vis' % modelImage
# USER: All the visibilities are combined.
        makeCatFile(range(0,40),range(0,200))
# USER: This is for option doQuick and is used for testing only.
    else :
        print 'Doing it quick, this should take a few minutes.'
        for ii in antTypes :
            print 'doing: ',ii
            visFile = ("%s.vis" % (ii))
            os.system("rm -rf %s" % visFile)
            [antL1,antL2] = getAntList(ii)
            os.system("uvcat vis=%s out=%s select='ant(%s)(%s)'" % \
                      (inputUV,visFile,antL1,antL2))
            if not isPoint : subtractItQuick(modelImage,visFile,nPoint,ii,\
                                             line=line)
            else : subtractItQuickPoint(modelImage,visFile,nPoint,ii,raOff,\
                                        decOff,line=line)
        os.system("rm -rf %s.vis" % modelImage)
# USER: This will not compile as is because the line had to be slipt in an
# USER: inelegant way.
```

```
        os.system("uvcat vis=carma.sub.real,ovro.sub.real,hatcreek.sub.real \
                   out=%s.vis" % (modelImage))


def subtractItQuickPoint(modelFile,visFile,nPoint=1,antType='ovro',\
    raOff=[0.0],decOff=[0.0,0.0],raLoc=raLocPoint,decLoc=decLocPoint,\
    line=None) :
# USER: used only in quick testing mode.
    raOff.reverse() ; decOff.reverse()
    demosFiles="%s.real" % (antType)
    subFiles  ="%s.sub.real" % (antType)
    os.system("rm -rf %s* %s*" % (demosFiles,subFiles))
    os.system("demos map=%s vis=%s out=%s" % (modelFile,visFile,demosFiles))
    [antL1,antL2] = getAntList(antType)
    for j in range(1,nPoint+1) :
        raI = raOff[j-1] ; decI = decOff[j-1]
# USER: The argument of {\it try} will not compile as is.
        try:
            fluxVal = float(\
                      os.popen("histo in=%s%i | grep Maximum | \
                      awk '{printf($3)}'" % (demosFiles,j)).read().\
                      replace('D','E'))
        except:
            fluxVal = 0.0
        newRa = raLocPoint-raI
        newDec = decLocPoint-decI
# USER: The following two commands will not compile as is.
        if line == None : os.system("uvmodel vis=%s options=subtract,\
                   selradec,mfs select='ant(%s)(%s),dra(%f,%f),ddec(%f,%f)' \
                   out=%s%i flux=%f offset=%f,%f" % (visFile,antL1,antL2,\
                   (raI-0.01),(raI+0.01),(decI-0.01),(decI+0.01),subFiles,\
```

```
                    j,fluxVal,newRa,newDec))
        else : os.system("uvmodel vis=%s options=subtract,selradec,mfs \
               select='ant(%s)(%s),dra(%f,%f),ddec(%f,%f)' out=%s%i flux=%f \
               offset=%f,%f line=%s" % (visFile,antL1,antL2,(raI-0.01),\
               (raI+0.01),(decI-0.01),(decI+0.01),subFiles,j,fluxVal,\
               newRa,newDec,line))
    os.system("uvcat vis='%s*' out=%s" % (subFiles,subFiles) )

def makeCatFile(has=range(0,10),pnts=range(0,20)) :
# USER: {\bf uvcat} all the files together into one.
    for i in has :
        for j in pnts :
            filename = ("ha%i.pnt%i.mod.vis" % (i,j) )
            os.system("rm -rf %s" % filename)
            print ("doing %s" % filename)
            os.system("uvcat vis=HA%i/PNT%i/'*'.mod.imag out=%s" % \
                     (i,j,filename) )
    for i in has :
        filename = ("ha%i.mod.vis" % (i) )
        print ("doing %s" % filename)
        os.system("rm -rf %s" % filename)
        os.system("uvcat vis=ha%i.pnt'*'.mod.vis out=%s" % (i,filename))
    filename = ("mod.vis")
    print "doing last cat!"
    os.system("rm -rf %s" % filename)
    os.system("uvcat vis=ha'*'.mod.vis out=%s" % filename)

def uvmodel_data_single(vis,realPart,imagPart,ant1,ant2,haNum=0,pNum=0,\
                        pointingInfo=[0.0,0.0],isReal=False,\
                        harange='-2,2,0.008',line=None) :
```

```
# USER: This function samples the model according to a single baseline
# USER: in the visibility.
# USER: Here visibility file names for baseline based data are created.
    outFileReal = "HA%i/PNT%i/a%i.a%i.mod.real" % (haNum,pNum,ant1,ant2)
    outFileImag = "HA%i/PNT%i/a%i.a%i.mod.imag" % (haNum,pNum,ant1,ant2)
    draH  = pointingInfo[0]+0.01
    draL  = pointingInfo[0]-0.01
    ddecH = pointingInfo[1]+0.01
    ddecL = pointingInfo[1]-0.01
    os.system("rm -rf %s %s" % (outFileReal,outFileImag) )
# USER: {\bf uvmodel} is called twice, once to handle the
# USER: real sky brightness distribution and again to handle
# USER: any imaginary component. If the imaginary component
# USER: is zero, the visibilities remain unchanged.
# USER: The {\bf uvmodel} calls are subtracting the model
# USER: visibilities from the dataset, i.e. options=subtract.
# USER: The option=imag handles the complex algebra.
# USER: Different paths are taken depending on the value of the line
# USER: parameter.
    if line==None :
# USER: The following two lines will not compile as is.
        os.system("uvmodel vis=%s model=%s out=%s select='ant(%i)(%i),\
                  dra(%f,%f),ddec(%f,%f)' options=subtract,selradec,mfs" % \
                  (vis,realPart,outFileReal,ant1,ant2,draL,draH,ddecL,ddecH) )
        if not isReal : os.system("uvmodel vis=%s model=%s out=%s \
                  select='ant(%i)(%i),dra(%f,%f),ddec(%f,%f)' \
                  options=subtract,selradec,imag,mfs" % \
                  (outFileReal,imagPart,outFileImag,ant1,ant2,draL,\
                  draH,ddecL,ddecH) )
        else : os.system("cp -r %s %s" % (outFileReal,outFileImag) )
```

```
    else :
# USER: The following two lines will not compile as is.
        os.system("uvmodel vis=%s model=%s out=%s select='ant(%i)(%i),\
                  dra(%f,%f),ddec(%f,%f)' options=subtract,selradec,mfs \
                  line=%s" % (vis,realPart,outFileReal,ant1,ant2,draL,\
                  draH,ddecL,ddecH,line) )
        if not isReal : os.system("uvmodel vis=%s model=%s out=%s \
                  select='ant(%i)(%i),dra(%f,%f),ddec(%f,%f)' \
                  options=subtract,selradec,imag,mfs line=%s" % \
                  (outFileReal,imagPart,outFileImag,ant1,ant2,draL,\
                  draH,ddecL,ddecH,line) )
        else : os.system("cp -r %s %s" % (outFileReal,outFileImag) )
# USER: A single visibility file is returned as this file has had
# USER: both the real and imaginary sky distribution subtracted.
    return [outFileImag]

def illuminateData(model,visfile,ra,dec,ant1,ant2,pointingInfo=[0.0,0.0],\
                  haNum=0,pointNum=0,illuminateType='miriad',freq=100.2,\
                  isReal=False,chi20=0) :
# USER: illuminateData multiplies the model image by the baseline
# USER: based primary beam.
    offRa  = pointingInfo[0]
    offDec = pointingInfo[1]
    draH  = (pointingInfo[0]+0.01) ; draL  = (pointingInfo[0]-0.01) ## these are
    ddecH = (pointingInfo[1]+0.01) ; ddecL = (pointingInfo[1]-0.01) ## in arcsec
    outFileReal = ("HA%i/PNT%i/a%i.a%i.real" % (haNum,pointNum,ant1,ant2))
    outFileImag = ("HA%i/PNT%i/a%i.a%i.imag" % (haNum,pointNum,ant1,ant2))
# USER: This line will not compile as is.
    os.system("rm -rf %s %s tempRealOff1 tempRealOff2 tempImagOff1 \
               tempImagOff2 tempReal tempImag" % (outFileReal,outFileImag) )
```

```
# USER: If illuminate type is MIRIAD, the program is quicker
# USER: in execution because it allows {\bf demos} to do the
# USER: beam times model multiplications. The imaginary
# USER: beam is set to zero in this case.
    if illuminateType=='miriad' :
        os.system("demos map=%s vis=%s out=%s select='dra(%s,%s),ddec(%s,%s)'" %\
                (model,visfile,outFileReal,draL,draH,ddecL,ddecH))
        os.system("mv %s1 %s" % (outFileReal,outFileReal) )
        os.system("imgen in=%s out=%s factor=0 object=level spar=0" % \
                (outFileReal,outFileImag) )
# USER: If the word 'style' appears in illuminateType,
# USER: the routine assumes all antennas of a fixed diameter
# USER: have the same voltage pattern.
# USER: In general here, the beam libraries are addressed
# USER: and the user will need to specify the location of their
# USER: own libraries.
    else:
        if 'style' in illuminateType.lower() :
            if ant1 < 7 and ant2 < 7 : monkey='ovro'
            elif ant1 < 7 and ant2 > 6 : monkey = 'carma'
            elif ant1 > 6 and ant2 > 6 : monkey = 'hatcreek'
            fileReal1="/export/sun2/sac/beamModels/%sBeams/paraAngle%i/%s.real" %\
                    (illuminateType,chi20,monkey)
            fileImag1="/export/sun2/sac/beamModels/%sBeams/paraAngle%i/%s.imag" %\
                    (illuminateType,chi20,monkey)
            fileReal2="/export/sun2/sac/beamModels/%sBeams/paraAngle%i/%s.real" %\
                    (illuminateType,chi20,monkey)
            fileImag2="/export/sun2/sac/beamModels/%sBeams/paraAngle%i/%s.imag" %\
                    (illuminateType,chi20,monkey)
# USER: If the word 'style' is not present in illuminateType,
```

```
# USER: all voltage patterns are assumed independent.
        else :
            fileReal1="/export/sun2/sac/beamModels/%sBeams/paraAngle%i/a%i.s.real"
                      (illuminateType,chi20,ant1)
            fileImag1="/export/sun2/sac/beamModels/%sBeams/paraAngle%i/a%i.s.imag"
                      (illuminateType,chi20,ant1)
            fileReal2="/export/sun2/sac/beamModels/%sBeams/paraAngle%i/a%i.s.real"
                      (illuminateType,chi20,ant2)
            fileImag2="/export/sun2/sac/beamModels/%sBeams/paraAngle%i/a%i.s.imag"
                      (illuminateType,chi20,ant2)
# USER: The model voltage pattern is offset to the proper pointing location
        prepareBeam(fileReal1,model,dec=dec,freq=freq,ra=ra,offRa=offRa,\
                    offDec=offDec)
        os.system("cp -r td3 tempRealOff1")
# USER: The second antenna voltage pattern is also offset.
        prepareBeam(fileReal2,model,dec=dec,freq=freq,ra=ra,offRa=offRa,\
                    offDec=offDec)
        os.system("cp -r td3 tempRealOff2")
# USER: If the beams have complex components (i.e. are not isReal), then the
# USER: imaginary components also have to be offset.
        if not isReal :
            prepareBeam(fileImag1,model,dec=dec,freq=freq,ra=ra,offRa=offRa,\
                        offDec=offDec)
            os.system("cp -r td3 tempImagOff1")
            prepareBeam(fileImag2,model,dec=dec,freq=freq,ra=ra,offRa=offRa,\
                        offDec=offDec)
            os.system("cp -r td3 tempImagOff2")
        else :
# USER: However, if voltage patterns are strictly real, then the imaginary
# USER: components are: generated to be exactly zero.
```

```
            os.system("imgen in=%s out=%s factor=0 object=level spar=0" %\
                      ('tempRealOff1','tempImagOff1') )
            os.system("imgen in=%s out=%s factor=0 object=level spar=0" %\
                      ('tempRealOff2','tempImagOff2') )
# USER: The product of the two voltage patterns is made into a
# USER: baseline based primary beam.
        makeBeams.makeBaseline("tempRealOff1","tempRealOff2","tempImagOff1",\
                               "tempImagOff2","tempReal","tempImag")
# USER: The beam is scaled to the proper frequency.
        makeBeams.changeFreq(freq,"tempReal")
        makeBeams.changeFreq(freq,"tempImag")
        os.system("rm -rf model_new")
# USER: The model is regrided to the beam scale
        os.system("regrid in=%s tin=tempReal axes=1,2 out=model_new" % model)
# USER: This offset beam multiplies the model with or without clipping.
        if beamClip == None :
            os.system("maths exp='(<tempReal>*<model_new>)' out=%s" %\
                      (outFileReal))
            os.system("maths exp='(<tempImag>*<model_new>)' out=%s" %\
                      (outFileImag))
        else :
# USER: The following two lines will not compile as is.
            os.system("maths exp='(<tempReal>*<model_new>)' out=%s \
                       mask='(<tempReal>.gt.%f)'" % (outFileReal,beamClip))
            os.system("maths exp='(<tempImag>*<model_new>)' out=%s \
                       mask='(<tempReal>.gt.%f)'" % (outFileImag,beamClip))
# USER: A real and imaginary sky brightness distribution are returned.
# USER: These are now attenuated by the primary beams.
    return [outFileReal,outFileImag]
```

```
def subtractItQuick(modelFile,visFile,nPoint=1,antType='ovro',line=None) :
# USER: This is used only for testing.
    demosFiles="%s.real" % (antType)
    subFiles  ="%s.sub.real" % (antType)
    os.system("rm -rf %s* %s*" % (demosFiles,subFiles))
    os.system("demos map=%s vis=%s out=%s" % (modelFile,visFile,demosFiles))
    [antL1,antL2] = getAntList(antType)
    for j in range(1,nPoint+1) :
        if line == None : \
# USER: The next two commands will not compile as is.
           os.system("uvmodel vis=%s model=%s%i options=subtract,\
                      selradec,mfs select='ant(%s)(%s)' out=%s%i" % \
                     (visFile,demosFiles,j,antL1,antL2,subFiles,j))
        else : \
           os.system("uvmodel vis=%s model=%s%i options=subtract,\
                      selradec,mfs select='ant(%s)(%s)' out=%s%i line=%s" % \
                     (visFile,demosFiles,j,antL1,antL2,subFiles,j,line))
    os.system("uvcat vis='%s*' out=%s" % (subFiles,subFiles) )

def getAntList(antType) :
# USER: The antenna list is constructed for 'style' based illuminateType.
    if antType.lower() == 'ovro' : return ['1,2,3,4,5,6','1,2,3,4,5,6']
    elif antType.lower() == 'carma' : \
           return ['1,2,3,4,5,6','7,8,9,10,11,12,13,14,15']
    else : return ['7,8,9,10,11,12,13,14,15','7,8,9,10,11,12,13,14,15']

def prepareBeam(beam,model,dec='30:00:00',freq=100,ra='00:00:00',offRa=0.0,\
                offDec=0.0,pntError=[0.0,0.0]) :
# USER: The beam is offset to the proper position and the
# USER: correct ra/dec center is put into the header.
```

```
    os.system("rm -rf td*")
    os.system("cp -r %s td1" % beam)
    makeBeams.adaptToImage("td1",dec='%s,dms' % dec,freq=freq,ra='%s,hms' % ra)
    cellSize = \
     float(os.popen("gethd in=td1/cdelt2 format=arcsec").read().replace('D','E'))
    makeBeams.offsetPositions("td1","td2",(-offRa+pntError[0])/cellSize,\
              (offDec+pntError[1])/cellSize)
    makeBeams.regridToImage("td2",model,"td3")
    cellSize = \
     float(os.popen("gethd in=td3/cdelt2 format=arcsec").read().replace('D','E'))
    makeBeams.offsetCenter("td3",(-offRa)/cellSize,(offDec)/cellSize)
    os.system("puthd in=%s/ra value=%s,hms" % ("td3",ra) )
    os.system("puthd in=%s/dec value=%s,dms" % ("td3",dec) )
    obsDec = convertSexDiff(dec,offDec,'dms')
    obsRa  = convertSexDiff(ra,\
             offRa/math.cos(convertSexToReal(dec)*math.pi/180.0),'hms')
    os.system("puthd in=%s/obsra value=%s,hms" % ("td3",obsRa) )
    os.system("puthd in=%s/obsdec value=%s,dms" % ("td3",obsDec) )
    os.system("puthd in=%s/crval1 value=%s,hms" % ("td3",obsRa) )
    os.system("puthd in=%s/crval2 value=%s,dms" % ("td3",obsDec) )

def makeHarange(start=-2.0,stop=2.0,step=0.008,refinement=0.5) :
# USER: The hour angle ranges are created according to the chopInterval,
# USER: called refinement here.
    harange=[]
    nSteps=int(math.ceil((stop-start)/refinement))
    for i in range(nSteps) :
        harangeT = '%f,%f,%f' % \
                   ((start+refinement*i),(start+refinement*(i+1)),step)
        harange.append(harangeT)
```

```
    return harange

def getAnts(visFile) :
# USER: This routine gets the antennas present in the dataset.
    antList = []
    os.system("rm -rf ant.temp")
    os.system('listobs vis=%s | grep "Antenna " | grep ": " > ant.temp' % \
              (visFile) )
    antInfo = fileIOPython.fileToTable("ant.temp",ignoreEmpty=True)
    for i in range(len(antInfo)) :
        try:
            antList.append(int(antInfo[i][1][:-1]))
        except:
            continue
    return antList

def getChi(vis,ant1=allAnts[0],ant2=allAnts[1]) :
# USER: This routine returns the parallatic angle range
# USER: in the input visibility dataset.
    os.system("rm -rf chi.temp")
    if ant2 < 10 : spacer= '   '
    else : spacer= '  '
# USER: All the parallatic angles are put into a file
# USER: The following line will not compile as is.
    os.system("uvlist vis=%s options=list,var recnum=100000 | \
                grep ' %i%s%i ' > chi.temp" % (vis,ant1,spacer,ant2) )
    chiInfo = fileIOPython.fileToTable("chi.temp",ignoreEmpty=True)
    print
    chiVals = []
    for i in range(len(chiInfo)) :
```

```
        try:
            chiVals.append(float(chiInfo[i][15]))
        except:
            continue
# USER: The angle is altered by 180 degrees to reflect
# USER: the fact that the beam library is defined
# USER: as a reflection, i.e. negative azimuth on the
# USER: beam library is actually positive azimuth on
# USER: the sky.  This step is needed because I
# USER: forgot this point initially when making the
# USER: beam libraries.
    try:
        meanChi= int(round(sum(chiVals)/len(chiVals)))
        if (meanChi) < 0 : meanChi=meanChi+180
        else : meanChi=meanChi-180
        if (meanChi) < 0 : meanChi=meanChi+360
        if (meanChi) > 360 : meanChi=meanChi-360
        return meanChi
    except:
        return None

def convertSexDiff(inp,diff,type='dms') :
# USER: This routine simply converts two numbers in hours or degrees
# USER: to a difference
    if type not in ['dms','hms'] : return 'ERROR: Incorrect format'
    inComp = convertSexToReal(inp)
    if type in ['dms'] : diff = diff
    elif type in ['hms'] : diff = diff/15.0
    diffA = diff/3600.0
    inDiff = inComp+diffA
```

```
    if type in ['hms'] and inDiff < 0.0 :
        inDiff = 24.0+inDiff
    return convertRealToSex(inDiff)

def convertRealToSex(inp) :
# USER: This routine converts a decimal number differences to
# USER: to sexagesimal values.
    inA = abs(inp)
    in1 = abs(int(inA))
    in2 = abs(int((inA-in1)*60.0))
    in3 = abs(((inA-in1-in2/60.0)*3600.0))
    if inp < 0 : strBase = '-'
    else : strBase=''
    intS = str(in1)
    strBase+=toString(in1)+':'+toString(in2)+':'+toString(in3)
    return strBase

def toString(inp) :
# USER: This routine converts a number to a string.
    if abs(inp) < 10 :
        out = '0'+str(abs(inp))
    else : out = str(inp)
    if inp < 0 : return '-'+out
    else : return out

def listToString(inp,sep=',') :
# USER: This routine converts a list to a string
# USER: with a user defined separator.
    outStr=''
    for i in inp :
```

```
        outStr+=str(i)+sep
    return outStr[:-1]

def convertSexToReal(inp) :
# USER: This routine converts sexagesimal numbers
# USER: to decimal numbers.
    inTrip = inp.split(':')
    for i in range(len(inTrip)) : inTrip[i] = float(inTrip[i])
    if inp[0] == '-' : return inTrip[0]-inTrip[1]/60.0-inTrip[2]/3600.0
    else : return inTrip[0]+inTrip[1]/60.0+inTrip[2]/3600.0

def cleanUp() :
# USER: This routine deletes all the files created by previous
# USER: runs of the program unless the user has moved
# USER: the results to a different location, i.e. is clean up
# USER: the default file names.
    for i in range(1,24) :
        print 'Doing antenna %i' %i
        os.system("rm -rf a%i.*" % i)
    for i in ['ovro','carma','hatcreek','sza','sza6','sza10'] :
        print 'Doing style %s' %i
        os.system("rm -rf %s.*" % i)
    os.system("rm -rf td*")
    os.system("rm -rf temp*")
    os.system("rm -rf freq* intermedFile chi.temp")
```

F.5 *uvmodel.py*

The package *uvmodel.py* is quite similar to *uvsubtract.py* except that the visibility dataset is not given to the routine, but is instead generated by parameters provided

by the user, i.e. the configuration, mosaic pointings, etc. The goal here is to simulate observations of a model and then compare the simulations to the model. Similar to *uvsubtract.py*, the comments and description are embedded within the code. Only cases where there is an important difference with *uvsubtract.py* are comments included. Several of the functions are redundant in the two packages.

```
#
import os,sys,time
import random,math
import makeBeams,makeModel
import fileIOPython
reload(makeBeams)
reload(makeModel)
# USER: Here, the imaging process is central to the package, so
# USER: the user needs to provide the number of {\bf mossdi} or {\bf mosmem}
# USER: iterations to be performed.
niters = 200
# USER: nchan is irrelevant, it gives the number of channels in the
# USER: simulated correlator. Given only continuum observations
# USER: are simulated.
nchan      = 1
# USER: ellim is the elevation limit
ellim      = 20
beamClip   = None
# USER: actLikePoint, when True, scales the gain error (discussed below)
# USER: by a factor of diameter/10.4.  If actLikePoint is False, the gain
# USER: errors are scaled by a factor of 1.
actLikePoint = False
# USER: The user here defines what type of deconvolution to use, valid
# USER: values are mosmem, default and joint.  The latter two options
# USER: require the use of single dish data which is not well developed
```

```
# USER: in this script except for sources that are about the size of the
# USER: 10.4 meter antenna primary beam, i.e. if single dish observations
# USER: need to be mosaiced, the script cannot handle this.
typeDecon  = 'mosmem'.upper()
# Batching
# USER: Below are several standard parameters that the user can provide
# USER: multiple values for and the script will execute over the range
# USER: of values provided.  The regular parameter (which will be discussed
# USER: later) simply has an 's' added to it here, i.e. configs (configurations)
# USER: is configss for multiple configurations and is defined as
# USER: [['A','B','C'],['C']] which would provide one simulation with three
# USER: configurations and another with only 'C' array.
# USER: cells is the cell sizes, making this value larger will make the
# USER: model image larger. This value replaces the pixel size in the model
# USER: image, so make this identical to the model cell size for zero change
# USER: in model size. gnoise is the percentage gain error to be applied,
# USER: i.e. 10 is 10%
configss    = [['D']]
cells       = [0.06]
gnoises     = [0.00]
# USER: WARNING! Pnoise in MIRIAD does not work as advertised on a baseline
# USER: basis.  Do not use this!
pnoises     = ['2.0,5.0,0.5,-0.5']
# USER: Real offset pointing errors can be input. A single pointing error can
# USER: have values like ['Random',[a,b,c],1] or ['User',ax1,ax2].  These
# USER: would result in Random errors of RMS a, b and c for 10-m, 6-m and 3.5-m
# USER: antennas, respectively.  The final value in the list beginning with
# USER: 'Random' controls how often the pointing errors are updated, every
# USER: refinement cycle (chopInterval above) for 1, every other refinement
# USER: cycle for 2, etc. Or, the user gives a list of constant offset for
```

```
# USER: each antenna.
pointingErrors = [None]#[['Random',[1.0,2.0],1],['Random',[2.0,3.5],1],
                       #['Random',[4.0,6.5],1],['Random',[6.0,9.0],1]]
                       # ['Random',[RMS],Persistence]; [User,ax1off,ax2off];
                       # pointing is altered for Random every persistence
                       # interval, measured in refinement intervals.
                       # RMS currently requires 1, 2 or 3 values.
                       # One could imagine making RMS function of time and
                       # different for different axes but this
                       # is not possible now.
                       # This has no effect if illuminateType is miriad,
                       # then gnoise controls pointing error.
# USER: User defined pointing patterns are given as a two column file with
# USER: ra offsets and dec offsets in arcseconds.
pointPats   = ['hex1_15']
illuminateTypes = ['miriad']
# USER: Starting and ending hour angle for the simulation.
haStarts = [-3]
haStops  = [ 3]
# USER: gaussianFits is not currently used.
gaussianFits = False
# USER: The list of models to be tested.
models=['diskModelHole_small']
# USER: The user needs to set the tau for the observation
# USER: as well as the parameters of the model.  On the
# USER: whole, only frequency and imsize need to be changed
# USER: with any regularity.
#
tau220     = 0.08
dec        = '20:00:00'
```

```
ra         = '04:00:00'
freq       = 230.0
lat        = 37.02
imsize     = 1025
flux       = float(os.popen("histo in=%s | grep Flux | awk '{printf($6)}'" % \
                   models[0]).read())
# USER: This sets the single dish RMS where relevant.
# USER: Particularity of MIRID require this to be non-zero
# USER: so if single dish is being used, gnoises[0] needs
# USER: to be non-zero.
sd_rms     = flux*gnoises[0]/100.0
#
ovroAnts = range(1,7)
bimaAnts = range(7,16)
if 'Z' not in configss[0] :
    print 'I am NOT using the SZA!'
    szaAnts  = range(0)
    allAnts = range(1,16)
    antTypes = ['carma','ovro','hatcreek']
else :
    print 'I am using the SZA!'
    szaAnts  = range(16,24)
    allAnts = range(1,24)
    antTypes = ['carma','ovro','hatcreek','sza10','sza6','sza']
# USER: There are antenna size, Jy/K and system temperatures for
# USER: the various MIRIAD primary beams types, these need not be changed.
teleInfo     = {'ovro'     : [10.4,  43.0, 80.0],
                'carma'    : [ 8.0,  73.0, 80.0],
                'hatcreek' : [ 6.1, 126.0, 80.0],
                'sza10'    : [ 6.0, 128.0, 80.0],
```

```
                'sza6'      : [ 4.6, 220.0, 80.0],
                'sza'       : [ 3.5, 383.0, 80.0]}
# USER: The simulation begins, wrapping through all the various parameters
# USER: defined above.
def uvmodel_sim_wrap() :
    xx = len(models)*len(cells)*len(configss)*len(gnoises)*len(pnoises)*\
         len(illuminateTypes)*len(pointingErrors)*len(haStarts)*\
         len(haStops)*len(pointPats)
    count=0
    print 'We are going to do: ',xx,' realizations.  Okay?  Press enter.'
    sys.stdin.readline()
    for i in models :
        for j in cells :
            for k in configss :
                for l in gnoises :
                    for m in pnoises :
                        for n in illuminateTypes :
                            for o in pointingErrors :
                                for p in haStarts :
                                    for q in haStops :
                                        for r in pointPats :
                                            uvmodel_sim(model=i,configs=k,\
                                                        cell=j,gnoise=l,\
                                                        pnoise=m,\
                                                        illuminateType=n,\
                                                        pointingError=o,\
                                                        haStart=p,\
                                                        haStop=q,pointPat=r,\
                                                        refinement=6,\
                                                        doQuick=True,\
```

```
                                                    doGainNoise=True)

def uvmodel_sim(model='casc.vla',configs=['D'],dec=dec,ra=ra,cell=0.125,\
                gnoise=0.1,pnoise='0,0,0,0',freq=freq,haStart=-2,haStop=2,\
                haStep=0.008,refinement=None,illuminateType='miriad',\
                doGainNoise=False,doQuick=True,pointingError=None,\
                pointPat='hex1_15') :
# USER: The simulation can be executed simply by calling this function with
# USER: import uvmodel
# USER: uvmodel.uvmodel_sim()
# USER: at a Python prompt.  However, it is usually easier to
# USER: define the parameter values and call this routine via
# USER: the wrapper, uvmodel_sim_wrap().
    cleanUp()
# USER: refinement is the same as chopInterval above.
    if refinement == None : refinement = haStop-haStart
    Harange = makeHarange(haStart,haStop,haStep,refinement)
# USER: refineModel takes the input model and sets its position,
# USER: cell size, and frequency to the desired values.
    refineModel(model,ra,dec,cell,freq)
    model = '%s.temp' % model
    print Harange
    if 1 :
# USER: This step reads in the pointing pattern.
        pointTable = fileIOPython.fileToTable(pointPat,ignoreEmpty=True)
        nPoint     = len(pointTable)
        dataFile = open('dataFile','w')
# USER: The loops over configuration and hour angle refinement begins.
        for config in configs :
            for ii in range(len(Harange)) :
```

```
                harange = Harange[ii]
# USER: This step makes creates the visibility points that will
# USER: will eventually sample the model.
                makeUvBaseline(config,dec=dec,harange=harange,freq=freq,\
                               haNum=ii,ra=ra,pointPat=pointPat)
                if ((not doQuick) or (illuminateType<>'miriad')) :
                    teleName = getTeleKey(allAnts[0],allAnts[1])
                    fileUv = ("%s.config%s.ha%i.uv" % (teleName,config,ii) )
                    chiVal = getChi(fileUv)
                    chiVal  = int(round(chiVal/20.0))*20
                    if chiVal > 340 : chiVal = 0
                    for jj in range(nPoint) :
                        pointingInfo = pointTable[jj][0].split(',')
                        for temp in range(len(pointingInfo)) : \
                             pointingInfo[temp] = float(pointingInfo[temp])
# USER: This step generates the random pointing offsets.
                        [pntA1,pntA2] = makePointingError(pointingError,ii)
# USER: Now, the loop over baselines begins.
                        for kk in allAnts :
                            for ll in allAnts :
                                if kk < ll :
                                    print 'Ha ',ii,' and pointing ',jj
                                    print 'baseline ',kk,' x ',ll
                                    teleName = getTeleKey(kk,ll)
                                    fileUv = ("%s.config%s.ha%i.uv" % \
                                             (teleName,config,ii) )
                                    if illuminateType in ['real'] : \
                                             isReal = False
                                    else : isReal = True
                                    [fileIllumReal,fileIllumImag] = \
```

```
                                    illuminateModel(model,fileUv,ra,dec,\
                                    kk,ll,pointingInfo,ii,jj,\
                                    illuminateType,pntA1,pntA2,freq=freq,\
                                    cell=cell,isReal=isReal,chi2O=chiVal,\
                                    config=config)
                                [fileModelImag] = \
                                    uvmodel_single(fileUv,fileIllumReal,\
                                    fileIllumImag,kk,ll,ii,jj,\
                                    pointingInfo,isReal,\
                                    doGainNoise=doGainNoise,\
                                    harange=harange,config=config,\
                                    gnoise=gnoise,pnoise=pnoise)
                                dataFile.write("%s\n" % (fileModelImag) )
                else :
                    print 'I am making it quick.'
                    makeItQuick(model,ii,harange,doGainNoise=doGainNoise,\
                                config=config,nPoint=nPoint,gnoise=gnoise,\
                                pnoise=pnoise)
                    for mm in antTypes : \
                        dataFile.write("%s.config%s.ha%i.mod.real\n" % \
                                       (mm,config,ii))
        dataFile.close()
    else : dataFile='dataFile'
# USER: The simulated dataset is imaged and then differenced from the model.
    makeImage(model,typeDecon=typeDecon,doQuick=doQuick,cell=cell)
    makeEquivModelAndDiff(model,cell)
# USER: Statistics of the run are recorded.
    writeStats(model,doGainNoise,illuminateType,refinement,haStart,haStop,\
               doQuick,gnoise,pnoise,configs,cell,pointingError,pointPat)
```

```
def illuminateModel(model,visfile,ra,dec,ant1,ant2,pointingInfo=[0.0,0.0],\
                    haNum=0,pointNum=0,illuminateType='miriad',pntA1=0.0,\
                    pntA2=0.0,freq=100,cell=0.162,isReal=False,chi20=0,\
                    config='D') :
# USER: The only difference between this illuminateModel
# USER: and the one in uvsubtract is that this one allows
# USER: for the pointing centers to be slightly modified.
    offRa  = pointingInfo[0]
    offDec = pointingInfo[1]
    pError1 = [pntA1[ant1-1],pntA2[ant1-1]]
    pError2 = [pntA1[ant2-1],pntA2[ant2-1]]
    draH  = (pointingInfo[0]+0.01) ; draL  = (pointingInfo[0]-0.01) ## these are
    ddecH = (pointingInfo[1]+0.01) ; ddecL = (pointingInfo[1]-0.01) ## in arcsec
    outFileReal = ("a%i.a%i.config%s.ha%i.pnt%i.real" % \
                   (ant1,ant2,config,haNum,pointNum))
    outFileImag = ("a%i.a%i.config%s.ha%i.pnt%i.imag" % \
                   (ant1,ant2,config,haNum,pointNum))
    os.system("rm -rf %s %s" % (outFileReal,outFileImag) )
    if illuminateType=='miriad' :
        os.system("demos map=%s vis=%s out=%s select='dra(%s,%s),ddec(%s,%s)'"%\
                  (model,visfile,outFileReal,draL,draH,ddecL,ddecH))
        os.system("mv %s1 %s" % (outFileReal,outFileReal) )
        os.system("imgen in=%s out=%s factor=0 object=level spar=0" % \
                  (outFileReal,outFileImag) )
    else:
        if 'style' in illuminateType.lower() :
            if ant1 < 7 and ant2 < 7 :
                fileReal1=\
                 "/export/sun1/sac/beamModels/%sBeams/paraAngle%i/ovro.real"%\
                 (illuminateType,chi20)
```

```
                fileImag1=\
                 "/export/sun1/sac/beamModels/%sBeams/paraAngle%i/ovro.imag" %\
                 (illuminateType,chi20)
                fileReal2=\
                 "/export/sun1/sac/beamModels/%sBeams/paraAngle%i/ovro.real" %\
                 (illuminateType,chi20)
                fileImag2=\
                 "/export/sun1/sac/beamModels/%sBeams/paraAngle%i/ovro.imag" %\
                 (illuminateType,chi20)
            elif ant1 < 7 and ant2 > 6 :
                fileReal1=\
                 "/export/sun1/sac/beamModels/%sBeams/paraAngle%i/carma.real"%\
                 (illuminateType,chi20)
                fileImag1=\
                 "/export/sun1/sac/beamModels/%sBeams/paraAngle%i/carma.imag"%\
                 (illuminateType,chi20)
                fileReal2=\
                 "/export/sun1/sac/beamModels/%sBeams/paraAngle%i/carma.real"%\
                 (illuminateType,chi20)
                fileImag2=\
                 "/export/sun1/sac/beamModels/%sBeams/paraAngle%i/carma.imag"%\
                 (illuminateType,chi20)
            elif ant1 > 6 and ant2 > 6 :
# USER: This next four commands will not compile as is.
                fileReal1=\
                 "/export/sun1/sac/beamModels/\
                 %sBeams/paraAngle%i/hatcreek.real" % (illuminateType,chi20)
                fileImag1=\
                 "/export/sun1/sac/beamModels/\
                 %sBeams/paraAngle%i/hatcreek.imag" % (illuminateType,chi20)
```

```
        fileReal2=\
         "/export/sun1/sac/beamModels/\
         %sBeams/paraAngle%i/hatcreek.real" % (illuminateType,chi20)
        fileImag2=\
         "/export/sun1/sac/beamModels/\
         %sBeams/paraAngle%i/hatcreek.imag" % (illuminateType,chi20)
else :
    fileReal1=\
     "/export/sun1/sac/beamModels/%sBeams/paraAngle%i/a%i.s.real" % \
     (illuminateType,chi20,ant1)
    fileImag1=\
     "/export/sun1/sac/beamModels/%sBeams/paraAngle%i/a%i.s.imag" % \
     (illuminateType,chi20,ant1)
    fileReal2=\
     "/export/sun1/sac/beamModels/%sBeams/paraAngle%i/a%i.s.real" % \
     (illuminateType,chi20,ant2)
    fileImag2=\
     "/export/sun1/sac/beamModels/%sBeams/paraAngle%i/a%i.s.imag" % \
     (illuminateType,chi20,ant2)
os.system("rm -rf tempRealOff* tempImagOff* tempReal tempImag")
prepareBeam(fileReal1,model,dec=dec,freq=freq,ra=ra,offRa=offRa,\
            offDec=offDec,pntError=pError1)
os.system("cp -r tb3 tempRealOff1")
prepareBeam(fileReal2,model,dec=dec,freq=freq,ra=ra,offRa=offRa,\
            offDec=offDec,pntError=pError2)
os.system("cp -r tb3 tempRealOff2")
if not isReal :
    prepareBeam(fileImag1,model,dec=dec,freq=freq,ra=ra,offRa=offRa,\
                offDec=offDec,pntError=pError1)
    os.system("cp -r tb3 tempImagOff1")
```

```
            prepareBeam(fileImag2,model,dec=dec,freq=freq,ra=ra,offRa=offRa,\
                        offDec=offDec,pntError=pError2)
            os.system("cp -r tb3 tempImagOff2")
        else :
            os.system("imgen in=%s out=%s factor=0 object=level spar=0" % \
                     ('tempRealOff1','tempImagOff1') )
            os.system("imgen in=%s out=%s factor=0 object=level spar=0" % \
                     ('tempRealOff2','tempImagOff2') )
        makeBeams.makeBaseline("tempRealOff1","tempRealOff2","tempImagOff1",\
                               "tempImagOff2","tempReal","tempImag")
        if beamClip == None :
            os.system("maths exp='(<tempReal>*<%s>)' out=%s" % \
                      (model,outFileReal))
            os.system("maths exp='(<tempImag>*<%s>)' out=%s" % \
                      (model,outFileImag))
        else :
# USER: The next two commands will not compile as is.
            os.system("maths exp='(<tempReal>*<%s>)' out=%s \
               mask='(<tempReal>.gt.%f)'" % (model,outFileReal,beamClip))
            os.system("maths exp='(<tempImag>*<%s>)' out=%s \
               mask='(<tempReal>.gt.%f)'" % (model,outFileImag,beamClip))
    return [outFileReal,outFileImag]

def uvmodel_single(vis,realPart,imagPart,ant1,ant2,haNum=0,pNum=0,\
    pointingInfo=[0.0,0.0],isReal=False,doGainNoise=False,\
    harange='-2,2,0.008',config='D',gnoise=0.1,pnoise='0,0,0,0') :
# USER: This is more or less the same function as in uvsubtract
# USER: except gain noise can be added and that the visibilities
# USER: associated with the blank field are added to the sampled
# USER: visibilities of the model instead of subtracted as they
```

```
# USER: were above.  This is the case because above, the visibility
# USER: file included the source whereas here there was no source
# USER: in the visibility file.
    outFileReal = "a%i.a%i.config%s.ha%i.pnt%i.mod.real" % \
                  (ant1,ant2,config,haNum,pNum)
    outFileImag = "a%i.a%i.config%s.ha%i.pnt%i.mod.imag" % \
                  (ant1,ant2,config,haNum,pNum)
    draH  = pointingInfo[0]+0.01
    draL  = pointingInfo[0]-0.01
    ddecH = pointingInfo[1]+0.01
    ddecL = pointingInfo[1]-0.01
    os.system("rm -rf %s %s" % (outFileReal,outFileImag) )
# USER: The next two commands will not compile as is.
    os.system("uvmodel vis=%s model=%s out=%s select='ant(%i)(%i),\
              dra(%f,%f),ddec(%f,%f)' options=add,selradec" % \
              (vis,realPart,outFileReal,ant1,ant2,draL,draH,ddecL,ddecH) )
    if not isReal : os.system("uvmodel vis=%s model=%s out=%s \
                    select='ant(%i)(%i),dra(%f,%f),ddec(%f,%f)' \
                    options=add,selradec,imag" % \
                    (outFileReal,imagPart,outFileImag,ant1,ant2,draL,draH,\
                    ddecL,ddecH) )
    else : os.system("cp -r %s %s" % (outFileReal,outFileImag) )
# USER: If gain noise is to be introduced it is generated here.
    if doGainNoise :
        teleType=getTeleKey(ant1,ant2)
        addGainNoise(outFileImag,teleType,harange,gnoise=gnoise,\
                     pnoise=pnoise,config=config)
    return [outFileImag]

def prepareBeam(beam,model,dec='30:00:00',freq=100,ra='00:00:00',offRa=0.0,\
```

```
                offDec=0.0,pntError=[0.0,0.0]) :
    os.system("rm -rf tb*")
    os.system("cp -r %s tb1" % beam)
    makeBeams.adaptToImage("tb1",dec='%s,dms' % dec,freq=freq,ra='%s,hms' % ra)
    cellSize = \
          float(\
          os.popen("gethd in=tb1/cdelt2 format=arcsec").read().replace('D','E'))
    makeBeams.offsetPositions("tb1","tb2",(-offRa+pntError[0])/cellSize,\
                              (offDec+pntError[1])/cellSize)
    makeBeams.regridToImage("tb2",model,"tb3")
    cellSize = \
         float(\
         os.popen("gethd in=tb3/cdelt2 format=arcsec").read().replace('D','E'))
    makeBeams.offsetCenter("tb3",(-offRa)/cellSize,(offDec)/cellSize)
    os.system("puthd in=%s/ra value=%s,hms" % ("tb3",ra) )
    os.system("puthd in=%s/dec value=%s,dms" % ("tb3",dec) )
    obsDec = convertSexDiff(dec,offDec,'dms')
    obsRa  = convertSexDiff(ra,\
             offRa/math.cos(convertSexToReal(dec)*math.pi/180.0),'hms')
    os.system("puthd in=%s/obsra value=%s,hms" % ("tb3",obsRa) )
    os.system("puthd in=%s/obsdec value=%s,dms" % ("tb3",obsDec) )
    os.system("puthd in=%s/crval1 value=%s,hms" % ("tb3",obsRa) )
    os.system("puthd in=%s/crval2 value=%s,dms" % ("tb3",obsDec) )

def addGainNoise(fileIn,teleType='ovro',harange='-2,2,0.5',newInterval=0.25,\
                 gnoise=0.1,pnoise='0,0,0,0',config='D') :
# USER: The gain noise is injected here.
# USER: First the proper antennas are identified.
    if ((teleType=='ovro') or (teleType=='carma') or (teleType=='sza10'))  :
        aL1 = listToString(ovroAnts)
```

```
        if (teleType=='ovro') : aL2=listToString(ovroAnts)
        elif (teleType=='carma') : aL2=listToString(bimaAnts)
        else : aL2=listToString(szaAnts)
    elif ((teleType=='hatcreek') or (teleType=='sza6')) :
        aL1=listToString(bimaAnts)
        if (teleType=='hatcreek') : aL2 = listToString(bimaAnts)
        else : aL2 = listToString(szaAnts)
    elif (teleType=='sza') :
        aL1=listToString(szaAnts)
        aL2=listToString(szaAnts)
    os.system("rm -rf gains.uv")
    systemp="%s,290,%s" % (teleInfo[teleType][2],tau220) # dsb rxtemp,
                                                         # sky temp,
                                                         # zenith opacity
    harangeT=harange.split(',')
    harangeT[2]=newInterval
    harangeT=listToString(harangeT)
    cycle ="%s,%s" % (newInterval*0.2,newInterval*0.8)
# USER: Gain noise is introduced by creating a visibility file associated
# USER: with a point source.  The gain error is injected directly here.
    if actLikePoint :
        print 'acting like point'
        print gnoise
# USER: The next two uvgen commands will not compile as is.
        os.system("uvgen ant=%s.ant baseunit=-3.33564 radec=%s,%s lat=%f \
                  harange=%s source=$MIRCAT/point.source systemp=%s \
                  jyperk=%f freq=%f corr=%i,1,0,4000 telescop=%s ellim=%f \
                  gnoise=%f pnoise=%s cycle=%s out=gains.uv" % \
                  (config,ra,dec,lat,harangeT,systemp,teleInfo[teleType][1],\
                  freq,nchan,teleType,ellim,\
```

```
                    float(gnoise*teleInfo[teleType][0]/10.4),pnoise,cycle) )
    else :
        print 'acting like surface'
        os.system("uvgen ant=%s.ant baseunit=-3.33564 radec=%s,%s lat=%f \
                    harange=%s source=$MIRCAT/point.source systemp=%s \
                    jyperk=%f freq=%f corr=%i,1,0,4000 telescop=%s ellim=%f \
                    gnoise=%f pnoise=%s out=gains.uv" % (config,ra,dec,lat,\
                    harangeT,systemp,teleInfo[teleType][1],freq,nchan,teleType,\
                    ellim,(gnoise),pnoise) )
# USER: The gain errors are applied to the main visibility file
# USER: by deriving a self-cal solution and copying the resulting
# USER: gain file over to the main file where they are applied.
    os.system("selfcal vis=gains.uv options=amp")
    os.system("gpcopy vis=gains.uv out=%s" % fileIn)
    os.system("mv %s temp.gains" % fileIn)
    os.system("uvcat vis=temp.gains out=%s" % fileIn)
    print pnoise,gnoise

def makeUvBaseline(config='D',ra='00:00:00',dec='30:00:00',\
                    harange='-2,2,0.008',freq=100.0,haNum=0,pointPat='hex1_15') :
# USER: Here visibilities associated with an empty field are created
# USER: according to the pointing pattern, configuration, source
# USER: location, system temperature, hour angle coverage,
# USER: frequency and correlator setup.
    for i in teleInfo.keys() :
        systemp="%f,290,%f" % (teleInfo[i][2],tau220) # dsb rxtemp,
                                                      # sky temp,
                                                      # zenith opacity
        fileOut = "%s.config%s.ha%i.uv" % (i,config,haNum)
        os.system("rm -rf %s" % (fileOut) )
```

```
# USER: The following uvgen command will not compile as is.
        os.system("uvgen ant=%s.ant baseunit=-3.33564 radec=%s,%s lat=%f \
                  harange=%s source=$MIRCAT/no.source systemp=%s jyperk=%f \
                  freq=%f corr=%i,1,0,4000 telescop=%s ellim=%f center=@%s \
                  out=%s" % (config,ra,dec,lat,harange,systemp,teleInfo[i][1],\
                  freq,nchan,i,ellim,pointPat,fileOut) )

def makeItQuick(model='casc.vla',haNum=0,harange='-2,2,0.008',\
                doGainNoise=False,config='D',nPoint=1,gnoise=0.1,\
                pnoise='0,0,0,0') :
# USER: Used for testing and quick sampling when 'miriad' illuminateType
# USER: is selected.
    for i in teleInfo.keys() :
        if ((i=='ovro') or (i=='carma') or (i=='sza10'))  :
            aL1 = listToString(ovroAnts)
            if (i=='ovro') : aL2=listToString(ovroAnts)
            elif (i=='carma') : aL2=listToString(bimaAnts)
            else : aL2=listToString(szaAnts)
        elif ((i=='hatcreek') or (i=='sza6')) :
            aL1=listToString(bimaAnts)
            if (i=='hatcreek') : aL2 = listToString(bimaAnts)
            else : aL2 = listToString(szaAnts)
        elif (i=='sza') :
            aL1=listToString(szaAnts)
            aL2=listToString(szaAnts)
        visFile="%s.config%s.ha%i.uv" % (i,config,haNum)
        demosFiles="%s.config%s.ha%i.all.real" % (i,config,haNum)
        modFiles  ="%s.config%s.ha%i.mod.real" % (i,config,haNum)
        os.system("rm -rf %s* %s*" % (demosFiles,modFiles))
        os.system("demos map=%s vis=%s out=%s" % (model,visFile,demosFiles))
```

```
        for j in range(1,nPoint+1) :
# USER: This uvmodel command will not compile as is.
            os.system("uvmodel vis=%s model=%s%i options=add,selradec \
                      out=%s%i select='ant(%s)(%s)'" % \
                      (visFile,demosFiles,j,modFiles,j,aL1,aL2))
        os.system("uvcat vis='%s*' out=%s" % (modFiles,modFiles) )
        if doGainNoise : addGainNoise(modFiles,i,harange,gnoise=gnoise,\
                         pnoise=pnoise,config=config)

def makeEquivModelAndDiff(model='casc.vla',cell=0.125) :
# USER: Here the model is convolved to the resolution of
# USER: the simulated data and regrided onto the size and
# USER: pixel scale of that image.
# USER: The simulation and convolved model are then differenced
# USER: creating a difference image.
    modelSize = float(os.popen("histo in=%s | grep Mean | awk '{printf($8)}'"%\
                      model).read()[1:])
    boxVal     = float(int(cell*((modelSize**0.5)/2.0)))
    region     = ("'arcsec,boxes(%s,-%s,-%s,%s)'" % \
                 (boxVal,boxVal,boxVal,boxVal) )
    regionSpecs = abs(float(region.split(',')[-2]))
    normFac = 1.2
    regionT=("'arcsec,boxes(-%f,-%f,%f,%f)'" % \
            (regionSpecs*normFac,regionSpecs*normFac,regionSpecs*normFac,\
             regionSpecs*normFac))
    b1 = float(os.popen("prthd in=%s.cm | egrep Beam | awk '{print $3}'" % \
         model).read())
    b2 = float(os.popen("prthd in=%s.cm | egrep Beam | awk '{print $5}'" % \
         model).read())
    b3 = float(os.popen("prthd in=%s.cm | egrep Position | awk '{print $3}'"%\
```

```
          model).read())
    os.system("rm -rf %s.conv %s.regrid %s.resid" % (model,model,model) )
    os.system("convol map=%s fwhm=%f,%f pa=%s out=%s.conv" % \
              (model,b1,b2,b3,model) )
    os.system("regrid in=%s.conv out=%s.regrid tin=%s.cm axes=1,2" % \
              (model,model,model) )#
# USER: This imdiff command will not compile as is.
    os.system("imdiff in1=%s.cm in2=%s.regrid resid=%s.resid region=%s \
               options=nox,noy,noex" % (model,model,model,regionT) )


def makeImage(model,typeDecon='MOSMEM',catFile='tempCat',dataFile='dataFile',\
               doQuick=False,cell=0.125) :
# USER: Here the simulated observations are imaged and deconvolved.
# USER: The type of deconvolution is selected at the top of the
# USER: simulation.
    modelSize = float(os.popen("histo in=%s | grep Mean | awk '{printf($8)}'"%\
                               model).read()[1:])
    boxVal     = float(int(cell*((modelSize**0.5)/2.0)))
    region     = ("'arcsec,boxes(%s,-%s,-%s,%s)'" % \
                 (boxVal,boxVal,boxVal,boxVal) )
    catFiles(dataFile,doQuick)
    supVal = 60
    robustVal= -2
# USER: The following two commands will not compile as is
    os.system("rm -rf %s.map %s.beam %s.cm %s.cl %s.sen %s.gain junk.map \
               junk.beam %s.psf" % (model,model,model,model,model,model,model))
    os.system("invert select='-shadow(3.5)' vis=%s map=junk.map beam=junk.beam \
               imsize=%i options=double,mosaic sup=%f robust=%f" % \
              (catFile,imsize,supVal,robustVal) )
    os.system("mospsf beam=junk.beam out=%s.psf" % model)
```

```
# USER: The following four commands will not compile as is.
    b1       = float(os.popen(\
               "imfit clip=0.05 in=%s.psf region='arcsec,boxes(-10,-10,10,10)' \
               object=gauss | grep 'Major axis' | awk '{printf($4)}'" % \
               model).read())
    b2       = float(os.popen(\
               "imfit in=%s.psf clip=0.05 region='arcsec,boxes(-10,-10,10,10)' \
               object=gauss | grep 'Minor axis' | awk '{printf($4)}'" % \
               model).read())
    b3       = float(os.popen(\
               "imfit in=%s.psf clip=0.05 region='arcsec,boxes(-10,-10,10,10)' \
               object=gauss | grep 'Position angle' | awk '{printf($4)}'" % \
               model).read())
    os.system("invert select='-shadow(3.5)' vis=%s map=%s.map beam=%s.beam \
              imsize=%i options=double sup=%f robust=%f" % \
              (catFile,model,model,imsize,supVal,robustVal) )
# USER: The following mosmem and mossdi command will not compile as is.
    if typeDecon=='MOSMEM' :
        print 'I am not doing single dish'
        if 'point' not in model : os.system("mosmem map=%s.map beam=%s.beam \
                          out=%s.cl niters=%i flux=%f rmsfac=1 region=%s" % \
                          (model,model,model,niters,flux,region) )
        else : os.system("mossdi map=%s.map beam=%s.beam out=%s.cl niters=%i \
                          flux=%f rmsfac=1 region=%s" % \
                          (model,model,model,niters,flux,region) )
        region="'arcsec,boxes(-2,-2,2,2)'"
# USER: This command will not compile as is.
        os.system("maxen rms=0.1 map=%s.map beam=%s.beam out=%s.cl niters=%i \
                  flux=%f rmsfac=1 region=%s" % \
                  (model,model,model,niters,flux,region) )
```

```
    else :
        makeSingleDish(model,'%s.map' % model)
        sd_rmsVal = sd_rms
        os.system("puthd in=%s.single.map/rms value=%f" % (model,sd_rmsVal) )
# USER: The following mosmem and mossdi commands will not compile as is.
        if typeDecon=='DEFAULT' :
            if 'point' not in model :
                os.system("mosmem map=%s.map default=%s.single.map beam=%s.beam\
                          out=%s.cl niters=%i rmsfac=1 region=%s" % \
                          (model,model,model,model,niters,region) )
            else :
                os.system("mossdi map=%s.map default=%s.single.map beam=%s.beam\
                          out=%s.cl niters=%i rmsfac=1 region=%s" % \
                          (model,model,model,model,niters,region) )
        elif typeDecon=='JOINT' :
            if 'point' not in model :
                os.system("mosmem map=%s.map,%s.single.map beam=%s.beam,\
                          %s.single.beam out=%s.cl niters=%i rmsfac=1,1 \
                          region=%s" % \
                          (model,model,model,model,model,niters,region) )
            else :
                os.system("mossdi map=%s.map,%s.single.map beam=%s.beam,\
                          %s.single.beam out=%s.cl niters=%i rmsfac=1,1 \
                          region=%s" % \
                          (model,model,model,model,model,niters,region) )
        else : return 'improper typeDecon'
    os.system("mossen in=%s.map sen=%s.sen gain=%s.gain" % \
              (model,model,model) )
# USER: This restor command will not compile as is.
    os.system("restor model=%s.cl map=%s.map beam=%s.beam out=%s.cm \
```

```
            fwhm=%f,%f pa=%f" % (model,model,model,model,b1,b2,b3) )

def refineModel(model,ra='00:00:00',dec='30:00:00',cell=0.162,freq=100) :
# USER: The model is altered to the location, size and frequency desired.
    fileName = "%s.temp" % model
    os.system("rm -r %s" % fileName)
    os.system("cp -r %s %s" % (model,fileName) )
    os.system("puthd in=%s/crval1 value=%s,hms"    % (fileName,ra) )
    os.system("puthd in=%s/crval2 value=%s,dms"    % (fileName,dec) )
    os.system("puthd in=%s/crval3 value=%f"        % (fileName,freq) )
    os.system("puthd in=%s/cdelt1 value=%f,arcsec" % (fileName,(-cell)) )
    os.system("puthd in=%s/cdelt2 value=%f,arcsec" % (fileName,cell) )

def makeHarange(start=-2.0,stop=2.0,step=0.008,refinement=0.5) :
    harange=[]
    nSteps=int((stop-start)/refinement)
    for i in range(nSteps) :
        harangeT = '%f,%f,%f' % ((start+refinement*i),\
                   (start+refinement*(i+1)),step)
        harange.append(harangeT)
    return harange

def getChi(vis,ant1=allAnts[0],ant2=allAnts[1]) :
    os.system("rm -rf chi.temp")
    if ant2 < 10 : spacer= '   '
    else : spacer= '  '
# USER: This uvlist command will not compile as is.
    os.system("uvlist vis=%s options=list,var recnum=100000 \
              | grep ' %i%s%i ' > chi.temp" % (vis,ant1,spacer,ant2) )
    chiInfo = fileIOPython.fileToTable("chi.temp")
```

```
    chiVals = []
    for i in range(len(chiInfo)) :
        try:
            chiVals.append(float(chiInfo[i][15]))
        except:
            continue
    meanChi= int(round(sum(chiVals)/len(chiVals)))
    if (meanChi) < 0 : meanChi=meanChi+180
    else : meanChi=meanChi-180
    if (meanChi) < 0 : meanChi=meanChi+360
    if (meanChi) > 360 : meanChi=meanChi-360
    return meanChi


def makePointingError(pointingError,ha_time=0) :
# USER: Most of the code here is to disentangle the
# USER: syntax of the pointing error list described above.
# USER: In the end the function is simple, create a list
# USER: of errors for each antenna to be applied for
# USER: this round of hour angle.
    if pointingError == None :
        pntA1 = [0.0]*len(allAnts) ; pntA2 = [0.0]*len(allAnts)
    else :
        if pointingError[0] == 'Random' :
            if len(pointingError[1])==1 : pointingError[1]=pointingError[1]*3
            elif len(pointingError[1])==3 : pointingError[1]=pointingError[1]
            elif len(pointingError[1])==2 : pointingError[1].append(0)
            else : return 'pointing error description invalid.'
            if not ha_time % pointingError[2] :
                pntA1 = gaussVec(0.0,pointingError[1][0],\
                        len(ovroAnts))+gaussVec(0.0,pointingError[1][1],\
```

```
                        len(bimaAnts))+gaussVec(0.0,pointingError[1][2],\
                        len(szaAnts))
                pntA2 = gaussVec(0.0,pointingError[1][0],\
                        len(ovroAnts))+gaussVec(0.0,pointingError[1][1],\
                        len(bimaAnts))+gaussVec(0.0,pointingError[1][2],\
                        len(szaAnts))
        elif pointingError[0] == 'User' :
            pntA1 = pointingError[1]
            pntA2 = pointingError[2]
    return [pntA1,pntA2]


def makeSingleDish(model='casc.vla',interferoImag='casc.vla',teleName='ovro',\
                   freq=freq) :
# USER: The single dish data is created here.  Again, it
# USER: only works when the source is on the order of
# USER: or slightly smaller than the 10.4 meter antenna
# USER: primary beam.  The model is convolved to the
# USER: resolution of the primary beam creating
# USER: an effective single dish map at a single pointing.
# USER: This next line will not compile as is.
    pbSingle = float(os.popen("pbplot telescop=%s freq=%f | grep FWHM | \
               awk '{print 60*$3}'" % (teleName,freq)).read())
    os.system("rm -rf %s.single.temp" % model)
    os.system("imframe in=%s frame=-1024,1024,-1024,1024 out=%s.single.temp"%\
              (model,model))
    os.system("rm -rf %s.single.temp.map" % model)
    os.system("convol map=%s.single.temp fwhm=%f,%f out=%s.single.temp.map"%\
             (model,pbSingle,pbSingle,model) )
    os.system("rm -rf %s.single.map" % model)
    os.system("regrid in=%s.single.temp.map tin=%s out=%s.single.map axes=1,2"%\
```

```
            (model,interferoImag,model) )
    os.system("rm -rf %s.single.beam" % model)
# USER: The next line will not compile as is.
    os.system("imgen in=%s.single.map factor=0 object=gaussian \
              spar=1,0,0,%f,%f,0 out=%s.single.beam" % \
              (model,pbSingle,pbSingle,model) )

def getTeleKey(ant1,ant2) :
# USER: The MIRIAD name for a baseline primary beam is determined
# USER: from the two constituent antennas, i.e. two 10.4 meter
# USER: antennas is OVRO while a 10.4 meter antenna and a 3.5 meter
# USER: antennas is a sza10.
    if (ant1 < 7) :
        if   (ant2 < 7)  : teleKey = 'ovro'
        elif (ant2 < 16) : teleKey = 'carma'
        else :             teleKey = 'sza10'
    elif (ant1 < 16) :
        if   (ant2 < 16) : teleKey = 'hatcreek'
        else :             teleKey = 'sza6'
    else :                 teleKey = 'sza'
    return teleKey

def gaussVec(mean=0.0,rms=1.0,numVar=1) :
# USER: This makes a list of Gaussian random numbers.
    outVec = []
    for i in range(numVar) : outVec.append(random.gauss(mean,rms))
    return outVec

def catFiles(dataFile,doQuick=False) :
# USER: All of the files are combined here in batches of 15.
```

```
# USER: The details of why this is necessary are beyond the
# USER: scope of this discussion.
# USER: The multi-line uvcat commands in this routine will not compile as is.
    os.system("rm -rf tempCat")
    if not doQuick :
        if len(szaAnts) == 0 :
            fileTable = fileIOPython.fileToTable(dataFile)
            os.system("uvcat vis=%s out=tempCat" % fileTable[0][0])
            for j in range(len(fileTable)/15) :
                os.system("rm -rf tempTempCat")
                i = j*15
                if j==0 :
                    os.system("uvcat vis=tempCat,%s,%s,%s,%s,%s,%s,%s,%s,%s,%s,%s,\
                              %s,%s,%s,%s out=tempTempCat" % \
                              (fileTable[i+1][0],fileTable[i+2][0],\
                              fileTable[i+3][0],fileTable[i+4][0],\
                              fileTable[i+5][0],fileTable[i+6][0],\
                              fileTable[i+7][0],fileTable[i+8][0],\
                              fileTable[i+9][0],fileTable[i+10][0],\
                              fileTable[i+11][0],fileTable[i+12][0],\
                              fileTable[i+13][0],fileTable[i+14][0]) )
                else :
                    os.system("uvcat vis=tempCat,%s,%s,%s,%s,%s,%s,%s,%s,%s,%s,%s,\
                              %s,%s,%s,%s,%s out=tempTempCat" % \
                              (fileTable[i][0],fileTable[i+1][0],\
                              fileTable[i+2][0],fileTable[i+3][0],\
                              fileTable[i+4][0],fileTable[i+5][0],\
                              fileTable[i+6][0],fileTable[i+7][0],\
                              fileTable[i+8][0],fileTable[i+9][0],\
                              fileTable[i+10][0],fileTable[i+11][0],\
```

```
                        fileTable[i+12][0],fileTable[i+13][0],\
                        fileTable[i+14][0]) )
            os.system("rm -rf tempCat")
            os.system("uvcat vis=tempTempCat out=tempCat")
    else :
        fileTable = fileIOPython.fileToTable(dataFile)
        os.system("uvcat vis=%s out=tempCat" % fileTable[0][0])
        for j in range(len(fileTable)/11) :
            os.system("rm -rf tempTempCat")
            i = j*11
            if j==0 :
                os.system("uvcat vis=tempCat,%s,%s,%s,%s,%s,%s,%s,%s,%s,%s\
                        out=tempTempCat" % \
                        (fileTable[i+1][0],fileTable[i+2][0],\
                        fileTable[i+3][0],fileTable[i+4][0],\
                        fileTable[i+5][0],fileTable[i+6][0],\
                        fileTable[i+7][0],fileTable[i+8][0],\
                        fileTable[i+9][0],fileTable[i+10][0]) )
            else :
                os.system("uvcat vis=tempCat,%s,%s,%s,%s,%s,%s,%s,%s,%s,%s,\
                        %s out=tempTempCat" % \
                        (fileTable[i][0],fileTable[i+1][0],\
                        fileTable[i+2][0],fileTable[i+3][0],\
                        fileTable[i+4][0],fileTable[i+5][0],\
                        fileTable[i+6][0],fileTable[i+7][0],\
                        fileTable[i+8][0],fileTable[i+9][0],\
                        fileTable[i+10][0]) )
            os.system("rm -rf tempCat")
            os.system("uvcat vis=tempTempCat out=tempCat")
else :
```

```
        if len(szaAnts) == 0 :
            os.system("uvcat vis=@%s out=tempCat" % dataFile)
        else :
            fileTable = fileIOPython.fileToTable(dataFile)
            os.system("uvcat vis=%s out=tempCat" % fileTable[0][0])
            for j in range(len(fileTable)/6) :
                os.system("rm -rf tempTempCat")
                i = j*6
                if j==0 :
                    os.system("uvcat vis=tempCat,%s,%s,%s,%s,%s \
                              out=tempTempCat" % \
                              (fileTable[i+1][0],fileTable[i+2][0],\
                              fileTable[i+3][0],fileTable[i+4][0],\
                              fileTable[i+5][0]) )
                else :
                    os.system("uvcat vis=tempCat,%s,%s,%s,%s,%s,%s \
                              out=tempTempCat" % \
                              (fileTable[i][0],fileTable[i+1][0],\
                              fileTable[i+2][0],fileTable[i+3][0],\
                              fileTable[i+4][0],fileTable[i+5][0]) )
                os.system("rm -rf tempCat")
                os.system("uvcat vis=tempTempCat out=tempCat")

def convertSexDiff(inp,diff,type='dms') :
    if type not in ['dms','hms'] : return 'ERROR: Incorrect format'
    inComp = convertSexToReal(inp)
    if type in ['dms'] : diff = diff
    elif type in ['hms'] : diff = diff/15.0
    diffA = diff/3600.0
    inDiff = inComp+diffA
```

```
    if type in ['hms'] and inDiff < 0.0 :
        inDiff = 24.0+inDiff
    return convertRealToSex(inDiff)

def convertRealToSex(inp) :
    inA = abs(inp)
    in1 = abs(int(inA))
    in2 = abs(int((inA-in1)*60.0))
    in3 = abs(((inA-in1-in2/60.0)*3600.0))
    if inp < 0 : strBase = '-'
    else : strBase=''
    intS = str(in1)
    strBase+=toString(in1)+':'+toString(in2)+':'+toString(in3)
    return strBase

def toString(inp) :
    if abs(inp) < 10 :
        out = '0'+str(abs(inp))
    else : out = str(inp)
    if inp < 0 : return '-'+out
    else : return out

def listToString(inp,sep=',') :
    outStr=''
    for i in inp :
        outStr+=str(i)+sep
    return outStr[:-1]

def convertSexToReal(inp) :
    inTrip = inp.split(':')
```

```
    for i in range(len(inTrip)) : inTrip[i] = float(inTrip[i])
    if inp[0] == '-' : return inTrip[0]-inTrip[1]/60.0-inTrip[2]/3600.0
    else : return inTrip[0]+inTrip[1]/60.0+inTrip[2]/3600.0


def cleanUp() :
    for i in range(1,24) :
        print 'Doing antenna %i' %i
        os.system("rm -rf a%i.*" % i)
    for i in ['ovro','carma','hatcreek','sza','sza6','sza10'] :
        print 'Doing style %s' %i
        os.system("rm -rf %s.*" % i)
    os.system("rm -rf gains* temp*")


def writeStats(model,doGainNoise=False,illuminateType='miriad',refinement=0.5,\
               haStart=-2,haStop=2,doQuick=False,gnoise=0.1,pnoise='0,0,0,0',\
               configs=['D'],cell=0.125,pointingError=None,pointPat='hex1_15'):
# USER: The image fidelity is recorded for a given run in this routine.
# USER: The statistics file is defined.
# USER: Some fine tuning of region is sometimes necessary.
    outputFile='imageRuns.stat'
# USER: This modelSize command will not compile as is.
    modelSize=float(os.popen("histo in=%s | grep Mean | awk '{printf($8)}'" % \
                             model).read()[1:])
    boxVal     = float(int(cell*((modelSize**0.5)/2.0)))
    region     = ("'arcsec,boxes(%s,-%s,-%s,%s)'" % \
                 (boxVal,boxVal,boxVal,boxVal) )
#    region     = "'arcsec,boxes(-150,-150,150,150)'"
# USER: The beam size is determined from the cleaned image.
# USER: The b values below will not compile as is.
    b1=float(os.popen("prthd in=%s.cm | egrep Beam     | awk '{print $3}'" % \
```

```
            model).read())
    b2=float(os.popen("prthd in=%s.cm | egrep Beam     | awk '{print $5}'" % \
            model).read())
    b3=float(os.popen("prthd in=%s.cm | egrep Position | awk '{print $3}'" % \
            model).read())
#
# USER: The residual rms, maximum and minimum are obtained from the map
# USER: obtained by differencing the simulation and model.
# USER: These SRMS/SMAX/SMIN commands will not compile as is.
    SRMS=float(os.popen("histo in=%s.resid region=%s | grep Rms | \
               awk '{printf($4)}'" % (model,region)).read())
    SMAX=float(os.popen("histo in=%s.resid region=%s | grep Maximum | \
               awk '{printf($3)}'" % (model,region)).read())
    SMIN=float(os.popen("histo in=%s.resid region=%s | grep Minimum | \
               awk '{printf($3)}'" % (model,region)).read())
# USER: The parameters of the model convolved to the resolution of the
# USER: simulation are obtained.
# USER: The Model and simulation flux and peak commands will not compile as is.
    Model_Flux = float(os.popen("histo in=%s.regrid region=%s  | grep Flux | \
                        awk '{printf($6)}'" % (model,region)).read())
    Model_Peak = float(os.popen("histo in=%s.regrid region=%s  | grep Maximum |\
                        awk '{printf($3)}'" % (model,region)).read())
# USER: Finally, the peak and flux of the simulated image are calculated.
    Flux       = float(os.popen("histo in=%s.cm region=%s    | grep Flux | \
                        awk '{printf($6)}'" % (model,region)).read())
    Peak       = float(os.popen("histo in=%s.cm region=%s    | grep Maximum |\
                        awk '{printf($3)}'" % (model,region)).read())
# USER: Again, gaussianFits is not typically used and
# USER: requires additional information not included here.
    if gaussianFits :
```

```
        baseFile = strJoinChar(model.split('.')[:-2],'.')
        [majors,minors,pas,fluxs,offsets,decons] = \
             makeModel.fitSimpleModel(baseFile,searchSize=15.0)
# USER: Fidelity and other statistics are printed to the statistics file.
    print Peak,SRMS
    Fidelity   = Peak/SRMS
    print Fidelity
    f=open(outputFile,'a')
    f.write("-------------------------------------------------------------\n")
    f.write("Date: %s\n" % str(time.gmtime()[0:6]))
# USER: The following write commands will not compile as is.
    f.write("DETAILS:  IllumType: %s  HaRange: %f,%f  Refinement: %f  Cell: \
            %f  doGainNoise: %s  actLikePoint: %s resolution: %8.3f,%8.3f,\
            %8.3f  configs: %s\n" % \
            (illuminateType,haStart,haStop,refinement,cell,str(doGainNoise),\
            str(actLikePoint),b1,b2,b3,configs) )
    f.write("DETAILS:  Model: %s  PointFile: %s  GNoise: %f  PNoise: %s  \
            PointError: %s  DeconType: %s doQuick: %s \n" % (model,pointPat,\
            gnoise,pnoise,str(pointingError),typeDecon,str(doQuick)) )
    if gaussianFits :  f.write("DETAILS: Major: %s  Minor: %s Pa: %s Flux: %s\
                               Offset: %s Decon: %s\n" % (majors,minors,pas,\
                               fluxs,offsets,decons) )
# USER: Beginning here, the commands should compile .
    f.write(" SRMS   SMAX   SMIN  M_Flux   M_Peak Flux    Peak  Fidelity\n")
    f.write("%7.4f %7.4f %7.4f %7.3f %7.3f  %7.2f %7.3f %6.2f\n" % \
            (SRMS,SMAX,SMIN,Model_Flux,Model_Peak,Flux,Peak,Fidelity))
    f.close()

def strJoinChar(input,char=None) :
    outStr=''
```

```
for i in input :
    if char==None : outStr=outStr+i
    else : outStr=outStr+i+char

if char==None :
    return outStr
else :
    return outStr[:-1]
```